UNIVERSITE LOUIS PASTEUR

ECOLE NATIONALE SUPERIEURE DE PHYSIQUE DE STRASBOURG

LABORATOIRE DES SYSTEMES PHOTONIQUES



# THESE

présentée pour obtenir

le titre de Docteur de L'Université Louis Pasteur

Discipline: Physique et Photonique

par

Katrin SCHMITT

Date de soutenance: 29 Juin 2006

# UN NOUVEAU DISPOSITIF INTERFEROMETRIQUE POUR LA DETECTION DE BIOMOLECULES SANS ADJUVANT

---

| | |
|---|---|
| Directeur de thèse | P. MEYRUEIS |
| Co-Directeur de thèse | A. BRANDENBURG |
| Rapporteur interne | J. FONTAINE |
| Rapporteur externe | E. WAGNER |
| Rapporteur externe | P. LAMBECK |



UNIVERSITE LOUIS PASTEUR

ECOLE NATIONALE SUPERIEURE DE PHYSIQUE DE STRASBOURG

LABORATOIRE DES SYSTEMES PHOTONIQUES

# THESIS

presented to obtain the

Doctorate Degree in the Louis Pasteur University of Strasbourg

in Physics

by

Katrin SCHMITT

## A NEW WAVEGUIDE INTERFEROMETER FOR THE LABEL FREE DETECTION OF BIOMOLECULES

June, 29th 2006 before the doctoral committee:

| | |
|---|---|
| Thesis supervisor | P. MEYRUEIS |
| Co-supervisor | A. BRANDENBURG |
| Rapporteur | J. FONTAINE |
| Rapporteur | E. WAGNER |
| Rapporteur | P. LAMBECK |

# Acknowledgements

Hereby I like to express my great gratitude to everyone who made this work possible.

I am deeply grateful to Prof. Patrick Meyrueis from the LSP in Strasbourg and to PD Dr. Albrecht Brandenburg from the IPM in Freiburg for assuming the supervision of this thesis as part of a joint project and for their unrestricted guidance and support. I also thank Prof. Elmar Wagner, Prof. Joël Fontaine and Prof. Paul Lambeck for their interest in this work and for their support in completing this dissertation.

I also like to thank Dr. Christian Hoffmann and Dr. Bernd Schirmer from the IPM for their aid and support wherever needed during my thesis work and all their helpful discussions. In particular for the final editing of this dissertation, I am indebted to Christian for his detailed corrections that have greatly helped to improve this document.

At the IPM, I would like to thank all the colleagues, especially the bioanalytics group and the OSS department, for the pleasant working atmosphere and their aid and support for the project. I also like to thank Alfred Huber, Karl Kulmus, Heinrich Schulte and Joachim Fuss for constructing the instruments and their aid in assembling, Monika Stefan for her help in the clean room, and Nicole Ebentheuer and Peter Oswald for carrying out some of the test measurements and their contributing in the nice lab atmosphere.

Further I like to thank the following persons for test measurement collaborations:
Dr. Kristian Müller from the Biological Institute of the University of Freiburg for making the BIACORE 1000 available to us and Dr. Steffen Hartmann from Novartis, Basel for his support during our measurement campaign with the BIACORE 2000. I also like to thank Unaxis Optics in Liechtenstein for supplying the waveguide chips and Dr. Jörg Kraus and Dr. Bernd Maisenhölder for the supportive and friendly cooperation.

Finally I am deeply grateful for the love and support from my family. They have always supported my decisions, no matter what. Most importantly, I like to thank Sebastian for sharing many joyful years with me and all his help and patience in completing this work.

# Résumé

Le développement rapide des sciences et technologies de la vie nécessite de nouvelles méthodes et de nouveaux dispositifs miniaturisés pour l'analyse des interactions biomoléculaires. Les systèmes optiques de détection de biomolécules basés sur la détection de champs évanescents pour l'analyse de liaisons biomoléculaires font l'objet d'un accroissement rapide de leurs applications en matière de diagnostic, monitoring de soins, développement de nouveaux médicaments. Pour être efficace un nouveau biocapteur photonique doit être un instrument à haute sensibilité, précis et fiable, tout en étant adapté ou adaptable à un large spectre d'application.
Dans le chapitre 1, nous précisons nos objectifs : proposer un microdispositif original à haute sensibilité de type biochip, opérant sans adjuvant exploitant le principe d'un micro interféromètre de Young. Nous décrivons l'architecture, le fondement technologique, et la nécessaire caractérisation théorique et expérimentale du dispositif ciblé.
Dans le chapitre 2 nous présentons les bases théoriques que nous avons exploitées pour développer le microsystème ciblé particulièrement la propagation de la lumière dans les guides d'onde planaires. Un résumé des points essentiels concernant les biocapteurs est ensuite introduit en le complétant par une présentation des méthodes de calcul d'optimisation que nous proposons d'utiliser. Une partie de ce chapitre est donc dévolue aux bases des méthodes interférométriques que nous avons mises en œuvre. Une autre partie concerne le traitement du signal, nous rappelons le principe du traitement de Fourier rapide et la méthode que nous avons sélectionnée pour sa mise en œuvre. Nous introduisons ensuite le processus d'implémentation de cette méthode du traitement du signal concernant notamment des réductions du bruit par filtrage.
Le chapitre 3 est dédié aux considérations théoriques ayant trait aux connaissances en biochimie nécessaires pour la fonctionnalisation des effets biophotoniques. Nous traitons ensuite de la théorie cinétique des interactions biochimiques comme les réactions anticorps-antigènes. Les mises en liaisons sont décrites en détail en préparant ainsi les mesures de validations décrites au chapitre 5. Une introduction est ensuite donnée à la stratégie de mesure expérimentale que nous avons retenue.
L'architecture finale du biocapteur interférométrique que nous proposons est présentée dans le chapitre 3 avec 2 variantes : un système à débit à deux canaux d'écoulement et une système statique MTP (microtiterplate). Le choix de l'architecture et des composants sélectionnés sont justifiés en détail. Nous en faisons de même pour la méthode d'analyse

et de discussion des performances. Il en résulte un certain nombre de conclusions qui nous permettent d'établir le choix définitif du matériau substrat de la source de lumière et du détecteur. Nous exposons comment nous avons optimisé l'architecture finale à partir de l'analyse des conséquences des différents choix que nous avons eu à effectuer, pour obtenir des performances globalement optimales. Des compléments de caractérisation par des tests réfractométriques sont ensuite décrits. Ce qui nous permet d'accéder à une comparaison pertinente entre les résultats théoriques et expérimentaux. Nous avons ainsi obtenu une résolution en indice de $6 \cdot 10^{-8}$ dans le cas des écoulements dynamiques avec un taux d'échantillonnage de 1 Hz. Cette résolution a été ensuite améliorée en introduisant un nouveau CCD. Nous avons pu en déduire que en ce cas le facteur limitant est en fait le CCD en ce qui concerne le bruit de phase. Le bruit de phase est par contre égal pour les 3 sources de lumière testées. Ces sources peuvent donc tre exclues comme origines majoritaires de bruit de phase. Nous complétons notre optimisation par l'adjonction de filtres dont nous discutons le processus d'exploitation. La sensibilité expérimentale globale est ainsi en pleine accordance avec la simulation. La stabilité est excellente avec une dérive inférieure à $10^{-6}$ par heure. Nous décrivons ensuite le montage de qualification pour le cas MTP avec 8 cellules. Nous justifions les choix technologiques en ce cas. Nous qualifions ensuite les résultats expérimentaux. Nous utilisons de l'éthanol pour les tests réfractométriques et nous obtenons une résolution en indice de $1.2 \cdot 10^{-6}$ et $4.5 \cdot 10^{-7}$ pour les modes TE et TM avec un échantillonnage à 1 Hz. Dans ce cas le CCD est aussi le composant limitant mais il faut lui associer comme source significative de perturbation une dérive de la répétabilité des valeurs enregistrées. La stabilité de la réponse par contre est inférieure à $5 \cdot 10^{-5}$ par heure. Dans le chapitre 5 nous présentons une validation opérationnelle des micro dispositifs que nous avons conçus et réalisés sur un cas biologique effectif. Nous discutons les résultats dans les 2 cas : statique et dynamique. Nous décrivons la procédure de test. Différents effets de surface sont caractérisés par la mesure de l'angle de contact. Nous comparons les résultats à ceux existants dans le littérature. Nous y ajoutons des expérimentations avec des effets fluorescents pour optimiser la caractérisation de différentes modifications de la surface que nous avons testées pour obtenir les fonctionnalités les plus robustes. La protéine G - IgG est enfin testée dans les cas statiques et dynamique. Tous ces résultats sont également conformes à ceux publiés dans la littérature. Nous pouvons même procéder avec nos micro dispositifs à une évaluation de la cinétique qui est aussi conforme aux données provenant de la littérature. Nous validons ensuite la détection de la protéine G par la protéine A. Les tests sont poursuivis sur cytochrome c biotinylé sur une surface sensibilisée à la streptavidine. Une comparaison avec les résultats obtenus avec un système commercialisé valide la conformité des fonctions implémentées par rapport aux objectifs. Dans le cas de validation que nous avons retenu, nous prouvons donc que notre micro système biophotonique donne des résultats équivalents à un des meilleurs systèmes commerciaux disponibles mais avec une bien plus grande simplicité d'utilisation et avec un encombrement très faible.

Dans le chapitre 6 nous faisons un bilan de notre travail théorique et expérimental en rappelant les points principaux de nos aboutissements de façon synthétique. Nous concluons par quelques éléments de prospective concernant les évolutions futures des concepts de la méthode et de la technologie que nous avons proposée.

# Summary

The rapid development in life science research requires continually new methods for the analysis of biomolecular interactions. Optical detection systems based on evanescent field sensing for biomolecular binding studies are marked by a fast increase of their applications in fields like diagnostics, health care, screening or assay development. For a successful implementation the optical biosensors need to be highly sensitive, selective and accurate while allowing a wide range of applications. In this thesis we present a highly sensitive label-free detection method based on the optical principle of a Young interferometer and describe the design and realization of the system including an experimental characterization and a validation of the biosensor system by application measurements.

In chapter 2, the theoretical basis of the propagation of light in planar waveguides and a background of evanescent field sensors is provided as well as calculations concerning the optimization of waveguide sensitivity for the interferometric biosensor proposed in this thesis. One section is devoted to the theoretical basis of interferometry, especially the optical principle of the Young interferometer since the proposed design for the interferometric biosensor is based on the Young configuration. For signal evaluation, algorithms based on Fast Fourier Transform are described and the implementation in the biosensor system proposed along with system principles and relationships and signal filtering methods for noise reduction.

Chapter 3 is devoted to theoretical considerations on the biochemistry for waveguide surface functionalization. The kinetic theory of biochemical interactions such as antibody-antigen binding events is described in detail with respect to the evaluation of the application measurements in chapter 5. Furthermore a biochemical background on the application measurement reagents is given.

The design of the interferometric biosensor is presented in chapter 4, describing two different readout schemes: a flow-cell system implementing a two-channel flow cell as fluidic element, and a system setup designed for the readout of microtiterplate (MTP)-formatted wellplates. The system components and system designs of the interferometric biosensor and their performance are discussed in detail. From the analysis of system components several conclusions can be made, such as the choice of waveguide chip materials, the light source and the CCD detector. The characteristics of the chosen components influence the final design and setup, leading to an optimal set of parameters for the interferometric biosensor. Further a detailed system characterization by refractometric test measurements

is provided including an evaluation of the experimental results compared to theoretical calculations and simulations. Initial refractometric test measurements on the flow-cell system with glycerin show an effective refractive index resolution of $\approx 6.0 \cdot 10^{-8}$, corresponding to a refractive index resolution of $\approx 7.5 \cdot 10^{-7}$ for TE mode and $\approx 2.7 \cdot 10^{-7}$ for TM mode, respectively, at a sampling rate of 1 Hz. It is also found that the CCD sensor is the limiting system component concerning phase noise, whereas the phase noise is approximately equal for all three light sources tested and therefore the light source can be excluded as limiting factor. Signal filtering methods such as average filters are described and analyzed concerning their suitability for phase noise reduction.
The experimentally derived sensitivity constants of the interferometer system are in very good accordance with the theoretical values derived from waveguide theory in chapter 2. The flow-cell system shows a good long-term stability with a typical drift of $< 1 \cdot 10^{-6}$/h in $\Delta n_{eff}$.
This chapter also presents the system design and describes the realized setup of the interferometric biosensor with an MTP-formatted 8-well frame as fluidic element and newly introduced system components that are different from the flow cell system are discussed. Suitable system components are chosen for an optimal set of design parameters for the interferometric biosensor. The proposed biosensor system is characterized by refractometric test measurements with ethanol solutions and the experimental results are evaluated and compared to theory and the results obtained with the flow cell system. The refractometric test measurements on the microplate system show an effective refractive index resolution of $\approx 1.0 \cdot 10^{-7}$, corresponding to a refractive index resolution of $\approx 1.2 \cdot 10^{-6}$ for TE mode and $\approx 4.5 \cdot 10^{-7}$ for TM mode, respectively, at a sampling rate of 1 Hz. We found that, apart from the CCD sensor being the limiting system component concerning phase noise, the resolution of the microplate system is finally limited by the repeatability of the recorded data values.
The experimentally derived sensitivity constants of the microplate interferometer system are also in good accordance with the theoretical values derived from waveguide theory in chapter 2. The system shows a long-term stability with a typical drift of $< 5 \cdot 10^{-5}$/h in $\Delta n_{eff}$ and a repeatability of $< 2 \cdot 10^{-7}$ in $\Delta n_{eff}$.
Chapter 5 presents a validation of the interferometric biosensor by biological application measurements on both systems and their discussion. In this chapter a detailed description of the materials and methods used for application and test measurements, a characterization of the surface chemistry on the $Ta_2O_5$ waveguide chips and finally application measurements on different affinity systems is provided. Differently functionalized surfaces are characterized by contact angle measurements and compared to literature values. Experiments with fluorescently labeled streptavidin allow a detailed characterization of different surface modifications and a direct comparison to measurements with the interferometric biosensor with the aim to find a stable and robust surface functionalization for the immobilization of biotinylated reagents.

The immunoassay protein G - IgG is tested on the flow-cell system as well as on the microplate system, yielding affinity rate constants that are in good agreement with values found in literature. Experimental data obtained with the two-channel flow-cell system allow an evaluation of the reaction kinetics, while the microplate system is suited for the parallel detection of several analyte concentrations. Furthermore the direct detection of IgG by immobilized protein A is shown and the affinity rate constants determined. Test measurements with biotinylated cytochrome *c* on a streptavidin-functionalized surface compared directly to the same assay performed on the commercial biosensor system BIACORE 1000 show the suitability of the developed surface chemistry for the $Ta_2O_5$ waveguide chips implemented in the interferometric biosensor.
The interferometric biosensor has been successfully used for the detection of the affinity system $\alpha$-NPT IgG - E2-NPT developed at Novartis in Basel. We tested the assay on both the interferometric biosensor (flow-cell system) and the commercial BIACORE 2000 system provided by Novartis. A comparison of the surface chemistries used on both biosensor systems is presented, and a series of measurements to detect the analyte from different sample buffers. We found that the performance of the interferometric biosensor system proposed in this thesis is approximately equal to the BIACORE system with a detection limit for the analyte in the low picomolar range. Measurements in cell lysate as sample matrix show that with the interferometric biosensor the analyte can be detected even out of a complex sample matrix without significant unspecific binding.
In chapter 6, conclusions concerning the development of the interferometric biosensor and the results from the experimental characterization and validation are presented. A comparison between the proposed interferometric biosensor and other label-free biosensors is given. The chapter concludes with an outlook concerning further improvements of the resolution and surface chemistry and further possibilities for developments to adapt the sensor design to high throughput applications.

# Contents

# List of Figures

# List of Tables

# Abbreviations

| | |
|---|---|
| AFM | Atomic force microscope |
| APTS | 3-Aminopropyl-triethoxysilane |
| BSA | Bovine serum albumin |
| CAD | Computer Aided Design |
| DFT | Discrete Fourier Transformation |
| DI | De-ionized |
| DLL | Dynamic link library |
| ELISA | Enzyme-linked Immunosorbent Assay |
| FFT | Fast Fourier Transformation |
| FT | Fourier Transformation |
| FWHM | Full Width at Half Maximum |
| GOPS | 3-Glycidoxypropyl-triethoxysilane |
| HTS | High throughput screening |
| IAD | Ion assisted deposition |
| IgG | Immunoglobulin G |
| kDa | kiloDalton |
| LED | Light emitting diode |
| MTP | Microtiterplate |
| MZI | Mach-Zehnder interferometer |
| PBS | Phosphate buffered saline |
| RifS | Reflectometric interference spectroscopy |
| SAM | Self-assembled monolayer |
| SAv | Streptavidin |
| SCM | Spectral correlation method |
| SDS-PAGE | Sodium Dodecyl Sulfate Polyacrylamide Gel Electrophoresis |
| SLD | Superluminescent diode |
| SNR | Signal-to-noise ratio |
| SPR | Surface plasmon resonance |
| TE | Transversal electric |
| TM | Transversal magnetic |
| WIOS | Wavelength interrogated optical sensor |
| YI | Young interferometer |

# Chapter 1

# Introduction

## 1.1 General introduction

Today many scientists are working on the same goal: to unravel the secrets of life. Several years after the completion of the human genome project the focus is now on another molecular species in the human body: the proteins. The constellation of all proteins in a cell is called proteome, and studies elucidating protein activity and function is named proteomics, a fast growing research field that will become even more important in the future. Proteomics has the potential to provide insights in structure, function and expression data of proteins and thus is of great interest in areas like drug discovery, diagnosis, pharmacological and toxicological studies.

Yet mapping the proteome is by far a more difficult and cost- and time-consuming task than mapping the genome, so there is a need to think about efficient ways and tools to help identifying the huge amount of different proteins in the body and their functions and activities. In the last years improvements in technologies like two-dimensional gel electrophoresis, mass spectrometry and the development of protein-based arrays and various kinds of biosensors have contributed to manage this task (*Hebestreit*, 2001).

Another issue is the screening for new molecules, predominantly in pharmaceutical research. Here it is important to detect even very small analyte molecules and get information about their reactivity with a huge amount of different receptors such as antibodies,

which also demands efficient tools to recognize these various affinity systems by monitoring several thousands of reactions every day. This research field is named high throughput screening (HTS), and 100000 assays in a miniaturized format are anticipated to be soon routine in laboratories (*Hertzberg and Pope*, 2000).

## 1.2 Label-free biosensors

In many cases, the molecule of interest is prepared with a label, such as fluorescent dyes, radioactive markers, or colorimetric reactands. The most popular labeling method is using fluorescent markers that are nowadays available at almost each wavelength within the visible spectrum of light, plus UV and near infrared. Established assay protocols and sophisticated detection technology make the use of these dyes easy and convenient, but also mean an additional step in the assay protocol for labeling. Furthermore, a certain level of photobleaching and/or quenching when exposed to light is inherent to fluorescent dyes, which is a drawback when quantitative information is needed. Also, a marker of any kind attached to a biomolecule might alter its functionality, conformation, or reactivity with its binding partner. In the worst case, a binding site gets occupied by the marker molecule and the binding event is totally impeded, leading to false negatives. Another disadvantage is a relatively high background signal that might give a false positive.
These facts, among the labeling step being cost- and time-consuming, have induced an increasing demand for technologies allowing a label-free detection of biomolecular interactions. One approach is the use of label-free biosensors. *Biosensors* are generally considered to be a subgroup of chemosensors, consisting of a selective biological component and a transducer (*Ramsden*, 1997; *Cammann*, 2000). This transducer transforms physical changes due to the recognition of the biomolecule into an electrical signal. A special kind of biosensor is the label-free optical biosensor. The first biosensors of this type appeared in the 1980s with the expanded development of surface plasmon resonance (SPR) and optical waveguide sensors (*Cooper*, 2002, 2003). Since then many other types of label-free optical biosensors evolved with a growing range of applications. A review of label-free optical biosensors can be found in (*Leatherbarrow and Edwards*, 1999) or (*Baird*

*and Myszka*, 2001).

The most commonly found label-free biosensor in laboratories is probably the SPR sensor, which relies on the detection of changes in the surface coverage within the evanescent field (*van der Merwe*, 2005). The evanescent field is an exponentially decaying part of the light of a guided mode found directly above (or below) the waveguide. In the case of SPR, a glass substrate is coated with a thin gold film. When illuminated with light from a certain angle, a maximum of light intensity is transferred into the gold layer where oscillating plasma waves (surface plasmons) are excited. Thus a minimum of light is reflected back into the substrate. This angle is called the surface plasmon resonance angle. Any kind of change in surface coverage on the gold film, caused by e.g. biomolecule binding, results in a change of this angle, and these changes are constantly monitored and evaluated. The optical setup and operation was first described by *Kretschmann and Raether* (1968).

Other label-free optical biosensors are for example the grating coupler (*Bilitewski et al.*, 1998; *Lukosz et al.*, 1991; *Polzius et al.*, 1997), narrow bandwidth guided-mode resonant filter systems (*Cunningham et al.*, 2002) or reflectometric interference spectroscopy (RifS) (*Kröger et al.*, 2002; *Schütz*, 2000). The grating coupler system consists of a waveguide chip with etched gratings and can be configured either as input or as output grating coupler and thus measures an incoupling or outcoupling angle, respectively, as a function of changes in surface mass coverage in the evanescent field. The guided-mode resonant filter system uses a sub-wavelength grating waveguide structure in a plastic substrate which reflects only a very narrow band when illuminated with white light at normal incidence. The resonantly reflected wavelength depends upon the surface optical density and thus the detection phenomenon actually occurs within the waveguide and not in an evanescent wave. This system has already been configured to work with up to 384 well microtiterplates (MTP) (*Cunningham et al.*, 2004) as an efficient tool for HTS.

The third system mentioned above, RifS, is based on the spectral distribution of reflectance of thin films on a glass substrate when illuminated with white light. This spectral pattern changes when the surface coverage is changing. The RifS system was the first label-free system set up to read 96 well MTPs, also for HTS (*Kröger et al.*, 2002). Another wide-spread class of label-free optical biosensors is represented by vari-

ous interferometric systems, among them the Rayleigh interferometer (*Chen et al.*, 2003), Mach-Zehnder interferometer (*Weisser et al.*, 1999), Hartmann interferometer (*Schneider et al.*, 1997, 2000) and Young interferometer setups (*Brandenburg et al.*, 2000; *Ymeti et al.*, 2002; *Cross et al.*, 2003). Other interferometric approaches include for example the integrated-optical (IO) difference interferometer (*Stamm et al.*, 1998) and the spectral correlation method (*Nikitin et al.*, 2003).
Theoretical estimations have compared the sensitivities of IO devices including interferometers and surface plasmon resonance sensors (*Lukosz*, 1991); here IO interferometric systems are predicted to have the highest sensitivity.

## 1.3 Aim of the Thesis

Among the various kinds of label free biosensors one approach for sensitive, label-free detection of biomolecules is the interferometric detection implementing optical waveguides as sensing elements, as proposed by Brandenburg (*Brandenburg et al.*, 2000). In his work a Young interferometer design based on a silicon oxinitride waveguide structure as beam splitter and sensing element is proposed.
The main goal of this thesis is then to elaborate an interferometric system based on a Young interferometer for the extremely sensitive detection of biomolecules which is suitable for high throughput biochemical and biological analysis. The core of this system is a planar optical waveguide chip where gratings are used as light coupling elements. Unlike the previous IO Young interferometer setup, where the waveguide chip combined the interferometer itself and the sensing area, this design is free-spaced, i.e. the waveguide chip operates solely as sensing element. Preliminary work on a two-channel prototype of such an interferometric system (*MacKenzie*, 2003) has shown that this configuration is efficient and suitable for various biological applications.
As a first step, the two-channel system is optimized in terms of signal-to-noise ratio and system stability in order to perform highly sensitive and reproducible measurements. For biological applications, appropriate surface chemistries are developed and tested. Different biochemical assays are realized and the resulting system is experimentally compared

with competing technologies based on SPR.
In a second step, the existing system is redesigned to an MTP reading format for high throughput analysis of biochemical interactions. The system setup is realized and test measurements for calibration and characterization are performed. Subsequently simple biological measurements show the suitability of this interferometer system for further use in research and medical diagnosis or screening.
In chapter 2, the basic theory of planar waveguides and of the Fast Fourier transformation for interferogram signal analysis is presented. Chapter 3 is devoted to theoretical considerations on the biochemistry needed for waveguide surface functionalization, along with the kinetic theory of biochemical interactions such as antibody-antigen binding events. In chapter 4, the design of both the two-channel configuration and the MTP readout interferometric system and their performance characteristics are discussed in detail. The following chapter presents biological application measurements on both systems and their discussion. Finally a general conclusion and an outlook are given in chapter 6.
This thesis is part of a joint project between the University of Strasbourg (ULP), France and the Fraunhofer Institute for Physical Measurement Techniques (IPM) in Freiburg, Germany. The project is part of the INTERREG IIIa-Rhenaphotonics project.

# Chapter 2

# Theoretical background in optics

## 2.1 Introduction

A brief overview on the theory of optical waveguides shall be given in this chapter to provide a background on our work. An optical waveguide, also known as dielectric waveguide, is a structure that is able to confine and guide light. There exist various kinds of optical waveguides, the most prominent probably being the optical fiber used in telecommunications. Integrated optics constitute another kind of optical waveguide. Here mostly planar optical waveguides are of interest. Since in the interferometric biosensor described in this thesis also a planar waveguide is used as sensing element, the theoretical considerations given here will focus on this type of waveguide. A more comprehensive description of the theory of optical waveguides can be found in (*Kogelnik*, 1988).

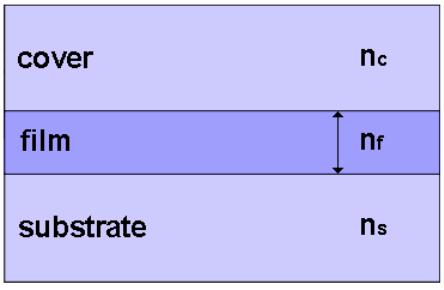


**Figure 2.1:** Cross-section of a planar waveguide. A medium of high refractive index $n_f$ is surrounded by media with lower refractive indices $n_c$ and $n_s$.

In the simplest case of a planar waveguide a substrate is coated with a thin film (typically with a thickness ranging from several hundred nanometers up to several hundred micrometers) of a high-refractive medium ($n_s < n_f$). The cover medium is air with $n_c < n_s < n_f$. In the following theoretical descriptions all the dielectric media are assumed to be ideal, i.e. homogeneous, isotropic and loss-free.

## 2.2 Refraction and reflection in ray optics

We consider two ideal dielectric media with refractive indices $n_1$ and $n_2$ separated by an interface in the xy-plane (*Kogelnik*, 1988). A monochromomatic and coherent light beam incident at an angle $\varphi_1$ between the wave normal and z is partially reflected at the same angle $\varphi_1$ and partially refracted into the adjacent medium at $\varphi_2$ as shown in Fig. 2.2.

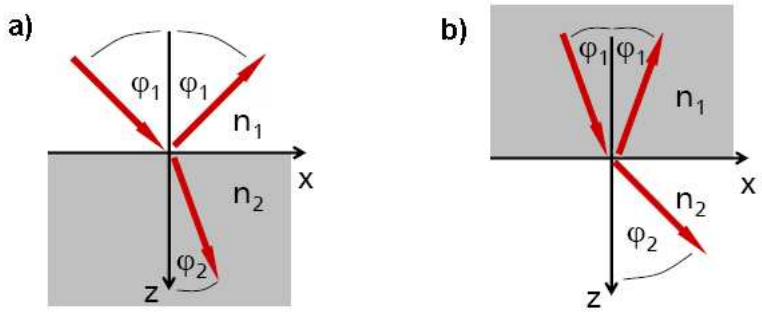


**Figure 2.2:** Refraction and reflection at a planar interface separating two media of refractive index $n_1$ and $n_2$. Shown is the wave normal with an angle of incidence $\varphi_1$. **a)** Transition into an optically denser medium ($n_1 < n_2$). **b)** Transition into an optically less dense medium ($n_1 > n_2$).

The angle $\varphi_2$ of the refracted wave is given by Snell's law:

$$n_1 \cdot sin\varphi_1 = n_2 \cdot sin\varphi_2. \tag{2.1}$$

The amplitudes of the refracted and reflected wave depend on the angle of incidence and on the polarization of the incident light. These amplitudes can be calculated using the reflection and transmission coefficients given by the Fresnel formulas. For $\sigma$-polarization (i.e. the electric field is perpendicular to the plane of incidence spanned by the wave

normal and the normal to the interface) we have

$$\begin{aligned} \rho_\sigma &= \frac{n_1 \cdot cos\,\varphi_1 - n_2 \cdot cos\,\varphi_2}{n_1 \cdot cos\,\varphi_1 + n_2 \cdot cos\,\varphi_2} \\ &= \frac{n_1 \cdot cos\,\varphi_1 - n_1 \cdot \sqrt{n_2^2 - n_1^2 \cdot sin^2\,\varphi_1}}{n_1 \cdot cos\,\varphi_1 + n_1 \cdot \sqrt{n_2^2 - n_1^2 \cdot sin^2\,\varphi_1}} \end{aligned} \tag{2.2}$$

$$\tau_\sigma = 1 - \frac{sin\,(\varphi_1 - \varphi_2)}{sin\,(\varphi_1 + \varphi_2)}, \tag{2.3}$$

with $\rho$ being the reflexion coefficient and $\tau$ the transmission coefficient for the electrical field. For $\pi$-polarization (i.e. the magnetic field is perpendicular to the plane of incidence) the corresponding formulas are

$$\begin{aligned} \rho_\pi &= \frac{n_2 \cdot cos\,\varphi_1 - n_1 \cdot cos\,\varphi_2}{n_2 \cdot cos\,\varphi_1 + n_1 \cdot cos\,\varphi_2} \\ &= \frac{n_2^2 \cdot cos\,\varphi_1 - n_1 \cdot \sqrt{n_2^2 - n_1^2 \cdot sin^2\,\varphi_1}}{n_2^2 \cdot cos\,\varphi_1 + n_1 \cdot \sqrt{n_2^2 - n_1^2 \cdot sin^2\,\varphi_1}} \end{aligned} \tag{2.4}$$

$$\tau_\pi = \left(1 - \frac{tan\,(\varphi_1 - \varphi_2)}{tan\,(\varphi_1 + \varphi_2)}\right) \cdot \frac{cos\,\varphi_1}{cos\,\varphi_2}. \tag{2.5}$$

The so-called critical angle $\varphi_{cr}$ is given by

$$sin\,\varphi_c = \frac{n_2}{n_1}. \tag{2.6}$$

As long as $\varphi_1 < \varphi_{cr}$ we have only partial reflection and $\rho$ remains real-valued. When $\varphi_1 > \varphi_{cr}$, we speak of total reflection and $\rho$ becomes complex valued. In the medium with the lower refractive index a propagating wave is generated which is attenuated exponentially in z-direction. This attenuated wave is called evanescent field and is described by the following expression called decay factor:

$$e^{-\frac{2\cdot\pi}{\lambda_0}\sqrt{n_1^2 \cdot sin^2\,\varphi_1 - n_2^2}\cdot z}, \tag{2.7}$$

with $\lambda_0$ being the vacuum wavelength.

The properties of this evanescent field and its use for planar waveguides as sensors is further described in chapter 2.4.

Additionally the reflected wave encounters a phase shift at the interface according to

$$tan\,\varphi_\sigma = \frac{2 \cdot \sqrt{n_1^2 \cdot sin^2\,\varphi_1 - n_2^2}}{n_1 \cdot cos\,\varphi_1}. \tag{2.8}$$

and

$$tan\,\varphi_\pi = \frac{n_1^2}{n_2^2} \cdot \frac{\sqrt{n_1^2 \cdot sin^2\,\varphi_1 - n_2^2}}{n_1 \cdot cos\,\varphi_1} \tag{2.9}$$

for $\sigma$ and $\pi$ polarization respectively. Introducing the effective refractive index, specifying the phase velocity of the guided light, with

$$n_{eff} = n_1 sin\varphi_1, \tag{2.10}$$

this can be written as (for $\sigma$)

$$\varphi_\sigma = 2 \cdot arctan\sqrt{\frac{n_{eff}^2 - n_2^2}{n_1^2 - n_{eff}^2}}. \tag{2.11}$$

Transferred to the planar waveguide, in the general case of $n_f > n_s > n_c$, there exist two critical angles at the two interfaces, $\varphi_s$ for the reflection at the film-substrate interface and and $\varphi_c$ for the film-cover interface. When the incident angle $\varphi_1$ is large enough, i.e. $> \varphi_s$ and $\varphi_c$, the light is confined in the waveguiding film due to total internal reflection at both interfaces, as depicted in Fig. 2.3.

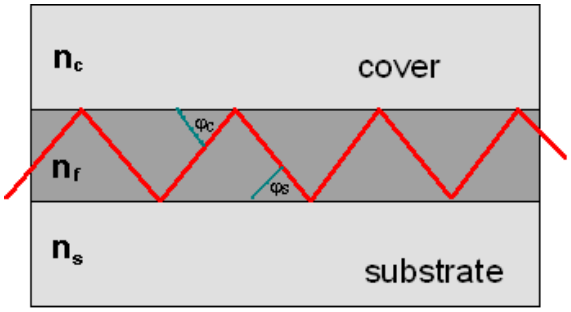


**Figure 2.3:** Total internal reflection in a planar waveguide. Light is confined in the waveguiding film of high refractive index $n_f$ with reflection angles $\varphi_c$ at the waveguide-cover interface and $\varphi_s$ at the waveguide-substrate interface.

The ray optics model is clearly an appropriate model for the illustration of reflection and refraction phenomena at interfaces. Due to the very small dimensions of the waveguide chip used for the interferometric biosensor the wave optics approach might be better suited and shall be discussed in the following chapter.

## 2.3 Electromagnetic theory of planar waveguides

### 2.3.1 Maxwell's equations

The fundamental theory for the description of electrical and magnetic fields is based on Maxwell's equations. In optics we consider the special case of charge- and current-free media, and the equations are expressed by (*Kühlke*, 2004):

$$\vec{\nabla} \times \vec{E} = -\mu \cdot \frac{\partial \vec{H}}{\partial t} \tag{2.12}$$

$$\vec{\nabla} \times \vec{H} = \frac{\partial \vec{D}}{\partial t} \tag{2.13}$$

$$\vec{\nabla} \vec{D} = 0 \tag{2.14}$$

$$\vec{\nabla}(\mu \cdot \vec{H}) = 0, \tag{2.15}$$

where

$\mu$ = magnetic permeability
$\vec{E}$ = electric field
$\vec{H}$ = magnetic field
$\vec{D}$ = electric displacement (with $\vec{D} = \epsilon \cdot \vec{E}$)
$\epsilon$ = permittivity

.

From these equations we can derive the basic equation of wave optics, the wave equation. Vectorial multiplication of eq. 2.10 and 2.11 with $\vec{\nabla}$ and using the identity $\vec{\nabla} \times \vec{\nabla} \times \vec{E} = \vec{\nabla}(\vec{\nabla}\vec{E}) - \vec{\nabla}^2\vec{E}$ as well as $\vec{\nabla}\vec{E} = 0$ yields the wave equations for the electrical and magnetic field:

$$\Delta \vec{E} = \frac{1}{c^2} \frac{\partial^2 \vec{E}}{\partial t^2} \tag{2.16}$$

$$\Delta \vec{H} = \frac{1}{c^2} \frac{\partial^2 \vec{H}}{\partial t^2} \tag{2.17}$$

with $\Delta = \vec{\nabla}\vec{\nabla}$ and $c^2 = (\epsilon\mu)^{-1}$.

The Maxwell equations and the wave equation imply a linear relationship between the two fields. This reflects the principle of superposition: the sum of two solutions is again a solution. Electromagnetic waves can superpose, and this is for example the theoretical background for the description of interference as a superposition of light waves according

to Huygen's principle, which will be discussed in greater detail in chapter 2.5.
In optics applications it is often the case that light transits from one medium to another (e.g. from air into glass), so it is important to know how the electric and magnetic field behave at the interface between two adjacent media with different relative dielectric constants $\epsilon_r^{(1)}$ and $\epsilon_r^{(2)}$ (equal to refractive indices $n_1$ and $n_2$). From Maxwell's equations it can also be derived that at the interface the tangential components of the electric and magnetic field have to be continuous:

$$E_t^{(1)} = E_t^{(2)}$$
$$H_t^{(1)} = H_t^{(2)}.$$

The normal components of both fields are discontinuous at the interface, whereas the normal components of $\epsilon\vec{E}$ (electric displacement) and $\mu\vec{H}$ have to be continuous:

$$\epsilon_0\epsilon_r^{(1)} E_n^{(1)} = \epsilon_0\epsilon_r^{(2)} E_n^{(2)}$$
$$\mu_0\mu_r^{(1)} H_n^{(1)} = \mu_0\mu_r^{(2)} H_n^{(2)}$$

with the permittivity $\epsilon = \epsilon_0\epsilon_r$ ($\epsilon_0$ the permittivity of free space and and $\epsilon_r$ the relative permittivity in the medium) and the permeability $\mu = \mu_0\mu_r$ ($\mu_0$ the permeability of free space and and $\mu_r$ the relative permeability in the medium). In dielectric waveguides $\mu_r$ is usually assumed to be unity.

### 2.3.2 Wave equations for planar waveguides

As a subset of solutions of the Maxwell equations the fields within a dielectric waveguide can be assumed as harmonic wave of the following form:

$$A(t) = A \cdot e^{i\omega_0 t} \tag{2.18}$$

with the angular frequency $\omega_0 = 2\pi c/\lambda$. Inserting this solution and $\vec{D} = \epsilon\vec{E}$ into eqs. 2.10 and 2.11 yields

$$\nabla \times \vec{E} = -i\omega_0\mu_0\vec{H} \tag{2.19}$$

$$\nabla \times \vec{H} = i\omega_0\epsilon\vec{E}. \tag{2.20}$$

For a planar waveguide where z is the direction of light propagation each solution can be described by

$$A(x, y, z) = A_\nu(x, y)e^{-i\beta_\nu z}, \tag{2.21}$$

with $\beta_\nu = \frac{2\pi}{\lambda} \cdot \mathrm{n_f} \cdot \sin\varphi_1$ being the propagation constant and $\nu$ the mode index. The different modes of a waveguide will be discussed in chapter 1.3.3 and the mode index here omitted for simplicity.

Substituting eq. 2.19 into 2.17 and 2.18 and separating x, y and z gives

$$\frac{\partial E_z}{\partial y} + i\beta E_y = -i\omega_0\mu H_x \tag{2.22}$$

$$i\beta E_x + \frac{\partial E_z}{\partial x} = i\omega_0\mu H_y \tag{2.23}$$

$$\frac{\partial E_y}{\partial x} - \frac{\partial E_x}{\partial y} = -i\omega_0\mu H_z \tag{2.24}$$

$$\frac{\partial H_z}{\partial y} + i\beta H_y = i\omega_0\epsilon E_x \tag{2.25}$$

$$i\beta H_x + \frac{\partial H_z}{\partial x} = -i\omega_0\epsilon E_y \tag{2.26}$$

$$\frac{\partial H_y}{\partial x} - \frac{\partial H_x}{\partial y} = i\omega_0\epsilon E_z. \tag{2.27}$$

As shown in Fig. 2.3, the confinement of the waveguide is in x-direction and the light propagating in z-direction. It is also assumed that the waveguide extends infinitely in y-direction, which leaves $\frac{\partial}{\partial y} = 0$, because the electric and magnetic field supported by the waveguide do not depend on this direction.

### 2.3.3 Modes of a planar waveguide

A guided light wave satisfying the condition that it reproduces itself after two reflections (resonance condition, i.e. no phase difference) is called eigenmode, or simply mode of a waveguide (*Saleh and Teich*, 1990). The mode equation for the three-layer planar waveguide discussed in this chapter is according to (*Tiefenthaler and Lukosz*, 1989):

$$2 \cdot k \cdot d\sqrt{n_f^2 - n_{eff}^2} + \varphi_c + \varphi_s = 2\pi m. \tag{2.28}$$

Two types of modes exist for a planar waveguide: the transverse electric (TE) and transverse magnetic (TM) mode. The TE mode only supports electric fields perpendicular to

the direction of propagation, i.e. $E_z = 0$, and the TM mode similarly contains no $H_z$-component. Applying this to eq. 2.20-2.25 and the condition $\frac{\partial}{\partial y} = 0$, the equations yield for TE:

$$\beta E_y = -\omega_0 \mu H_x \tag{2.29}$$

$$\frac{\partial E_y}{\partial x} = -i\omega_0 \mu H_z \tag{2.30}$$

$$\frac{\partial H_z}{\partial x} + i\beta H_x = -i\omega_0 \epsilon E_y. \tag{2.31}$$

Similar for TM:

$$i\beta E_x + \frac{\partial E_z}{\partial x} = i\omega_0 \mu H_y \tag{2.32}$$

$$\beta H_y = \omega_0 \epsilon E_x \tag{2.33}$$

$$\frac{\partial H_y}{\partial x} = i\omega_0 \epsilon E_z. \tag{2.34}$$

Introducing the wave vector $\mathrm{k} = \frac{2\pi}{\lambda}$, the propagation constant $\beta$ is bounded by the following condition for guided modes:

$$\mathrm{k} \cdot \mathrm{n_c}, \mathrm{k} \cdot \mathrm{n_s} \leq \beta \leq \mathrm{k} \cdot \mathrm{n_f}.$$

The solutions satisfying this boundary condition are therefore for TE:

$$\mathrm{E_y} = \begin{cases} Ae^{-\gamma x} & x \geq 0 \\ A\left(cos(\delta x) - \frac{\gamma}{\delta} sin(\delta x)\right) & 0 \geq x \geq -d \\ A\left(cos(\delta h) + \frac{\gamma}{\delta} sin(\delta h)\right) e^{\alpha(x+h)} & -d \geq x \end{cases} \tag{2.35}$$

and for TM

$$\mathrm{H_y} = \begin{cases} Ae^{-\gamma x} & x \geq 0 \\ A\left(cos(\delta x) - \left(\frac{n_f}{n_c}\right)^2 \frac{\gamma}{\delta} sin(\delta x)\right) & 0 \geq x \geq -d \\ A\left(cos(\delta h) + \left(\frac{n_f}{n_c}\right)^2 \frac{\gamma}{\delta} sin(\delta h)\right) e^{\alpha(x+h)} & -d \geq x. \end{cases} \tag{2.36}$$

$$\mathrm{A} = \text{arbitrary constant}$$

$$\alpha = \sqrt{\beta^2 - \mathrm{k}^2 \mathrm{n_s}^2}$$

$$\gamma = \sqrt{\beta^2 - \mathrm{k}^2 \mathrm{n_c}^2}$$

$$\delta = \sqrt{\mathrm{k}^2 \mathrm{n_f}^2 - \beta^2}$$

From these equations the eigenvalue equation can be determined:

$$\tan(\delta \mathrm{d} - \nu\pi) = \frac{\delta(\mathrm{r_c}\gamma + \mathrm{r_s}\gamma)}{\delta^2 - \mathrm{r_c}\mathrm{r_s}\gamma\alpha}, \tag{2.37}$$

where

$$\mathrm{r_{c,s}} = \begin{cases} 1 & \text{for TE modes} \\ \left(\frac{n_s}{n_c}\right)^2 & \text{for TM modes.} \end{cases} \tag{2.38}$$

For the illustration of the results from eq. 2.36 the normalized field distribution $\mathrm{H_y}$ for a TM-mode and mode index m=0 is shown in Fig. 2.4.

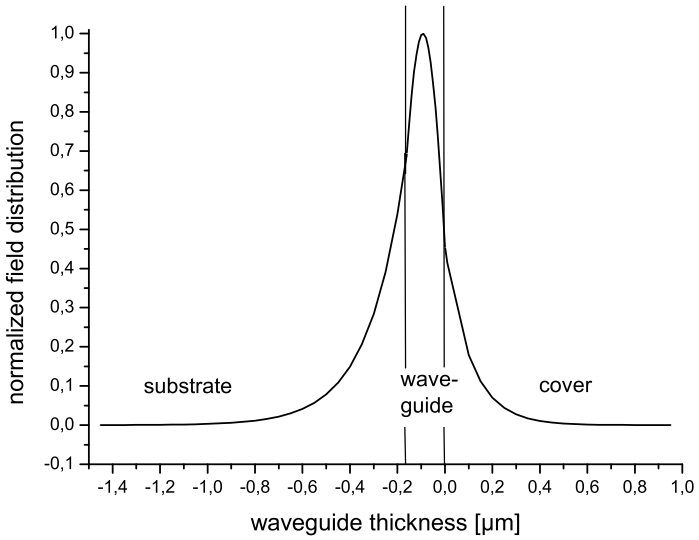


**Figure 2.4:** TM-mode field distribution for a planar waveguide with refractive indices of $\mathrm{n_s} = 1.52$, $\mathrm{n_f} = 2.1$, $\mathrm{n_c} = 1.333$ at $\lambda$=675 nm and m=0.

The eigenvalue equation (2.37) can be solved either graphically or numerically. From eq. 2.28 we see directly that with increasing ratio of waveguide thickness d to the wavelength $\lambda$ more modes can exist. A waveguide is called *monomode* when only one mode (with mode index 0) exists, otherwise it is referred to as *multimode*. Fig. 2.4 and 2.5 show the calculated mode diagrams for TE and TM modes using following parameters: $\mathrm{n_s} = 1.52$, $\mathrm{n_f} = 2.1$, $\mathrm{n_c} = 1.333$ at $\lambda$=675 nm.

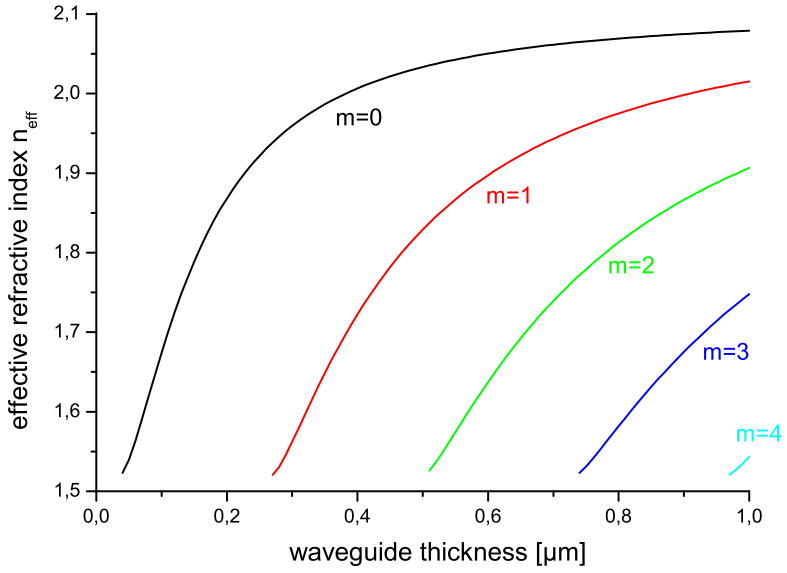


**Figure 2.5:** Mode diagram for TE modes calculated for a dielectric planar waveguide with refractive indices of $n_s = 1.52$, $n_f = 2.1$, $n_c = 1.333$ at $\lambda$=675 nm

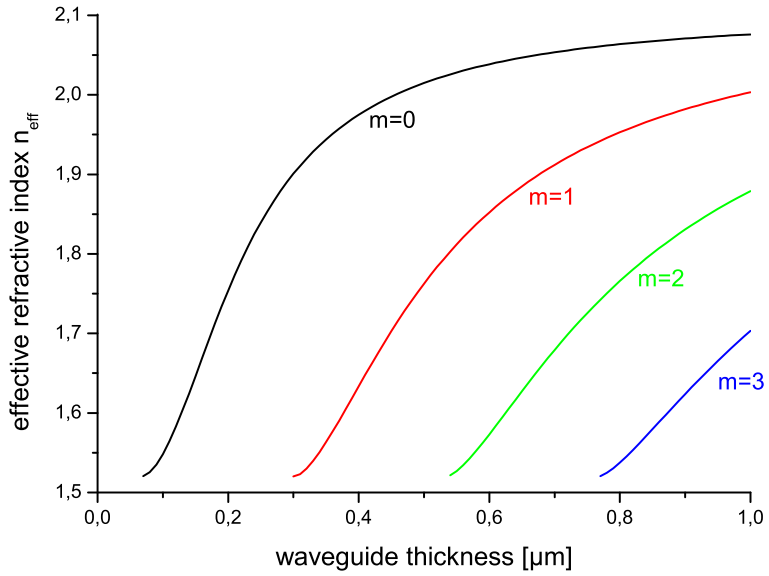


**Figure 2.6:** Mode diagram for TM modes calculated for a dielectric planar waveguide with refractive indices of $n_s = 1.52$, $n_f = 2.1$, $n_c = 1.333$ at $\lambda$=675 nm

## 2.4 Evanescent field sensors

The basis for all integrated-optical and many other sensors based on planar waveguides is the discovery by Lukosz and his colleagues in the 1980's that waveguides with a high refractive index react to changes in their environment, e.g. changes in humidity, altering the properties of the guided light. This phenomenon has been evaluated theoretically in *Tiefenthaler and Lukosz* (1989) and is since then used extensively for chemical and biochemical sensors: the evanescent field.

The principle of evanescent field sensing can be described as follows: outside a (planar) waveguide structure where light is guided lies an exponentially decaying part of the light (see also eq. 2.7), since the light is not confined totally within the waveguide. This evanescent field, typically comprising 30-100 nm, is sensitive to two types of changes in the ambient: either, a liquid sample is covering the sensing region, altering the cover refractive index $n_c$, or molecules from a gaseous or liquid sample adsorb to the waveguide surface forming a thin adlayer of a specific refractive index $n_c$. While in the first case the sensor operates as a pure refractometer, it can be used in the second case as a tool for monitoring the adsorption/binding of any kind of biochemical or biological molecules. When now any of these changes occur at the surface of a waveguide, the phase velocity of the guided mode is decreased according to

$$v_p = \frac{c}{n_{eff}}. \tag{2.39}$$

The effective refractive index of a waveguide depends on following parameters:

$$n_{eff} = n_{eff}(\lambda, n_s, n_f, n_c, d, n_{ad}, t_{ad}, polarization). \tag{2.40}$$

Several ways of detecting the change in phase velocity and thus the effective refractive index in optical systems have evolved, among them grating couplers (*Bilitewski et al.*, 1998; *Lukosz et al.*, 1991) and various interferometers (*Weisser et al.*, 1999; *Schneider et al.*, 1997; *Brandenburg et al.*, 2000; *Ymeti et al.*, 2002). In Fig. 2.7 a schematic of a waveguide chip illustrates the principle of evanescent field sensing with influences on the effective refractive index caused by either a change in $n_c$ or a change the adlayer thickness due to adsorption of biomolecules. The considerations above are only valid for

nonporous waveguides, i.e. only changes on the waveguide surface are detected and no diffusion processes into the waveguide layer causing a change in $n_f$ occur. The general expression for changes in $n_{eff}$ is therefore given by

$$\Delta n_{eff} = \left(\frac{\partial n_{eff}}{\partial t_{ad}}\right) \Delta t_{ad} + \left(\frac{\partial n_{eff}}{\partial n_c}\right) \Delta n_c + \left(\frac{\partial n_{eff}}{\partial n_f}\right) \Delta n_f, \tag{2.41}$$

where the last summand can be omitted for nonporous waveguides and will not be treated in the following chapters.

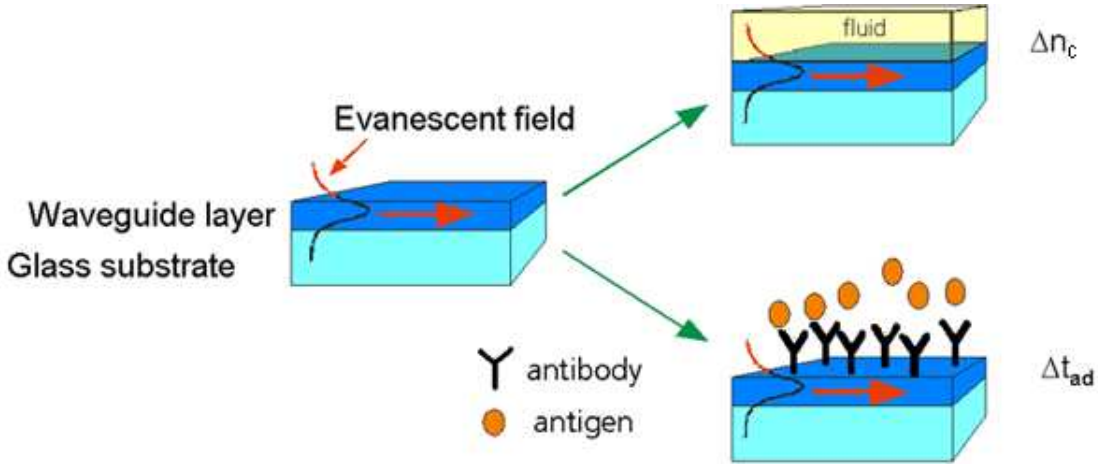


**Figure 2.7:** The principle of evanescent field sensing. A waveguide layer on a substrate is guiding a light mode with phase velocity $v_1$. A change in the effective refractive index and thus a decrease in phase velocity $v_2 < v_1$ is caused by either a change in the cover refractive index $\Delta n_c$ or a change the adlayer thickness $\Delta t_{ad}$ due to molecule adsorption.

### 2.4.1 Sensitivity to cover refractive index changes $\Delta n_c$

From the mode equation 2.28 and expression 2.41 the sensor sensitivity to cover refractive index changes $\frac{\partial n_{eff}}{\partial n_c}$ can be derived, again for a three-layer planar waveguide. These calculations are described in greater detail in *Tiefenthaler and Lukosz* (1989), and here only the main results shall be given.

Assuming an effective waveguide thickness of

$$d_{eff} = d + \Delta z_{f,c} + \Delta z_{f,s}, \tag{2.42}$$

comprising the waveguide thickness d and the penetration depths of the evanescent field in substrate and cover with

$$\Delta z_{f,c} = \frac{\lambda}{2\pi}\sqrt{n_{eff}^2 - n_c^2}\left[\left(\frac{n_{eff}}{n_f}\right)^2 + \left(\frac{n_{eff}}{n_c}\right)^2 - 1\right]^{\rho} \tag{2.43}$$

$$\Delta z_{f,s} = \frac{\lambda}{2\pi}\sqrt{n_{eff}^2 - n_s^2}\left[\left(\frac{n_{eff}}{n_f}\right)^2 + \left(\frac{n_{eff}}{n_f}\right)^2 - 1\right]^{\rho}, \tag{2.44}$$

where $\rho = 0$ for TE and $\rho = 1$ for TM, we get for the sensitivity to refractive index changes in the cover medium

$$\frac{\partial n_{eff}}{\partial n_c} = \left(\frac{n_c}{n_{eff}}\right)\left(\frac{n_f^2 - n_{eff}^2}{n_f^2 - n_c^2}\right)\left(\frac{\Delta z_{f,c/s}}{d_{eff}}\right)\left[2\left(\frac{n_{eff}}{n_c}\right)^2 - 1\right]^{\rho}. \tag{2.45}$$

This equation can again be solved by numerical iteration. Fig. 2.8 shows the sensitivities $\frac{\partial n_{eff}}{\partial n_c}$ versus waveguide thickness for the first two TE- and TM modes (0 and 1). It can be seen that TM modes yield higher sensitivities for the given parameters and that a waveguide thickness of 150-160 nm should be optimal for TM. Eq. 2.45 also implies that

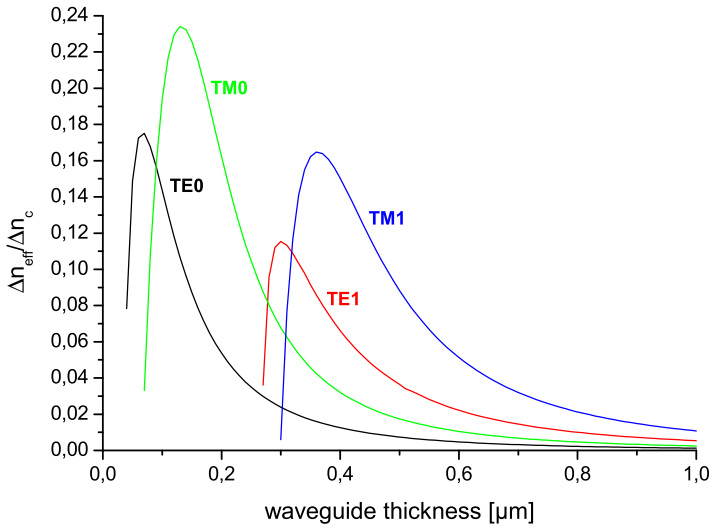


**Figure 2.8:** Theoretical sensitivity of a waveguide to refractive index changes in the cover medium versus waveguide thickness. Parameters for calculation: $n_s = 1.52$, $n_f = 2.1$, $n_c = 1.333$ at $\lambda$=675 nm

high sensitivities are reached for monomode waveguides with a high difference between the film refractive index and the substrate refractive index.

### 2.4.2 Sensitivity to adlayer formation

The sensitivity to changes in the surface adlayer becomes important when considering the adsorption or binding of molecules, in many cases biomolecules. In the following it is assumed that the molecules form a homogeneous adlayer and $t_{ad} \ll \lambda$. Again, the complete derivation can be found in *Tiefenthaler and Lukosz* (1989) and here only the result is given:

$$\frac{\partial n_{eff}}{\partial t_{ad}} = \left(\frac{n_f^2 - n_{eff}^2}{n_{eff} \cdot d_{eff}}\right)\left(\frac{n_{ad}^2 - n_c^2}{n_f^2 - n_c^2}\right)\left[\frac{\left(\frac{n_{eff}}{n_c}\right)^2 + \left(\frac{n_{eff}}{n_{ad}}\right)^2 - 1}{\left(\frac{n_{eff}}{n_c}\right)^2 + \left(\frac{n_{eff}}{n_f}\right)^2 - 1}\right]^{\rho}. \qquad (2.46)$$

Fig. 2.9 shows the sensitivities $\frac{\partial n_{eff}}{\partial n_{ad}}$ versus waveguide thickness for the first two TE- and TM modes (0 and 1) obtained by numerically solving eq. 2.46. Again TM-modes show higher sensitivity than TE-modes and waveguides with 150-160 nm are suitable when a high sensitivity to surface adlayer changes is desired.

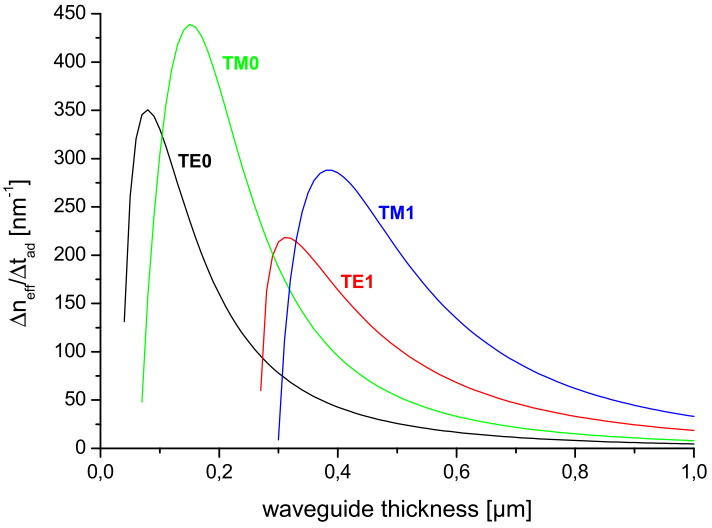


**Figure 2.9:** Theoretical sensitivity of a waveguide to surface adlayer changes. Parameters for calculation: $n_s = 1.52$, $n_f = 2.1$, $n_c = 1.333$ at $\lambda$=675 nm

### 2.4.3 Molecule adsorption and binding

Apart from determining the surface adlayer thickness of an adsorbed molecule layer, it is interesting to know about the surface coverage to have an easier comparison with other techniques available for monitoring biomolecule interactions. The formation of a homogeneous adlayer on the waveguide surface due to molecule adsorption or binding with $t_{ad} \ll \lambda$ is used as a model.

Starting from eq. 2.42 describing the changes in $\Delta n_{eff}$ with surface adlayer changes and considering only the first summand

$$\Delta n_{eff} = \left( \frac{\partial n_{eff}}{\partial t_{ad}} \right) \Delta t_{ad}, \tag{2.47}$$

we can expand this equation to get:

$$\Delta \Gamma = \left( \frac{\partial \Gamma}{\partial t_{ad}} \right) \cdot \left( \frac{\partial t_{ad}}{\partial n_{eff}} \right) \cdot \Delta n_{eff}. \tag{2.48}$$

The surface coverage $\Gamma$ is given by (*de Feijter et al.*, 1978)

$$\Gamma = t_{ad} \left( \frac{n_{ad} - n_c}{\frac{\partial n_{ad}}{\partial c}} \right), \tag{2.49}$$

with its derivation

$$\frac{\partial \Gamma}{\partial t_{ad}} = \frac{n_{ad} - n}{\frac{\partial n_{ad}}{\partial c}}. \tag{2.50}$$

For $\frac{\partial n_{ad}}{\partial c}$ a literature value of 0.188ml/g is considered to be suitable for most proteins (*Sober*, 1970) as well as a refractive index of $n_{ad}$ of 1.45. Inserting eq. 2.50 and the derived sensitivity constant from 2.46 into 2.48 yields

$$\Delta \Gamma = 2.72 \cdot 10^{-6} \cdot \Delta n_{eff} \ [g/mm^2], \tag{2.51}$$

for d = 154 nm, $n_c = 1.333$ and $n_{ad} = 1.45$ and TE mode, and

$$\Delta \Gamma = 1.42 \cdot 10^{-6} \cdot \Delta n_{eff} \ [g/mm^2] \tag{2.52}$$

for TM mode and the same parameters as above.

## 2.5 Interferometry

### 2.5.1 Diffraction and interference

As discussed in chapter 2.3, we can describe optical phenomena using the electromagnetic wave theory. Recall that the wave equations 2.16 and 2.17 are homogeneous linear partial differential equations and thus fulfill the principle of superposition, i.e. the field intensity $E$ at a point where two light waves overlap is equal to the vectorial sum of the two individual waves. Therefore we can define "interference" as "interaction of two or more light waves resulting in a total field intensity equal to the sum of the individual field intensities"(*Hecht*, 2001). Interferometers are devices that make use of the interference of electromagnetic waves to measure for example distances, temperature, pressure etc. with very high resolution. The interferogram is then quite literally the diagram of the interference pattern, characterized by light fringes which are bright where the light waves interfere constructively and dark where they interfere destructively.
According to eq. 2.18 a light wave is described by the following expression:

$$\begin{aligned} E(\vec{r},t) &= E_0 e^{i(\omega t - \vec{k}\vec{r})} \\ &= E_0 e^{i\varphi} \end{aligned} \tag{2.53}$$

with $\varphi = \omega t - \vec{k}\vec{r}$ being the phase. The total intensity is proportional to the square of the field amplitudes and can be written as

$$\begin{aligned} I\ |E|^2 &= E \cdot E^* \\ &= (E_1 + E_2)(E_1 + E_2)^* \\ &= E_1 E_1^* + E_2 E_2^* + E_1 E_2^* + E_2 E_1^*. \end{aligned} \tag{2.54}$$

where the * denotes the complex conjugate. Since $\mathrm{E_1 E_1^* = I_1}$ and $\mathrm{E_2 E_2^* = I_2}$, we only need to expand the last two summands:

$$\begin{aligned} E_1 E_2^* &= E_{10}\, e^{-i(\omega t - \vec{k_1}\vec{r_1})} \cdot E_{20} e^{-i(\omega t - \vec{k_2}\vec{r_2})} \\ &= E_{10} \cdot E_{20}\, e^{i(\vec{k_2}\vec{r_2} - \vec{k_1}\vec{r_1})} \end{aligned}$$

and

$$\begin{aligned} E_2 E_1^* &= E_{20}\, e^{-i(\omega t - \vec{k_2}\vec{r_2})} \cdot E_{10} e^{-i(\omega t - \vec{k_1}\vec{r_1})} \\ &= E_{10} \cdot E_{20}\, e^{-i(\vec{k_2}\vec{r_2} - \vec{k_1}\vec{r_1})}, \end{aligned}$$

which yields the interference term:

$$\begin{aligned} E_1 E_2^* + E_2 E_1^* &= E_{10} \cdot E_{20} \left( e^{i\left(\vec{k_2}\vec{r_2} - \vec{k_1}\vec{r_1}\right)} + e^{-i\left(\vec{k_2}\vec{r_2} - \vec{k_1}\vec{r_1}\right)} \right) \\ &= 2E_{10} \cdot E_{20}\, cos(\vec{k_2}\vec{r_2} - \vec{k_1}\vec{r_1}) \\ &= 2\sqrt{I_1 I_2}\, cos(\partial) \end{aligned} \tag{2.55}$$

with $\partial = \vec{k_2}\vec{r_2} - \vec{k_1}\vec{r_1}$. The total field intensity is thus

$$I = I_1 + I_2 + 2\sqrt{I_1 I_2}\, cos\partial. \tag{2.56}$$

For different points in space this total field intensity can now be, depending on $I_{12}$, bigger, smaller or equal to $I_1 + I_2$. For $cos\partial = 1$ the total field intensity becomes maximal:

$$I_{max} = I_1 + I_2 + 2\sqrt{I_1 I_2} \tag{2.57}$$

for

$$\partial = 0, \pm 2\pi, \pm 4\pi, .....$$

In this case the two waves interfere constructively because the phase difference is equal to a multiple of $2\pi$. A minimum in the total field intensity, i.e. destructive interference is reached for

$$I_{max} = I_1 + I_2 - 2\sqrt{I_1 I_2} \tag{2.58}$$

when

$$\partial = \pm\pi, \pm 3\pi, \pm 5\pi, .....$$

In a special case, when the amplitudes $E$ of both waves are equal, i.e. setting $I_1 = I_2 = I_0$, eq. 2.56 can be written as

$$I = 2\, I_0\, (1 + cos\partial) = 4\, I_0\, cos^2 \frac{\partial}{2}. \tag{2.59}$$

Fig. 2.10 illustrates the visible light fringes resulting from single slit diffraction and double slit diffraction for a coherent light source, e.g. a helium-neon laser.

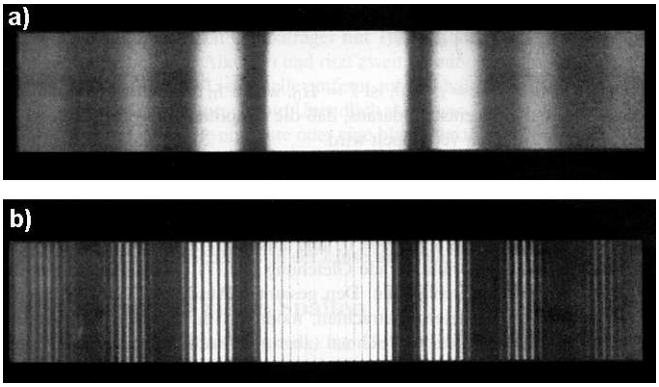


**Figure 2.10:** Light fringes from **a)** single and **b)** double slit diffraction using a monochromatic light source. From (*Hecht*, 2001).

### Single slit diffraction

The phenomenon that plane waves are bend when interacting with obstacles is generally called diffraction. The obstacle considered here is a narrow slit of width w. Depending on the distance D to the obstacle one distinguishes between Fresnel diffraction (near-field) or Fraunhofer diffraction (far-field, $\lambda \ll$ D). As the interferometric setup descibed in chapter 4 operates in the far field, only the Fraunhofer diffraction will be of interest. The intensity distribution in the far field resulting from single slit diffraction is given by (*Hecht*, 2001)

$$I(\theta) = I(0)\left(\frac{sin\beta}{\beta}\right)^2, \tag{2.60}$$

where

$$\beta = \left(\frac{\pi w}{\lambda}\right) sin\,\theta. \tag{2.61}$$

Fig. 2.11 shows the Fraunhofer diffraction caused by a narrow slit. From eq. 2.61 it can be seen that the intensity function has minima equal to zero when $\theta = \pm\pi, \pm 2\pi, \pm 3\pi, ....$, i.e. $\sin\theta = 0$, so that the envelope of an interferogram, which is dominated by the intensity distribution resulting from a single slit, is approximately given by

$$W = \frac{2\lambda D}{w}. \tag{2.62}$$

With increasing distance D from the slit the envelope function also increases, as well as with decreasing slit width w.

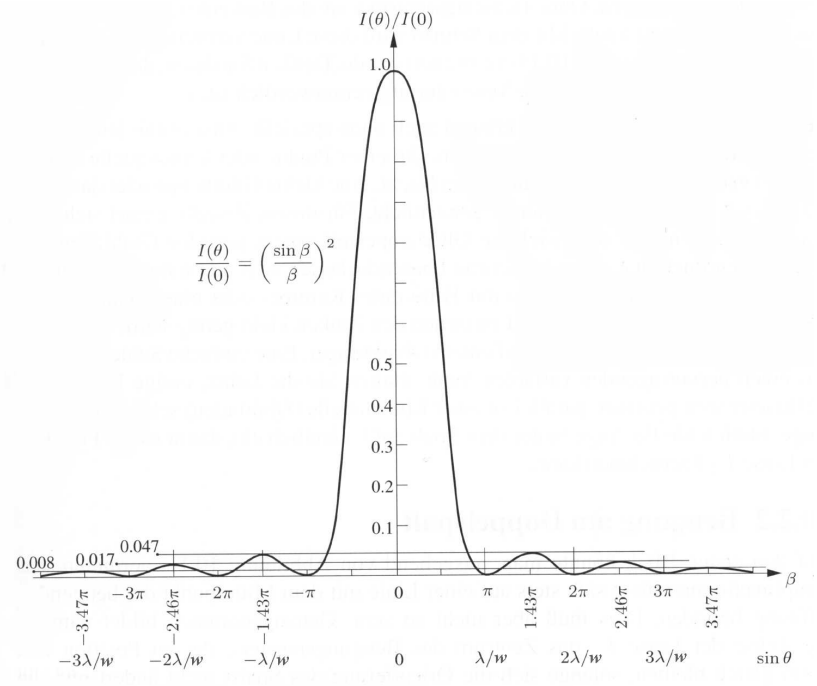


**Figure 2.11:** Intensity distribution from Fraunhofer diffraction at a single slit. From (*Hecht*, 2001)

### Double slit diffraction

The phenomenon of double slit diffraction is similar to the single slit diffraction, but implementing two narrow slits of width w and distance d from each other. The intensity distribution is still governed by the single slit diffraction, provided that w≪d, but modulated with a $cos^2\,\alpha$-function:

$$I(\theta) = 4\,I(0)\left(\frac{sin^2\beta}{\beta}\right)\,cos^2\alpha \tag{2.63}$$

with

$$\alpha = \left(\frac{\pi d}{\lambda}\right) sin\,\theta. \tag{2.64}$$

Fig. 2.12 illustrates the intensity distribution for the double slit in the far field condition. If the slit width w would be very small compared to the slit distance resulting in $\frac{sin^2\beta}{\beta} \approx 1$, the intensity distribution would be governed by the $cos^2$-function given in eq. 2.59. On the other hand, if the slit distance d decreases, the $cos^2$-function goes to zero and the remaining function again resembles the distribution given for the single slit. The

geometrical relationships for the double slit will be further discussed in chapter 2.5.3 along with the Young interferometer.

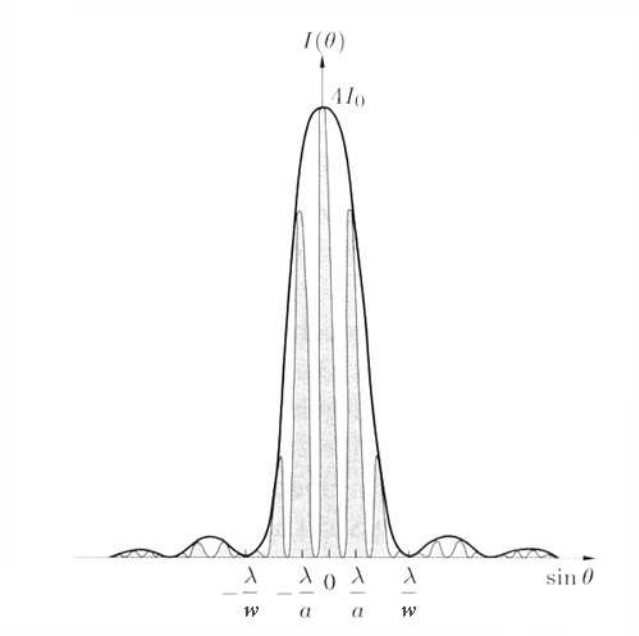


**Figure 2.12:** Intensity distribution from Fraunhofer diffraction at a double slit for d=3w. From (*Hecht*, 2001).

### 2.5.2 Young's interferometer

The interferometric biosensor design proposed in this thesis is based on Young's double slit experiment, which was the earliest experimental arrangement for demonstrating the interference of two light beams (*Born and Wolf*, 1999). In Young's configuration a small hole simulated a point light source emitting a coherent light ray falling then on two pinholes. Indeed he observed a pattern of bright and dark fringes behind the two pinholes. These fringes can be analyzed by direct geometry, as illustrated in Fig. 2.13.
Following relationships can be directly derived from the graph:

$$tan\,\theta = \frac{\Delta x}{D} \tag{2.65}$$

and

$$sin\,\theta = \frac{\Delta s}{d}. \tag{2.66}$$

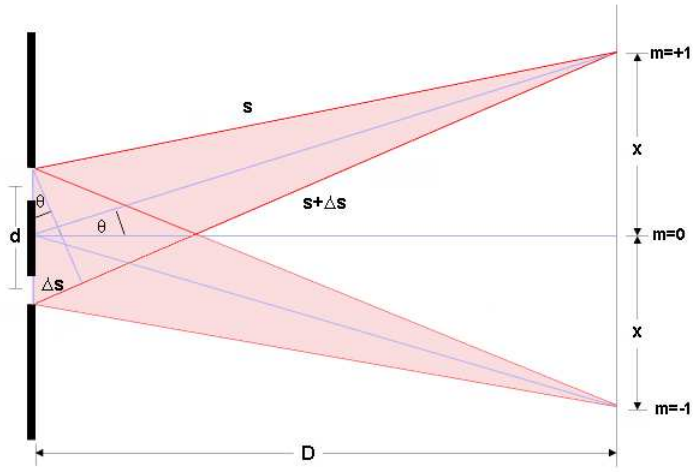


**Figure 2.13:** Young's experiment. Two slits of width w are separated by a distance d to each other and located at distance D to a screen in the far field. $\Delta$s denotes the difference in path length of the two light beams.

Assuming that w$\ll$D we can use the small-angle approximation to get

$$tan\,\theta \approx sin\,\theta = \frac{\Delta x}{D} \tag{2.67}$$

and

$$\Delta s = \frac{d\Delta x}{D}. \tag{2.68}$$

Thus maxima of the intensity can be observed for

$$x = \frac{mD\lambda}{d}, \tag{2.69}$$

when m=0,1,2.... and minima for $m = \frac{1}{2}, \frac{3}{2}, \frac{5}{2}, .. .$

### 2.5.3 Influence of coherence length

So far, interference phenomena have been described provided that the light source is monochromatic. Since the interferometric biosensor described here is mainly operated with a partially coherent superluminescent diode (SLD), it is important to consider the main characteristics of interference of partially coherent light. A more comprehensive and mathematical description of the coherence properties of light can be found in (*Born and Wolf*, 1999; *Hecht*, 2001).

The term "coherence"describes in general the ability of two waves to combine and produce an interference pattern. Incoherent waves are not able to produce a visible interference pattern. Coherence can be further identified as spatial or temporal coherence (*Hecht*, 2001). When a wave is coherent to itself, i.e. it is combined with a time-delayed copy of itself, we speak of temporal coherence and define a coherence time of the wave $\Delta\tau_c$, which is the duration of the delay still resulting in visible interference. From this, the coherence length $\Delta x_c = c\Delta\tau_c$ is derived. This temporal coherence correlates with the spectral bandwidth of the light source as the coherence time is inversely proportional to the bandwidth. For example lasers, which are the most monochromatic light sources, have very large coherence times and lengths.

Young's experiment in fact relies on spatial coherence, which describes the ability of any spatial position of the wave to interfere with any other spatial position. Fig. 2.14 illustrates the interference at point P of wave groups originating from point sources $S_1$ and $S_2$. If the difference in path length is larger than the coherence length $\Delta l_c$, the wave group $H_1$ for example cannot interfere with its respective wave group $H_2$ in P due to the relative phase difference. If now the difference in path length is smaller than the coherence length, the wave groups can overlap and produce a stable interference pattern.

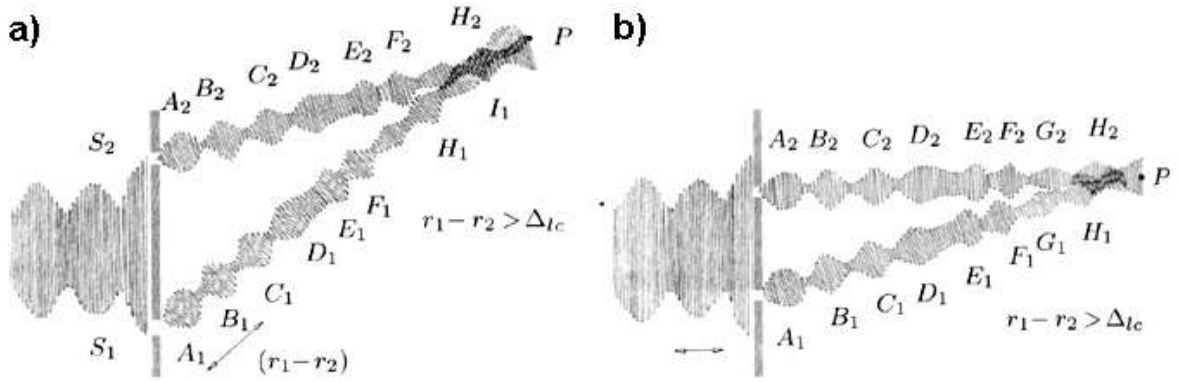


**Figure 2.14:** Schematic representation of double slit interference of partially coherent light with coherence length $\Delta l_c$. **a)** for a path length $\Delta r > \Delta l_c$ **b)** for a path length $\Delta r < \Delta l_c$. From (*Hecht*, 2001).

To describe the coherence mathematically, we define a so-called complex degree of coherence $\gamma_{12}(\tau)$ and insert it into eq. 2.56 (*Born and Wolf*, 1999):

$$I = I_1 + I_2 + 2\sqrt{I_1 I_2}\,\gamma_{12}(\tau)\,cos\partial \tag{2.70}$$

We now consider quasi-monochromatic light where the spectral bandwidth $\Delta\nu$ is sufficiently small. Provided that the intensities are equal, i.e. $I_1 = I_2$, the visibility of the fringes is then equal to the degree of coherence. As illustrated in Fig. 2.14, for the case of coherent light, the visibility is fully modulated with 4I, for partially coherent light the visibility becomes less modulated with 2I, and for an incoherent superposition the visibility equals zero. Transferred to an interferogram pattern as observed in the Young

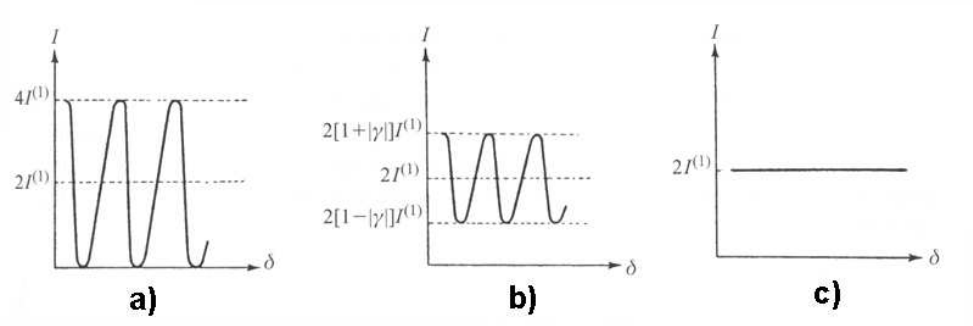


**Figure 2.15:** Intensity distribution in the interferogram produced by a quasi-monochromatic light source. For equal intensities $I_1$ and $I_2$ and a degree of coherence $\gamma_{12}$ **a)** coherent superposition with $\gamma_{12} = 1$ **b)** partially coherent superposition with $0 < \gamma_{12} < 1$ **c)** incoherent superposition with $\gamma = 0$. From (*Born and Wolf*, 1999).

configuration, we obtain an interferogram with high visibility for a coherent light source with a narrow bandwidth, and a less modulated interferogram for a partially coherent light source with a broader bandwidth, as shown in Fig. 2.15. Both interferograms can be obtained with the Young interferometric setup described in chapter 4, but with different spectral filtering methods. Especially for signal analysis purposes it is important that both signatures can be evaluated with different algorithms. Flowcharts of these algorithms are presented in Appendix D.

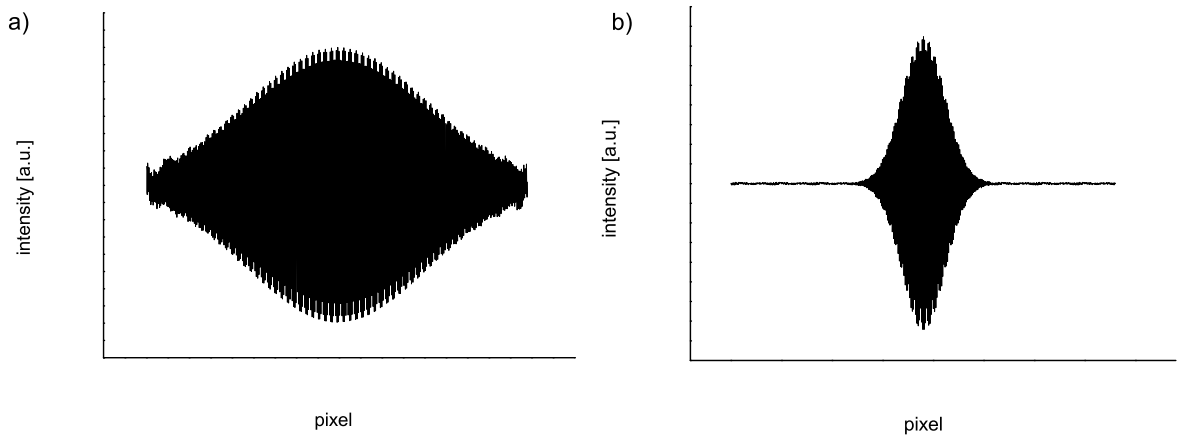


**Figure 2.16: a)** Far-field interference pattern of a coherent light source, simulated. The interferogram is characterized by a high degree of coherence and thus a high visibility ($\approx 1$). **b)** Far-field interference pattern of a partially coherent light source, simulated. The region of interference is narrower than in a).

## 2.6 Fourier transform analysis for signal processing

The interferometric biosensor is designed to obtain phase information from a periodic signal, the interferogram. The question is how to process this phase information with appropriate and efficient mathematical algorithms to determine a change in signal. Signal analysis provides many different transform algorithms suited for such applications. Since the interferograms obtained from the interferometric biosensor are periodic signals, the main approach evaluating these signals is the Fourier transform and shall be presented briefly in this chapter.

A profound description of Fourier transform analysis is clearly beyond the scope of this thesis and is described elsewhere (*Lang and Pucker*, 1998; *Meyer*, 2003; *Schrüfer*, 1992).

### Fourier series

The Fourier Transform (FT) has been developed in the beginning of the 19th century by Joseph Fourier based on the discovery that any periodic signal consists of single sine and cosine waves that can be used to reproduce the signal:

$$a_k = \frac{2}{T} \int_0^T x(t)\, cos(k\omega_0 t)\, dt \tag{2.71}$$

$$b_k = \frac{2}{T} \int_0^T x(t)\, sin(k\omega_0 t)\, dt, \tag{2.72}$$

with $T = \frac{1}{f_0}$ being the period of the function. Without the proof given here these two functions can be represented by the *Fourier series* given by

$$x(t) = \frac{a_0}{2} + \sum_{k=1}^{\infty} \left(a_k\, cos(k\omega_0 t) + b_k\, cos(k\omega_0 t)\right). \tag{2.73}$$

With *Euler's identity*

$$e^{ik\omega_0 t} = cos(k\omega_0 t) + sin(ik\omega_0 t) \tag{2.74}$$

we get the Fourier series in complex form:

$$x(t) = \sum_{k=1}^{\infty} c_n\, e^{ik\omega_0 t}. \tag{2.75}$$

By multiplication of eq. 2.75 with $e^{-ik\omega_0 t}$ and integration we obtain the complex Fourier coefficients:

$$c_n = \frac{1}{T} \int_0^T x(t)\, e^{-ik\omega_0 t}\, dt \tag{2.76}$$

for integration over exactly one period T. A problem arises when applying the FT on aperiodic signals, because then the period approaches infinity and thus the fundamental frequency approaches zero. With this limit, as $f_0 \to 0$, the sum in the Fourier series can be replaced by an integral. The new function in frequency is represented X($\omega$), and the *Fourier transform* of this function can be written as

$$x(t) = \frac{1}{2\pi} \int_{-\infty}^{\infty} X(\omega)\, e^{i\omega t}\, d\omega. \tag{2.77}$$

From the Fourier transform of a function of time the original function of time can always be recovered, i.e. either x(t) or X($\omega$) describe a function uniquely, which is also stated by the *Inverse Fourier transform* given by

$$X(\omega) = \int_{-\infty}^{\infty} x(t)\, e^{-i\omega t}\, dt. \tag{2.78}$$

These two equations are the fundamentals for the interferogram signal evaluation, where a position-dependent periodic function is detected and analyzed by a FT in the spatial frequency domain to obtain the period of the interferogram and thus the information about changes in the phase velocity of the two optical beams.

### Discrete signals and Discrete Fourier Transform

The considerations above are clearly valid for continuous signals, i.e. along an axis a data value exists for any infinitesimal interval on this axis. In digital signal analysis, however, mostly discrete signals have to be dealt with. Discrete signals are simply signals that are not continuous in time or space. For example a CCD camera would detect a data value for each single pixel. In this case the signal is described as discrete along the spatial axis. The question is if discrete signals provide the same information than continuous signals, and if there is a minimum of signal values needed to obtain useful information. *Nyquist's Theorem* (*Meyer*, 2003) states that a continuous signal with frequency $f_c$ can be reconstructed without error from its sampled version with frequency $f_s$ if

$$f_s \geq 2\, f_c. \tag{2.79}$$

In words, the sampling frequency for the discrete signals must be greater than twice the maximum frequency of the signal being sampled.
Transferred to the interferometric biosensor this means that, the CCD detector regarded as a spatial axis, each pixel corresponds to a single detector having a certain intensity value. Nyquist's Theorem is fulfilled as long as the period of the detected interferogram is greater than 2 pixels.

### Fast Fourier Transform

As described above, in most cases data points are sampled in a discrete, equidistant form and not as a continuous function. Consequently the Fourier integrals have to be modified, i.e. the Fourier sum in exponential form and the calculation of the coefficients (2.75 and 2.76) have to be converted into a discrete form with a finite number of data points (Discrete Fourier Transform, DFT). In numerical applications the integrals over functions are approximated by weighted sums over the data points at so-called nodes.

Choosing N equidistant nodes x = 2πk/N allows the calculation of N Fourier coefficients:

$$\begin{aligned} c_n &= \frac{1}{N}\sum_{k=0}^{N-1} y_k e^{-inx_k} \\ &= \frac{1}{N}\sum_{k=0}^{N-1} y_k e^{-2i\pi kn/N} \\ &= \frac{1}{N}\sum_{k=0}^{N-1} y_k z^{kn}, \ \left(z \equiv e^{-2i\pi/N}\right) \end{aligned} \tag{2.80}$$

This relation is , without the proof shown here, invertible and we get

$$y_j = \sum_{n=0}^{N-1} c_n e^{2i\pi nj/N}. \tag{2.81}$$

For each of the N coefficients N summands would have to be calculated resulting in $N^2$ operations. Due to the periodicity of the trigonometric functions several calculations of spectral values are identical and thus redundant. Based on this a powerful algorithm has been developed called Fast Fourier Transform (FFT) avoiding these redundant calculations, but giving the same result as a DFT. Especially when only one spectral value is of interest, the implementation of the FFT is more efficient than a DFT.

The basic idea of the FFT is to split a long time sequence by successive bisection into many short sequences and then calculate the DFT, which mathematically corresponds to a decomposition into prime factors. This is even more advantageous if N is a power of two, resulting in short sequences of length 2 and at the same time utilizing the symmetry of the trigonometric functions. With the FFT the total number of calculations thus reduces from $N^2$ to $N \log_2 N$.

The advantage of N being a power of two can yet be fulfilled by any finite number of $\tilde{N}$ when including an appropriate number of trailing zeros, thereby extending the signal to the next power of two. This method is known as zero-padding and represented by the following relationship:

$$\text{Zeropadding[f(x)]} = \begin{cases} \text{f(x)} & |\text{x}| < \tilde{\text{N}}/2 \\ 0 & \text{otherwise} \end{cases} \tag{2.82}$$

The FFT algorithm is essential for the signal analysis of the interferometric biosensor since it operates preferentially at short exposure times, which is demanding for the software

and fast processing is needed. Therefore a FFT algorithm using zero-padding has been implemented into the signal analysis software as described in Appendix D and chapter 4.2.4.

## 2.7 Signal analysis and processing

### 2.7.1 System principles and relationships

For signal processing and evaluation the basic system principles and relationships have to be known. These relationships have already been described in *Brandenburg* (1997); *MacKenzie* (2003) and shall be summarized here.
Recall the intensity distribution from Young's double slit experiment (eq. 2.59):

$$I(x) \propto cos^2(\phi(x) - \delta), \tag{2.83}$$

where $\phi$(x) = 2$\pi$x/p with p being the spatial period of the cos$^2$-function and x the offset along the detection axis. $\delta$ denotes an additional phase shift. The period of the interferogram is given by

$$p = \frac{D\lambda}{d}. \tag{2.84}$$

Inserting eq. 2.84 into eq. 2.83 yields

$$\begin{aligned} \Delta\phi &= \frac{2\pi d\Delta x}{D\lambda} \\ &= \frac{2\pi\Delta s}{\lambda}. \end{aligned} \tag{2.85}$$

The phase shift is a measure for a change in phase velocity, and thus a change in the effective refractive index, on one of both channels. According to (*Brandenburg*, 1997), this phase shift is given by the following relationship:

$$\Delta\phi = \frac{2\pi L\Delta n_{eff}}{\lambda}, \tag{2.86}$$

with L being the interaction length. For the spatial offset follows:

$$\Delta x = \frac{DL\Delta n_{eff}}{d}. \tag{2.87}$$

This result gives us the direct relationship between the phase difference and the effective refractive index and is essential for the interferogram signal processing, since after the period of the interferogram has been determined, all parameters are known to determine the phase difference $\Delta\phi$ and thus the effective refractive index by rearranging:

$$\Delta n_{eff} = \frac{\lambda \Delta\phi}{2\pi L}. \tag{2.88}$$

By defining a multiplication constant

$$K = \frac{\lambda}{2\pi L}, \tag{2.89}$$

we can see that the phase difference and the effective refractive index are related by a simple multiplication, which is only dependent on the wavelength of the light source and the interaction length on the transducer chip. For the interferometric biosensor values of $\lambda = 675$ nm and $L = 5$ mm, K can be calculated to $21.486 \cdot 10^{-6}$.

### 2.7.2 Noise sources and distortion effects

Any measurement signal detected with the interferometric biosensor contains noise or other distortion effects to a certain extend. Noise is generally any unwanted contribution to the signal distorting or falsifying the true signal value. A crucial issue is to identify the sources of these effects and implement suitable methods in signal processing to reduce the influence of noise effects. For the quantification of noise in a given data set the standard deviation is used. Particularly noise sources contributing to random signal noise are of interest. The following section gives an overview on different possible sources of noise and other distortion effects.

#### Phase error from path differences

For highly sensitive sensing with the interferometric biosensor the accuracy of phase determination is the most important. Several noise sources can contribute to the phase error, which is described in detail in *Nakadate* (1988).

Recalling eq. 2.86 it is obvious that phase errors can also be caused by path length differences $\Delta$L. Here we can distinguish between internal path differences, i.e. only concerning

the sensing area on the transducer chip, and external path differences, i.e. path differences in the system mainly caused by misalignment or displacements of optical components.
An internal path difference $\Delta L = L_2 - L_1$ is limited by differences in the interaction lengths $L_1$ and $L_2$ on the transducer chip, i.e. between the two gratings. However, even if $L_1$ differs from $L_2$ due to fabrication defects in the gratings, this path difference would be static and not contributing to phase noise. Internal path differences can thus only be influenced by wavelength fluctuations of the light source, which will be discussed below.
External path differences can occur anywhere in the optical beam path e.g. by misaligned optical components. Yet this path difference would also be of a static nature and not cause noise or fluctuations in the measurement signal. Here the limiting factors would be external vibrations or again wavelength instabilities leading to fluctuating path differences. A continuous temperature change, i.e. wavelength instability, would therefore cause a drift in the interferogram signal.

**Noise from light source instability**

Since the interferometric biosensor is mostly operated with an SLD, the instability of this light source is the most important. When recalling eq. 2.86, we can see that a fluctuation in wavelength would directly lead to a phase change and therefore in $\Delta n_{eff}$. The uncertainty in wavelength of the SLD can, as described in more detail in the experimental section, be estimated to be $\approx 10^{-3}$ `nm`. This results in a contribution to the total signal noise in the order of $\approx 10^{-9}$ in $\Delta n_{eff}$.

**Mechanical noise sources**

Mechanical noise sources can mainly arise from disturbances in the hardware components of the system, e.g. component construction defects or misalignment of the components resulting in a path length difference. Another source for mechanical noise are physical vibrations in the system also causing path length differences contributing to phase noise.

### Electronic noise sources

In electronical systems there exist various types of electronic noise sources, among them thermal noise, shot noise and readout noise which shall be described here briefly (*Lindner et al.*, 1999):

- Thermal noise: in a CCD camera, single electrons in the sensor chip may have enough energy from random thermal motion to overcome the difference of potential and accumulate with the photoelectrons, contributing to the total photocurrent. This additional current is called dark current, which is linearly dependent on the exposure time of the camera. Since it also depends on the ambient temperature, it is feasible to cool the camera for long exposure times ($> 1$s). Thermal noise is white noise, i.e. the frequency amplitudes are characterized by a Gaussian distribution.

- Shot noise (quantum noise): shot noise is caused by frequent fluctuations of the current in a conducting material resulting from diffusion of charge carriers and the random generation or recombination of electron-hole pairs. Shot noise is also white noise.

- Readout noise: contains noise caused by transfer noise (readout of photoelectrons in the CCD sensor), noise caused by analog-digital conversion and noise in the signal amplifier. Readout noise is characteristic for the type of camera, independent on exposure time, and contributes to a large extend to the total noise in a system.

The total noise is calculated from contributions from dark current and noise in the signal:

$$\sigma_{tot} = \sqrt{\sigma_{signal}^2 + \sigma_{DC}^2} \tag{2.90}$$

For short exposure times the noise caused by dark current can be neglected.

### Quantization noise and aliasing

These two sources of noise are associated with the FFT and its obtained accuracy. Quantization noise arises from quantization processes, i.e. the conversion from an analog into its digital approximation, in our case in the CCD camera and its electronics. As stated

by *Kujawinska and Wojciak* (1991), quantization noise can be neglected when converting the signals with more than 6bit. As the CCD sensor used for the interferometric biosensor operates with either 12bit or 16bit conversion, phase errors resulting from quantization are negligible. Aliasing is an effect occuring when the Nyquist Theorem (2.6) is not fulfilled, i.e. the chosen sampling frequency is too low. In this case the signal frequency is overlaid by a higher frequency distorting the reconstructed signal. As mentioned in chapter 1.6, aliasing occurs in our case only if the interferogram period was less than two pixels on the CCD camera.

### 2.7.3 Signal filtering methods

In data sampling the standard deviation of a data distribution is considered to be a measure for variation in the signal. Since the standard deviation is higher in noisier data, it is an important task of signal processing to apply filtering methods to reduce the noise in data distributions, here in phase noise. An efficient way of reducing phase noise is the application of averaging filters, or sometimes window functions. Two averaging filters shall be introduced here briefly considering their use for the interferometer signal processing software.

#### Implementation of window functions

One method in digital filtering is to apply a window function to the detected data set for a more precise extraction of information. Typical window functions for interferogram distributions shown in chapter 2.5.2 would be the von Hann-window or Hamming window function. These two common functions have already been tested for their suitability for noise reduction in the interferometric biosensor by *MacKenzie* (2003). It was shown that the implementation of window functions within the signal processing algorithm used for the interferometric biosensor has no significant effect on noise reduction.

### Block average filter

The block average filter, as the name implies, calculates the average of a block of n data points by adding all n data values and subsequently dividing by an averaging factor N. Fig. 2.17 illustrates the flow chart of a block average filter.

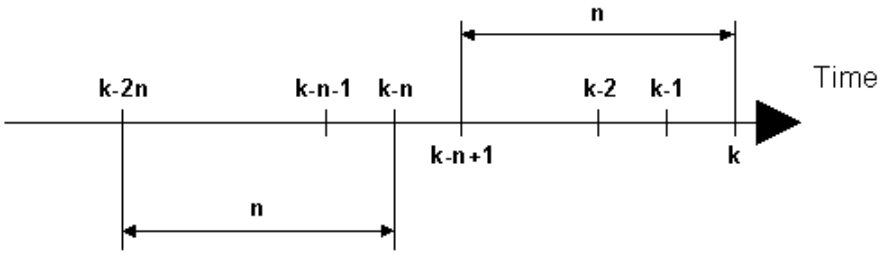


**Figure 2.17:** Flow chart of a block average filter for averaging a data series of size n. Adapted from (*MacKenzie*, 2003)

Applying this filter means a reduction of N input data points to $\tilde{n}$=n/N. This filter is useful when a reduction of the number of data points is desired, e.g. to save memory due to a smaller data file. However, the filter is quite calculation intensive and can only be applied after the complete sequence of n data points has been recorded.

### Moving average filter

To improve the calculation efficiency, a so-called recursive filter may be applied that only depends on the previously calculated value and the most recently sampled data value. Fig. 2.18 illustrates this graphically.
This filter is known as moving average filter because a moving window of the most recent n data points is used to calculate the average. In other words, the oldest data value in the buffer is continuously replaced by the newly measured one, maintaining a constant number of n data values in the buffer. Thus the total number of averaged values for a given time is the same as without averaging. Furthermore, the buffer is filled only once at the beginning of the filtering process unlike the block average where the buffer is consistently filled and emptied. This method of filtering has the feature of weighting all data points

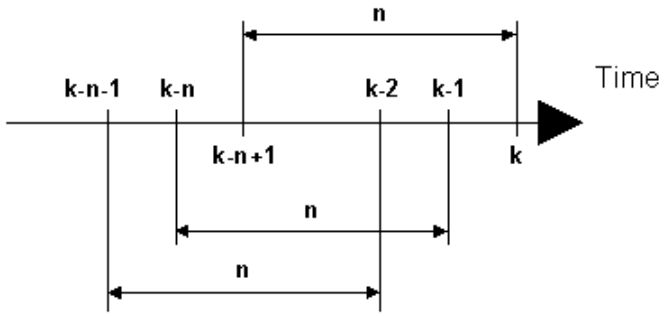


**Figure 2.18:** Flow chart of a moving average filter for averaging a data series of size n. Adapted from (*MacKenzie*, 2003)

equally, i.e. a given data point in the past within the buffer has the same influence on the averaged value than a more recent one. However, this equal weighting of all data points by the moving average is only feasible when the mean value of all data points remains approximately constant (baseline). As soon as the data curve follows a certain trend, in our case e.g. a binding event, care has to be taken to not choose the buffer size n too large as then the averaged data might distort the real data.

# Chapter 3

# Theoretical background in biochemistry

## 3.1 Introduction

The core of any label-free biosensor is represented by the transducer with its actual sensor surface, since it acts as a functional linker between the biochemical reaction and the transducer. Ideally a sensor surface should be prepared in such a way that a variety of immunoassays can be performed. In this chapter a brief overview of immunoassay design, surface chemistry and preparation, and binding reaction kinetics will be given. Detailed experiments on the characterization of the linking chemistry for the interferometric biosensor will be described in chapter 5 along with the application measurements.

## 3.2 Immunoassays

Since the late 1960's, immunoassays have proven to be very powerful tools in life science, pharmaceutical and medical research for the elucidation of biochemical processes (*Davies*, 2001). Immunoassays use antibodies to detect, usually labeled, analyte molecules, e.g. antigens, with high specificity and strong binding characteristics. A typical assay comprises at

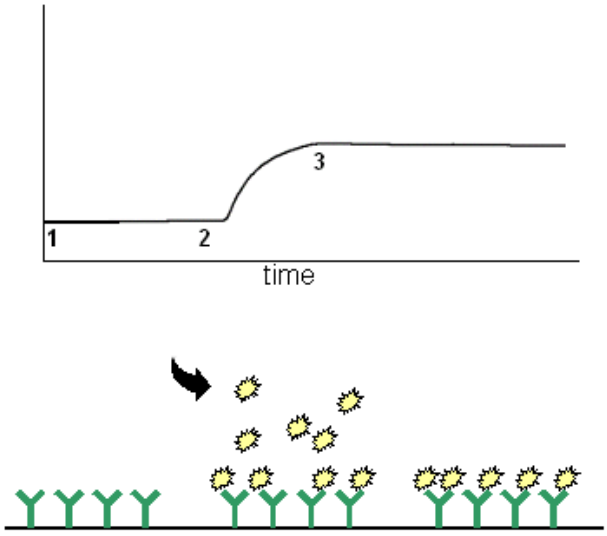


**Figure 3.1:** One-step immunoassay. 1. Buffer is run over a surface with immobilized antibodies (baseline). 2. The analyte solution with antigen is added, antigen binds to the antibodies until an equilibrium of free/bound antigen is reached. 3. Buffer is run again over the surface so that unbound antigen is washed away.

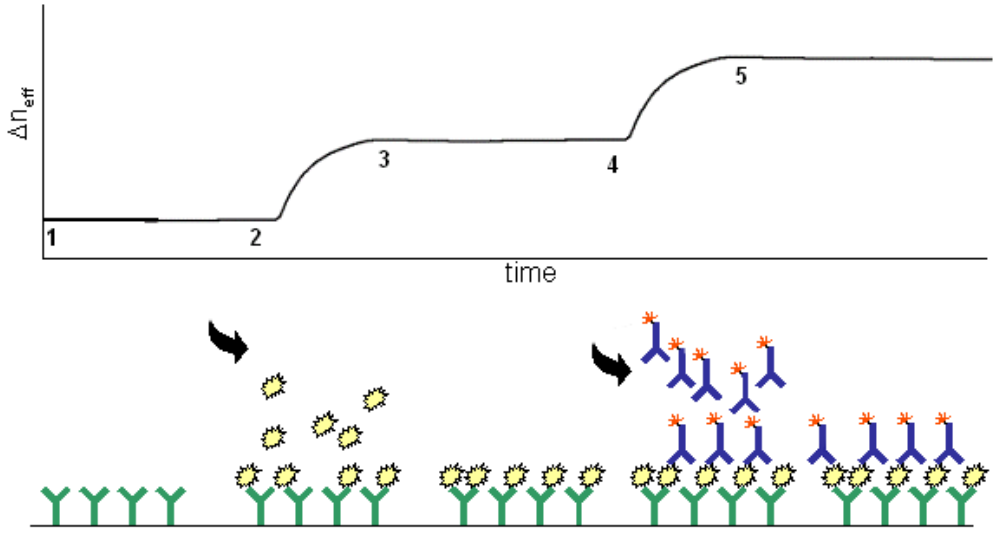


**Figure 3.2:** Multi-step immunoassay. 1. Buffer is run over a surface with immobilized antibodies (baseline). 2. The analyte solution with antigen is added, antigen binds to the antibodies until an equilibrium of free/bound antigen is reached. 3. Buffer is run again over the surface so that unbound antigen is washed away. 4. Analyte solution with a secondary antibody is added, antibody binds to the antigen until equilibrium is reached. 5. Buffer wash to remove unbound antibody.

least one immobilized capture molecule, i.e. bound to a solid phase, in our case the waveguide surface, and an analyte in solution which is captured by the immobilized molecules. The simplest immunoassay is the so-called immunometric one-step assay, where an antibody is immobilized on the sensor surface, and its corresponding antigen is bound from the liquid phase. Multistep assays would work with a labeled secondary antibody binding to the antigen, giving the detection signal, as it is the case for the so-called sandwich assay. A comprehensive description of different types of immunoassays including labeled reagents can be found in *Davies* (2001).

Label-free immunoassays usually work as one-step assay with an immobilized capture molecule and its corresponding analyte in solution, as the signal depends on a change in surface mass coverage and a label for signal detection is not needed. This saves both reagents for labeling such as fluorescent dyes and time for realization of the assay.

## 3.3 Surface chemistry

For the realization of a stable and reproducible immunoassay, the molecules of interest have to be linked to the waveguide surface in an appropriate way. The $Ta_2O_5$ surface is relatively hydrophilic by nature, so that most proteins or antibodies, when brought on the surface, would merely stick to the surface in a random orientation and could be washed away quite easily. For this reason a stable, bifunctional linking molecule is desirable, which can be covalently bound to the $Ta_2O_5$ surface with one end and at the same time provide a functional group for the oriented immobilization of biomolecules on the other end. Depending on the waveguide substrate, there exists a wide variety of linking chemistries, e.g. reagents forming self-assemled monolayers (SAM), among them modified alkyl thiols or modified silanes. For $Ta_2O_5$ , mostly the use of silanes has been described in literature (*Polzius et al.*, 1996; *Laureyn et al.*, 2001). For the interferometric biosensor, two different silanes have been tested and characterized, 3-Aminopropyl-triethoxysilane (APTS) and 3-Glycidoxy-propyl-triethoxysilane (GOPS). Both silanes are trifunctional, i.e. provide three hydrolyzable functional head groups, and are able to form a two-dimensional network on the waveguide surface (*Tovar*, 1995). Due to these crosslinks, a trifunctional

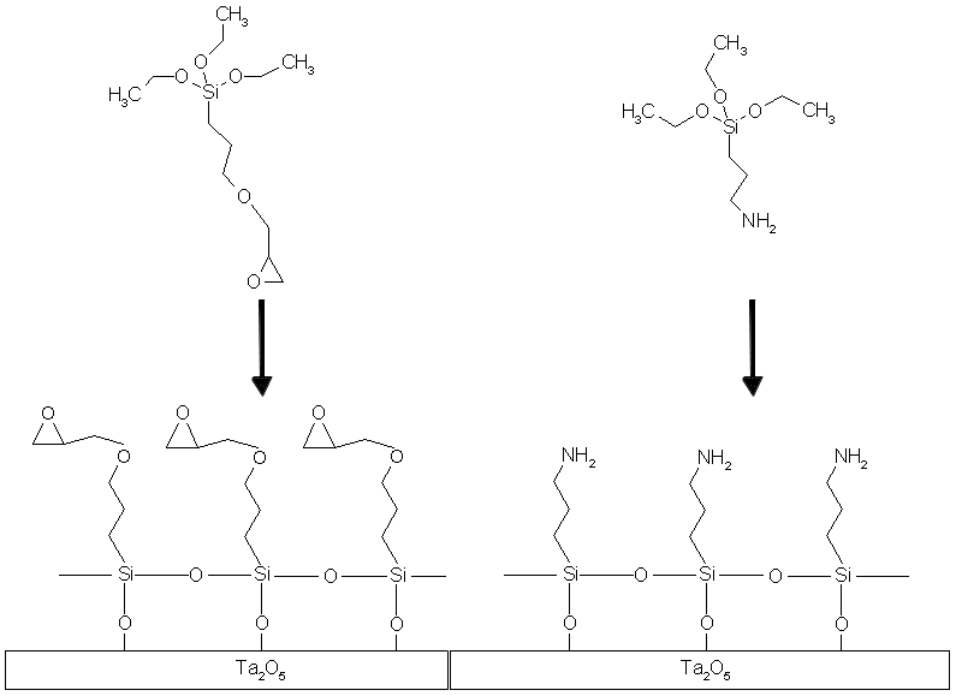


**Figure 3.3:** Chemical formulas for 3-Glycidoxypropyl-triethoxysilane (left) and 3-Aminopropyl-triethoxysilane (right). The silane is covalently coupled to the waveguide surface via hydroxyl groups, the functional group for biomolecule binding is an epoxy-group for GOPS and an amino-group for APTS.

silane yields a greater stability than mono- or bifunctional silanes.

APTS provides an amino-group as functional linker for the covalent coupling of biomolecules, GOPS an epoxy-group. Depending on the assay and the proteins/antibodies involved, these functional groups can be further modified for a stable immobilization. For example, biotin with a special linker can be attached to the amino-modified surface to bind streptavidin (see chapter 3.5). This streptavidin surface is a commonly used basis for assays with biotinylated reagents (*Morgan and Taylor*, 1992; *Busse et al.*, 2002).

The kind of capture molecule immobilization always depends on the kind of assay and purpose of study. For kinetics and affinity measurements, preferably a rather low receptor density which is still giving a good signal should be used to avoid any secondary effects such as mass transport limitations or steric hindrances. In this case immobilization can be done by mere adsorption of the receptor to the waveguide. The kind of immobilization should also be taken into consideration when choosing the appropriate regeneration

buffer.

In contrast, for concentration measurements the receptor density needs to be as high as possible to detect even smallest concentrations of the ligand. Here, silanization of the waveguide surface for oriented coupling of the receptor is advisable to reach a high receptor density. The same is valid for studies with molecules of low molecular weight.

## 3.4 Kinetics of binding reactions

With the interferometric biosensor it is feasible to monitor binding reactions time-resolved and thus information about kinetics of the reaction is accessible. Binding kinetics play a crucial role in the successful development of an immunoassay and new methods of assay optimization are developed constantly. Each immunoassay consists of at least one binding reaction, usually between an antibody and its antigen. Here a brief theoretical description about binding kinetics for a pseudo-first order reaction shall be given. More detailed considerations can be found in *Davies* (2001).

### 3.4.1 The 1:1 interaction model

A biochemical interaction like the antibody-antigen reaction can simplistically be described by the Law of Mass Action (*Karlsson and Löfas*, 1998):

$$c_{Ag} + c_{Ab} \overset{k_a,k_d}{\leftrightarrow} c_{Ab-Ag} \tag{3.1}$$

where

| | | |
|---|---|---|
| $c_{Ag}$ | = concentration of antigen | [M] |
| $c_{Ab}$ | = concentration of antibody | [M] |
| $c_{Ab-Ag}$ | = antibody-antigen complex | [M] |
| $k_a$ | = association rate constant | $[M^{-1} \cdot s^{-1}]$ |
| $k_d$ | = dissociation rate constant | $[s^{-1}]$. |

This model implies a 1:1 binding reaction, i.e. one immobilized molecule captures exactly one analyte molecule (monovalent) from the solution. Further it is assumed that the detected signal $\Delta n_{eff}$ is directly proportional to the change in surface mass coverage. Also, there should be no unspecific binding caused by any other substances in the analyte

solution which could possibly contribute to the signal and thereby giving a false positive. This can be avoided by assay optimization and will be further discussed in chapter 6. Taking all this into account, we can describe the time-dependence of the binding reaction as follows:

$$\begin{aligned} \frac{\partial c_{Ab-Ag}}{\partial t} &= k_a \cdot c_{Ag} \cdot c_{Ab} - k_d \cdot c_{Ab-Ag} \\ &= k_a \cdot c_{Ag} \cdot c_{Ab_t} - k_a \cdot c_{Ag} \cdot c_{Ab-Ag} - k_d \cdot c_{Ab-Ag} \\ &= k_a \cdot c_{Ag} \cdot c_{Ab_t} - c_{Ab-Ag} \cdot (k_a \cdot c_{Ag} + k_d), \end{aligned} \tag{3.2}$$

with

$c_{Ab_t} = c_{Ab-Ag} + c_{Ab}$ being the total concentration of antibody.

Assuming

$$c_{Ab-Ag}(t = 0) = 0 \text{ (boundary condition)},$$

it can be easily proven that

$$c_{Ab-Ag}(t) = \frac{k_a \cdot c_{Ag} \cdot c_{Ab_t}}{k_a \cdot c_{Ag} + k_d} \cdot (1 - e^{-(k_a \cdot c_{Ag} + k_d) \cdot t}) \tag{3.3}$$

is a solution of this differential equation giving the time-dependence of the binding reaction. For $t \to \infty$, i.e. when reaching equilibrium, this can be expressed by

$$c_{Ab-Ag_{equil.}} = \frac{k_a \cdot c_{Ag} \cdot c_{Ab_t}}{k_a \cdot c_{Ag} + k_d}, \tag{3.4}$$

which is also known as the Langmuir isotherm for a one-site binding model. Introducing the affinity constant of the system

$$K = \frac{k_a}{k_d} \ [M^{-1}], \tag{3.5}$$

we get

$$c_{Ab-Ag_{equil.}} = \frac{c_{Ag} \cdot c_{Ab_t}}{\frac{1}{K} + c_{Ag}}. \tag{3.6}$$

On the other hand, for small t, i.e. $t \ll \frac{1}{k_d + k_a \cdot c_{Ag}}$, eq. (3.3) can be expanded in a Taylor series:

$$c_{Ab-Ag}(t) = \frac{k_a \cdot c_{Ag} \cdot c_{Ab_t}}{k_a \cdot c_{Ag} + k_d}[(k_d + k_a \cdot c_{Ag}) \cdot t + O^2(t)], \tag{3.7}$$

where the linear approximation shows that

$$\frac{\partial c_{Ab-Ag}}{\partial t} \approx k_a \cdot c_{Ab_t} \cdot c_{Ag}. \tag{3.8}$$

Equation (3.8) implies that the initial binding rate $\frac{\partial c_{Ab-Ag}}{\partial t}$ is linear in $c_{Ag}$. Thus it is possible to determine the binding rate constants $k_a, k_d$ and the affinity constant $K$ from a time-resolved measurement curve comprising several, at least five, different concentrations of the analyte: a plot of the end signal values of each concentration versus the concentration itself (dose-response curve) can be fitted to the Langmuir isotherm given in eq. 3.6, yielding the maximum antigen concentration (which equals $c_{Ab_t}$, since in this case each antibody has bound one antigen and a so-called antigen monolayer has been formed) and the affinity constant $K$.

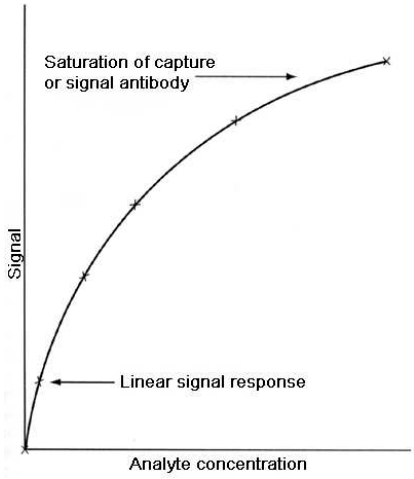


**Figure 3.4:** Dose-response curve. The end signal values are plotted versus the respective concentration and fitted to the Langmuir isotherm described in eq. 3.6 to obtain the maximum antigen concentration (monolayer) signal and the affinity constant $K$ of the system. Adapted from *Davies* (2001).

Resulting from eq. (3.8), the initial binding rate plotted versus $c_{Ag}$ gives the association rate constant $k_a$ and, since $K$ is known from the Langmuir fit, $k_d$ can be derived. These constants are important parameters to characterize the strength of the binding of the reacting molecules. The higher the affinity constant, the stronger is the binding. Typical values for antibody-antigen systems are around $10^6$-$10^{10}$ $M^{-1}$, for the affinity system biotin-avidin it is exceptionally high with $10^{15}$ $M^{-1}$ (*Weber et al.*, 1989).

### 3.4.2 Evaluation of non-equilibrium kinetic data

The last chapter described the evaluation of kinetic data under the assumption that an equilibrium has been reached (see eq. 3.4). In practical applications, however, it might be inconvenient to wait for each analyte concentration until equilibrium and would also mean very high sample consumptions. Therefore it seems feasible to stop the association phase at a certain time and start the dissociation phase, evaluating again the obtained end signal value by fitting the data to the Langmuir model. If for each concentration the same time intervals for association and dissociation phases are chosen, the determination of the affinity rate constant is still possible, as illustrated in Fig. 3.5. This simulation shows

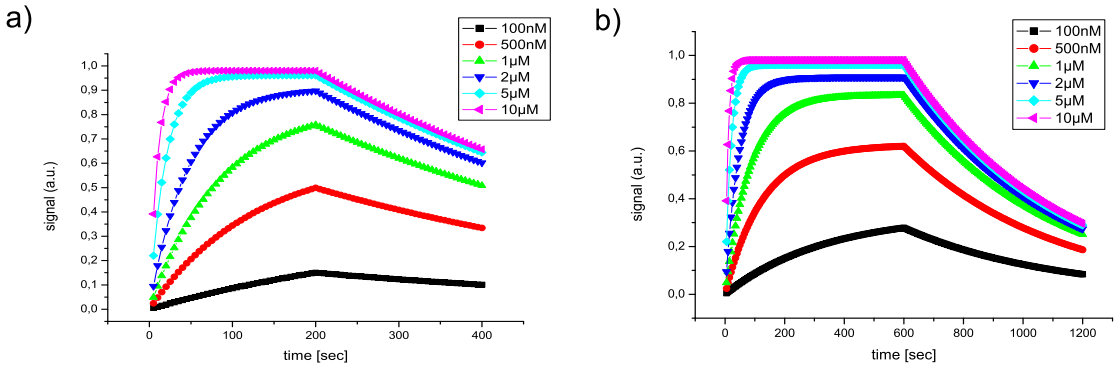


**Figure 3.5:** Comparison of binding data for time intervals of **a)** 200 sec and **b)** 600 sec for association and dissociation phase, respectively. The signal obtained at the end of the dissociation phase is taken for further evaluation.

the association and dissociation of a complex with the following parameters: $k_a = 1 \cdot 10^4$, $k_d = 2 \cdot 10^{-3}$ and $c_{Ab,t} = 1$. For the time intervals 200 sec and 600 sec evaluation of the kinetic data by fitting to the Langmuir model (data not shown) yields affinity rate

constants of $K = 2.05 \cdot 10^6$ M$^{-1}$ and $K = 3.7 \cdot 10^6$ M$^{-1}$, respectively. This result shows that the affinity rate constant is underestimated by less than a factor of two when only time intervals of 200 sec are allowed for the binding reaction instead of 600 sec, where the reaction is clearly closer to equilibrium. Thus it seems feasible to use time intervals of 240 sec for application test measurements on the interferometric biosensor.

### 3.4.3 Influences of mass transport on kinetic data

Upon binding of the analyte from the liquid phase to the immobilized receptor the concentration of the analyte solution close to the surface decreases compared to the bulk solution, which is counterbalanced by diffusion towards the surface called mass transfer. If the rate of binding of the analyte to the receptor exceeds the diffusion rate from the bulk to the surface, the binding is mass-transport limited and influence the kinetics of the binding. Kinetic data obtained from biosensor signal curves may be in practice distorted by mass-transport effects or for example non-specific binding or rebinding of the analyte. One way of checking the binding curves for the influence of any unwanted side effects has been proposed by *Karlsson and Löfas* (1998).

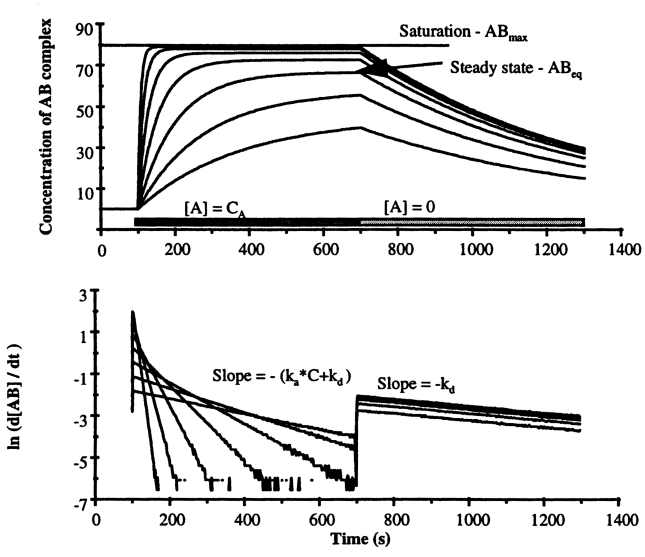


**Figure 3.6:** Ideal binding curves (above) give linear $\ln\left(\frac{\partial c_{\mathrm{Ab-Ag}}}{\partial t}\right)$ vs. t plots. Adapted from (*Karlsson and Löfas*, 1998).

Plots of $\ln\left(\frac{\partial c_{\mathrm{Ab-Ag}}}{\partial t}\right)$ vs. time are linear in the case of ideal binding curves (see Fig. 3.6),

and deviate from this linearity when the measurement data is distorted by mass transport or other side effects. In practice lower receptor capacities or higher flow rates ensure that mass-transport limitations do not occur (*Myszka*, 1999). Another mathematical model (*Myszka et al.*, 1998) describes how to interpret mass transport-influenced data in cases when mass transport limitating assay conditions cannot be avoided. Furthermore it is necessary to check for rebinding, i.e. analyte molecules rebind to another receptor molecule during the dissociation phase leading to a falsified dissociation curve. It has been shown that rebinding is a crucial issue when small molecules are involved and binding rate constants derived from biosensor binding curves may vary significantly from rate constants obtained by measurements in solution (*Nieba et al.*, 1996).

## 3.5 Biochemical background on the application measurement reagents

The quality of a biosensor response clearly depends on the quality and specificity of the biochemical reagents. A subclass of biosensors are called immunosensors, i.e. immobilized antibodies or antigens are used as receptors for their respective immunoreaction ligand. Two affinity systems used in our experiments will be introduced briefly concerning their biochemical background, the immunoreaction system immunoglobulin G-protein G (or protein A) and the affinity system biotin-streptavidin, which is the basis for measurements with biotinylated reagents. Further information about the biochemical backgrounds beyond the scope of this thesis can be found in (*Lehninger et al.*, 1994; *Lottspeich and Zorbas*, 1998).

### 3.5.1 Immunoreactands Immunoglobulin G - Protein G or A

Antibodies are glycoproteins belonging to the immunoglobulin family comprising many proteins involved in immune recognition and host defense systems (*Davies*, 2001). Immunoglobulins (Ig's) are divided into five subclasses - IgG, IgM, IgA, IgD and IgE, differing in size, charge, amino acid composition and carbohydrate content. Here the IgG shall be

described briefly as it is relevant for the experiments shown in chapter 5.
The basic structure of an IgG looks Y-shaped and consists of four different polypeptide chains (see Fig. 3.7) with a total molecular weight of 156kDa : two larger ones (designated as "H" for heavy) and two smaller chains (with "L" for light). All these chains (primary structures) are mixes of $\alpha$-helices and $\beta$-pleated sheets (secondary structures). The four chains are linked by disulfide bonds as indicated by the dots to create an overall tertiary structure. Both H and L chains end in a highly individualized portion (blue), and these pairs are specific for a type of antigen. Therefore each IgG is bivalent, i.e. able to bind two antigens of the same type. Regions of antigens recognized and bound by the antibody are called epitopes. As each IgG out of millions of different IgG's has different blue ends, these ends are called variable ("V"). In contrast, the parts shown in white are uniformly structured among the IgG molecules and are therefore called constant ("C") regions. In fact, by the constant regions the different Ig subclasses can be distinguished.

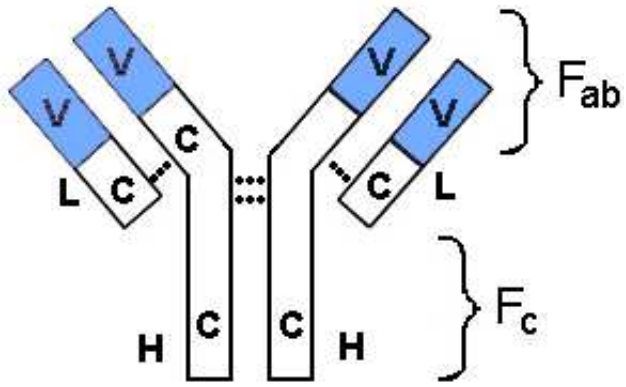


**Figure 3.7:** Schematic structure of an IgG antibody. The molecule (M=156 kDa) consists of four polypeptide chains, two heavy chains ("H") and two light chains ("L"). The four chains are linked by disulfide bonds. The constant part common to all IgG's is denoted with "C"(white), the variable part different for each IgG in blue with "V".

IgG is used almost exclusively in immunoassays due to its high yield in the immunization process, high binding affinity to its epitope and comparably high stability during purification and isolation (*Davies*, 2001). Furthermore it possesses several functional sites for antigen binding and can easily be fractionated into its $F_{ab}$ and $F_c$ fragments, resulting in a higher specificity for particular assays. Two different IgG-binding proteins have been

used in our experiments, protein G and protein A, and their kinetic interaction evaluated (see chapter 5).

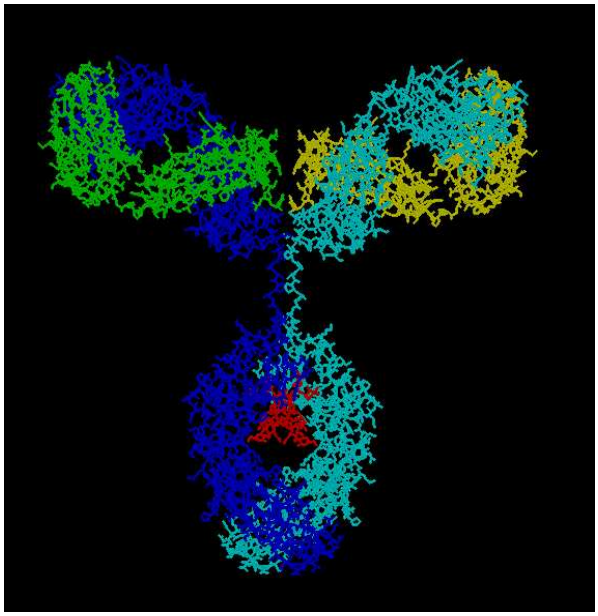

**Figure 3.8:** Stick model of a human immunoglobulin G antibody created with *RasMol* software (*Sayle*, 1993). Different colors represent the four polypeptide chains: the two heavy chains dark and bright blue, the two light chains in yellow and green and the carbohydrate attached to the heavy chains in red. The rotational symmetry about a vertical axis can be clearly recognized.

Protein G is a bacterial cell wall protein with affinity for IgG, isolated from the cell walls of group G *Streptococcus sp.* It has a molecular weight of approx. 33.8 kDa and is capable of binding two IgG Fc-sites (*Bjorck and Kronwall*, 1984).
Protein A is a surface protein of *Staphylococcus aureus* with a molecular weight of approx. 41 kDa (*Surolia et al.*, 1982) and also binds the $F_c$-fragment of IgG. Protein G has a higher affinity to IgG than protein A.

### 3.5.2 Affinity system biotin - streptavidin

As mentioned above, the biotin-streptavidin complex is of special interest for immobilization purposes because this complex has the largest free energies of association yet

observed for noncovalent binding of a protein and a small ligand. The complex is also very stable over a wide range of temperature and pH and unaffected by many organic solvents and other denaturing agents (*Savage*, 1992). Avidin, which is closely related to streptavidin, is a protein originally isolated from chicken egg white and consists of four subunits. Streptavidin is a tetrameric, biotin-binding protein isolated from the bacterium *Streptomyces avidinii*. It also consists of four subunits, i.e. it binds four moles of biotin per mole protein, with a subunit molecular weight of 16.5 kDa. Although avidin and streptavidin show an equally high affinity to biotin, they are different in molecular weight and isoelectric point and differ greatly in overall amino acid composition. Streptavidin exhibits reportedly less non-specific binding than avidin (*Lane*, 1998), which is the main reason for using streptavidin in our experiments. Fig. 3.9 shows a stick model of streptavidin with biotin.

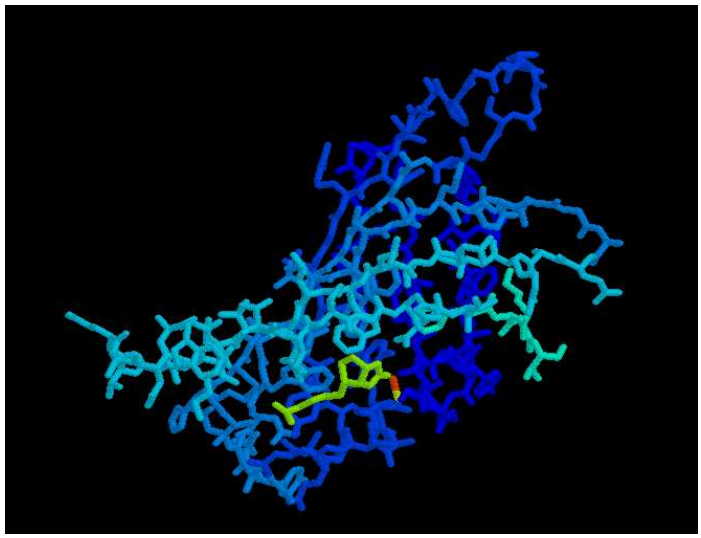

**Figure 3.9:** Stick model of a streptavidin-biotin complex created with *RasMol* software (*Sayle*, 1993). The different blue shades represent the four subunits, the biotin molecule is shown in green.

Biotin is the naturally occuring vitamin H found in every living cell with a molecular mass of only 244.31 Da. The biotin molecule used in our experiments is modified with an N-Hydroxysuccinimide (NHS)-ester and a long-chain (LC) spacer arm of 22 Å. Ad-

ditionally it carries a sulfonate group on the NHS-ring rendering it water-soluble. The long chain spacer arm of NHS-LC-biotin reduces steric hindrance associated with binding multiple biotinylated molecules on streptavidin. Fig. 3.10 shows the chemical structure of sulfo-NHS-LC-biotin with a total molecular weight of 556.59 Da. The NHS-ester reacts

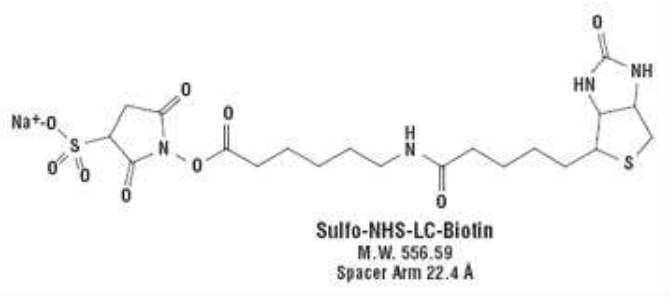


**Figure 3.10:** Chemical structure of NHS-LC-biotin. From *Pierce* (2005).

quite efficiently with primary amine groups that are also commonly found in most proteins and many peptides to form a stable amide (peptide) bond (*Hermanson et al.*, 1992). Fig. 3.11 shows the chemical reaction in detail. The basis for coupling NHS-LC-biotin is provided by amine groups on the surface, e.g. via silanization with aminosilane, or using epoxysilane with ethylene diamine as linker. During the reaction a stable amide bond is formed between the biotin and the amine group under separation of the NHS ester.

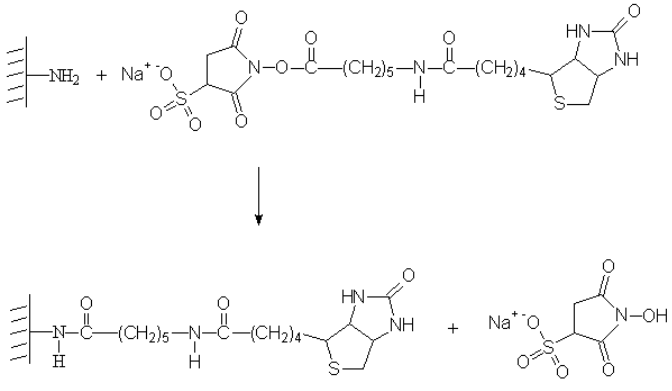

**Figure 3.11:** Reaction NHS-biotin with amine-modified surface. The biotin forms a stable amide bond under separation of the NHS ester.

### 3.5.3 Cytochrome *c*

Cytochrome *c* is a small heme protein with a molecular weight of 12.4 kDa *Lehninger et al.* (1994). This soluble protein consists of a single polypeptide chain and contains a heme group. As an essential component of the mitochondrial respiratory chain, its main function is the transfer of electrons, since it does not bind oxygen, but is capable of being oxidized or reduced. Fig. 3.12 displays a three-dimensional model of cytochrome *c*, where the functional heme group is shown in red.

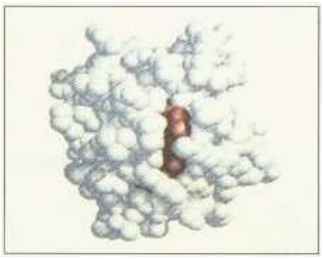

**Figure 3.12:** Three-dimensional model of cytochrome *c*. The heme group is shown in red. Adapted from *Lehninger et al.* (1994).

Cytochrome *c* is a very stable and well characterized molecule and therefore suited for biosensor application measurements. We used biotinylated cytochrome *c* to monitor its binding to a streptavidin-functionalized surface. The experiments will be further described in chapter 5.

# Chapter 4

# Sensor design and characterization

## 4.1 Introduction

This section describes the setup of the interferometric biosensor implementing a two-channel flow cell as fluidic element (IBS 201). The system is based on the optical principle of a Young interferometer. A sketch of the setup is given on the next page.
The key component of the interferometric biosensor is the $Ta_2O_5$ transducer chip provided by Unaxis Balzers, Liechtenstein. In the realized setup the radiation of a red light source (several light sources have been tested, see below) is focused as a line on the first chip grating and guided in two separate paths in a thin $Ta_2O_5$ film. One path serves as sensing branch, where for example antibodies can be immobilized for antigen detection, the other beam is used as reference branch. The two beams are coupled out by a second grating and pass a double slit. On a CCD line sensor the resulting interference pattern can be recorded.
When the analyte is added, i.e. binding molecules cause a local change in surface mass coverage, the phase velocity of the light in the waveguide is decreased and the interference pattern is laterally shifted. This shift is then further evaluated.

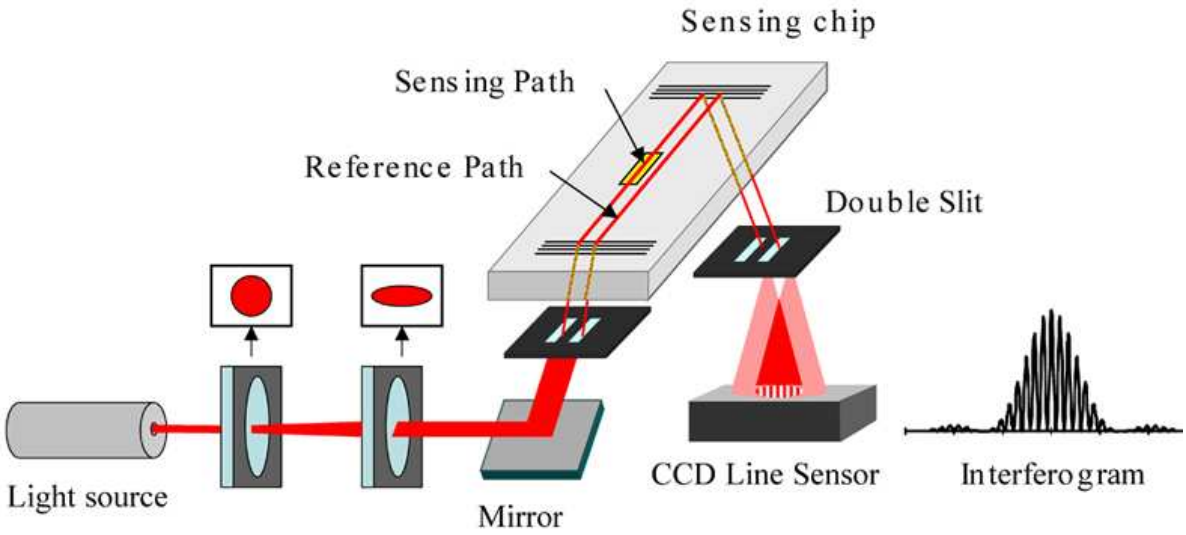


**Figure 4.1:** Schematic design of the interferometric biosensor. Light from a light source (left) passes several optical elements before being split in two beams and coupled into the waveguide chip via a grating. The two beams are then guided separately to the second grating and are coupled out. After a double slit the typical interference pattern can be recorded by a CCD line camera (right).

### 4.1.1 Requirements for the interferometric biosensor system

As it holds true for all label-free biosensors, several requirements have to be fulfilled for the sensor system in order to produce feasible and reliable results. The sensor should be sensitive and selective in terms of biomolecule recognition, give stable, fast and reproducible results, should be multipurpose with respect to applications and easy-to-handle without much effort for maintenance and calibration. Furthermore, in practical use the sample consumption should be as low as possible and the system be working parallel to achieve as many results as possible in short time. Another economical aspect is that the sensor system itself should be available at a reasonable price and consumables like the waveguide chip should be either cheap and disposable or easy to reuse.

These are certainly requirements that, taken all together, are not easy to meet. So there is an ongoing development in the field of optical biosensor technology to better fulfill these requirements. The issue of sensitivity is one of the most complicated for sure, since sensitivity has two contradictionary aspects: on the one hand, increased sensitivity allows

the detection of even lower concentrations of a molecule (or smaller molecules), on the other hand the sensor system inevitably shows also an increased sensitivity to disturbing factors like temperature fluctuations, technological imperfections, unspecific binding of unwanted reactants and many more. These disturbing influences have to be compensated for with optimization of the assay design and advanced technology. In the following the design and realization of the interferometer system will be presented in detail taking these aspects into account.

## 4.2 Interferometric biosensor: flow cell system

### 4.2.1 Biosensor setup - components

#### Light sources

During the development and especially for reasons of signal-to-noise (SNR) reduction three different light sources have been tested and evaluated for their suitability. Initially a helium-neon laser emitting at $\lambda = 632.8\,\mathrm{nm}$ and a maximum output power of $3\,\mathrm{mW}$ has been used. A laser source like a helium-neon has the advantage of being almost monochromatic ($\Delta\lambda = 0.1\,\mathrm{nm}$). Another distinct feature of lasers is their very good spatial and temporal coherence, therefore being well suited for interference experiments. Yet the helium-neon laser is operated without temperature stabilization, rendering it more sensitive to temperature fluctuations in the ambient resulting in wavelength fluctuations. As described in chapter 2.7, wavelength fluctuations can lead to signal distortions when the two beam pathways are of unequal length.

During most experiments described in this thesis, a superluminescent diode (SLD, $\lambda = 675\,\mathrm{nm}$, Superlum, Moscow) with a maxmimum output power of $3.5\,\mathrm{mW}$ served as light source in the system. A SLD is essentially a semiconductor laser carrying antireflection coatings on the end facets. Unlike lasers, it has no optical built-in feedback mechanism so that lasing cannot occur. SLDs generally need operation with temperature stabilization. The main reason for using the SLD in the interferometric system is the feature of partial coherence due to its larger spectral bandwidth compared to a laser source, which allows

the implementation of different evaluation algorithms for the interferogram signal, also with respect to the development of the plate-reading system. One disadvantage of the SLD has shown to be its incomplete linear polarization, requiring extra polarization measures to allow guiding of proper TE or TM modes in the waveguide chip (see chapter 4.4.1). For this reason, the suitability of a laser diode ($\lambda$ = 670 nm, Sanyo, Japan) for the interferometer system has been examined. In general, laser diodes have the advantages of being quite small in size (5.6 mm package size) and reasonably priced, yet they are temperature sensitive. Since in our experiments a laser diode with a maximum output power of 7 mW was used, but only around 1.5 mW needed, possible heating of the diode has been diminished by mounting it in a heat sink, without use of further temperature stabilization.

**Optical elements**

For beamforming in front of the waveguiding chip, essentially two lenses have been implemented (see also Fig. 4.1). Since all the light sources used have a certain angle of divergence, an aspheric lens with a focal length of $f_1 = 8$ mm is adjusted accordingly in front of the light source to collimate the beam. This collimated beam is afterwards focused by a cylindrical lens with a focal length of $f_2 = 130$ mm to form a line-shaped beam on the first grating of the waveguide chip. Practically the grating can also be located slightly out of focus in case of the IBS 201, since here focusing on the grating is only done to couple in enough power which would otherwise be lost outside the chip holder. All lenses used in the system were ordered from Thorlabs, USA and are made of BK7 glass (n=1.52) coated with an antireflection coating to maximize power transmission and avoid reflections back into the light source.

**Chip mount**

The chip mount for the IBS 201 is a special design and has been built at the IPM. It implements several functions as illustrated in Fig. 4.3 and 4.4 and allows quick replacement and adjustment of the waveguide chip. The light beam, focused to a line by the cylindrical

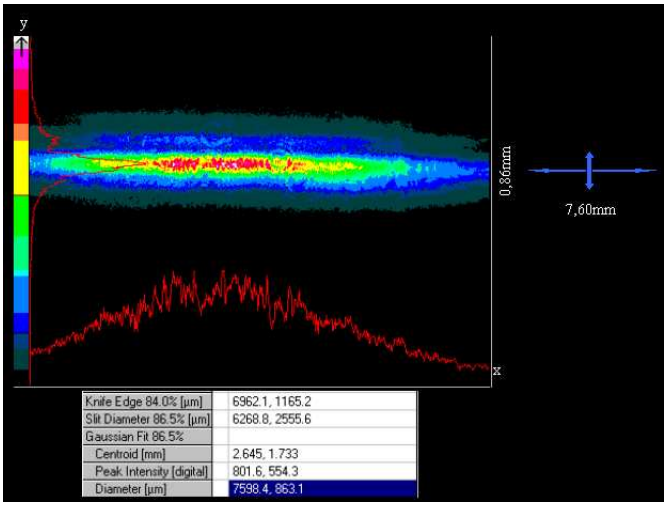


**Figure 4.2:** Beam profile of the SLD after beamforming by an aspherical and a cylindrical lens. The intensity distribution has a Gaussian profile in both axes.

lens in front, enters the small hole on the left. A small mirror (3 mm x 7 mm) redirects the beam almost orthogonally outwards to the chip and can be rotated (approx.±10 °) by a screw on the side to adjust the incoupling angle. The chip is placed vertically on pins and held in this position by the flow cell. Horizontally one pin on the right side, which can be moved to four different positions depending on which pair of gratings is to be used, ensures that the gratings are positioned correctly for coupling. The small double slit plate is located vertically right behind the chip (see Fig. 4.4) and fixed against the chip mount to prevent it from shifting. The first pair of double slits (slit width 100 µm) cuts out two beams which are then guided in the waveguide layer. This reduces the problem of light scattering in the flow cell. A second pair of double slits (slit width between 3 µm and 5 µm), after the beams have been coupled out again by a second grating, forms the actual Young interferometer. The two rays leave the chip mount through another small hole behind the second double slit pair.

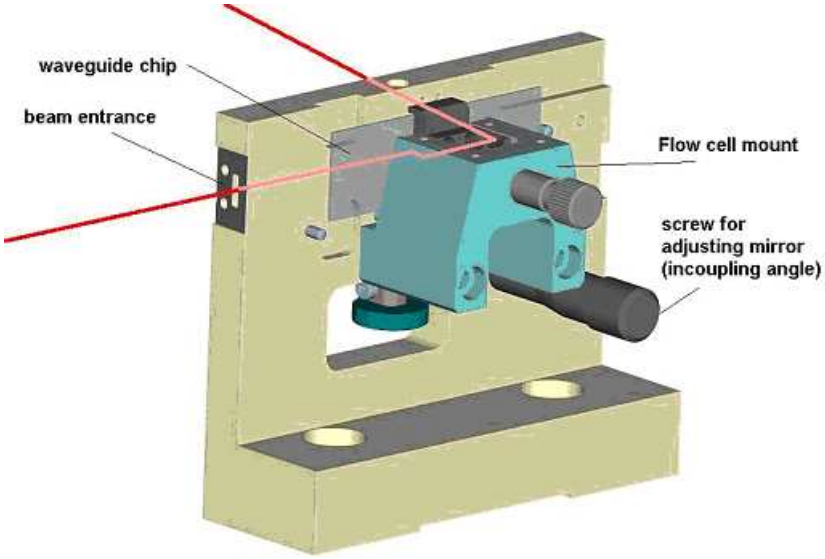


**Figure 4.3:** Chip mount design (CAD drawing). The red line represents the beam path from left to right. Light enters through a small hole on the left, is redirected by a small mirror, adjustable for incoupling, coupled into the waveguide and coupled out again on the right in direction of the CCD camera.

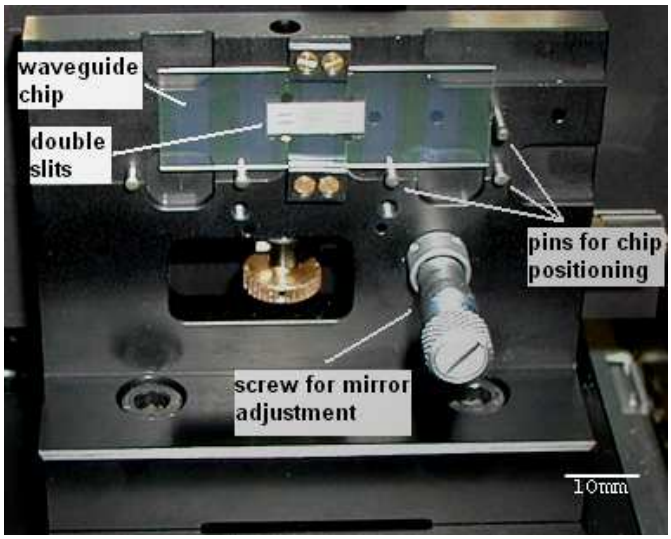


**Figure 4.4:** Photograph of the chip mount without the flow cell being mounted. The double slit plate behind the waveguide chip is now visible as well as the pins for chip positioning.

### Double slits

A schematic drawing of the double slit plate used for the majority of the measurements presented in this thesis is shown in Fig. 4.5. The double slit plates were fabricated at the IPM by photolithographic structuring and etching of an aluminum coated glass wafer. The plates comprise a double slit on the incoupling side with a slit width of 100 µm for spatial filtering to form two separate beams in the waveguide, and a double slit with 3 µm or 5 µm width on the outcoupling side to generate the interference pattern in the far field. The slit distance of 1.3 mm matches exactly the distance between the two flow

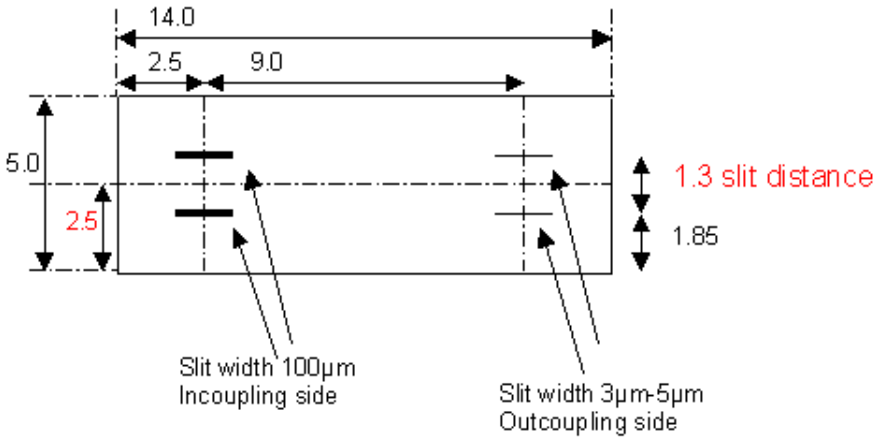


**Figure 4.5:** Double slit plate design and dimensions (in mm unless otherwise noted).

cell chambers. This ensures that the flow cell completely covers the two beams and no scattering can occur at the flow cell borders. The slit width w on the outcoupling side is an important parameter for the generation of the interference pattern, since it determines directly the period of the interferogram and thus the number of sampled points. Previous to the fabrication of these plates double slits with $w = 20$ µm have been used. Table 4.1 summarizes the parameters for the interferogram for various slit widths using eq. 2.62 for diffraction at a single slit to approximate the total width of the interferogram. It can be seen that for smaller slit widths at a constant distance the interferogram becomes wider and contains more periods. Furthermore the Nyquist theorem is fulfilled for the double slit distance of 1.3 mm since the period of the interferogram calculates to $\approx 9$ pixels for a CCD pixel size of 7 µm.

| Slit width w [µm] w | Period [µm] p=λD/d | Width [mm] B=2λD/w | Contained periods (B-d)/p |
|---|---|---|---|
| 3 | 62.31 | 54 | 845.77 |
| 5 | 62.31 | 32.4 | 499.12 |
| 20 | 62.31 | 8.1 | 109.13 |

**Table 4.1:** Sample calculation for different double slit widths w with a detection distance of D = 120 mm, slit separation d = 1.3 mm at $\lambda = 675$ nm

### Waveguide chips

The core of the interferometric biosensor are the waveguide chips supplied by Unaxis Balzers, Liechtenstein. A 16x48 mm glass wafer with five 0.5 mm wide etched gratings (9 mm separation) is coated with a 154 nm film of $Ta_2O_5$. The gratings are covered by an $\approx$ 500 nm thick and 4 mm wide protective layer of $SiO_2$ leaving a 5 mm interaction length for each of the four measurement positions. Fig. 4.6 shows the chip design and dimensions, Fig. 4.7 illustrates the refractive index profile for a waveguide chip with the relevant parameters given in Table 4.2.

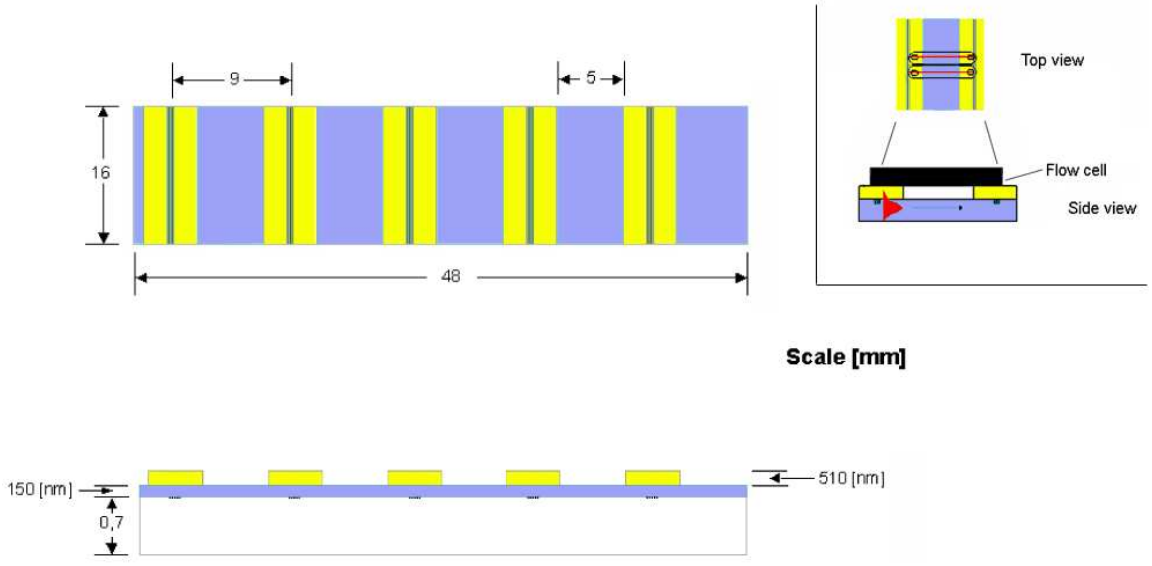


**Figure 4.6:** Waveguide chip design and dimensions. A 154 nm thick $Ta_2O_5$ film is deposited on a 16x48 mm glass wafer comprising five etched gratings. $SiO_2$ layers protect the gratings leaving a total interaction length of 5 mm.

| | | | |
|---|---|---|---|
| substrate | AF45 | n=1.52 | d=0.7 mm |
| waveguide | $Ta_2O_5$ | n=2.1 | d=154 nm |
| covering layer | $SiO_2$ | n=1.46 | d≈500 nm |
| gratings | period = 360 nm | depth = 12-40nm | coupling angle TE: $-5.35°$ (with $SiO_2$-layer: $-3.574°$) coupling angle TM: $-15.422°$ (with $SiO_2$-layer: $-10.476°$) |
| evanescent field | TE : FWHM=30.9 nm | $\frac{P_{ev.field}}{P_{tot}}$=11.27% | TE: $\frac{dn_{eff}}{dt_{cover}} = 229 \cdot 10^{-6}\ nm^{-1}$ |
| | TM : FWHM=37.9 nm | $\frac{P_{ev.field}}{P_{tot}}$=13.23% | TM: $\frac{dn_{eff}}{dt_{cover}} = 439 \cdot 10^{-6}\ nm^{-1}$ |

**Table 4.2:** Unaxis waveguide chip parameters. Calculations for $\lambda$=675 nm and $n_{cover} = 1.45$.

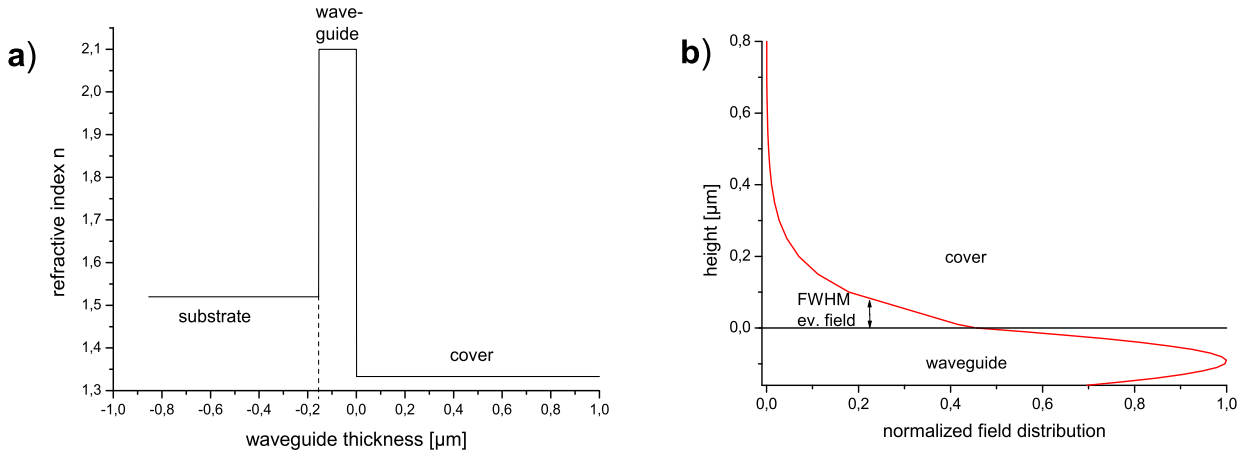


**Figure 4.7: a)** Refractive index profile for a planar waveguide with refractive indices of $n_s = 1.52$, $n_f = 2.1$, $n_c = 1.333$ **b)** Field distribution in waveguide and cover at the same parameters. The extension of the evanescent field is given as FWHM.

The coupling angles are given by the grating equation (*Goodman*, 1988):

$$n_{eff} = n_c\, sin\alpha + \frac{m\lambda}{\Lambda} \tag{4.1}$$

with $\alpha$ being the coupling angle and $\Lambda$ the grating period.

The extension of the evanescent field (given as FWHM, full width at half maximum), the light intensity in the evanescent field and the sensitivity constants are calculated according to (*Tiefenthaler and Lukosz*, 1989). The additional protective layer of $SiO_2$ above the optical gratings represents an alteration to the supplied chips. These protective

layers were fabricated at the IPM by ion assisted deposition (IAD) to ensure that the flow cell never comes into contact with the evanescent field and thus prevents light from scattering at the flow cell and disturbing the signal. Moreover, since the flow cell is made of silicone and an equal and reproducible contact pressure is almost impossible to achieve, the flow cell might alter its shape during a measurement and lead to signal drifts or other distortions if it was not prevented to interact with the evanescent field. As the effective thickness of the evanescent field is less than 100 nm for the given waveguide parameters and wavelength, a thickness of ≈500 nm for the protective layers is sufficient. The inset in Fig. 4.6 illustrates the effect of the protective layers on the waveguide film when a light mode is guided.

Gratings with different diffraction grating depths were supplied by Unaxis with 12 nm, 22 nm, 30 nm and 40 nm and tested for their coupling characteristics and total power transmission of the waveguide chip as described in the experimental section. Fig. 4.8 shows an atomic force microscope (AFM) picture of a diffraction grating in glass with a grating depth of 12 nm.

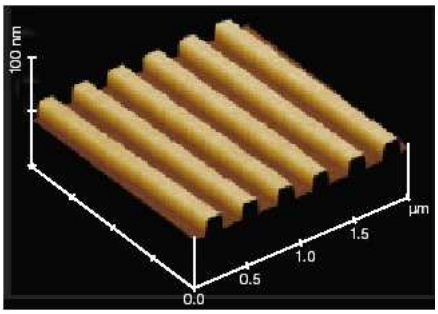


**Figure 4.8:** Atomic force microscope (AFM) image of a diffraction grating in glass, 2 µm x 2 µm. The grating period is 318 nm and the grating depth is 12 nm. (Courtesy of Unaxis)

### Flow cell mount and flow cell

Both the flow cell mount and the flow cells have been constructed and fabricated at the IPM and are a special design for the interferometric biosensor. Two types of flow cells can be used according to the application: a two-channel flow cell as shown in the

photograph and the CAD design of the mounted flow cell in Fig. 4.9. A single-channel flow cell covering both channels as shown in Fig. 4.10 allows a simultaneous application of analyte solutions on differently immobilized channels and therefore referencing of for example refractive index differences. The flow cells are made of two-component silicone-based fluid (Sylgard 170, Corning, USA) which is formed and heat-treated to a flexible flow cell shape. Over time, usually several months depending on the degree of usage, the silicone deteriorates and the flow cell has to be renewed.

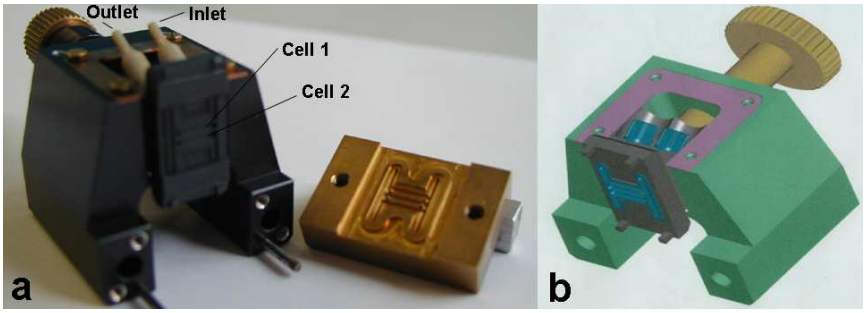


**Figure 4.9: a)** Photograph of the two-channel flow cell **b)** CAD design of the mounted flow cell.

**Figure 4.10:** Photograph of the single-channel flow cell and its casting mold.

The two-channel flow cell has dimensions of ≈5.6 x 1.8 x 0.3 $mm^3$ equating a volume of ≈3 µl per channel. The single channel flow cell has a volume of ≈3.5 µl with dimensions of 6.9 x 1.7 x 0.3 $mm^3$.

### CCD camera

The device mainly used for signal detection was a CCD1000 (Stresing, Berlin, Germany) with an integrated ILX 526A sensor (Sony, Tokyo, Japan). A CCD is basically a semi-conductor chip sensitive to light and subdivided into many discrete rectangular areas

called pixels. Each photon impinging on a pixel results in a charge, which is accumulated for all photons within the exposure time and stored for readout as a measurable voltage signal. The ILX526A sensor is a line sensor comprising 3200 pixels at a pixel size of 7 µm x 200 µm. The camera is usually used at exposure times between 50 ms and 250 ms for experiments. Previously the same camera, but with an ILX 511 line sensor (2048 pixels, pixel size 14 µm x 200 µm) has been used. Further, a full-line binned CCD (Hamamatsu, Japan) comprising a total number of pixels of 2048 x 14 with a pixel size of 14 µm x 14 µm has been tested.

**Peristaltic pump**

A peristaltic pump (Ismatec, Wertheim, Germany) installed externally allows continuous pumping of analyte solutions in up to four channels through the system. All required tubing is obtained from Novodirect, Kehl, Germany. Silicone tubing with an inner diameter of 0.5 mm has proven suitable as well as outlet tubing of silicone with an inner diameter of 0.64 mm. Silicone has the advantage of being biocompatible and chemically inert to most buffers used during the experiments. For biological applications it is advisable to renew the inlet tubing previous to a new measurement run. Since the two channels can be used either as sensing path or as reference path, it is not necessary to predefine the channels. Dragging of the liquids through the system instead of pumping seems more advantageous, because in this configuration the inlet tubing can be chosen very short and thus mixing of sample liquids is reduced. The pumping velocity is programmable, as standard velocity the setting 0.10 ml/min on the pump, being equal to an effective velocity of ≈80 µl/min per channel for the given tubing configuration, was chosen. With ≈20 cm inlet tubing length this corresponds to a response time of the system of around 30 sec.

### 4.2.2 Biosensor setup - realization

This section describes the realized setup of the interferometric biosensor implementing the components introduced above. The system setup has to meet certain requirements, such as being robust, compact and adjustable without major efforts. Fig. 4.11 illustrates

the current setup of the flow cell instrument in top view. Light from the light source (1) is collimated by an aspherical lens with f=8 mm (2) and passes a polarizer (3) for linear polarization. Several optical density filters from 0.1 to 2 (4) decrease the light intensity if necessary. A cylindrical lens focuses the collimated beam onto the waveguide chip grating. The complete chip holder and the fluidics are hidden behind the black lid (6), which can be opened separately to access these components. An optional cylindrical lens (7) allows refocusing onto the CCD line sensor (8), depending on available light intensity coming out of the waveguide chip. The CCD camera (9) transmits the recorded data from the sensor to a PCI card in a computer connected to the system where the data are processed by an FFT algorithm.


**Figure 4.11:** Functional design of the interferometric biosensor IBS 201. Refer to the text for the meaning of the numbered components.

**Figure 4.12:** Front view photograph of the interferometric biosensor IBS 201.

Fig. 4.12 shows a photograph of the interferometric biosensor (side view). The black lid can be opened to access the chip mount and fluidic components without disturbing the rest of the optical setup. All optical components are firmly screwed to a base plate which is isolated against the casing to avoid vibrational fluctuations.

### 4.2.3 Experimental characterization of the components

#### Characterization of the SLD

For most experiments an SLD-260-MP from Superlum, Moscow was used with a specified wavelength of $\lambda = 676.1\,\text{nm}$ and a spectral bandwidth of $\Delta\lambda = 14.8\,\text{nm}$ at a current of 150 mA at 25 °C (*Superlum*, 2003). Since the wavelength and the spectral bandwidth vary with current and temperature, detailed measurements were done to investigate these dependences.

An SLD essentially operates like an edge-emitting LED at low current levels whereas at higher currents the power increases superlinearly and the spectral bandwidth narrows. Fig. 4.13 shows the light-current characteristics at different resistances.

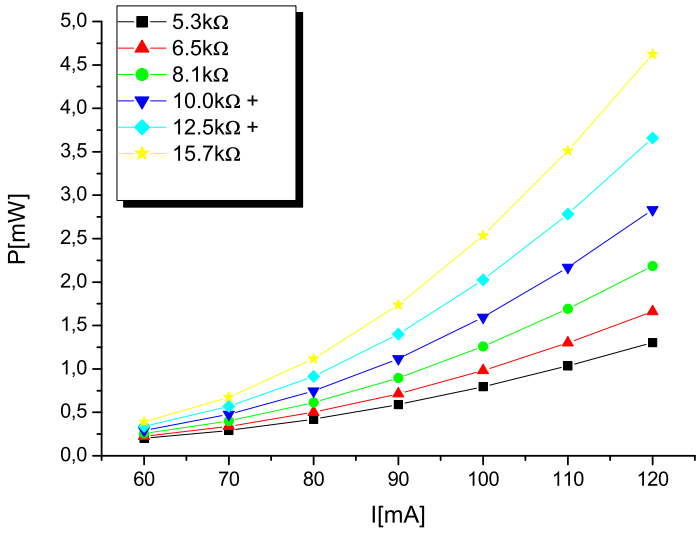


**Figure 4.13:** Light-current characteristics of the SLD at different resistances. Resistance values marked with + are specified as stabilization points with temperatures of T=25 °C for R=10 kΩ and T=20 °C for R=12.5 kΩ. Measurement performed with the optical power meter described in chapter 5.

The measurement shows a superlinear power-current dependence and an increasing power at higher resistances, i.e. lower thermistor temperatures. Due to the fact that the SLD should be operated at high power to obtain a high light intensity and the highest stable resistance is specified for 12.5 kΩ, this resistance value was chosen for all experiments. Another crucial parameter is the spectral bandwidth of the light source, since it directly correlates with the coherence length and thus influences the interference pattern. The corresponding test series (Fig. 4.14) shows the dependences of wavelength and spectral bandwidth on current or resistance. Extrapolation of the obtained data yields for a resistance of 12.5 kΩ and a current of 100 mA a wavelength of $\lambda$=675.5 nm and a spectral bandwidth of $\Delta\lambda$=10.35 nm which is in good accordance with the specifications.

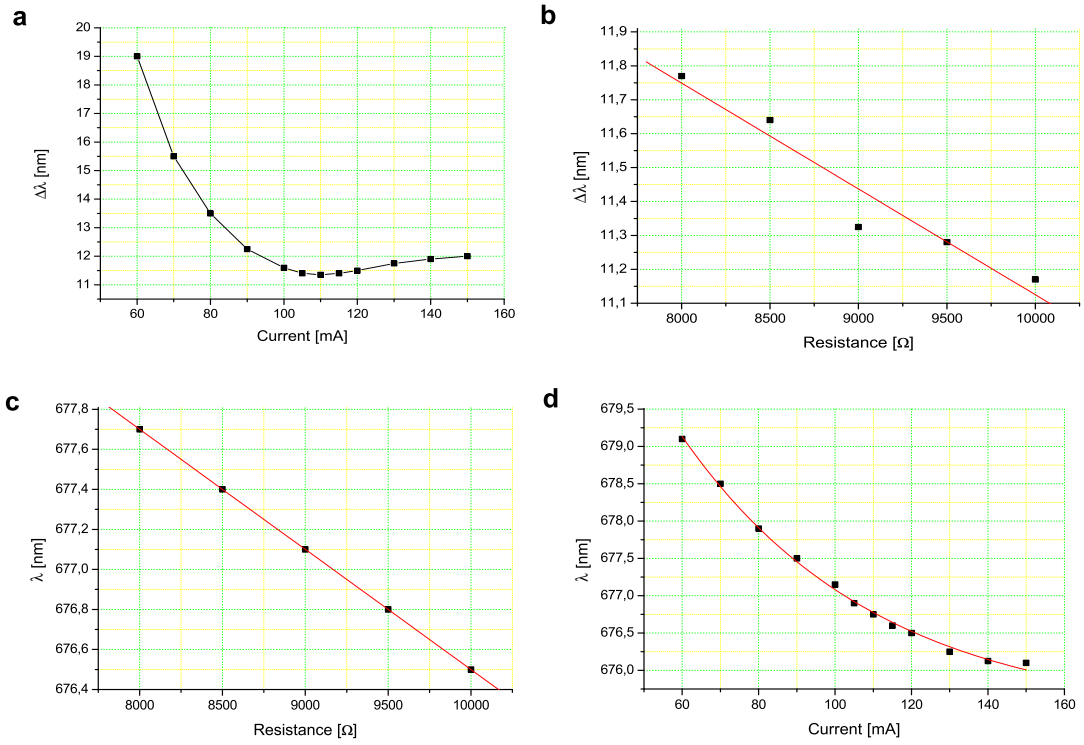


**Figure 4.14:** Wavelength-current and wavelength-resistance characteristics of the SLD.
**a)** Spectral bandwidth $\Delta\lambda$ versus diode current at a constant resistance of 9 kΩ
**b)** Spectral bandwidth $\Delta\lambda$ versus thermistor resistance at a constant current of 100 mA (red line denotes linear fit)
**c)** Wavelength versus diode current at a constant resistance of 9 kΩ (red line denotes linear fit)
**d)** Wavelength versus thermistor resistance at a constant current of 100 mA (red line denotes fit to an exponential decay model of power 2.

The fundamental correlation between coherence length and spectral bandwidth is described by the following expression (*Kühlke*, 2004):

$$\Delta f \approx \frac{1}{\tau_c} = \frac{c_0}{l_c} \tag{4.2}$$

i.e. the larger the spectral bandwidth of the light source, the smaller the coherence time (and coherence length, respectively). Eq. 4.2 can be expanded to obtain a relationship between the wavelength and the coherence length:

$$\begin{aligned} \Delta f &= \frac{\partial f}{\partial \lambda}\Delta\lambda \\ &= -\frac{c_0}{\lambda^2}\Delta\lambda \\ \Rightarrow l_c &= \frac{\lambda^2}{\Delta\lambda} \end{aligned} \tag{4.3}$$

With the given values for wavelength and spectral bandwidth the theoretical coherence length of the SLD can be determined to $l_c = 44\,\mu m$. Experimentally the coherence length can be derived from the coherent region of the interference pattern, as shown in Fig. 4.15 according to:

$$\frac{B_c}{p} = \frac{l_c}{\lambda} \tag{4.4}$$

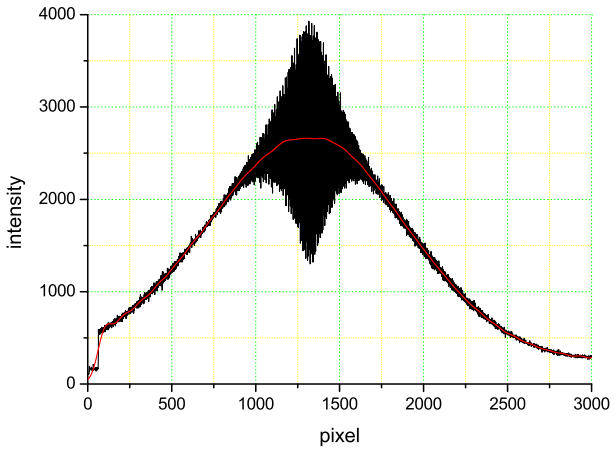


**Figure 4.15:** Interferogram from a double-slit experiment recorded with the SLD in TM mode as light source.

where $\frac{B_c}{p}$ is given by the number of periods p in the coherent region $B_c$. From the interferogram a total number of periods of ≈50 is obtained, yielding a coherence length of ≈33 µm which is in good accordance with the theoretical value.

### Characterization of the laser diode

As alternative light source for the interferometric biosensor a laser diode can be implemented. Laser diodes have the advantages of being compact and small sized, however they are very sensitive to back reflections. Like all lasers, laser diodes have the feature of operating like an LED below a certain threshold current, therefore emitting semicoherent light in this case. Above threshold current these light sources are characterized by a high degree of coherence and linearity between output power and input current. For the interferometric biosensor, especially the power range below threshold current is interesting due to the semicoherence feature. Fig. 4.16 shows the light-current characteristics of a Sanyo DL3149 laser diode (Sanyo, Japan) with a peak wavelength of $\lambda = 670\,\text{nm}$. The threshold current has been determined to 25 mA, the slope efficiency above threshold to 308 µW/mA.

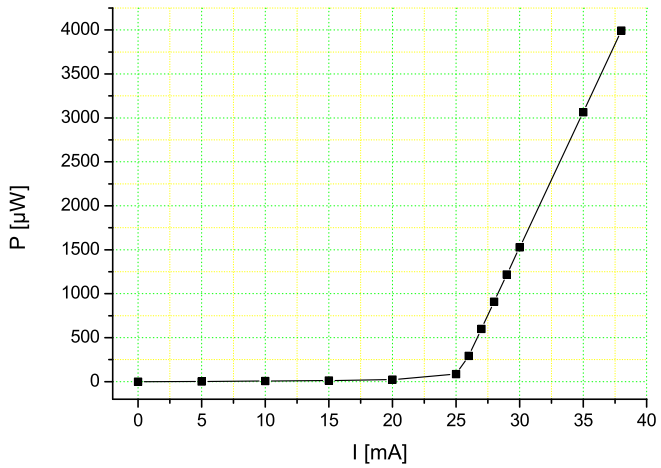


**Figure 4.16:** Light-current characteristics of the Sanyo DL3149 laser diode operated without temperature stabilization. The threshold current is 25 mA, the slope efficiency has been determined to 308 µW/mA. Measurement performed with the optical power meter described in chapter 5.

Despite the fact that this type of laser diode has a comparatively high threshold current, the available power right below threshold is only ≈100 µW. In this case the remaining low light intensity on the CCD has to be compensated with higher exposure times. In addition, this laser diode is not temperature stabilized in contrast to the SLD, so that the SLD remains the preferred light source for our applications.

### Characterization of different CCD sensors

The camera system used for the interferometric biosensor is the CCD1000 where different sensors have been integrated and tested concerning dark current and signal-to-noise. A high signal-to-noise ratio is important for the signal evaluation, since pixel noise directly correlates with phase noise, as will be shown in section 4.2.5. Dark current measurements have been performed with all three sensors described in Table 4.3.

| | Sony ILX 511 | Sony ILX 526A | Hamamatsu S9840 |
|---|---|---|---|
| no. of pixels | 2048 | 3200 | 2048 x 14 |
| pixel size | 14 x 200 µm (14 µm pitch) | 7 x 200 µm (7 µm pitch) | 14 x 14 µm |
| sensor length | 28.67 mm | 21 mm | 28.67 mm |

**Table 4.3:** Comparison of the CCD sensors used for the interferometric biosensor

Fig. 4.17 summarizes the results for exposure times for up to 800 ms. The results show a significantly lower dark current noise for the arrayed sensor than for the line sensors at comparable exposure times. Based on these findings it was expected that the signal noise should also be lower for the arrayed sensor, resulting in an increased signal-to-noise ratio. Thus another measurement was performed investigating the signal noise dependent on the gray value. For this, the SLD was collimated by the aspheric lens and the signal intensity on the camera varied by either varying the driving current of the SLD or the exposure time. The results are illustrated in Fig. 4.18. As expected, the arrayed sensor shows a significantly lower signal noise at comparable gray values than the other sensors. A simulation has been performed to study the correlation of pixel noise and phase noise, and a linear dependence thereof can be observed (see Fig. 4.19. Thus it is expected that the implementation of the arrayed sensor should yield the lowest phase noise.

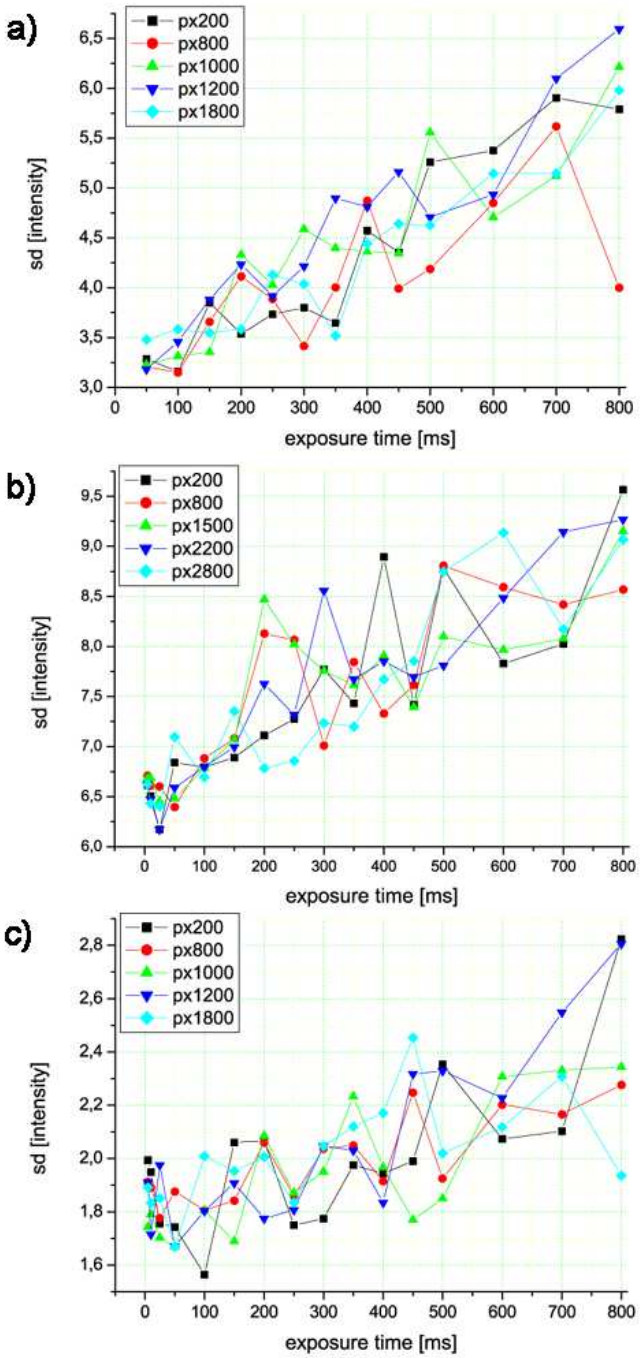


**Figure 4.17:** Dark current measurement of CCD sensors. Shown is the standard deviation of the mean of 5 arbitrarily selected pixels versus exposure time.
**a)** Sony ILX 511 (2048 pixels)
**b)** Sony ILX 526A (3200 pixels)
**c)** Hamamatsu S9840 (2048 x 14 pixels)

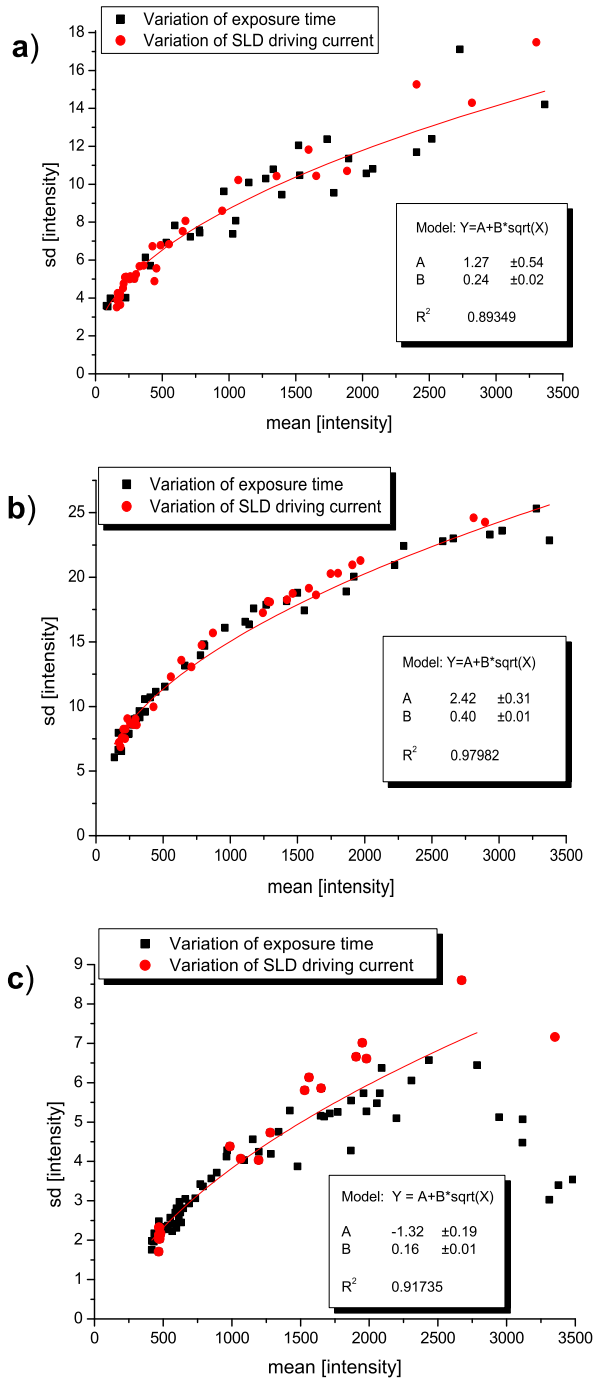


**Figure 4.18:** Signal noise measurement of CCD sensors. Shown is the standard deviation of the mean of 5 arbitrarily selected pixels versus the mean intensity.
**a)** Sony ILX 511 (2048 pixels)
**b)** Sony ILX 526A (3200 pixels)
**c)** Hamamatsu S9840 (2048 x 14 pixels)

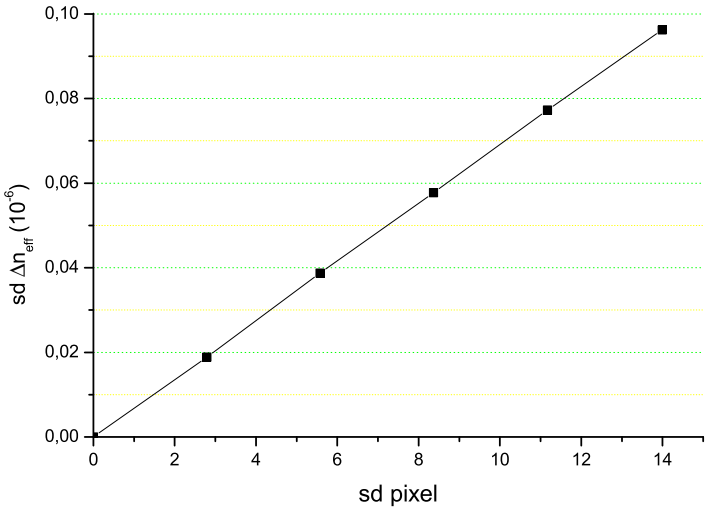


**Figure 4.19:** Correlation of phase noise and pixel noise, simulation. A linear dependence of phase noise versus pixel noise can be observed.

### Characterization of waveguide chips

As the key element of the interferometric biosensor, the waveguide chips have been experimentally characterized with respect to coupling angle, coupling efficiency and power transmission for both TE and TM modes, and for the different grating depths of the supplied chips.

The coupling angle has been measured with a separate setup where the chip is placed on a rotating table and the direct transmission from the first grating is monitored by a photodiode, as shown in Fig. 4.20. This setup allows the direct measurement of the incoupling angle and the coupling tolerance for different focusing. When the coupling condition is fulfilled while the chip is rotated, the intensity of the transmitted light on the photodiode decreases by the amount of light coupled into the waveguide and is detected by a change in photodiode current. The FWHM of the detected curve represents a measure for the coupling tolerance where a significant part of the light can still be coupled into the waveguide.

The coupling angles have been determined for both TE and TM mode and grating depths of 12 nm, 22 nm, 30 nm and 40 nm and are summarized in Table 4.4. The 22 nm wave-

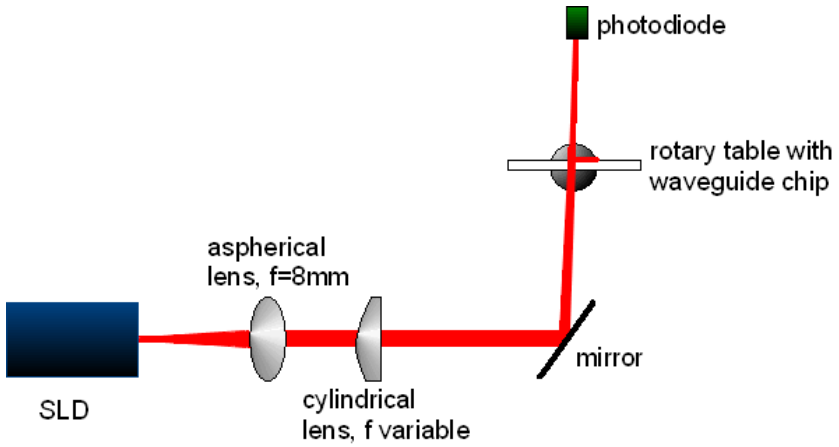


**Figure 4.20:** Setup for the determination of the coupling angles. The chip is placed on a rotating table and the direct transmission from the first grating monitored by a photodiode for angle intervals of 0.5 °. The focal length of the cylindrical lens can be varied.

| | TE | TM |
|---|---|---|
| 12 nm | 5.10 ° | 15.0 ° |
| 22 nm[1] | 3.40 ° | 9.90 ° |
| 30 nm | 5.23 ° | 14.95 ° |
| 40 nm | 5.45 ° | 15.35 ° |

**Table 4.4:** Coupling angles for TE and TM and different grating depths. [1]: the 22 nm waveguide chips were already coated with the $SiO_2$-layer at the time of measurement.

guide chips were already coated with the $SiO_2$-layer at the time of measurement.

The averaged FWHM of all measurements depending on grating depth and focal length of the cylindrical lens determine the coupling tolerance as shown in Fig. 4.21 for TE mode. An optimal focal length for incoupling appears to be f=100 mm, independent of the grating depth. This result can be interpreted using eq. 4.1 and calculating the coupling angles taking the spectral bandwidth of the SLD into account, which yields a required tolerance of $\approx\pm 1$ ° to couple the complete spectrum. With a given beam diameter of 3.5 mm for TE mode this results in a required focal length of ≈100 mm.

Another crucial point is the total coupling efficiency of the waveguide chip, since the output power is eventually detected by the CCD camera and therefore needs to be sufficiently high. Power measurements were carried out for TE mode for the transmission

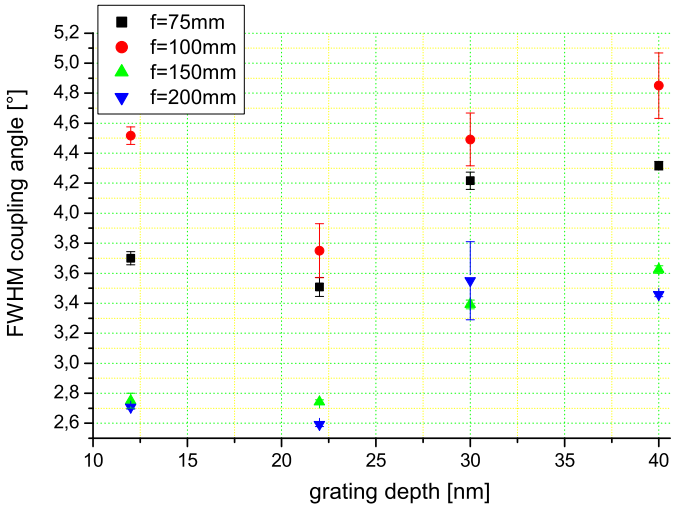


**Figure 4.21:** Coupling angle tolerances (FWHM) for focal lenghts of 75 mm, 100 mm, 150 mm and 200 mm and grating depths of 12 nm, 22 nm, 30 nm and 40 nm. The optimal focal length is 100 mm independent of grating depth.

T, the output power $A_1$ and the output power $A_2$. $A_1$ corresponds to the light intensity available on the CCD camera. Values for reflection from the first grating $R_1$, $R_2$,..., $R_n$ are calculated from the total power. The results are presented in Fig. 4.22. The total coupling efficiency can be estimated to ≈16%.

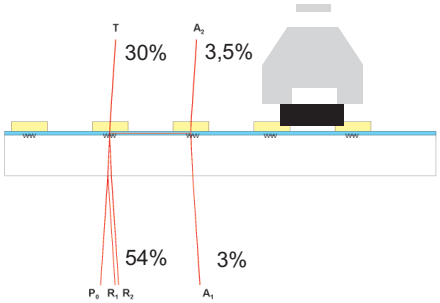


**Figure 4.22:** Input and output coupling of light intensity in TE mode. Measurements performed with the optical power meter described in chapter 5.

The difference between TE and TM mode concerning power transmission can be estimated from the coupling experiments described before, since the transmitted power directly correlates with the measured photodiode voltage. For the mostly used grating depth of 30 nm, the results are illustrated in Fig. 4.23. It can be seen that the coupling efficiency

is about three times higher for TE mode than for TM mode. Yet also in TM mode operation the light intensity is sufficient for signal detection.

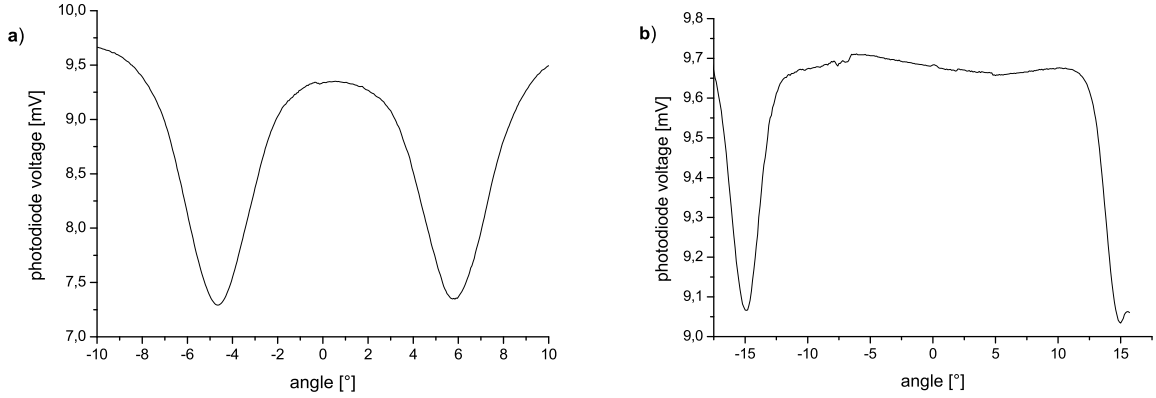


**Figure 4.23:** Comparison of coupling efficiencies for TE and TM mode. **a)** Measurement diagram for TE mode coupling. **b)** Measurement diagram for TM mode coupling.

### 4.2.4 Signal analysis and processing

This section presents an overview on the signal analysis software based on the Fourier Transform described in chapter 2.6, and further signal processing steps and their evaluation regarding a refining of the signal.

#### Fast Fourier Transform algorithm

A software algorithm environment in LabView™ based on a Fast Fourier Transform of the interferogram has been designed for the interferometric biosensor. A detailed description of the Fourier Transform analysis of a fringe pattern can be found in (*Kujawinska and Wojciak*, 1991). Several calculation-intensive parts of the algorithm have been programmed as C++ subroutines and are implemented as dynamic link library (DLL) to work with the Labview™ interface.

The starting point of the signal analysis is the signal itself, here an interferogram. The CCD camera samples images with a predefined exposure time that are displayed on a customized LabView™ user interface. Depending on the CCD sensor either 2000 or 3000 pixels are displayed. The region of interest depends on the coherent area within the inter-

ference pattern and thus on the light source characteristics. Fig. 4.24 shows an example of an interferogram sampled by the ILX 526A sensor and the corresponding region of interest.

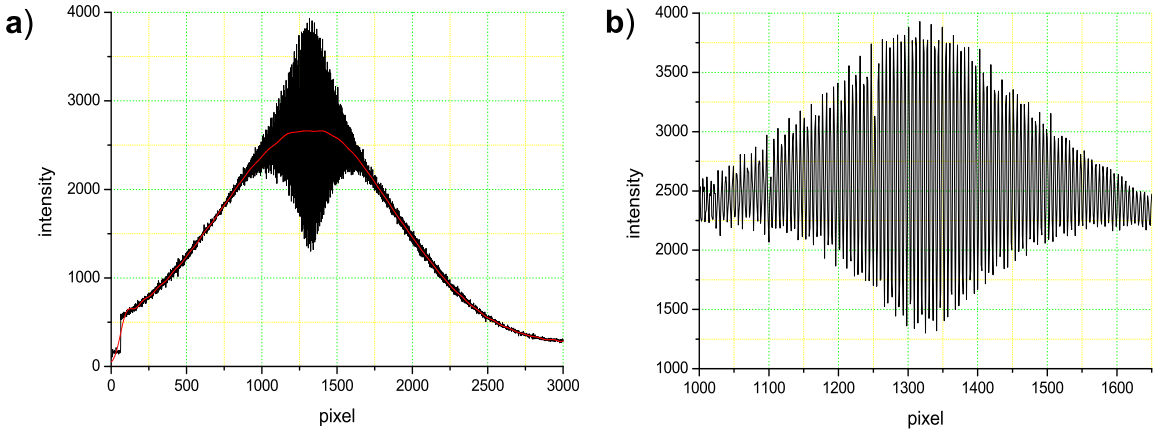


**Figure 4.24: a)** Interferogram recorded by the CCD camera (3000px) **b)** The region of interest (i.e. coherent area of the interferogram) from a)

Before the actual FFT is applied to the signal, the sampling properties of the CCD have to be investigated to ensure that the Nyquist Theorem (see ch. 2.6) is fulfilled for a correct transform. The pixel sizes of the CCD sensors vary from 7 µm to 14 µm, so that every 7 µm or 14 µm the interferogram is sampled (sampling period). This results in a sampling frequency of $f_s$=1/7 µm$^{-1}$ or $f_s$=1/14 µm$^{-1}$. From Fig. 4.24b an interferogram period of ≈9 pixels can be determined, equivalent to 63 µm or 126 µm, respectively. Thus the maximum interferogram frequency is 1/63 µm$^{-1}$. The Nyquist Theorem states that the sampling frequency must be greater than twice the frequency of the signal being sampled, and with $1/14 \geq 2 * 1/63$ this requirement is fulfilled and there should be no error due to aliasing for the current interferometer setup.

The sampled signal then undergoes an FFT in order to accurately estimate the spatial period of the interferogram and thus the spatial frequency which corresponds to the maximum of the signal peak of the FFT (see Fig. 4.25). However, the FFT does not give any information on possible distortions of the signal peak, and, due to discretization, the true signal peak probably lies between two discrete data points in the FFT spectrum. One way to improve the estimation accuracy of the signal peak is zeropadding of the sampled

signal, thereby increasing the resolution in the FFT response by linear interpolation. Details on the effects of zeropadding will be described in the following subsection.

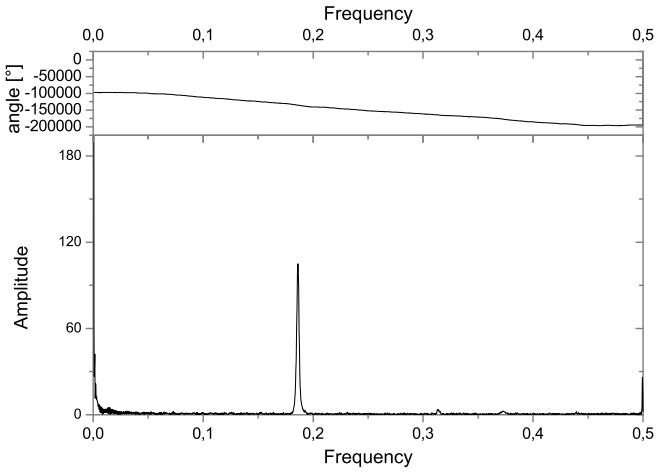


**Figure 4.25:** FFT Plot of the interferogram signal from Fig. 4.24.

After determination of the spatial frequency of the interferogram, the corresponding phase value is extracted from the FFT spectrum and passed to a routine to calculate $\Delta n_{eff}$. The phase values are obtained in phase fringes (phase modulo $2\pi$) and have to be unwrapped to get a continuous phase information, i.e. when a discontinuity is detected by the software routine, $2\pi$ are added or subtracted. Both phase values and $\Delta n_{eff}$ values are displayed on the user interface in real-time and stored in a datafile for post-processing, e.g. with Origin©. Note that in the following "phase"and "$\Delta n_{eff}$"are used interchangeably, since they are related through a simple scalar multiplication. A flowchart and a snapshot of the current user interface of the FFT software routine can be found in Appendix D.

### Signal processing - zeropadding

Recall from chapter 2.6 that for an effective application of an FFT the signal length has to be a power of two, which can be accomplished by extending the signal with trailing zeros. Extending the original signal with more trailing zeros than the next power of two leads to a linear interpolation of the discrete data points in the spectrum of the FFT and thus a more accurate determination of the signal peak corresponding to the spatial frequency.

The question is, if a more accurate determination of the spatial frequency results in a more accurate phase value and thus less phase noise. Fig. 4.26 illustrates this difference

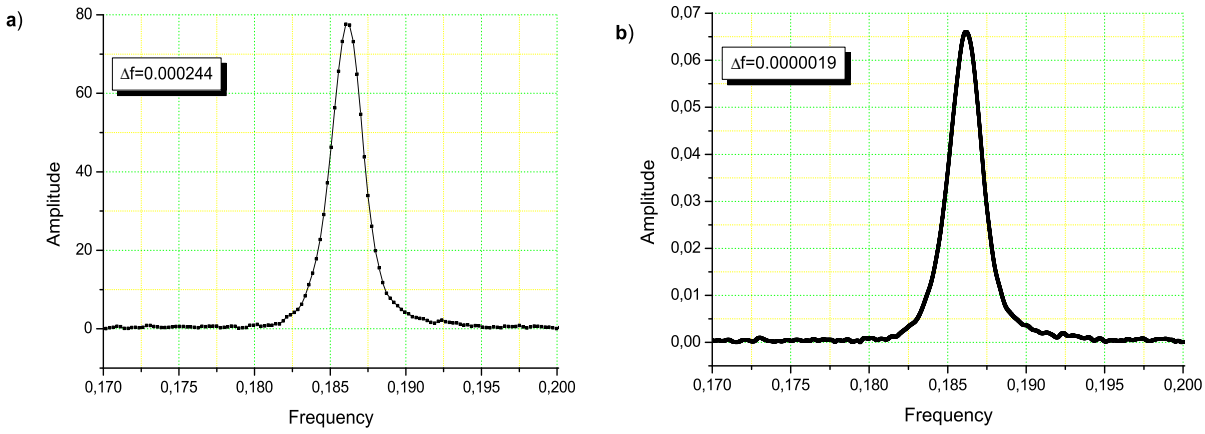


**Figure 4.26:** Influence of zeropadding on the FFT signal peak. The FFT was applied to the interferogram signal from Fig. 4.24 with an original signal length of 3200 pixels. **a)** Extension of the original signal to effectively 4096 pixels resulting in $\Delta$f=0.000244 with $f_{max} = 0.186035$. **b)** Extension of the original signal to effectively 524288 pixels resulting in $\Delta$f=0.0000019 with $f_{max} = 0.1861629$.

where the FFT has been applied to the interferogram signal from Fig. 4.24 with an original signal length of 3200 pixels (CCD readout). In the first case, the signal is extended to effectively 4096 pixels ($2^{12}$), in the second case to effectively 524288 pixels ($2^{19}$). Due to the linear interpolation, the signal peak can be determined more accurately in the second case. However, a better estimation of the true spatial frequency does not necessarily lead to an improvement in phase noise, as the next figure shows. The phase trends differ slightly in their absolute values, while the phase noise remains the same. In summary, the implementation zeropadding seems useful for an efficient FFT calculation and a more accurate estimation of the spatial frequency, whereas an improvement in phase noise cannot be observed.

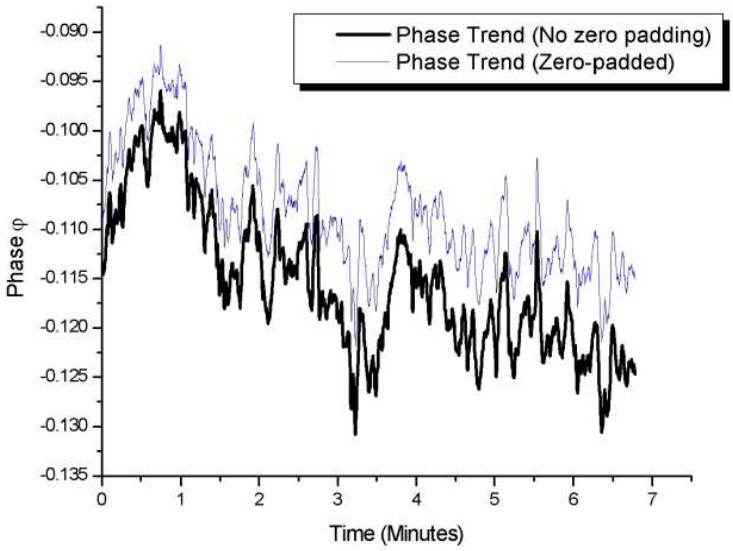


**Figure 4.27:** Influence of zeropadding on the phase trend. No improvement of phase noise due to a more accurate determination of the spatial frequency by zeropadding can be observed. Adapted from (*MacKenzie*, 2003).

### Signal processing - averaging

Recall from chapter 2.7.3 the two types of average filters implemented into the software algorithm - block average and moving average. Whereas the block average reduces the sampling rate by the averaging factor n, the recursive moving average filter maintains a constant buffer size without altering the sampling rate. Another effect of averaging is a reduction in signal noise according to:

$$\sigma \propto \frac{1}{\sqrt{n}} \tag{4.5}$$

where $\sigma$ denotes the phase noise.

Fig. 4.28 shows the results of a simulation of phase trends filtered by block or moving average or both.

The results show an equal reduction in phase noise for both filtering methods. However, when both filters are applied simultaneously, no further noise reduction can be observed. Thus both filtering methods can be recommended to accomplish phase noise reduction in the interferometer system. Yet a few things have to be considered before strongly averaging the signal: both filters do not only influence the phase trend by reducing the peak-to-peak noise, but also have long-term effects. Since the block average filter reduces

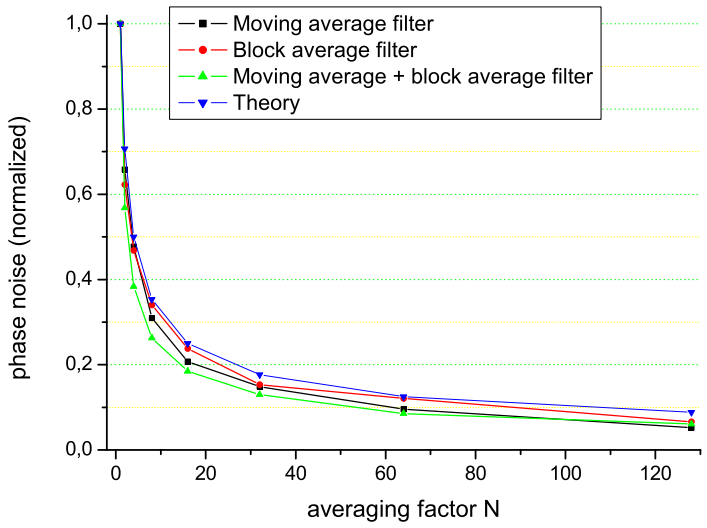


**Figure 4.28:** Simulation of phase noise reduction by averaging, normalized.

the sampling rate by the averaging factor n, the time resolution of the measurement is consequently reduced by the same factor. For example, given an exposure time of $\tau$=200 ms and a block averaging factor of n=5, the resulting sampling rate T is given by:

$$\mathrm{T} = \tau \cdot \mathrm{n} \tag{4.6}$$

i.e. reduced from 5 Hz to only 1 Hz. For most applications of the interferometric biosensor, it is recommended that the sampling rate does not fall below 1 Hz, corresponding to maximum averaging factors of n=16 or n=32, depending on the chosen exposure time.
The moving average filter also influences the long-term phase trend, but in a different way. Since here the oldest value in the buffer is constantly replaced by the newly measured one, each averaged phase value is influenced by all values in the buffer. This fact has to be considered especially for reaction kinetics measurements, where a short-term phase change determines kinetic rate constants and a large buffer size would lead to distorted phase values. Therefore the same recommendation applies for the moving average filter, that the averaging factor, i.e. buffer size, should not exceed 16-32 resulting in a sampling rate of ≈1 Hz.

### 4.2.5 Experimental characterization of the biosensor system

#### Refractive index measurements

Since the principle of evanescent field sensing can be used to detect changes in the bulk refractive index of a cover fluid, refractive index measurements were performed with glycerin dilutions in order to test and calibrate the system with respect to its physical characteristics, i.e. signal noise, signal drift and sensitivity constants. Glycerin has been the sample of choice due to its low cost, neutrality and easy handling. All measurements were prepared and performed as follows:

- A sufficient amount of $DI - H_2O$ ($\approx$150 ml) is degassed for at least 1 h. This reduces built-up of air bubbles in the fluidic system that could disturb the measurement
- Preparation of a stock solution of 10 % (w/v) glycerin in degassed $DI - H_2O$ (corresponds to 793 µl glycerin per 10ml $DI - H_2O$)
- Preparation of glycerin dilutions from the stock solution in the range of 0.5 % to 5 % (w/v) in separate reaction vessels
- The interferometer system is prepared by connecting inlet- and outlet tubing, inserting a clean waveguide chip, starting the peristaltic pump and monitoring a baseline with $DI - H_2O$ on both channels
- All system parameters like exposure time, SLD current and averaging should be reasonably set (typical values: t = 100-400 ms, I = 100-120 mA and averaging 2-10)

When a stable baseline with a drift of less than $1 \cdot 10^{-6}$ in $\Delta n_{eff}$ is reached, the measurement can be started by pausing the pump for placing the inlet tubing of the measurement channel into the reaction vessel containing the lowest glycerin concentration, resuming pumping, changing back to $H_2O$, and applying the same concentration at least three times to check on repeatability and stability of the signal change, and then move on to the next higher concentration. Typical time intervals for applying the samples are between two and four minutes, followed by running buffer (in this case $DI - H_2O$) for the same time interval, while the reference channel is continuously kept under running buffer.

Fig. 4.29 presents a measurement of glycerin solutions from 1 % to 5 % (w/v) based on this measurement procedure with the SLD in TE mode as light source.

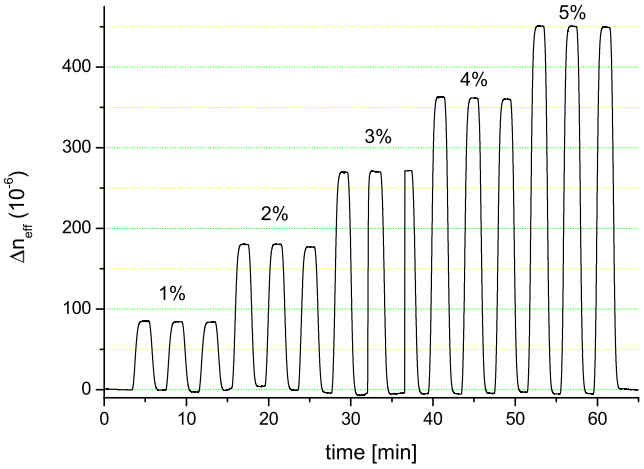


**Figure 4.29:** Refractive index measurement with glycerin solutions from 1 % to 5 % (w/v) as sample with the SLD in TE mode as light source. Measurement parameters: R=12.5 kΩ, I=120 mA, $\tau$=250 ms.

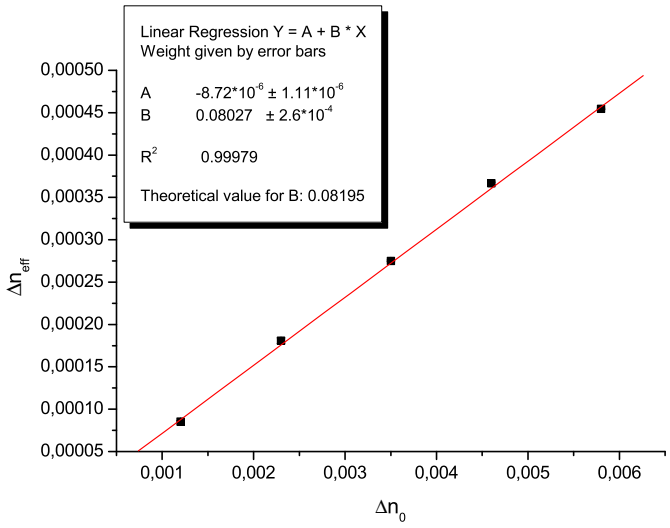


**Figure 4.30:** Calibration curve derived from glycerin concentration measurements for TE mode. The mean signal change in $\Delta n_{eff}$ for each concentration is plotted versus the refractive index n. From the slope of the linear fit the sensitivity constant can be determined to $\frac{\Delta n_{eff}}{\Delta n_0} = 0.08027$.

Fig. 4.30 shows the calibration curve corresponding to this measurement, where the mean signal change in $\Delta n_{eff}$ for each concentration is plotted versus the refractive index n obtained from literature (*Weast*, 1976). See also Appendix C for further details. The data were then fitted to a linear regression model to determine the sensitivity constant for the interferometric biosensor operating in TE mode and compared to the theoretical value derived from waveguide theory (ref. chapter 2.4.1). The same glycerin test measurement has been performed using the SLD in TM mode, while all other system components and the measurement procedure were kept identical. The same glycerin stock solution was used for the glycerin solutions again ranging from 1 % to 5 % (w/v). Fig. 4.31 shows the measurement curve. Clearly visible is the higher response in $\Delta n_{eff}$ for each glycerin concentration, while the noise in $\Delta n_{eff}$ remains the same. This results in a higher signal-to-noise ratio (factor ≈2.7) and therefore in a higher sensitivity constant for the system, as illustrated in Fig. 4.32. Based on these findings the preferred mode for the interferometric biosensor is TM.

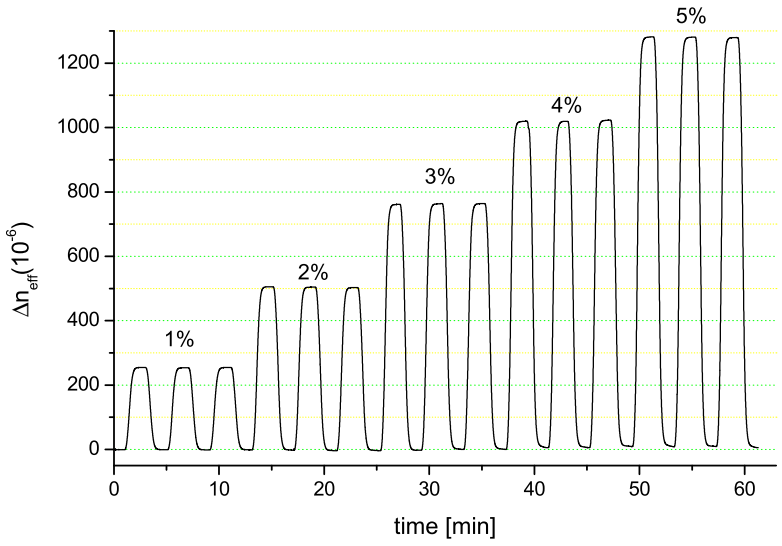


**Figure 4.31:** Refractive index measurement with glycerin solutions from 1 % to 5 % (w/v) as sample with the SLD in TM mode as light source. Measurement parameters: R=12.5 kΩ, I=120 mA, $\tau$=250 ms.

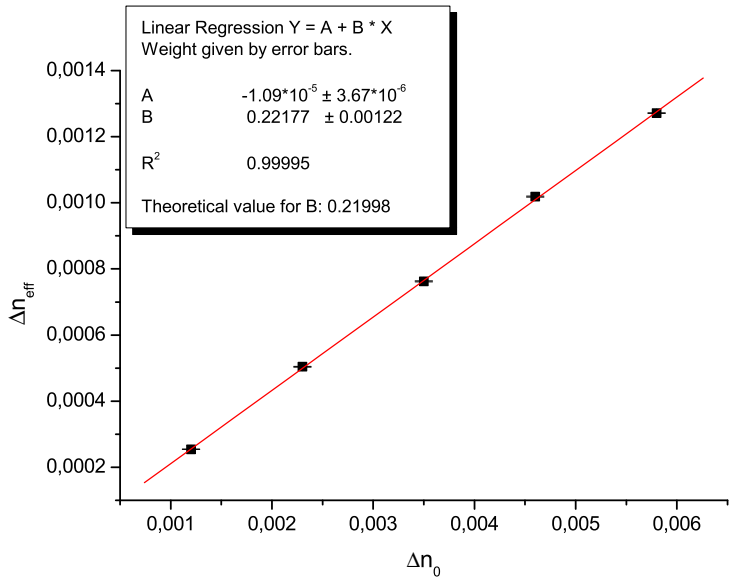


**Figure 4.32:** Calibration curve derived from glycerin concentration measurements for TM mode. The mean signal change in $\Delta n_{eff}$ for each concentration is plotted versus the refractive index n. From the slope of the linear fit the sensitivity constant can be determined to $\frac{\Delta n_{eff}}{\Delta n_0} = 0.22177$.

### Characterization of signal noise

In chapter 2.7.2 several noise sources were introduced and described in detail. From the refractometric test measurements presented in the last section, not only the sensitivity constants can be derived, but also a detailed noise analysis is possible. At first, a section from the baseline in Fig. 4.31 was investigated concerning the properties of the overall noise. One method of checking a noisy signal for randomness is the autocorrelation of the signal as illustrated in Fig. 4.33. A large central peak indicates the statistical structure, i.e. randomness, of the signal. From the same baseline the noise in $\Delta n_{eff}$ has been determined to $2 \cdot 10^{-8}$ (standard deviation), leading to a resolution of $3 \cdot \sigma = 6 \cdot 10^{-8}$. This resolution, achieved with the Sony ILX526 CCD line sensor, could be reduced by implementing the binned Hamamatsu S9840 CCD sensor. Fig. 4.34 illustrates the baselines recorded with both sensors at a sampling rate of 1 Hz. At identical measurement parameters, the Hamamatsu sensor showed a ≈3 x higher SNR than the Sony sensor, resulting in an achievable resolution of $9 \cdot 10^{-9}$ in $\Delta n_{eff}$.

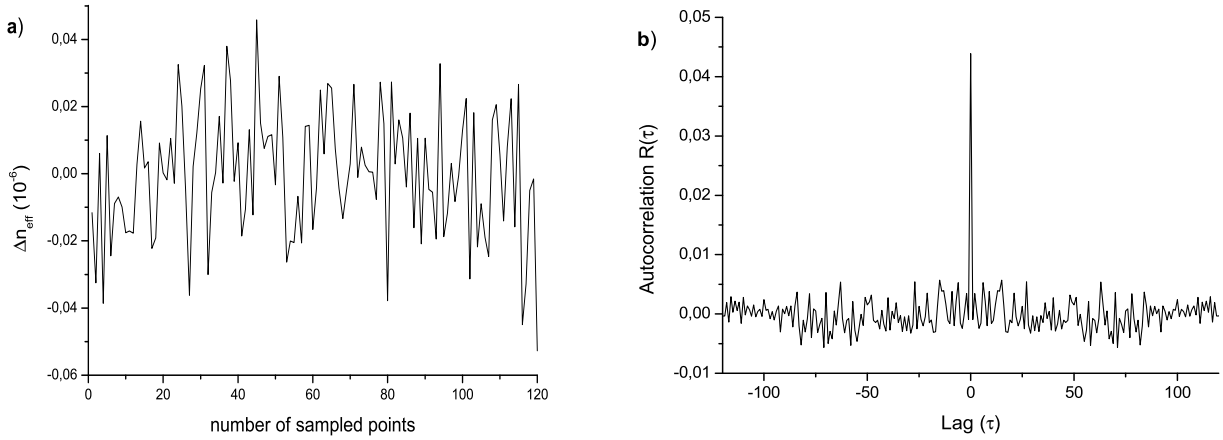


**Figure 4.33:** Autocorrelation of a measurement baseline. **a)** Sample signal: randomly chosen section of the baseline from the measurement illustrated in Fig. 4.31. **b)** Autocorrelation of the measurement signal. A large central peak indicates a random signal noise.

With this result, we further expected that the phase noise can be significantly reduced by statistical methods such as signal averaging. This was tested in a measurement series where the same signal (interferogram) has been filtered either by a moving average filter or a block average filter to suppress phase noise. The results in Fig. 4.35 show that the phase noise can indeed be reduced up to a certain level, when the phase noise increases again despite a higher averaging factor and therefore deviates from the theoretical model. This might be due to a drift in the signal, since for a higher averaging factor the measurement

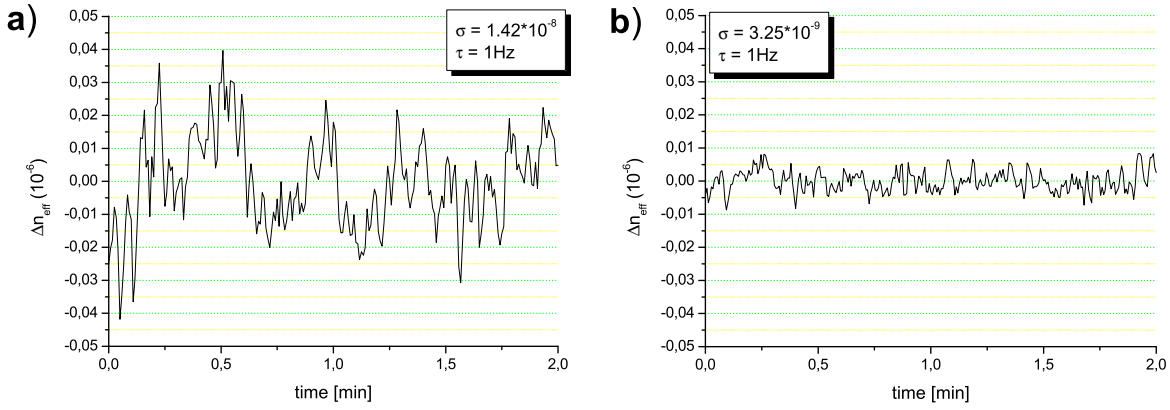


**Figure 4.34:** Comparison of CCD sensors concerning phase noise. **a)** Sony ILX525, 12bit **b)** Hamamatsu S9840, 16bit. Baselines recorded at 1 Hz. The Hamamatsu sensor shows a ≈3 x higher SNR than the Sony sensor.

time has to be increased to reach a statistically significant amount of sampled values, i.e. in this case long-term effects in the signal show up. Yet the good agreement with the

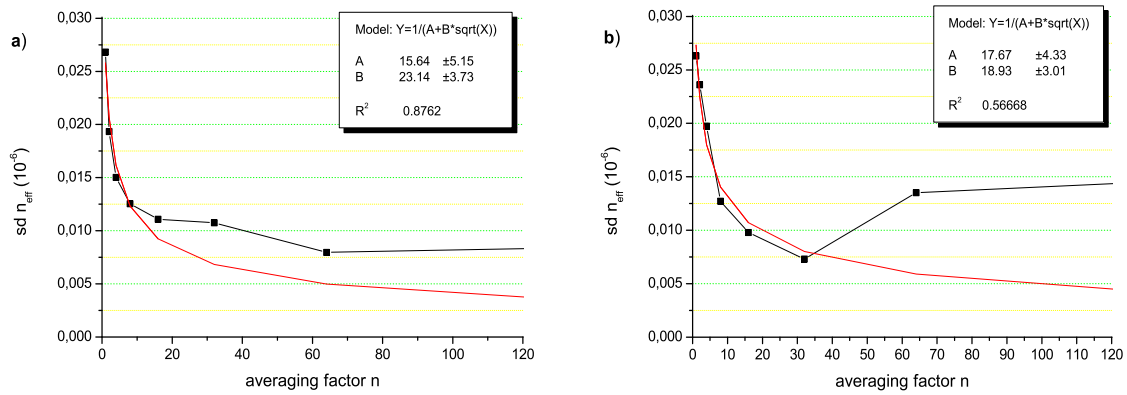


**Figure 4.35:** Phase noise reduction by signal averaging. **a)** Application of a moving average filter **b)** Application of a block average filter. Measurement parameters: R=12.5 kΩ, I=115 mA, $\tau$=400 ms.

fit model for averaging factors up to 16-32 support the theoretical correlation between phase noise reduction and averaging factor described in the previous section. Apart from the statistical structure of the baseline noise non-random effects can occur: an example of a signal distortion arising due to program conflicts with the Windows operating system is shown in Fig. 4.36.

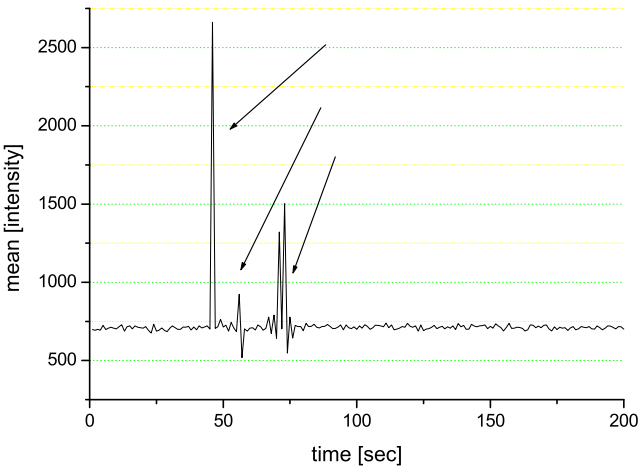


**Figure 4.36:** Non-random signal distortion in the CCD readout due to a program conflict with the Windows operating system.

These distortions occur mainly at short exposure times below 50 ms and are characterized by an over-saturation of the CCD pixels caused by a delayed readout of the CCD camera. To avoid these distortions during a running experiment, it is recommended to only run the interferometer software and work at exposure times above 50 ms. Furthermore phase fluctuations due to light source instability combined with path length differences in the setup can severely distort the signal as illustrated in Fig. 4.37. *Fox et al.* (1999) estimated an uncertainty in wavelength of a Helium-Neon laser to $\frac{\Delta\lambda_{\mathrm{Doppler}}}{\lambda} = 3.2 \cdot 10^{-6}$ caused by the Doppler width of the Ne emission line. Assuming a misalignment of the two beam paths of only 200 µm, this results in a fluctuation on the order of $1 \cdot 10^{-7}$, representing a major disturbance in the signal. Yet the short-term noise in $\Delta n_{\mathrm{eff}}$ remains on the order of $3 \cdot 10^{-8}$, the same value as it has been found with the SLD as light source. Based on these findings the SLD was chosen as main light source due to its better wavelength stability.

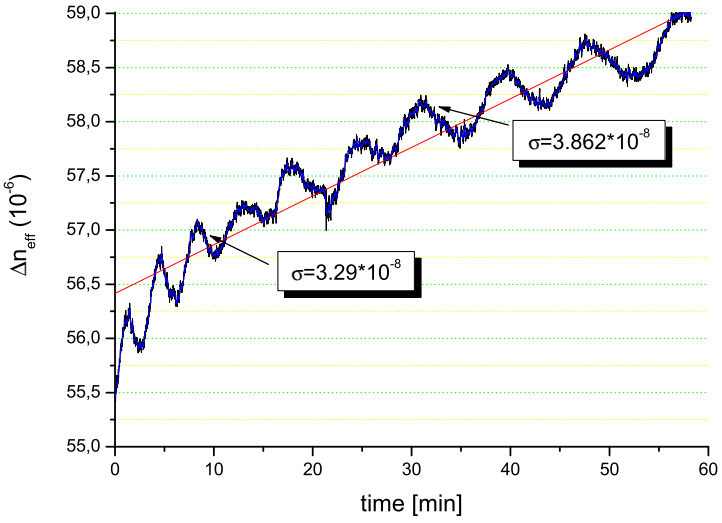


**Figure 4.37:** Influence of light source instability on signal noise. Measurement recorded with a Helium-Neon laser at $\lambda = 632.8$nm. Severe fluctuations in the signal can be observed, which are mainly due to wavelength fluctuations from the laser combined with path length differences in the optical setup.

### 4.2.6 Conclusion

This chapter describes the realized setup of the interferometric biosensor with a flow cell as fluidic element, discussing all system components and their characterization in detail. From the analysis of system components a number of conclusions can be made, such as the choice of materials for the waveguide chips, the light source and the CCD detector. The characteristics of the chosen components influence the final design and setup, leading to an optimal set of parameters for the interferometric biosensor. Further a detailed system characterization by refractometric test measurements is provided including an evaluation of the experimental results compared to theoretical calculations and simulations.

Initial refractometric test measurements with glycerin have shown an effective refractive index resolution of $\Delta n_{eff} \approx 6.0 \cdot 10^{-8}$, corresponding to a refractive index resolution of $\Delta n \approx 7.5 \cdot 10^{-7}$ for TE mode and $\Delta n \approx 2.7 \cdot 10^{-7}$ for TM mode, respectively, at a sampling rate of 1 Hz. This resolution has been improved by a factor of 3 by implementing a new CCD sensor with full-line binning on the CCD chip. It was also found that the CCD sensor is the limiting system component concerning noise, whereas the phase noise is approximately equal for all three light sources tested and therefore the light source can be excluded as limiting factor. Signal filtering methods such as averaging have been implemented and analyzed concerning their suitability for phase noise reduction.

The experimentally derived sensitivity constants of the interferometer system are in very good accordance with the theoretical values derived from waveguide theory. The system shows a good long-term stability with a typical drift of $< 1 \cdot 10^{-6}$/h in $\Delta n_{eff}$.

## 4.3 Interferometric biosensor: microplate system

### 4.3.1 Introduction

The use of microtiterplates (MTP) has become a standard for laboratory routine screening tests (e.g. enzyme-linked immunosorbent assays (ELISA)), where a high sample throughput is required (*Blake*, 2001). MTP's are commonly configured as 96-, 384- or 1536-well plates in a standard format of 127.8 mm x 85.6 mm, compatible with the majority of commercially available readout systems. In general, the assay of interest is performed before inserting the MTP into the readout system. Yet a direct monitoring of the assay performance including intermediate steps could be of great advantage. This section describes the development of the interferometric biosensor implementing an MTP-formatted frame (IBS 801). This combination of a standard MTP format with label-free detection allows the direct readout of assay results.

A main part of the work has been devoted to the development of a prototype setup with an 8-well microplate (see Fig. 4.38). The microplate is formatted as a section of a 96-well MTP. First refractometric test measurements and a biological test measurement will be presented in chapter 5. The system design allows an extension to read plates in the commonly known 96- or 384 well MTP formats.

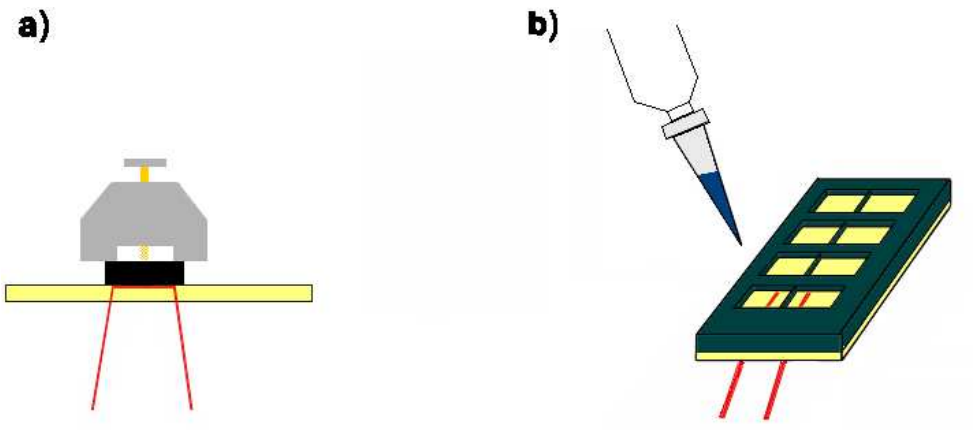


**Figure 4.38:** Reader options. **a)** Flow cell system, 2 channel **b)** Microplate system, 8-well configuration

Basically, the interferometer system implementing an MTP readout underlies the same detection principle as the flow cell system described in the last section and follows the same schematic design as in Fig. 4.1. The difference in both systems is the fluidic element. While the flow cell system runs on two channels, allowing the detection only of a single analyte at a time, the MTP system implementing a 96 well plate can read up to 96 samples within one measurement, allowing the system to be used for screening applications where a high throughput is needed. The differential detection principle of the interferometric biosensor supports two different types of wellplate layout, as shown in Fig. 4.39:

- Two adjacent wells are used as signal and reference well
- The use of a single well with partial surface modification (e.g. immobilized specific antibody). This could be realized by a small barrier subdividing each well into a 4.5 x 9 mm sensing area and 4.5 x 9 mm reference area


**Figure 4.39:** Microplate options. **a)** Two adjacent wells as signal and reference well **b)** Single well with partial surface modification (e.g. immobilized specific antibody)

The configuration of two adjacent wells where all well pairs are scanned successively for readout has been chosen for the prototype setup described in this section.

### 4.3.2 Biosensor setup - components

#### Light source

For the development of the IBS 801 the SLD also used for the IBS 201 served as light source, mainly due to its semicoherence needed for the end-point evaluation software. For this reason the optical elements in the beampath have to be adapted to couple all

spectral contributions into the waveguide chip and focus them onto the CCD camera to achieve a narrow interference area. The laser diode described in chapter 4.2.1 also emits semicoherent light below threshold, yet the available power is too low to operate the system in TM mode.

### Optical elements and double slit

The optical elements that have been integrated into the system are similar to the ones used for the flow cell system (see also Fig. 4.42). The divergent beam emitted by the SLD is collimated by an apherical lens with a focal length of $f_1 = 8$ mm and focused as a line onto the chip grating by a cylindrical lens with $f_2 = 100$ mm. Focusing on the grating ensures in this case the coupling of all spectral contributions into the waveguide and further to couple a high light intensity. In contrast to the setup of the flow cell system, yet another cylindrical lens is needed in the beampath between the double slits and the CCD detector to focus again all spectral contributions. As illustrated in Fig. 4.42, each wavelength is coupled out at a different angle, and the cylindrical lens focuses the divergent beam onto the CCD camera so that the complete spectrum is detected. Again all lenses were ordered from Thorlabs, USA and are made of BK7 glass with a refractive index of 1.52, carrying an antireflection coating.
The double slit plate used has the same design and dimensions as described in chapter 4.2.1, except that the slit distance has been changed to 2 mm to adapt the distance of the two beams to the dimensions of the microplate frame.

### Optics mount

The optics mount for the IBS 801 is a special design and fabricated at the IPM. It essentially comprises two adjustable mirrors (≈3 mm x 7 mm) that redirect the beam almost orthogonally, as illustrated in Fig. 4.40. By two screws placed in front the mirrors can be adjusted for incoupling, or directing the outcoupled beam centrically through the cylindrical lens onto the CCD camera. The optics mount provides a small cutout on top for the double slit plate.

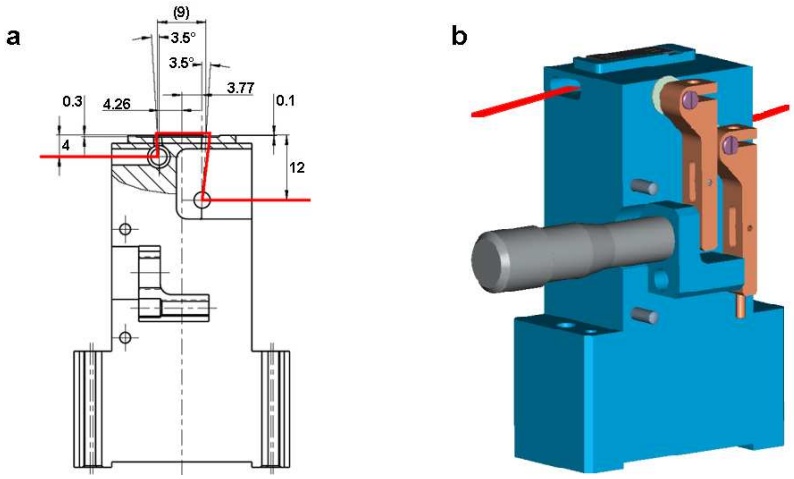


**Figure 4.40:** Design of the IBS 801 optics mount (CAD drawing). Two mirrors for in- and outcoupling can be adjusted by screws. The double slit plate is placed on top.

### Waveguide chips and CCD camera

The same waveguide chips as for the IBS 201 supplied by Unaxis Optics have been used for the IBS 801 prototype setup. For a 96-well MTP a complete wafer of accordant size would be implemented.

The CCD device mainly used during the system development is the CCD1000 described in chapter 4.2.1 with the ILX 526A line sensor.

### Microplate frames

An MTP-formatted 8-well frame represents the fluidic element of the IBS 801. It is made of the chemically inert thermoplastic PEEK™ and has been specially designed at the IPM for use with the available waveguide chip format provided by Unaxis. Basically it can be classified as section of a bottomless 96-well MTP as commercially available. A schematic drawing of the 8-well frame attached to a waveguide chip is shown in Fig. 4.41. The four gratings lie directly below the bars of the MTP frame, and each pair of adjacent wells serves as measurement and reference well. A step motor moves the MTP frame successively to the next well pair; hence four parallel measurements can be performed by scanning the plate. A specially designed frame holder mounted on the step motor keeps the waveguide chip including the MTP frame ≈1 mm above the optics mount and the

double slit plate. A second frame holder suited for a 96-well MTP has also been designed and fabricated at the IPM.

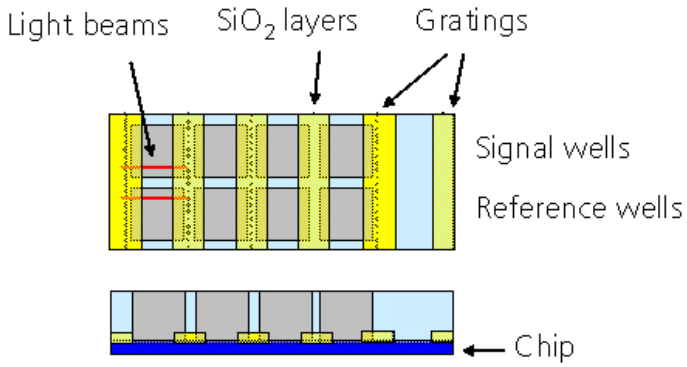


**Figure 4.41:** Layout of the 8-well MTP frame for the IBS 801 prototype setup. The chip gratings are located directly below the bars of the MTP frame. Two adjacent wells are used as measurement and reference well.

#### Step motors

Two identical linear stage step motors (PLS-85, Micos, Germany) were implemented into the system for moving the MTP frame holder in two perpendicular directions. The motors have a travel range of 102 mm with a bi-directional repeatability of $\pm 0.2$ µm. A LabView™ user interface has been realized for simple motor positioning tasks including a scanning routine. A screenshot of the user interface can be found in Appendix D.

### 4.3.3 Biosensor setup - realization

This section describes the setup of the interferometric biosensor implementing an 8-well MTP configuration and the components introduced above. Fig. 4.42 illustrates schematically the setup from side view. Light from the SLD is collimated by an aspherical lens with a focal length of $f_1 = 8$ mm and focused on the chip gratings by a cylindrical lens with a focal length of $f_2 = 100$ mm. A small mirror in the optics mount redirects the beam almost orthogonally onto the first grating for incoupling. Before a double slit with a slit width of 100 µm and a distance of 2 mm cuts out two beams which separately travel along the waveguide in two adjacent wells of the MTP. After outcoupling by the second grating

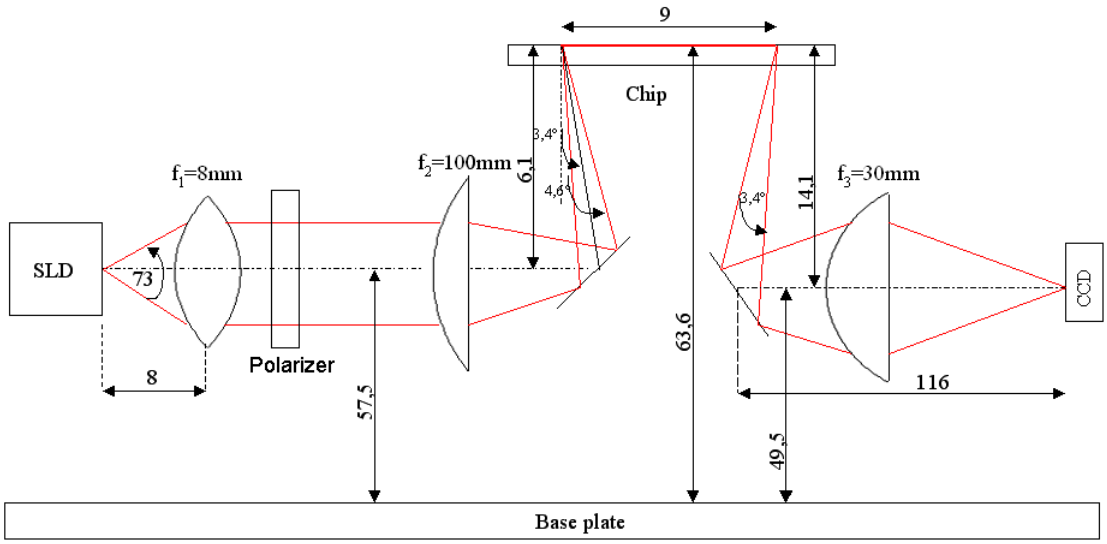


**Figure 4.42:** Schematic drawing of the IBS 801 setup - side view. An aspheric lens collimates the divergent beam emitted by the SLD, followed by a cylindrical lens to focus a line on the grating. After passing the waveguide chip in two separate beams, the outcoupled, divergent beam is refocused on the CCD camera to ensure all spectral contributions are maintained in the interferogram.

the beams pass again a double slit with a slit width of 3 µm or 5 µm and the resulting interferogram is finally, refocused by a second cylindrical lens, recorded by the CCD camera. Fig. 4.43 displays a schematic drawing of the setup in top view. Special attention

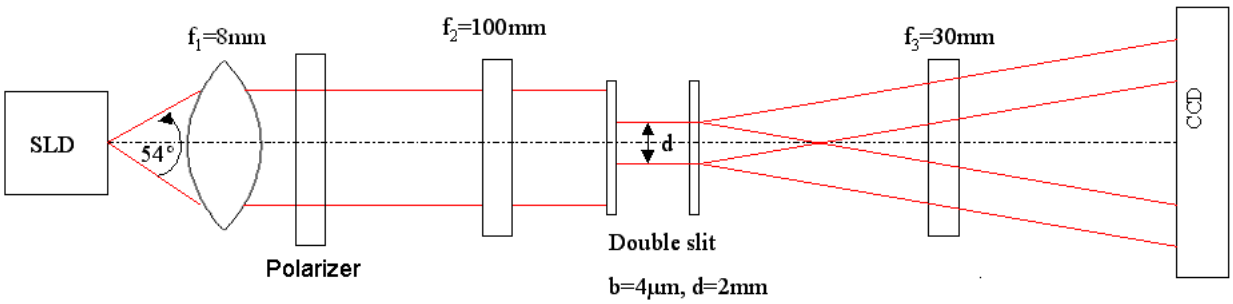


**Figure 4.43:** Schematic drawing of the IBS 801 setup - top view.

has been paid to choose the suitable focal lengths of the cylindrical lenses, since they represent the crucial elements for coupling the complete spectral bandwidth of the SLD. A focal length of 100 mm to focus on the incoupling grating seemed appropriate to couple the total spectral bandwidth of the SLD, as calculated and discussed in chapter 4.2.3.

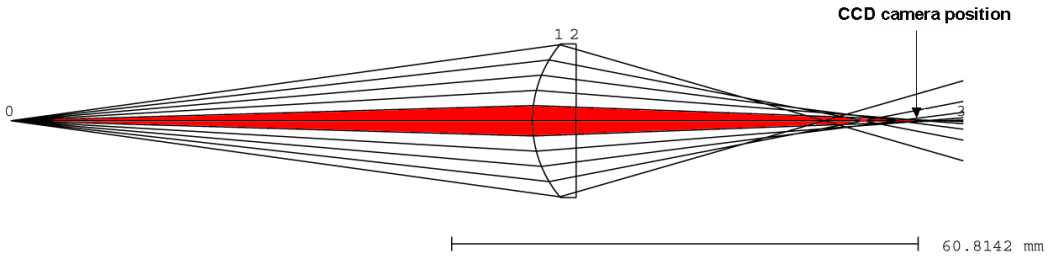


**Figure 4.44:** Simulation of the beampath from the outcoupling grating (left) to the CCD sensor (right) with Optalix™. The optimal position for the cylindrical lens has been determined to 43 mm from the CCD sensor.

A simulation program for calculating optical lenses and their foci (Optalix™) has been used to model the beampath extending from the outcoupling grating to the CCD sensor. Resulting from this simulation the optimal position for the CCD sensor is at a distance of 120 mm from the outcoupling grating, with the rear surface of the cylindrical lens located at a distance of 43 mm from the CCD sensor. Fig. 4.44 illustrates the beampath starting at the outcoupling grating (left) to the CCD sensor (right). Fig. 4.45 presents the current prototype setup of the IBS 801 used for the measurements described in the next section and in chapter 5.

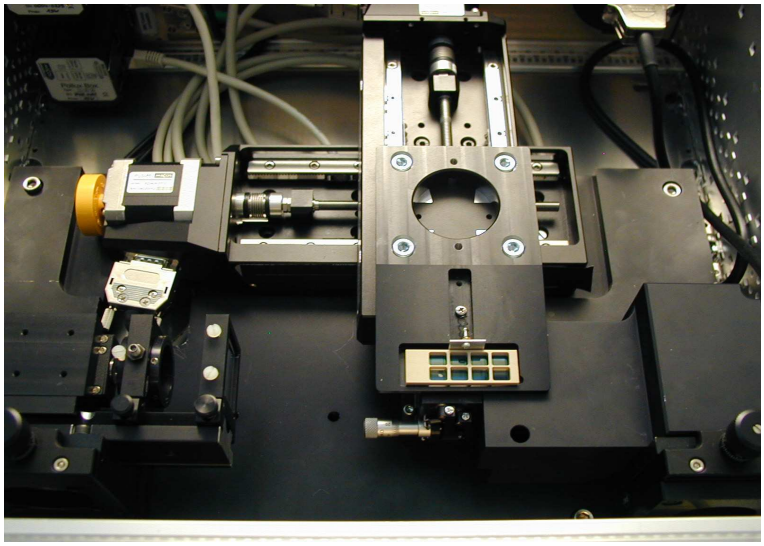

**Figure 4.45:** Top view photograph of the interferometric biosensor IBS 801. Refer to Fig. 4.42 for details on the optical components.

### 4.3.4 Signal analysis and processing

In this section the signal analysis implemented for the interferometric biosensor IBS 801 shall be presented, since it differs from the FFT algorithm in various points. The decisive difference between the two kinds of biosensors described in this thesis is the readout format: while with the flow cell system only one pair of gratings is used for the measurement at a time and thus the same interferogram signal is evaluated with respect to phase changes over time, the readout of the MTP system relies on successive scanning of different pairs of gratings. In other words, would the FFT algorithm described in chapter 4.2.4 be used for the MTP system and a phase change of more than $2\pi$ occured at a given detection spot, this phase change would be missed during scanning due to the ambiguity of the interferogram and therefore not monitored. The FFT algorithm implemented in the flow cell system overcomes this ambiguity by phase unwrapping, which is feasible in this case since the same interferogram is constantly monitored over time.

Recall the importance of a semi-coherent light source for the MTP system: the interferogram signature is characterized by a decreasing amplitude of the cosine function with an increasing phase difference of the interfering beams (ref. chapter 2.5.3 and especially Fig. 2.16). The cosine function itself would be unambiguously evaluable over a range of only $2\pi$. However, since the region of interference is sufficiently narrow, this problem is overcome by analyzing the lateral shift of the interferogram on its envelope function, as illustrated in Fig. 4.46.

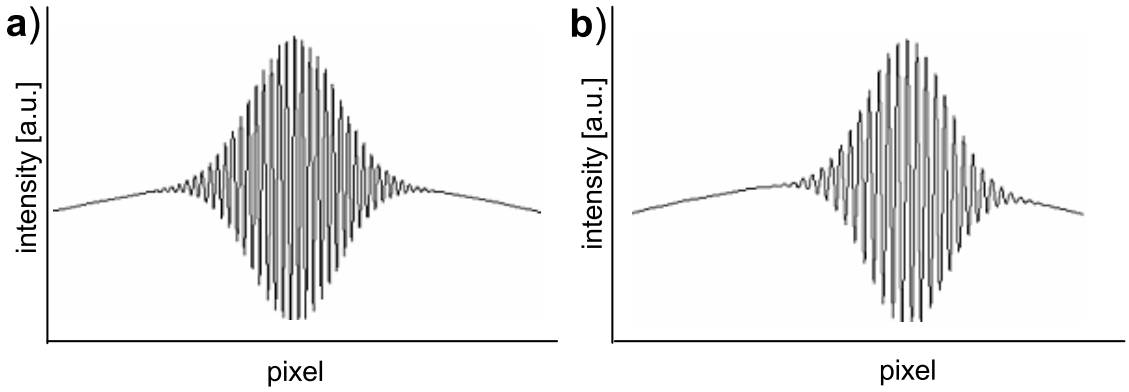


**Figure 4.46:** Simulation of an intensity distribution as generated by semi-coherent light. **a)** phase difference $\delta$=0 **b)** phase difference $\delta$=15$\pi$.

The maximum of the envelope function determines the interference order so that an unambiguous evaluation, i.e. a so-called end-point evaluation, of the interferogram signal is achieved (*Brandenburg*, 1997). The implemented algorithm basically consists of two steps: first, the maximum of the envelope function is determined by evaluating the cross-correlation of a reference distribution with the sampled interferogram signal. In a second step the phase of the respective interference order is calculated. Once the spatial period of the interferogram has been determined by an FFT, two reference distributions $s_i$ and $c_i$ with the same spatial resolution are calculated by the algorithm according to:

$$s_i = \begin{cases} \sin(\frac{2\pi i}{p})[1+\cos(\frac{2\pi i}{b})] & \text{for } -\frac{b}{2} \le i \le \frac{b}{2} \\ 0 & \text{for } i > \frac{b}{2} \text{ and } i < -\frac{b}{2} \end{cases} \tag{4.7}$$

and

$$c_i = \begin{cases} \cos(\frac{2\pi i}{p})[1+\cos(\frac{2\pi i}{b})] & \text{for } -\frac{b}{2} \le i \le \frac{b}{2} \\ 0 & \text{for } i > \frac{b}{2} \text{ and } i < -\frac{b}{2} \end{cases} \tag{4.8}$$

with b being the width of the envelope function and p the period; i denotes an integer number corresponding to the pixels of the CCD camera. Fig. 4.47 shows examples of such reference distributions with b=50 and p=5.8.

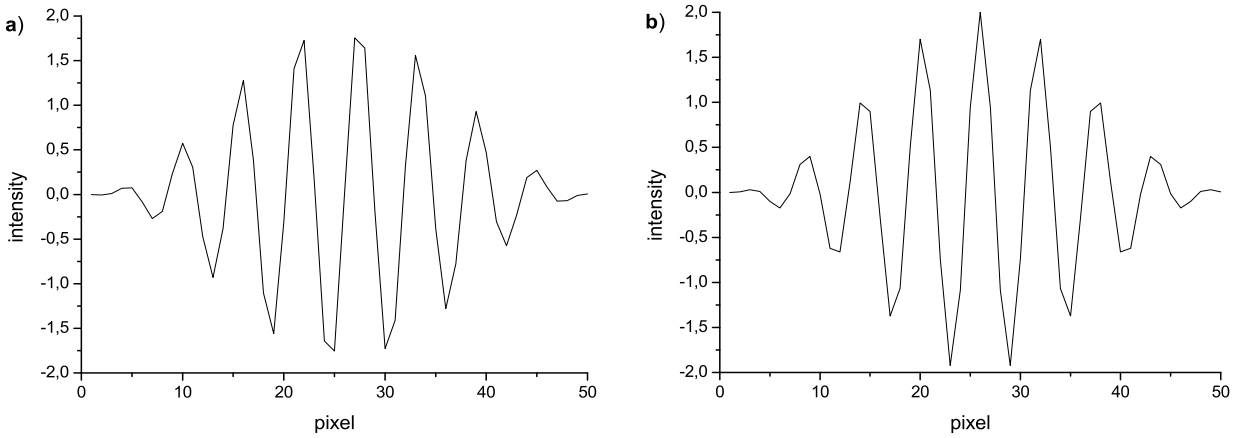


**Figure 4.47:** Calculated sine and cosine reference distributions for cross-correlation with the interferogram signal **a)** Sine function **b)** Cosine function

Once the reference distributions are determined, the interferogram signal is cross-correlated with the reference distributions according to:

$$S_k = \sum x_i s_{i-k} \tag{4.9}$$

$$C_k = \sum x_i c_{i-k} \tag{4.10}$$

where k denotes the pixel number for all pixel values from 0 to 2048 (or 3000). Fig. 4.48 displays this cross-correlation graphically. The maximum of the cross-correlation function, indicating the interference order, is given by:

$$T = S_k^2 + C_k^2 \tag{4.11}$$

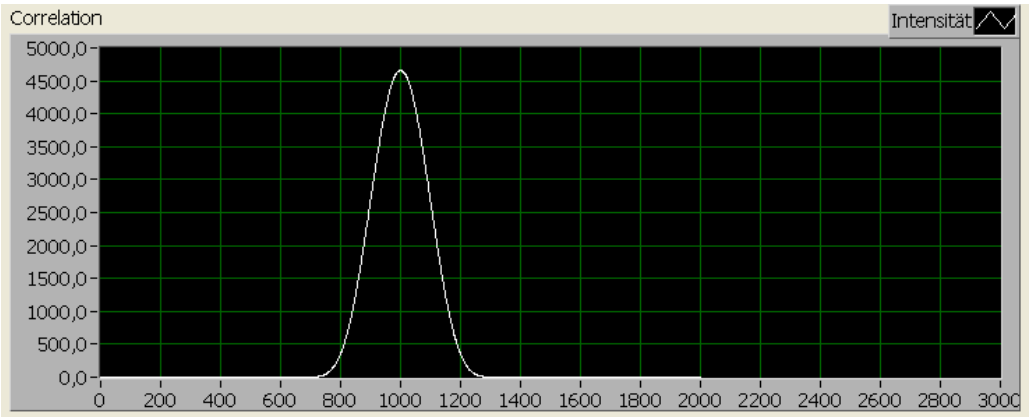


**Figure 4.48:** Intensity distribution resulting from the cross-correlation of an interferogram signal with its respective reference distributions. The maximum of this distribution determines the maximum of the interferogram's envelope function and thus the interference order.

After the interference order has been found, the phase of the interferogram can be calculated by using the similar reference distributions, but with envelope widths b corresponding approximately to the envelope width of the original signal and taking the coefficients:

$$S_0 = \sum x_i s_i \tag{4.12}$$

$$C_0 = \sum x_i c_i \tag{4.13}$$

The corresponding phase is given by:

$$\phi = -\arctan\frac{\mathrm{S_0}}{\mathrm{C_0}} \tag{4.14}$$

For the calculation of the effective refractive index and the refractive index the same formula apply as for the FFT algorithm. A flowchart of the complete cross-correlation algorithm can be found in Appendix D.
The same signal filtering methods (zeropadding, average filters) have been added to the algorithm for signal refining and noise reduction. The effects of these filters within the cross-correlation algorithm correspond to the results shown with the FFT algorithm and will therefore not be discussed further in this section.

### 4.3.5 Simulation algorithm for signal analysis

Based on the two signal evaluation algorithms described before, a separate routine for interferogram simulation has been developed in order to test newly implemented routines. Interferogram parameters characterizing the envelope function and the coherence function can be chosen, as well as the addition of random pixel noise to the signal. This test function has been implemented into the Labview™ interface instead of the CCD readout routine and undergoes the same FFT and cross-correlation, or filtering routines, as an original signal. A snapshot of the user interface can be found in Appendix D along with the DLL routine of the test function.

### 4.3.6 Experimental characterization of the biosensor system

The experimental characterization of the relevant system components has already been described in section 4.2.3. Here only a characterization of the biosensor system implementing these components shall be given and compared to the results obtained with the flow cell system.

#### Refractive index measurement

A refractometric test measurement has been performed as a preliminary test of the system and for calibration. Here ethanol has been chosen as sample to prepare solutions of different refractive indices due to its neutrality and fast dissolving in $H_2O$. All measurements were performed as follows:

- Preparation of a stock solution of 1% (v/v) ethanol in DI – $H_2O$
- Preparation of dilutions from the stock solution in the range of 0.2% to 1% in a total volume of 100 µl in separate reaction vessels; the concentrations need to be twice as high as the desired concentration for measurement
- The interferometer system is prepared by inserting the MTP-chip, checking for incoupling (i.e. interferogram) at each well pair and filling all 8 wells with 100 µl DI – $H_2O$
- All system parameters like exposure time, SLD current and averaging factors should be reasonably set and adjusted. Ideally the intensity of the detected interferogram signal is similar for all well pairs

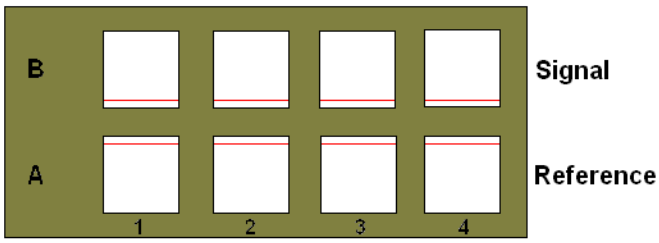


**Figure 4.49:** Layout of the 8-well MTP chip

Before the measurement is started, all four well pairs need to be scanned and the signal drift observed ($H_2O$-baseline). Once the drift falls below $5 \cdot 10^{-6}$ in $\Delta n_{eff}$, the measurement can be started by pipetting 100 µl of each ethanol solution in well B1-B4, keeping A1-A4 as reference (see Fig. 4.49). Since ethanol dissolves very quickly in $H_2O$, scanning of the well pairs can be resumed and the respective values for $\Delta n_{eff}$ determined. Typically each well pair is scanned for a time interval of 10 sec in 8-10 repetitive measurements. Fig. 4.50 presents the results of a test measurement with ethanol concentrations ranging from 0.1% to 0.5% (v/v).

Fig. 4.51 shows the calibration curve corresponding to this measurement, where the mean signal change in $\Delta n_{eff}$ for each concentration is plotted versus the refractive index obtained from literature (*Weast*, 1976). Values below 0.5% are estimated by a polynomial

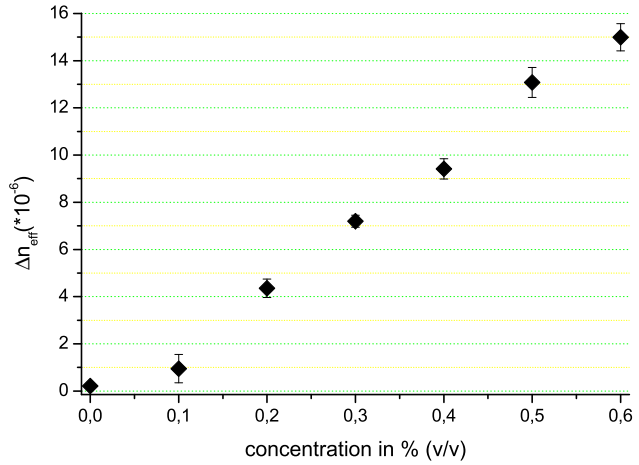


**Figure 4.50:** Refractive index measurement with ethanol solutions from 0.1% to 0.5% (v/v) as sample. Measurement parameters: SLD TE, R=12.5 kΩ, I=55 mA, $\tau$=200 ms. Error bars denote the standard deviation from the mean of eight repeated measurements.

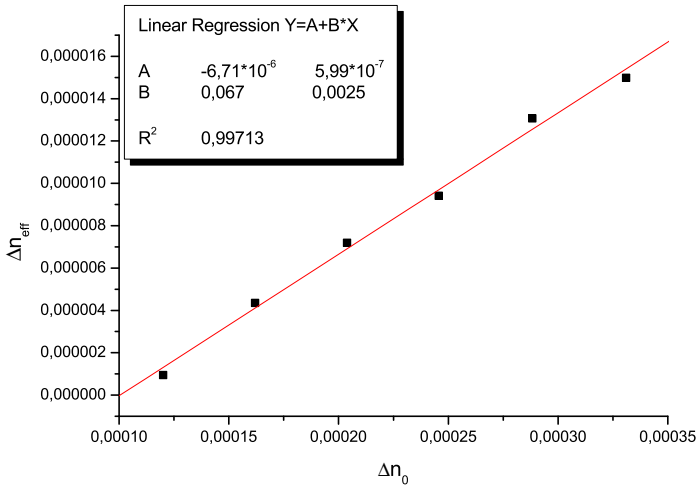


**Figure 4.51:** Calibration curve derived from ethanol concentration measurements for TE mode. The mean signal change in $\Delta n_{eff}$ for each concentration is plotted versus the refractive index n. From the slope of the linear fit the sensitivity constant can be determined to $\frac{\Delta n_{eff}}{\Delta n_0} = 0.067$.

fit (cf App. C). The data were then fitted to a linear regression model to determine the sensitivity constant. Yielding an experimental value of $\frac{\Delta n_{eff}}{\Delta n_0} = 0.067$ compared to the theoretical value of $\frac{\Delta n_{eff}}{\Delta n_0} = 0.082$, it can be seen that the measurement is diffusion limited.

### Comparison with flow cell system

In order to compare the characteristics of the microplate system with the flow cell system, the same test measurement with ethanol concentrations has also been performed with the flow cell system. All preparations were in accordance with the description given in chapter 4.2.5. Fig. 4.52 illustrates the results obtained from both systems.

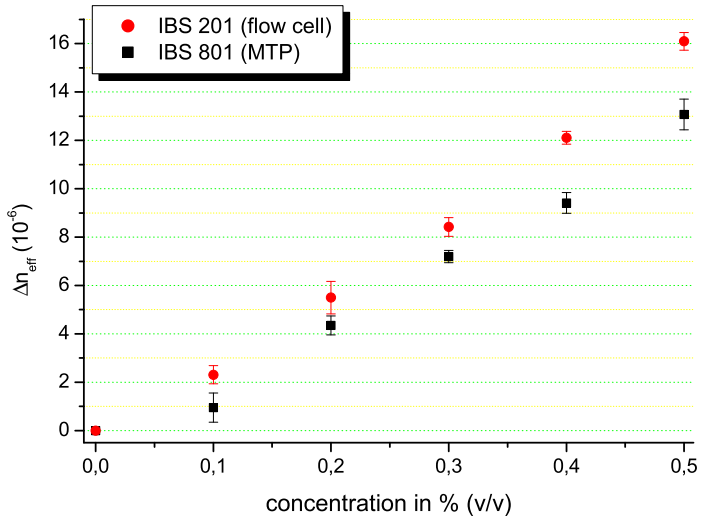


**Figure 4.52:** Comparison of refractive index measurements with ethanol concentrations ranging from 0.1% to 0.5% (v/v), performed on both bionsensor systems. The signal values in $\Delta n_{eff}$ are systematically lower in the microplate system.

It can be observed that the $\Delta n_{eff}$ values obtained with the microplate system are systematically lower than the values obtained with the flow cell system, as already seen in Fig. 4.50. This might be due to a limited diffusion in the MTP wells, whereas the sample solution is brought directly in contact with the waveguide surface in the flow cell.

### Characterization of signal noise and repeatability

Equivalent to the flow cell system, the characterization of the MTP system included the determination of signal drift and noise. Additionally, the repeatability, i.e. the variation of measurement values influenced by scanning, has to be considered. The repeatability mainly depends on the bi-directional repeatability of the step motors, and possible mis-

alignments of the optical components including the waveguide chip. As a first test, a waveguide chip without liquid samples has been scanned for 8 data values as illustrated in Fig. 4.53. The standard deviation of the mean yields the information about the repeatability, which was found to be on the order of $1 \cdot 10^{-7}$ in $\Delta n_{eff}$ for all well pairs.

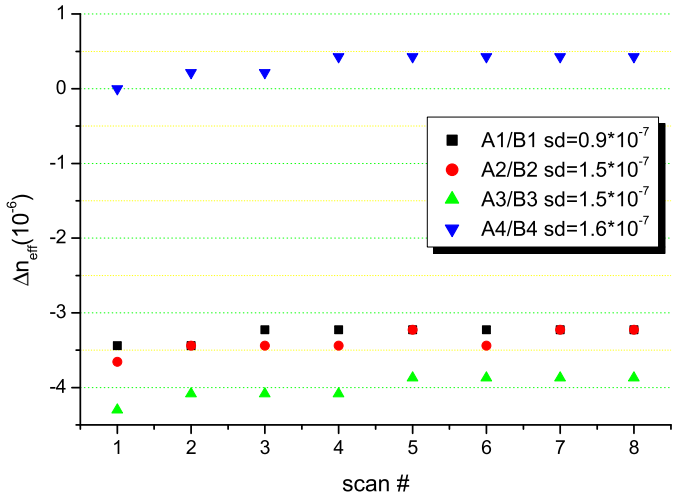


**Figure 4.53:** Repeatability characteristics of the microplate system. The standard deviation of the mean of eight recorded $\Delta n_{eff}$ values determines the repeatability of the measurement data.

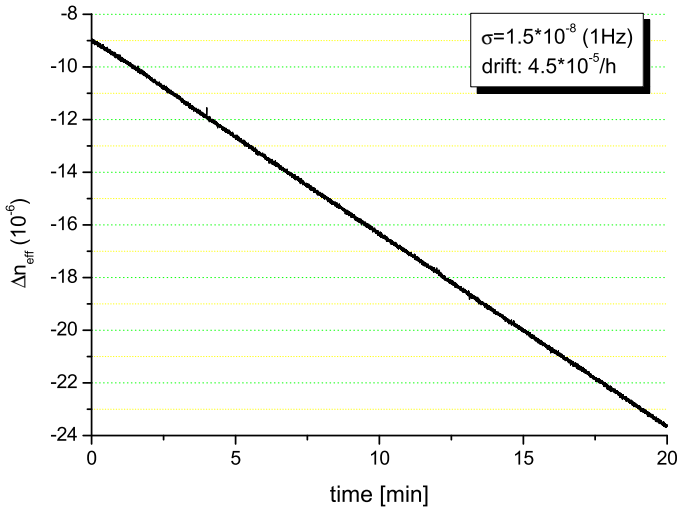


**Figure 4.54:** Baseline recorded with the microplate system showing a drift of $4.5 \cdot 10^{-5}$/h in $\Delta n_{eff}$. Parameters: R=12.5 kΩ, I=120 mA, $\tau$=1000 ms

To characterize the signal noise and drift over time, a simple baseline measurement was performed and is presented in Fig. 4.54. While the signal noise is equal to the signal noise of the flow cell system, a larger signal drift can be observed, being typically around $5 \cdot 10^{-5}$/h in $\Delta n_{eff}$. This estimation is however only valid provided that the MTP chip has been inserted into the system about half an hour before the measurement. With newly inserted chips, the system shows an increased drift. To avoid disturbances of the measurement data due to a large drift, the chip should be inserted and not moved again about half an hour previous to measurements. To compensate the influence of signal drifts in application measurements, one well pair (typically A1/B1) should always be kept under buffer conditions and the drift thereof determined. This allows a baseline correction and thus drift compensation for the other measurement data.

### 4.3.7 Conclusion

This chapter describes the realized setup of the interferometric biosensor with an MTP-formatted 8-well frame as fluidic element and discussing newly introduced system components that are different from the flow cell system. Again, the choice of suitable system components influences the design and setup of the interferometer system with an optimal set of parameters. Further a detailed system characterization by refractometric test measurements is provided including an evaluation of the experimental results compared to theory and the results obtained with the flow cell system.

Initial refractometric test measurements with ethanol have shown an effective refractive index resolution of $\approx 1.0 \cdot 10^{-7}$, corresponding to a refractive index resolution of $\approx 1.2 \cdot 10^{-6}$ for TE mode and $\approx 4.5 \cdot 10^{-7}$ for TM mode, respectively, at a sampling rate of 1 Hz. It was also found that, apart from the CCD sensor being the limiting system component concerning noise, the resolution of the system is finally limited by the repeatability of the recorded data values. The experimentally derived sensitivity constants of the microplate interferometer system are also in good accordance with the theoretical values derived from waveguide theory (82%). The system shows a long-term stability with a typical drift of $< 5 \cdot 10^{-5}$/h in $\Delta n_{eff}$ and a repeatability of $< 2 \cdot 10^{-7}$ in $\Delta n_{eff}$.

# Chapter 5

# Application measurements

## 5.1 Introduction

This chapter presents the materials and methods used for the application measurements as well as a detailed description and characterization of the surface chemistry for the functionalization of the waveguide sensor chips. The interferometric biosensor is used to monitor different immunoreactions and their binding kinetics are evaluated and discussed. A streptavidin-functionalized surface is compared with fluorescent detection to characterize the surface chemistry.

## 5.2 Materials and methods

### 5.2.1 Materials

#### Chemicals and biochemicals

A complete list of all chemicals and their vendors can be found in Appendix A.
The following buffers and regeneration solutions were used for the experiments:

- PBS: Phosphate buffered saline; running buffer prepared from PBS concentrate 1 : 10 diluted with $DI - H_2O$. Isoosmotic buffered saline to provide a stable environment for biological substances with a pH of ≈7.4 at a temperature of 25 ° C.

To prevent analyte molcules from attaching to vial or tubing walls or denaturing in pure PBS, BSA in concentrations from 0.1% to 1% (w/v) can be added

- NaOH, 50-100 mM: alkaline regeneration solution
- HCl, 50-100 mM: acidic regeneration solution
- $H_3PO_4$, 10-100 mM: acidic regeneration buffer, adjusted to pH=2 with NaOH
- Analyte buffer: Cleaned cell lysate from *Escherichia coli*
- Washing buffer: Mix 100 ml SSC (20x concentrate) with 10 ml SDS and 0.5 ml Tween 20 and fill with $DI - H_2O$ to a total volume of 1000 ml

**Devices and transducers**

Apart from the IBS 201 and IBS 801 setup and their components described in chapter 4, following devices have been used for the experiments:

- SPR devices: BIACORE 1000 Upgrade and BIACORE 2000, BIACORE AB, Uppsala, Sweden
- Sensorchip for BIACORE: Sensor Chip SA (Streptavidin-coated dextran matrix)
- Fluorescence reader: BCR 101 laser reader, Fraunhofer IPM Freiburg
- pH-meter: MP 225, Mettler Toledo, Giessen, Germany
- Powermeter: Newport Model 1830C, detector 818-IR
- Optical spectrum analyzer: Ando, AQ 6315A-B
- Microarray printer: Genetix $QArray_{mini}$
- Micro balance: Sartorius CP225D

All data are evaluated and represented with Microcal Origin© (versions 5.0 and 6.1).

**SPR devices: BIACORE 1000 Upgrade and BIACORE 2000**

For the cytochrome *c* test measurement described in 5.6, the BIACORE 1000 Upgrade was chosen as sensor system. Another comparative test measurement series at the Novartis Research Facility in Basel has been performed on the BIACORE 2000 system. Essentially both systems are quite similar concerning device characteristics like setup, components, or sensitivity. One difference makes the better automatization and fluid handling on the BIACORE 2000. Table 5.1 lists a summary of technical data on the BIACORE 1000 Upgrade compared to the BIACORE 2000. Both systems contain an SPR optical detection unit first described by Kretschmann and Raether (*Kretschmann and Raether*, 1968), which is illustrated in Fig. 5.1. An integrated microfluidic cartridge (IFC) allows to pass the analyte solutions continuously and pulse-free over the sensor chip. Up to four channels in serial mode are addressed simultaneously, giving the possibility for three references. The systems are further temperature controlled to maintain a stable baseline signal.

| Specification | BIACORE 1000U | BIACORE 2000 |
|---|---|---|
| Refractive index range | $1.33 - 1.36$ | $1.33 - 1.36$ |
| Baseline drift | $< \pm 0.3$RU/min | $< \pm 0.3$RU/min |
| Noise | $< 2.0$ RU rms (10Hz) | $< 0.3$ RU rms (10Hz) |
| | $< 0.6$ RU rms (1Hz) | $< 0.3$ RU rms (1Hz) |
| Flow cell volume | 60 nl | 60 nl |
| Number of flow cells | 4 | 4 |

**Table 5.1:** Technical data of BIACORE instruments 1000 Upgrade and 2000

The microfluidic system works with two highly precise syringe pumps allowing flow rates between 1-100 µl/min. One fluidic loop handles the running buffer, in the second loop analyte solutions are taken out of the respective vials on the vial rack and injected into the flow system directly before the IFC, so that diffusion processes in the fluidic system and dead volumes are kept at a minimum. With special routines it is even possible to recover small sample volumes for reuse. The autosampling unit has a capacity of two microtiterplates for a maximum of 192 samples.

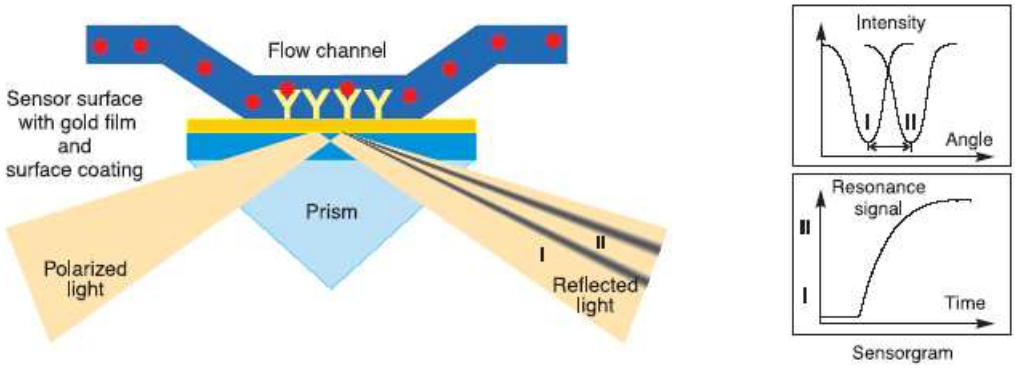


**Figure 5.1:** SPR setup based on Kretschmann and Raether. Depending on the refractive index in the evanescent field above the gold layer, the angle of the reflected light changes. This variation is seen as a dip in the intensity distribution and can be very sensitively monitored as resonance signal. The signal intensity is given in resonance units (R.U.). One resonance unit corresponds to a surface coverage of $1\mathrm{pg/mm^2}$. Adapted from *www.biacore.com* (2003).

A customized software controls all steps of the measurement routine and performs the evaluation of the binding curves for obtaining binding constants and surface coverages. In-line referencing is done by subtracting the binding curves from different flow cell channels. Furthermore, readily immobilized chips with a variety of surface chemistries for different assay applications are available (*van der Merwe*, 2005).

### Biochip Reader BCR 101

For all experiments with labeled molecules the biochip reader BCR 101 was used for fluorescence imaging. The system comprises a Helium-Neon laser (633 nm) for the excitation of the fluorescent dyes and allows wavelength-selective imaging at (680±15)nm. The images are recorded by a cooled CCD camera (Apogee, USA) with an array of 765 x 512 pixels. The 16 bit information (intensity) can be illustrated in false color. A customized software controls the exposure time and the CCD parameters. Optional routines include dark current correction and illumination correction of the recorded image. All images in experiments described below are dark current corrected.

### 5.2.2 Methods

#### Cleaning of waveguide chips

The waveguide chips have to be cleaned thoroughly before silanization or measurements according to the degree of possible previous contamination and usage. Generally, using a new chip for each measurement is advisable, but not necessary since they can be regenerated to an acceptable level after silanization and reused. Table 5.2 gives an overview of cleaning procedures that have proven to be suitable and do not cause any damage to the waveguide and protective layers (see also 5.2.1).

| Degree of contamination/usage | Cleaning procedure |
|---|---|
| new<br>for refractometric test measurement | 10 min in isopropanol in ultrasonic bath,<br>rinsing with DI – $H_2O$, drying<br>or: 30 min in 0.5 % (v/v) Hellmanex solution<br>(using more than 0.5 % causes the $SiO_2$<br>protective layers to come off) |
| new, for silanization | 30min at 75 °C in 3:1 25% $NH_3$ : 30% $H_2O_2$,<br>rinsing with DI – $H_2O$, drying |
| used, not silanized | 15sec in 10M NaOH, rinsing with DI – $H_2O$,<br>10 min in isopropanol in ultrasonic bath,<br>rinsing with DI – $H_2O$, drying |
| used, silanized<br>(complete regeneration) | up to 40sec in 10M NaOH, rinsing with DI – $H_2O$,<br>30 min at 75 °C in 3:1 25% $NH_3$ : 30% $H_2O_2$,<br>rinsing with DI – $H_2O$, drying |

**Table 5.2:** Cleaning procedures for waveguide chips

#### Silanization

The treatment with 3:1 25% $NH_3$ : 30% $H_2O_2$ previous to silanization turns the chip surface highly hydrophilic (caused by $OH^-$-groups). Each hydroxyl group should ideally capture one silane molecule, resulting in a silane monolayer, and the amount of silane

molecules on the surface increases with the degree of hydroxyl groups (*Le Grange and Markham*, 1993). A high density of silanes on the surface ensures a stable and reproducible surface modification and reduces unspecific binding to a minimum. The silanization for all experiments described has been done at the IPM in a special silanization device for working under an argon atmosphere. Argon acts in this case as cover gas to prevent the reagents from coming into contact with humidity. Even a very small water content in the silane solvents would cause the silane molecules to polymerize, resulting in an unordered, multi-layered silane surface not suitable for reproducible measurements. A schematic drawing of the silanization device is shown in Fig 5.2.

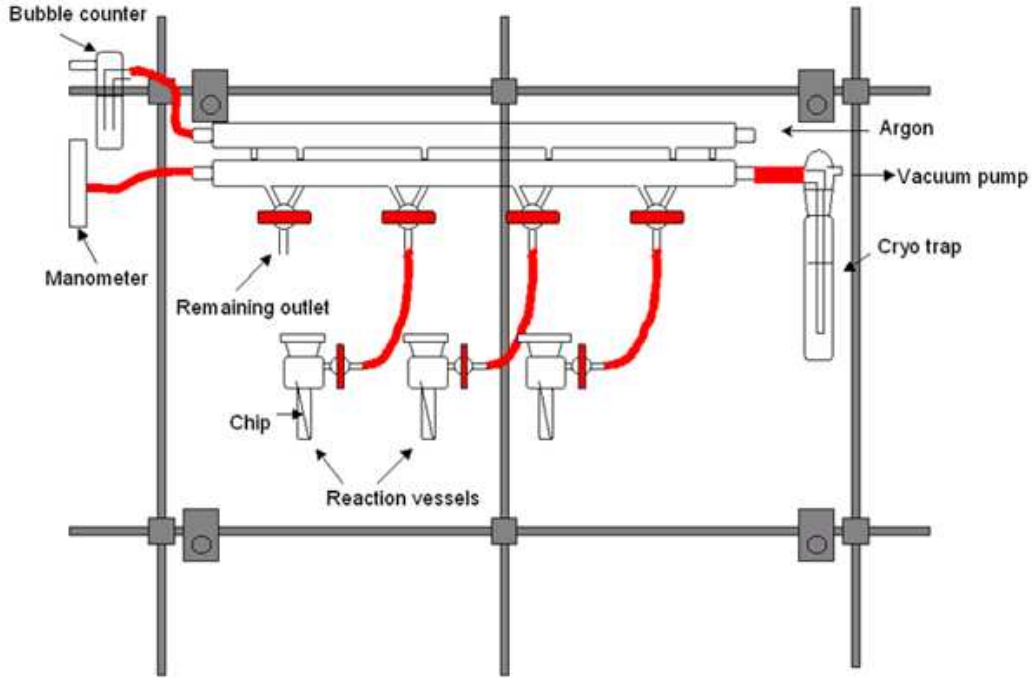


**Figure 5.2:** Silanization device. Chips and silanization reagents are handled in glass reaction vessels. After vacuuming, the whole device is flooded with argon cover gas to protect the silane from humidity.

The complete protocol for silanization can be found in Appendix B. After cleaning the chips are placed in the reaction vessels. The whole device is evacuated to a pressure below 1 mbar (manometer for control) and subsequently flooded with argon. The remaining outlet can be used to keep the reagents under argon during handling. Under argon flow 10 ml toluene, 28.8 µl triethylamine and 28.8 µl (epoxy-) silane are filled into each reaction

vessel. After a reaction time of at least 16 hours the chips are placed in a glass petri dish and cured in an oven at 120 °C for 4 hours, rinsed with DI − $H_2O$ and dried under nitrogen. These epoxy- (or amino-) functionalized chips can now be further modified according to the application and assay.

### Surface modification

Reaction with a spacer molecule for functionalization with amino-groups
Newly epoxy-silanized transducers are placed into pure ethylene diamine for at least 12 hours, rinsed with methanol and DI − $H_2O$ and dried. Ethylene diamine is a small spacer molecule with a short two-carbon length that does not cause any steric problems. The amino terminals can now be used to couple for example NHS-LC-biotin and further preparation of a streptavidin (SAv) surface. For this, a solution containing at least 1 mg/ml NHS-LC-biotin (M = 556Da) in PBS is pipetted onto the transducer chip placed in a humid glass chamber and incubated for at least 2 hours. After incubation the chip is washed for 5 min in a washing buffer, rinsed with DI − $H_2O$ and dried. For subsequent streptavidin incubation the same is done with a solution of at least 100 µg/ml SAv in PBS. SAv-functionalized chips should be stored at 4 °C until usage.

### Surface characterization: contact angle measurements

One way to characterize surface properties is the measurement of a contact angle that acts as an indicator for hydrophobicity or hydrophilicity of a (usually solid) surface. A water drop on a solid surface represents a so-called *three-phase system* (*Adam et al.*, 1995) as shown in Fig. 5.3 with surface energies between a solid and a liquid phase ($\gamma_{SL}$), solid and gaseous ($\gamma_{SV}$) and liquid and gaseous ($\gamma_{LV}$). The tangent to the drop boundary with the solid surface gives the contact angle at equilibrium of the interfacial energies according to *Young's equation*:

$$\gamma_{SV} - \gamma_{SL} = \gamma_{LV} * cos\theta \tag{5.1}$$

Contact angle values range from 0° on extremely hydrophilic surfaces (spreading of liquid) up to 180° for extremely hydrophobic surfaces. Usually clean oxidic surfaces tend to be

more hydrophilic, whereas on silanized surfaces, which are more hydrophobic, contact angles around 60° can be measured (*Elender et al.*, 1996; *Tsukruk et al.*, 1999).

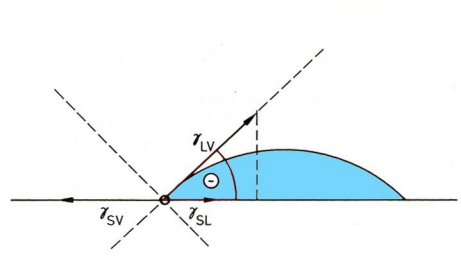


**Figure 5.3:** Contact angle $\theta$ of a liquid (water) drop on a plain solid surface. $\gamma_{SL}, \gamma_{SV}$ and $\gamma_{LV}$ denote the surface energies between the three phases. From (*Adam et al.*, 1995).

The contact angle can be quite easily experimentally determined. A small drop of liquid (1 µl) on the surface of interest is imaged through a monocular telescope and monitored by a digital camera. From the image the contact angles are quantified with the help of an image processing software.

Fig. 5.4 shows a schematic of the setup used for our experiments. In all experiments a total volume of 1 µl of $DI - H_2O$ was applied to the chip surface at several different positions by a microliter syringe with a minimal dispensable volume of 0.1 µl. The water drop was

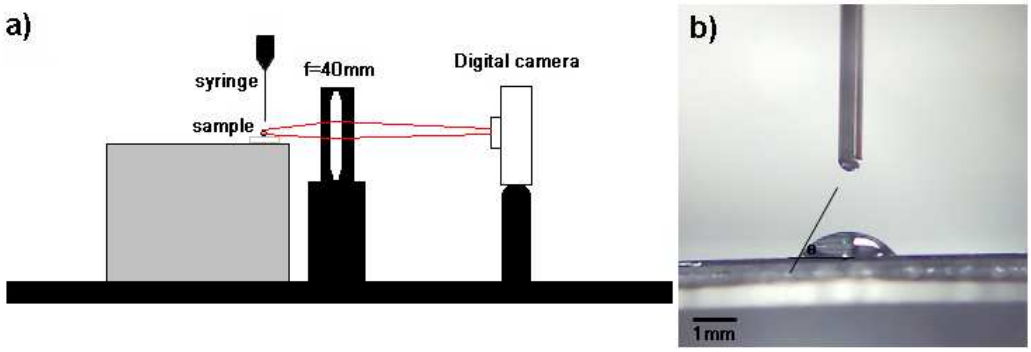


**Figure 5.4: a)**: Setup for contact angle experiments. A water drop is placed on the surface by a microliter syringe and monitored by a digital camera. A biconvex lens (f=40 mm) is used for magnification. Drawing not to scale. **b)**: typical image taken by the digital camera for contact angle determination.

subsequently imaged through a magnifying lens by a digital camera (Aiptek MegaCam, USA) and the contact angle on both the left and the right boundary determined by the image processing software ImageJ© (version 1.34, open source software).

Sometimes it is distinguished between an advancing contact angle which is determined while the liquid drop is applied to the surface, and a receeding contact angle while the liquid is taken away. Here only the equilibrium contact angle was determined.

**Surface characterization: binding of fluorescently labeled streptavidin**

Another issue that has to be taken into account for successful immobilization on silanized surfaces is the total concentration of molecules that can be homogeneously bound to the silane. Since immobilization of biotinylated reagents is a wide-spread tool for immunoassays, we have worked on a procedure of streptavidin coupling to the waveguide chip so that this preparation can be used as basis for biochemical assays. In order to probe different techniques of streptavidin immobilization and obtain information about the homogeneity and reproducibility of the functionalized surface, the binding of fluorescently labeled streptavidin has been studied concerning these characteristics.

## 5.3 Characterization of the surface chemistry

### 5.3.1 Contact angle measurements

The contact angle measurements provide a basis for both controlling different cleaning and regeneration methods for silanized transducers, and for characterizing the quality and reproducibility of the silanization process. Therefore measurements were done once directly after chip cleaning, and once after silanization with epoxysilane and modification with ethylene diamine. Five waveguide chips with different pretreatment and history were chosen and cleaned according to different cleaning protocols (see 5.1.2) and afterwards placed on the setup for measuring contact angles. Since on each chip four measurement positions on $Ta_2O_5$ are available and three subsequent pictures were taken after deposition of the water drop, a total of 12 images giving two contact angles were evaluable. The same applies to the $SiO_2$-layers. The results are shown in Fig. 5.5. Fig. 5.5a depicts the contact angles on $Ta_2O_5$ , Fig. 5.5b on the $SiO_2$-layers. Since chip no. II was completely new before cleaning, it served as reference for the effectiveness of the cleaning procedure.

| Chip number | Pretreatment/history | Cleaning procedure |
|---|---|---|
| I | silanized, used | NaOH, 25% $NH_3$ : 30% $H_2O_2$ |
| II | new | 25% $NH_3$ : 30% $H_2O_2$ |
| III | silanized, used | 25% $NH_3$ : 30% $H_2O_2$ |
| IV | silanized, used | 25% $NH_3$ : 30% $H_2O_2$ |
| V | used for glycerol measurement | 25% $NH_3$ : 30% $H_2O_2$ |

**Table 5.3:** Pretreatment and history of waveguide chips chosen for contact angle measurements and their cleaning procedures.

Chip no. I and V showed about the same contact angle on $Ta_2O_5$ as chip no. II ($(55\pm3)^\circ$). In comparison chip no. III and IV showed a higher contact angle on $Ta_2O_5$. On $SiO_2$, the

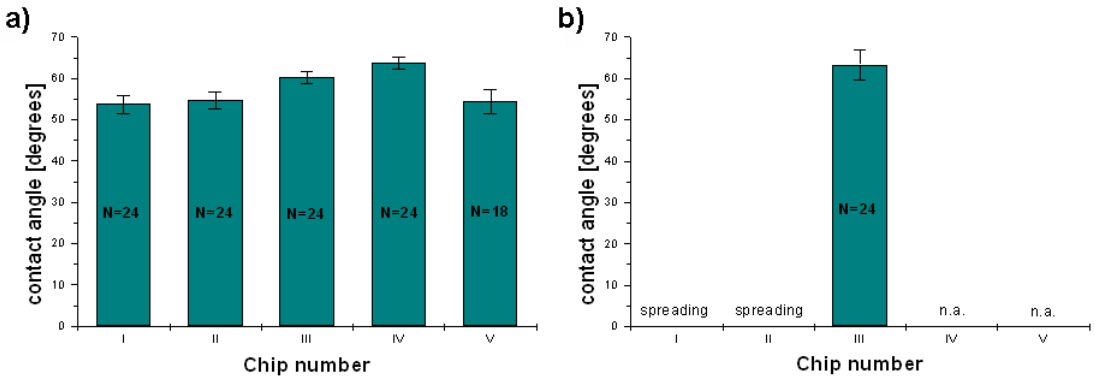


**Figure 5.5:** Contact angles on cleaned waveguide chips no. I-V as indicated in Table 5.3. **a)** Contact angles on the $Ta_2O_5$ surface (mean and standard deviation, N = number of measurements). Chip no. I, II and V show lower contact angles than no. III and IV. **b)** Contact angles on the protective layers ($SiO_2$). On chip no. I and II the water drop was spreading completely on the surface, chip no. III still showed a significant contact angle; for chips IV and V the values are not applicable due to $SiO_2$-layer degradation.

liquid drop spreaded on chips no. I and II, while chip no. III still showed a significant contact angle. Due to degradation of the $SiO_2$-layers on chips no. IV and V (might be due to long-term storage (>1 yr) at the time of the measurement), here no values are applicable.

The same measurements were also performed on the same chips after silanization with GOPS, and directly after conversion of the epoxy-groups to amino terminals with ethylene

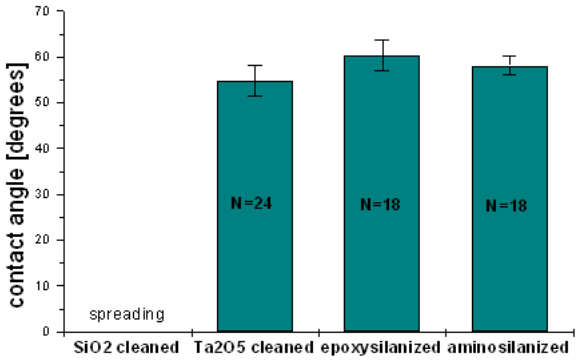


**Figure 5.6:** Contact angles on cleaned compared to silanized waveguide chips (mean and standard deviation, N = number of measurements).

diamine. Fig. 5.6 compares the results to the contact angles determined for cleaned surfaces. Contact angles on epoxysilane were found to be $(60 \pm 3)°$, on the amino-modified surface $(58 \pm 2)°$, which compares well with values reported in literature (*Elender et al.*, 1996; *Tsukruk et al.*, 1999). Noticably the contact angle on cleaned $Ta_2O_5$ is quite close to the contact angles of the silanized surfaces, whereas on clean $SiO_2$ the water drop is spreading. Therefore it has proven useful to check on the $SiO_2$-layers for a control after cleaning since spreading is here a clear indication. These results also show that the chips need to be regenerated with the proposed 10M NaOH to completely remove the silane, while treatment with 25% $NH_3$ : 30% $H_2O_2$ does not suffice.

In practice the epoxy-silanized chips have shown a higher long-term stability and better surface homogeneity than amino-silanized chips. We have preferred epoxy-silanization to amino-silanization for our experiments and performed the amino-functionalization with ethylene diamine always shortly before further preparation steps or measurements, since the aminosilane has a higher tendency to polymerize during storage.

### 5.3.2 Binding of fluorescently labeled streptavidin

In addition to the contact angle measurements for probing the silane coupling to the surface, binding studies involving labeled streptavidin offered valuable information about the surface functionalization. The experiments described in this section compare different coupling techniques of AlexaFluor® 647 streptavidin to the pretreated waveguide surface.

Fig. 5.7 provides the absorption and emission spectrum. This fluorescent dye with a molecular weight of 1250 Da is excited at a maximum of 650 nm and shows a Stokes shift of 18 nm, so that the maximum emission wavelength can be found at 668 nm. The labeled streptavidin has to be stored at -20 ° C and needs to be prevented from absorbing daylight to avoid bleaching of the fluorophore.

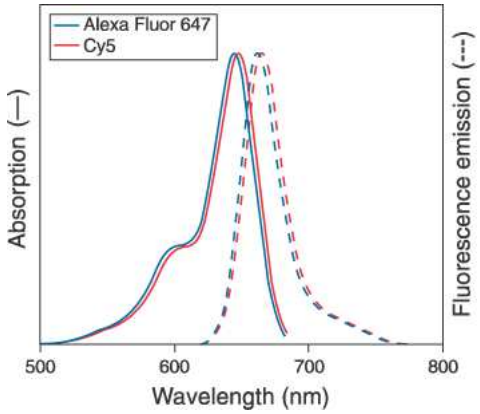


**Figure 5.7:** Absorption and emission spectrum of AlexaFluor® 647 and the comparable Cy5® dye. From *www.invitrogen.com* (2005).

All experimental data described here were obtained with the Fluorescence Reader system BCR 101. The spotting of the waveguide chips was performed on the Genetix $\text{QArray}_{\text{mini}}$ according to the following protocol:

- Preparation of 300 µl NHS-LC-biotin solution in PBS with a concentration of 1 mg/ml
- Transfer of 60 µl biotin solution into wells A1 and B1 of a 384 MTP
- Insert the MTP and an amino-functionalized waveguide chip into the QArray
- Previous to spotting, the pin is washed with ethanol and $\text{DI} - \text{H}_2\text{O}$ and dried
- Spotting is performed at following parameters: one/two dot arrays with a dot pitch of 560 µm on the $\text{Ta}_2\text{O}_5$ surface at a stamp time of 100 ms (contact time pin-chip) and an ink time of 120 ms (contact time pin-sample solution); the humidity in the device is kept at 60% during spotting; according to the manufacturer these parameters give an approximate dot diameter of 240 µm and a dot volume of 2.3 nl using a solid pin

- After spotting the chip is transferred into a humid chamber and incubated at 4 ° C for at least 2h

Following incubation, the chip is washed for 5 min in the washing buffer described in 5.1.1, rinsed with $DI - H_2O$ and dried. Subsequently the chip is incubated by pipetting 1 ml streptavidin solution (100 µg/ml SAv-AF 647 in PBS) for 1-2h, followed by the same washing procedure. Fig. 5.8 shows an example of a biotinylated waveguide chip incubated with labeled streptavidin.

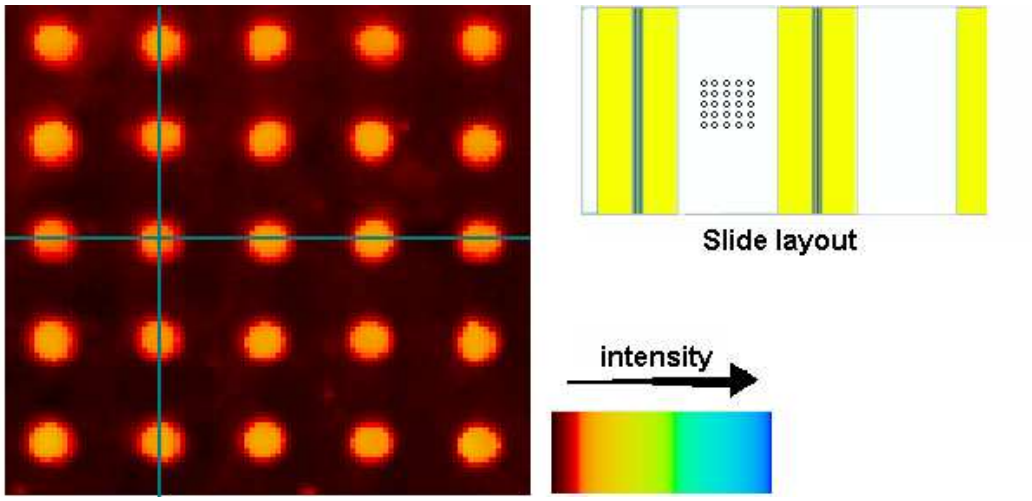


**Figure 5.8:** Binding of SAv-AF 647 on biotin dots. Exposure time: 3 sec. Blue lines denote the positions for the line scans shown in Fig. 5.9. The upper right graph shows the position of the spotted array on the waveguide chip.

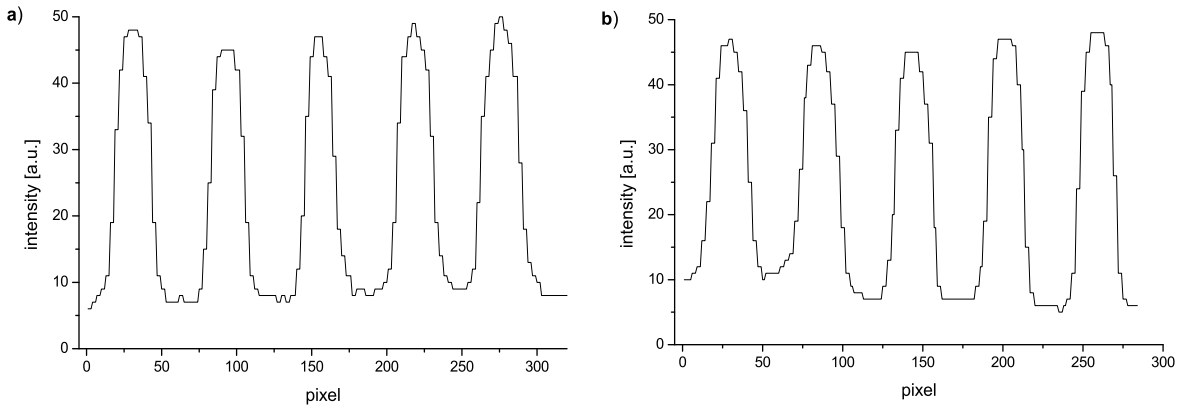


**Figure 5.9:** Horizontal and vertical line scans of Fig. 5.8. The results show a dot homogeneity of >95%.

Horizontal and vertical line scans illustrate the intensity distribution versus pixels. The line scans can be evaluated with respect to homogeneity within a single dot, and homogeneity among the total number of dots on the chip. The blue lines in Fig. 5.8 denote the positions for the line scans in Fig. 5.9 and are assumed to be representative for all dots on the chip. The dot homogeneity was found to be very good with a standard deviation of <5% of the mean signal value.

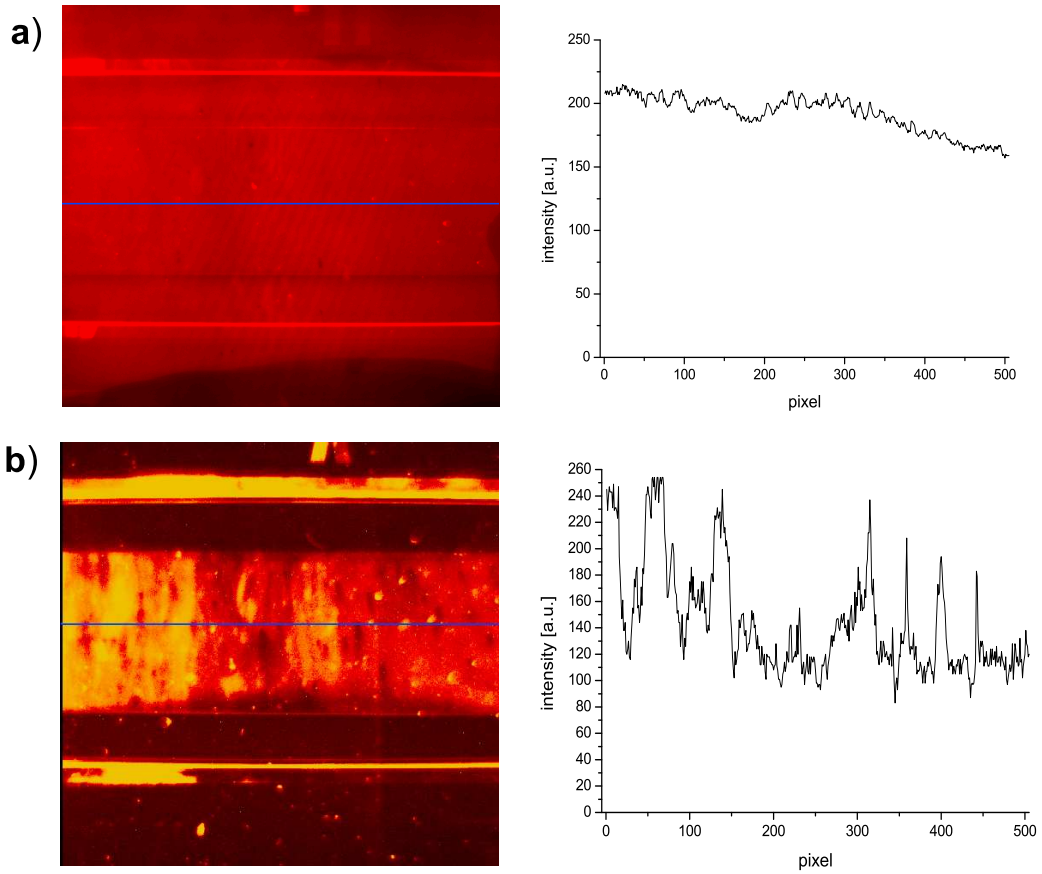


**Figure 5.10:** Binding of SAv-AF 647 to biotinylated surface compared to adsorption on waveguide. **a)** Binding of SAv-AF 647 to biotinylated surface and the respective horizontal linescan. Exposure time: 5 sec. **b)** Adsorption of SAv-AF 647 to clean waveguide chip and the respective horizontal linescan. Exposure time: 30 sec.
The images show clearly that the biotinylated surface results in a more homogeneous binding of SAv-AF 647 (sd<5%) than direct adsorption of SAv-AF 647 onto the waveguide surface (sd<20%).

Further tests included the comparison of the binding/adsorption of SAv-AF 647 to differently pretreated surfaces with the aim to find the coupling technique best suited for a

homogeneous and reproducible surface functionalization. Fig. 5.10 illustrates the binding of SAv-AF 647 to a biotinylated surface compared to mere adsorption of SAv-AF 647 to a clean waveguide surface. A horizontal line scan on the $Ta_2O_5$ area visualizes the great difference in surface homogeneity. While on the biotinylated surface the standard deviation of the mean total signal is less than 5%, the standard deviation of the mean for the blank surface where SAv-AF 647 has adsorbed is around 20%. Therefore it can be concluded that the biotinylated surface will yield more reproducible measurement results. Besides the biotinylated surface compared to the blank surface, the binding characteristics of SAv-AF 647 has also been tested on epoxy- and amino-functionalized surfaces (images not shown). Table 5.4 gives a complete comparison of the different coupling techniques with respect to the obtained total signal intensity for the same exposure time. It can be seen that the biotinylated surface not only yields the best result concerning surface homogeneity, but also shows the highest signal intensity and therefore provides the highest surface capacity for further immobilization of biotinylated reagents.

| Surface modification | mean signal intensity [a.u.] |
|---|---|
| $Ta_2O_5$ , cleaned | no homogeneous surface |
| background signal | 4±2 |
| epoxy-functionalized | 65±10 |
| amino-functionalized | 55±10 |
| biotinylated (on aminosilane) | 150±20 |

**Table 5.4:** Comparison of SAv-AF 647 binding to different surfaces. The biotinylated surface yields the best result with respect to surface homogeneity as well as the highest mean signal intensity.

## 5.4 Affinity system biotin-streptavidin

The binding of unlabeled streptavidin to NHS-LC-biotin has also been characterized in real time with the interferometric biosensor IBS 201. For all experiments, the waveguide surface has been prepared to provide amino-groups for biotin binding following the de-

scription in 5.1.2. Also recall Fig. 3.11 for the detailed binding reaction. In addition to the surface characterizations performed with labeled streptavidin where only surface homogeneity could be quantified, the biosensor data allows an evaluation of the binding reaction with respect to total surface capacity and monolayer thickness.

Fig. 5.11 shows a typical sensorgram of SAv binding to immobilized biotin on an amino-functionalized surface obtained in TE mode and at a flow rate of ≈83 µl/min. First, a baseline under continuous PBS flow on both channels of the two-channel flow cell is monitored for ≈10 min, followed by an injection of 1 mg/ml NHS-LC-biotin on the measurement channel for ≈45 min (close to equilibrium). A washing step with PBS removes unbound biotin, and a signal increase in $\Delta n_{eff}$ of $49 \cdot 10^{-6}$ has been determined for the remaining bound biotin monolayer. Following the biotin immobilization step, streptavidin with a concentration of 6 µg/ml has been injected for ≈20min until equilibrium, and washed again with PBS to remove unbound analyte. A signal increase of $\Delta n_{eff}$=$570 \cdot 10^{-6}$ can be attributed to streptavidin binding. During the complete measurement, the reference channel has been kept under continuous PBS flow. All buffers and sample solutions were degassed before use.

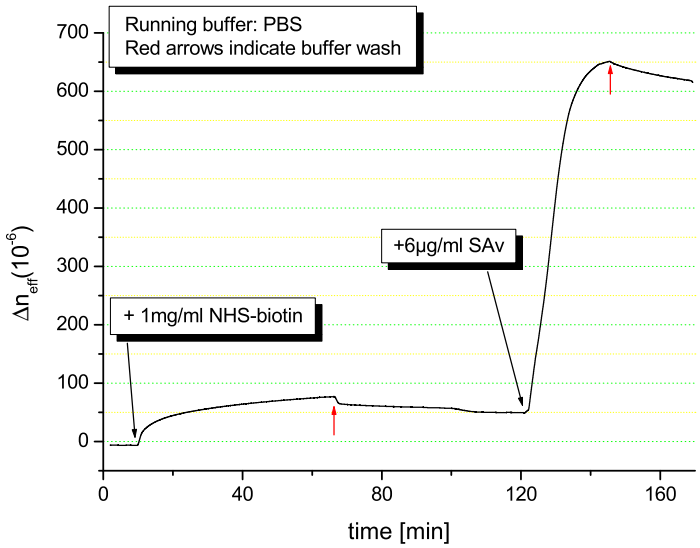


**Figure 5.11:** Sensorgram of SAv binding to immobilized biotin on an amino-functionalized surface. Measurement parameters: R=12.5 kΩ, I=105 mA, $\tau$=800 ms

Assuming n=1.45 as refractive index for the protein layers, the layer thickness of the bound biotin calculates to 0.2 nm, and of streptavidin to 3 nm, which corresponds to values found in literature (*Weisser et al.*, 1999). Repeated measurements (n=5) of the biotin-streptavidin binding event showed signal values for biotin binding of $\Delta n_{eff} = (39 \pm 4) \cdot 10^{-6}$(SE), and for streptavidin binding of $\Delta n_{eff} = (707 \pm 54) \cdot 10^{-6}$(SE), which lies within the experimental error.

When using a refractive index of n=1.45 (*Prime and Whitesides*, 1991, 1993) for both the biotin and the streptavidin monolayer, estimations can be made also concerning the surface coverage of both analyte molecules. Once the surface coverage has been determined, it is possible to draw inferences on the stoichiometry of the binding event. Recall from chapter 3 that each streptavidin molecule has four binding sites for biotin. From the experiment described here, it follows that a biotin monolayer of $\Delta n_{eff}=39 \cdot 10^{-6}$ equals a surface coverage of $\Gamma=109\,pg/mm^2$. Using a molecular weight of the bound biotin (after separation of the NHS ester) of 341.5 Da, this surface coverage corresponds to $3.2 \cdot 10^{-13} mol/mm^2$. The calculated surface coverage of bound streptavidin gives $\Gamma=2.0\,ng/mm^2$, which equates $3.0 \cdot 10^{-14} mol/mm^2$ using a molecular weight of 66 kDa. Assuming that 100% of the signal increase is caused by specific binding, this is a ratio of about 10:1 biotin molecules to streptavidin molecules. This discrepancy might be attributed to the different immobilization, taking the molecule sizes into account: since the streptavidin molecule is considerably larger in size ($4.5 \times 4.5 \times 5.2 nm^3$ (*Hendrickson et al.*, 1989)), the streptavidin molecule, when acting as the immobilized binding partner, will capture two biotin molecules. However, when the biotin is immobilized, the probability that one streptavidin molecule is bound by exactly two biotin molecules is considerably low due to steric hindrances caused by the large difference in molecule size, so that many biotins might remain unbound. Yet the large excess of biotin molecules available for streptavidin binding indicates the formation of a streptavidin monolayer during the binding event.

In a further experiment we studied the binding of labeled streptavidin (SAv-AF647) to immobilized biotin in a printed dot array compared to flow cell immobilization to calibrate the fluorescence intensity to the signal change in $\Delta n_{eff}$. The preparation of the surface chemistry was identical to the protocol described in 5.2.2. The amino-functionalized chip

was first spotted with two dot arrays on $Ta_2O_5$ as illustrated in Fig. 5.12 with a biotin concentration of 1 mg/ml and afterwards inserted into the interferometric biosensor and the same biotin solution applied on the measurement channel (with PBS as reference and washing buffer). This was followed by incubation of the complete surface with 100 µg/ml SAv-AF647 for 2h. The readout of the fluorescence intensity was performed with the BCR 101 at an exposure time of 1 sec. Fig. 5.12 shows the results, where a horizontal line scan through the flow cell area and two adjacent printed dots indicates that the binding has been approximately equal for both immobilization techniques yielding an intensity value of ≈30 (a.u.). Compared to the signal increase monitored with the interferometric biosensor, this value can serve as reference value for the fluorescence signal intensity at a given exposure time for a streptavidin layer.

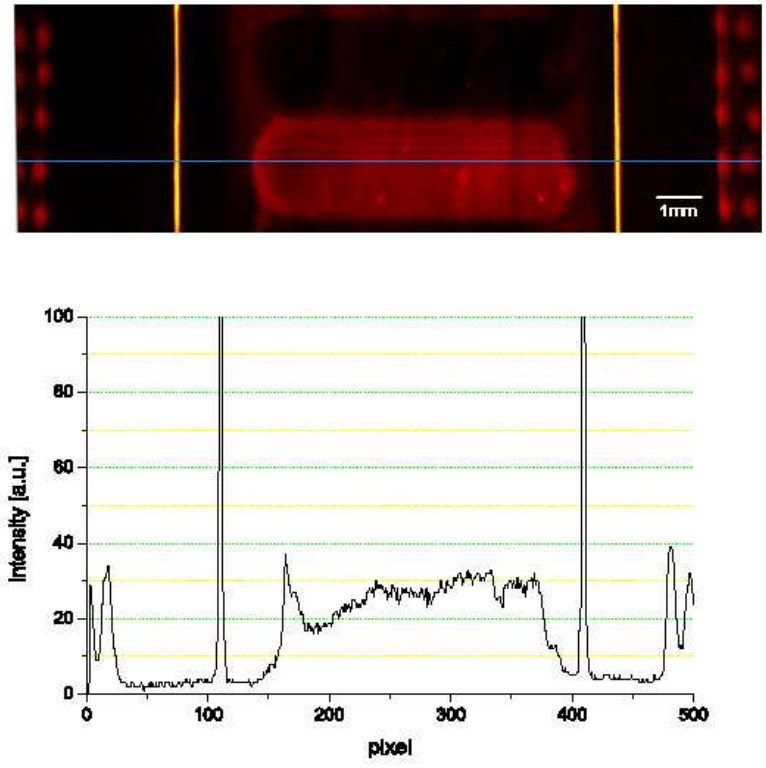


**Figure 5.12:** Binding of SAv-AF647 (Image readout: BCR 101, exposure time: 1 sec) on a biotin dot array compared with immobilization in the two-channel flow cell (IBS 201). The blue line in the upper image denotes the position for the line scan shown in the lower graph.

## 5.5 Immunoreaction Protein G-Immunoglobulin G

### 5.5.1 Flow cell system: kinetic analysis

This section describes the experiments on a commonly known standard immunoassay: protein G and its corresponding antigen immunoglobulin G (IgG). Kinetic measurements were performed applying several concentrations of IgG to previously immobilized protein G, since protein G has two binding sites to capture the $F_c$-fragment of the IgG antibody. The application of several concentrations of the analyte allows evaluation of the reaction kinetics and the determination of the affinity constant of this immunoassay. For the purpose of kinetic measurements a rather low receptor density is advisable (cf. chapter 3), and therefore the adsorption of protein G to the waveguide surface was chosen as immobilization.

Degassed PBS with pH=7.4 served as running buffer as well as sample buffer, the reference channel was kept under continuous PBS flow during the measurement.

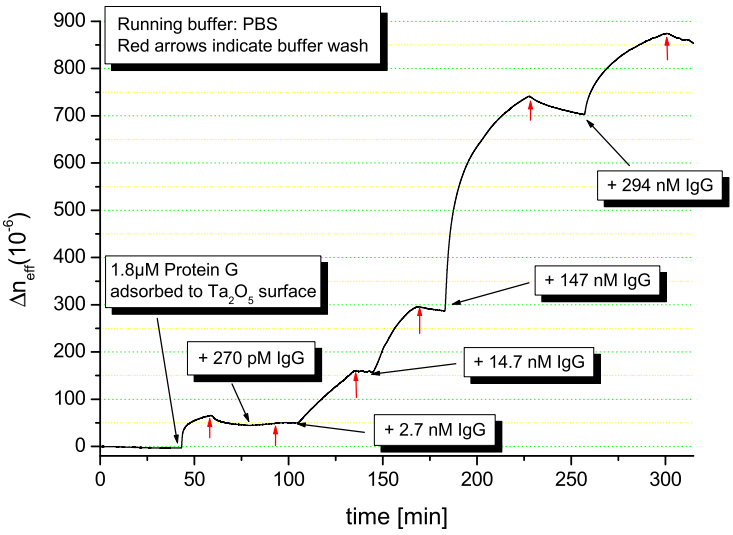


**Figure 5.13:** Sensorgram of an IgG concentration series ranging from 270 pM to 294 nM on 1.8 µM immobilized protein G. Red arrows indicate buffer wash with PBS. The reference channel was kept under continuous PBS flow. Measurement parameters: R=12.5 kΩ, I=108 mA, $\tau$=400 ms, TE mode.

The complete measurement was run in the two-channel flow cell at a flow rate of ≈40 µl/min. Fig. 5.13 shows the sensorgram of the IgG concentration series on protein G. After monitoring of the PBS baseline for ≈45 min, 1.8 µM protein G in PBS has been applied on the measurement channel for 15 min until equilibrium, followed by PBS to remove unbound protein. Subsequently IgG concentrations of 270 pM, 2.7 nM, 14.7 nM, 147 nM and 294 nM were injected, each followed by PBS buffer. It can be seen from the sensorgram that the 294 nM-concentration is close to equilibrium, so that the injection of higher concentrations was not expected to cause further IgG binding. Fig. 5.14a shows the PBS baseline previous to protein G immobilization, where the inset shows a linear fit to the baseline to determine signal noise and drift. The signal noise at a sampling rate of $\tau$=400 ms was determined to $3.1 \cdot 10^{-8}$ with a drift of $< 1 \cdot 10^{-6}$/h. Fig. 5.14b illustrates a single concentration of 313 pM IgG binding to immobilized protein G, indicating that the experimental limit of detection lies in the low pM range.

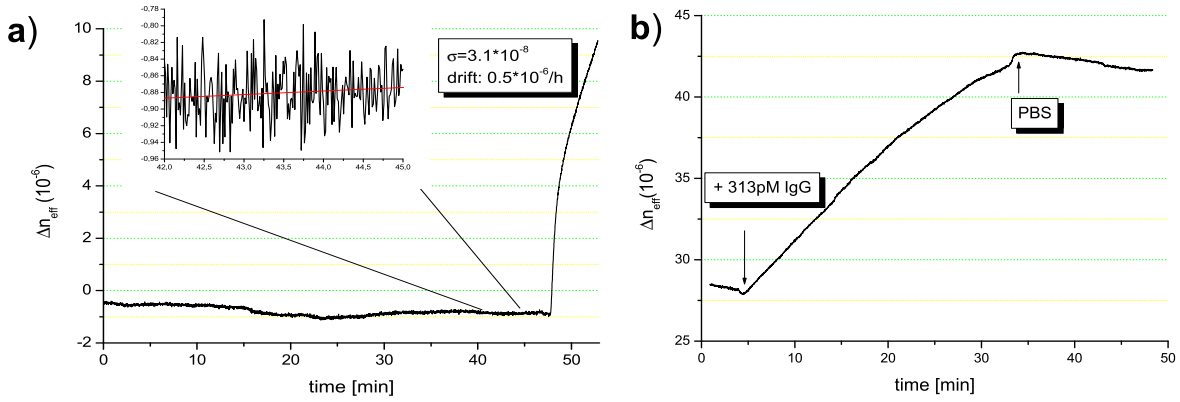


**Figure 5.14: a)** 45 min-baseline of the protein G - IgG immunoassay. The inset shows a linear fit to the baseline to determine signal noise and drift. The signal noise at a sampling rate of $\tau$=400 ms was determined to $3.1 \cdot 10^{-8}$ with a drift of $< 1 \cdot 10^{-6}$/h. **b)** Single concentration of 313 pM IgG on immobilized protein G.

From the sensorgram the binding rate constants $k_a$, $k_d$ and the affinity constant K have been obtained as described in chapter 3.4.1. A plot of the end signal values versus the respective concentration (dose-response-curve), fitted to the Langmuir isotherm, yields the affinity constant K and the signal change equivalent to the maximum analyte concentration. The end signal values are obtained from Fig. 5.13 for each concentration

shortly before the next concentration is injected. Fig. 5.15a illustrates the Langmuir fit to the experimental data and the results. From the Langmuir isotherm an affinity constant of K=$2.6 \cdot 10^7\,\mathrm{M}^{-1}$ and a maximum analyte concentration (=$c_{Ab_t}$) equivalent to $\Delta n_{eff} = (877 \pm 58) \cdot 10^{-6}$ has been determined. From the Langmuir fit we can also obtain the theoretical detection limit for IgG by applying the $3\sigma$ criterion and calculating the detection limit in units of $\Delta n_{eff}$ to $1 \cdot 10^{-7}$: this corresponds to 4.3 pM IgG.

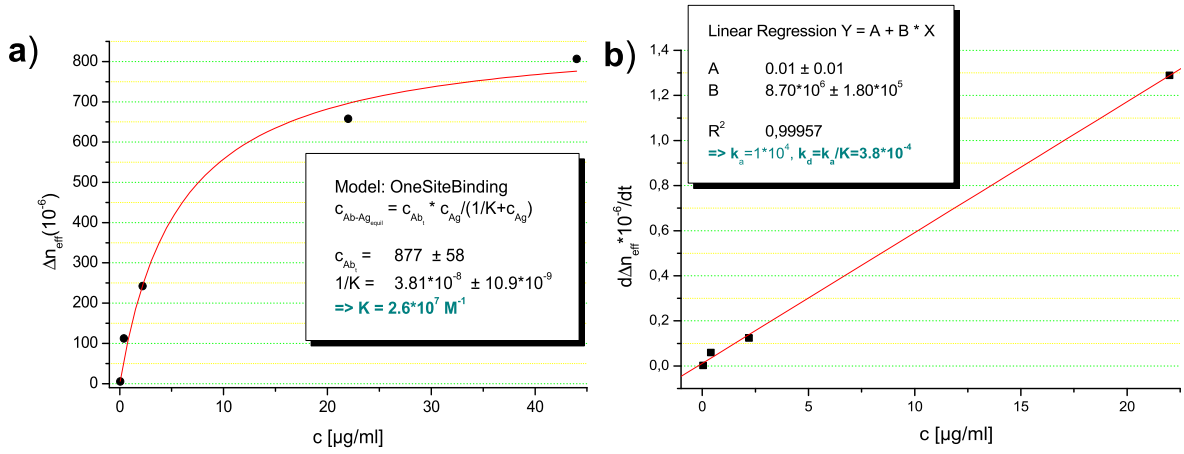


**Figure 5.15:** Evaluation of the binding kinetics of the protein G- IgG affinity system. **a)** Dose-response curve and fit to the Langmuir isotherm (one-site binding model). An affinity constant of K=$2.6 \cdot 10^7\,\mathrm{M}^{-1}$ and a maximum analyte concentration (=$c_{Ab_t}$) equivalent to $\Delta n_{eff} = (877 \pm 58) \cdot 10^{-6}$ has been determined. **b)** The initial binding rate $\partial \Delta n_{eff}/\partial t$ versus concentration gives an association rate constant of $k_a = 1 \cdot 10^4\,\mathrm{M}^{-1} \cdot \mathrm{s}^{-1}$ according to eq. 3.8.

Furthermore it it possible to determine the binding rate constants $k_a$ and $k_d$ by evaluating the initial binding rate $\partial \Delta n_{eff}/\partial t$. In general this requires that each analyte concentration is monitored separately, i.e. the surface needs to be regenerated with an appropriate regeneration buffer to remove all bound analyte before the next analyte concentration is applied. However, the choice of the analyte concentrations for the measurement shown in Fig. 5.13 allows to extract the initial binding rate since the first four concentrations are 5-10 times higher than the prior concentration, and the influence of the previously bound analyte is estimated to be negligible. The initial binding rate has thus been determined by a linear fit to the first 80 sec to the sensorgram of the concentrations 270 pM to 147 nM and plotted versus the respective concentration as shown in Fig. 5.15b. Recalling eq. 3.8

the linear fit yields an association rate constant of $k_a = 1 \cdot 10^4\,M^{-1}s^{-1}$ and with $k_d = \frac{k_a}{K}$ a dissociation rate constant of $k_d = 3.8 \cdot 10^{-4}\,s^{-1}$. These values for the binding rate constants slightly deviate from experimental values found in literature for this affinity system (*Saha et al.*, 2003). Calculating the surface coverages for protein G and IgG from the $\Delta n_{eff}$-values in Fig. 5.13 and the corresponding molecular weights (cf. chapter 3), we find $4.1 \cdot 10^{-15}\,mol/mm^2$ protein G and $1.5 \cdot 10^{-14}\,mol/mm^2$ IgG, resulting in a ratio of 1:3.8. Yet the protein G provides only two binding sites for the IgG antibody, so that the deviation might be explained by a certain amount of unspecifically bound IgG. Therefore it can be concluded that the binding rate constants slightly differ from literature values due to this unspecific binding.

The maximum antigen concentration corresponding to an antigen monolayer determined by the Langmuir fit in Fig. 5.15 has been further experimentally verified as illustrated in Fig. 5.16, where a high concentration of 250 µg/ml IgG has been injected over immobilized protein G according to the same procedure as described above for the concentration series. It can be seen that the binding comes close to equilibrium after ≈20 min and a signal increase of $\Delta n_{eff} = 835 \cdot 10^{-6}$ can be attributed to IgG binding.

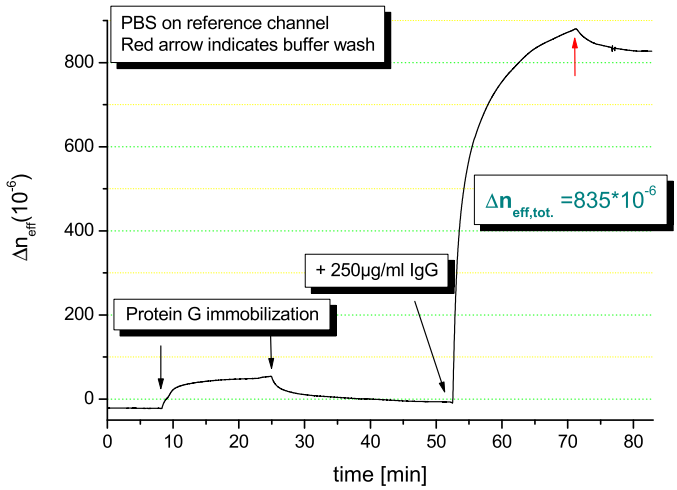


**Figure 5.16:** Binding of 250 µg/ml IgG to immobilized protein G. Red arrow indicates buffer wash with PBS. The reference channel was kept under continuous PBS flow. Measurement parameters: R=12.5 kΩ, I=107 mA, $\tau$=800 ms, TE mode. A signal increase of $\Delta n_{eff} = 835 \cdot 10^{-6}$ indicates the formation of an IgG monolayer.

### 5.5.2 Microplate system: parallel detection

The same immunoassay has further been probed on the microplate system in 8-well configuration, which allowed the parallel detection of three different analyte concentrations. By repeated scans the time-resolved measurement showed all binding events. One well pair has been kept under buffer as negative control and for drift correction. Fig. 5.17 illustrates the layout of the microplate for this experiment, where wells in row A serves as reference for the measurement wells in row B.

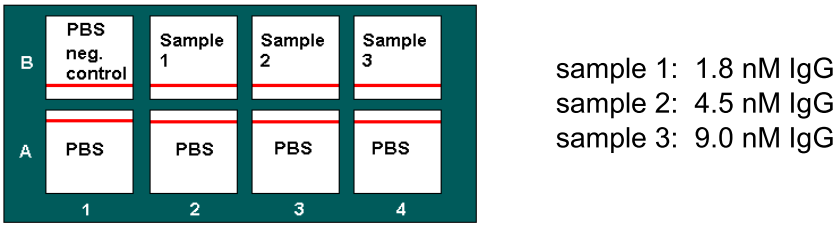


**Figure 5.17:** Microplate layout for protein G-IgG measurement and sample allocation. A1/B1 serve as negative control and for drift correction.

Before the measurement, the microplate has been cleaned in isopropanol in an ultrasonic bath for 5 min, rinsed with $DI - H_2O$, dried and inserted in the interferometer system. Wells A1-A4 and B1 were filled with 100 µl PBS. Wells B2-B4 were filled with 100 µl protein G in PBS with a concentration of 100 µg/ml and incubated for 30 min, followed by 5x rinsing with 100 µl PBS. Subsequently wells B2-B4 were filled with 100 µl pure PBS and 100 µl of 4.5 nM IgG in PBS added to B2, 9.0 nM IgG in PBS added to B3 and 18.0 nM IgG in PBS added to B4 and mixed, so that each well contained half of the concentration added (cf. Fig. 5.17). Now the scanning and readout of the microplate was started and each well pair monitored for 5 sec before moving to the next well pair, followed by an idle period of 40 sec, so that data values for each well pair were obtained in 60 sec-intervals. Fig. 5.18 shows the measurement results. In wells A1/B1 a baseline with a signal drift of $\Delta n_{eff} = 2.1 \cdot 10^{-4}$/h can be observed, whereas in wells A2-A4/B2-B4 IgG binds to the immobilized protein G (association phase). The measurement data for these wells were corrected for drift, i.e. the A1/B1-baseline subtracted from the original data. The cor-

rected data values were then fitted according to eq. 3.3 and are given in Fig. 5.18b-d. The results obtained from the fit yield the equilibrium signal change $c_{Ab-Ag_{equil.}}$ for each concentration. Compared to theoretical estimations for $c_{Ab-Ag_{equil.}}$ from eq. 3.6 and inserting $c_{Ab_t} = 877 \cdot 10^{-6}$ and K=$2.6 \cdot 10^7$ $M^{-1}$ obtained with the flow cell system, the experimental results lie well within the experimental error for wells A3/B3 and A4/B4, yet the theoretical value for $c_{Ab-Ag_{equil.}}$ for A2/B2 lies about a factor 2 below the experimental value, which might be attributed to unspecific IgG binding to the waveguide surface in the case of a low protein G density.

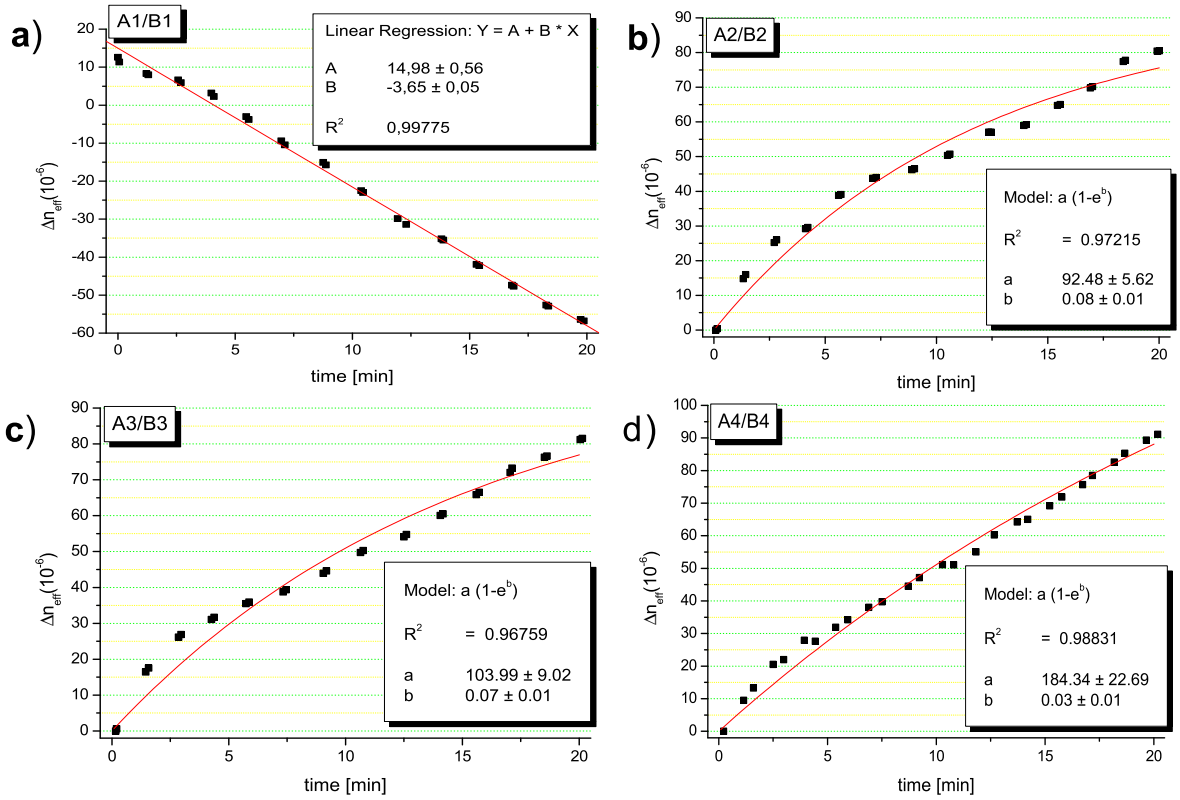


**Figure 5.18:** Microplate-based measurement of IgG concentrations on immobilized protein G. Measurement parameters: R=12.5 kΩ, I=85 mA, $\tau$=200 ms, TE mode.
**a)** A1/B1: negative control, PBS/PBS
**b)** A2/B2: 1.8 nM IgG on immobilized protein G/PBS, baseline corrected
**c)** A3/B3: 4.5 nM IgG on immobilized protein G/PBS, baseline corrected
**d)** A4/B4: 9.0 nM IgG on immobilized protein G/PBS, baseline corrected

## 5.6 Immunoreaction Protein A-Immunoglobulin G

In addition to the immunoassay protein G-IgG, the immunoassay protein A-IgG has been studied in order to obtain information about the binding kinetics and the binding rate constants. The experimental procedure is identical to the protein G measurement on the flow cell system described above. First, protein A is adsorbed to the waveguide surface, and subsequently a concentration series ranging from 2.9 nM to 576 nM was applied to the immobilized protein A, each concentration followed by PBS to remove unbound analyte. Degassed PBS with pH=7.4 served as running buffer as well as sample buffer, the reference channel was kept under continuous PBS flow during the measurement. The complete measurement was run in the two-channel flow cell at a flow rate of ≈83 µl/min. Fig. 5.19 shows the sensorgram of the IgG concentration series on protein A. After monitoring of

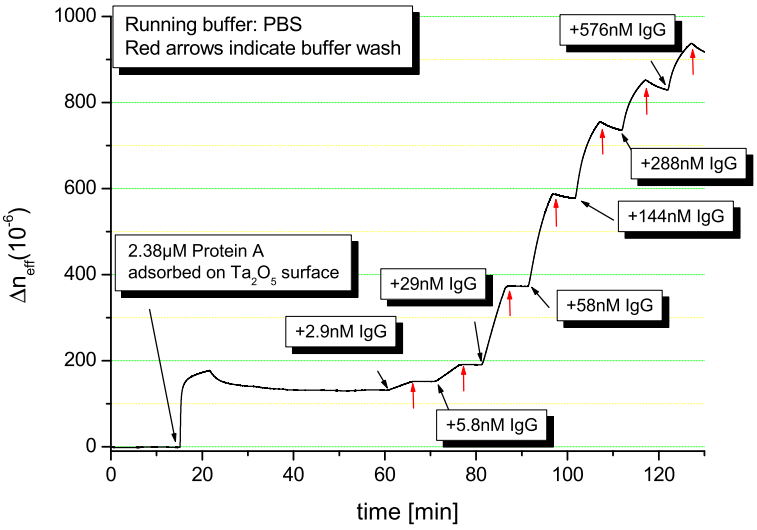


**Figure 5.19:** Sensorgram of an IgG concentration series ranging from 2.9 nM to 576 nM on 2.38 µM immobilized protein A. Red arrows indicate buffer wash with PBS. The reference channel was kept under continuous PBS flow. Measurement parameters: R=12.5 kΩ, I=108 mA, $\tau$=200 ms, TE mode.

the PBS baseline for ≈15 min, 2.38 µM protein A in PBS has been applied on the measurement channel for 7 min, followed by PBS to remove unbound protein. Subsequently IgG concentrations of 2.9 nM, 5.8 nM, 29 nM, 58 nM, 144 nM, 288 nM and 576 nM were

injected, each followed by PBS buffer. Again from the sensorgram the binding rate constants and the affinity constant K have been obtained. The dose-response curve, fitted to the Langmuir isotherm, yields the affinity constant K and the signal change equivalent to the maximum antigen concentration. The end signal values are obtained from Fig. 5.19 for each concentration shortly before the next concentration is injected. Fig. 5.20a illustrates the Langmuir fit to the experimental data and the results. From the Langmuir isotherm an affinity constant of K=$1.6 \cdot 10^7\,\mathrm{M}^{-1}$ and a maximum antigen concentration (=$c_{Ab_t}$) equivalent to $\Delta n_{eff} = (859 \pm 24) \cdot 10^{-6}$ has been determined. From the Langmuir fit the theoretical detection limit for IgG calculates to 7.2 pM IgG.

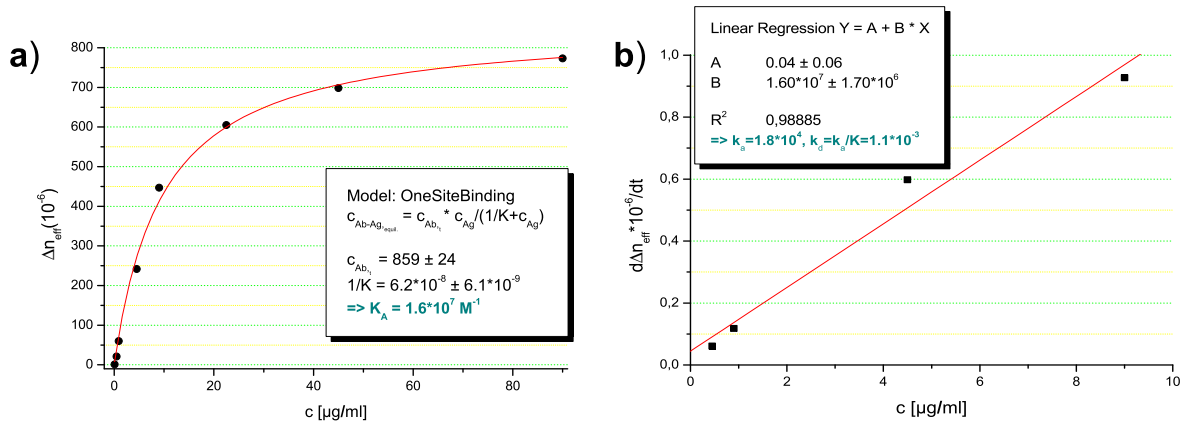


**Figure 5.20:** Evaluation of the binding kinetics of the protein A- IgG affinity system. **a)** Dose-response curve and fit to the Langmuir isotherm (one-site binding model). An affinity constant of K=$1.6 \cdot 10^7\,\mathrm{M}^{-1}$ and a maximum antigen concentration (=$c_{Ab_t}$) equivalent to $\Delta n_{eff} = (859 \pm 24) \cdot 10^{-6}$ has been determined. **b)** The initial binding rate $\partial \Delta n_{eff}/\partial t$ versus concentration gives an association rate constant of $k_a = 1.8 \cdot 10^4\,\mathrm{M}^{-1} \cdot \mathrm{s}^{-1}$ according to eq. 3.8.

In order to determine the association rate constant $k_a$, the initial binding rate of the concentrations ranging from 2.9 nM to 58 nM have been evaluated as described in 5.4.1 and plotted versus the respective concentration to obtain $k_a = 1.8 \cdot 10^4\,\mathrm{M}^{-1}\mathrm{s}^{-1}$. With K=$1.6 \cdot 10^7\,\mathrm{M}^{-1}$ this results in a dissociation constant of $k_d = 1.1 \cdot 10^{-3}\,\mathrm{s}^{-1}$. These binding rate constants compare quite well with literature values (*Saha et al.*, 2003). Table 5.5 summarizes the binding rate constants for both affinity systems studied. As expected, protein A shows a lower affinity to IgG than protein G.

A calculation of the surface coverages for this affinity system yields $9.0 \cdot 10^{-15}$ mol/mm$^2$ protein A binding $1.4 \cdot 10^{-14}$ mol/mm$^2$ IgG, equivalent to a reaction stoichiometry of ≈1.5:1 IgG to protein A. Protein A has a binding capacity of four $F_c$-fragments of the IgG antibody, i.e. higher than the experimentally determined stoichiometry. This can be explained by the fact that not all four binding sites can be available for IgG binding when the protein A is immobilized to the surface.

| Affinity system | $k_a$ [$M^{-1} \cdot s^{-1}$] | $k_d$ [$s^{-1}$] | K [$M^{-1}$] |
|---|---|---|---|
| protein G-IgG | $1.0 \cdot 10^4$ | $3.8 \cdot 10^{-4}$ | $2.6 \cdot 10^7$ |
| protein A-IgG | $1.8 \cdot 10^4$ | $1.1 \cdot 10^{-3}$ | $1.6 \cdot 10^7$ |

**Table 5.5:** Experimentally determined binding constants for the affinity systems protein G-IgG and protein A-IgG.

## 5.7 Biotinylated Cytochrome *c*: Comparison with BIACORE 1000 technology

In section 5.2 and 5.3 the surface chemistry using the affinity system biotin-streptavidin and test measurements with the interferometric biosensor have been described. This section provides measurements with biotinylated cytochrome *c*, a small mitochondrial protein, on the streptavidin-funtionalized surface. The same experiment has been performed on the BIACORE 1000 Upgrade in order to compare the interferometric biosensor to a commercially available system. The measurement on the BIACORE was conducted in cooperation with the Institute for Biology III of the University of Freiburg. The biotinylated cytochrome *c* was kindly provided by the Fraunhofer IGB in Stuttgart.

The interferometer measurement has been performed on the flow cell system at a flow rate of ≈83 µl/min using degassed PBS as running buffer and as reference. A biotinylated sensor chip was inserted into the interferometric biosensor and a PBS baseline monitored previous to the injection of 50 µg/ml SAv on the measurement channel. After buffer wash with PBS the binding of 17.5 µg/ml biotinylated cytochrome *c* to SAv was monitored. Fig. 5.21 shows the sensorgram of the binding reaction. A signal increase of

$\Delta n_{eff} = 797 \cdot 10^{-6}$ indicates SAv binding, a signal increase of $\Delta n_{eff} = 219 \cdot 10^{-6}$ can be attributed to cytochrome *c* binding.

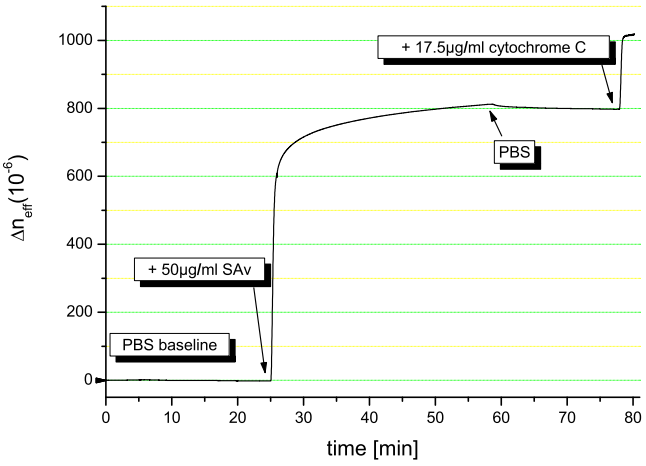


**Figure 5.21:** Sensorgram of biotinylated cytochrome *c* binding to immobilized SAv. Measurement performed with the interferometric biosensor IBS 201 at following parameters: R=12.5 kΩ, I=120 mA, $\tau$=400 ms, TE mode.

For comparison, the binding of the same concentration of biotinylated cytochrome *c* has been studied on the BIACORE 1000 Upgrade using an SA sensor chip supplied by BIACORE. The gold surface of this sensor chip is coated with a carboxymethylated dextran matrix pre-immobilized with streptavidin. The measurement was performed with degassed PBS as running buffer and reference at a flow rate of ≈10 µl/min and a sampling rate of 1 Hz, using a new sensor chip. After monitoring of a PBS baseline, as shown in Fig. 5.22, the binding of cytochrome *c* was detected and a signal increase of 2821 R.U. determined.

Both sensorgrams have been evaluated with respect to signal noise, baseline drift and the signal increase due to cytochrome *c* binding. Table 5.6 illustrates the comparison of the measurement data from both systems. The baseline drift as well as the signal noise is higher in the BIACORE compared to the interferometer system, and a deviation of the experimental values from the specifications for the BIACORE could be observed. The signal-to-noise ratio of cytochrome *c* binding was calculated to $1.56 \cdot 10^4$ for the IBS 201 and $3.1 \cdot 10^3$ for the BIACORE by dividing the signal increase by the baseline noise.

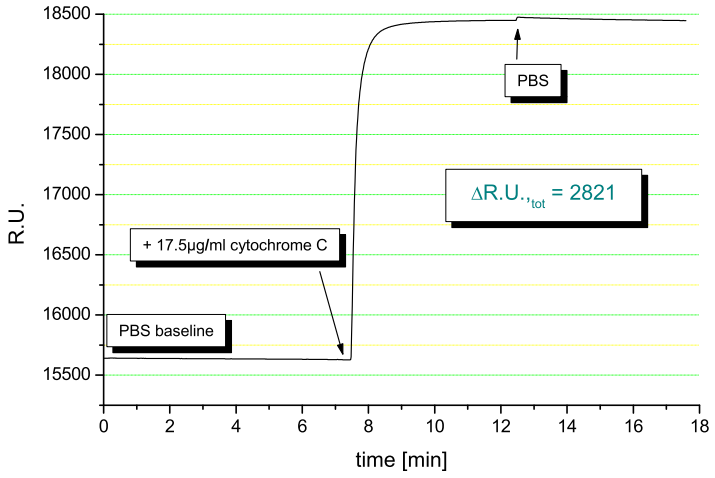


**Figure 5.22:** Sensorgram of biotinylated cytochrome *c* binding to immobilized SAv. Measurement performed with the BIACORE 1000 Upgrade at a sampling rate of 1 Hz.

The effective signal changes obtained from the interferometer sensorgram again provide information about the stoichiometry of the binding reaction. Ideally the immobilized streptavidin captures two biotinylated cytochrome *c* molecules. Assuming M=66 kDa for SAv calculates with $\Delta n_{eff} = 797 \cdot 10^{-6}$ to $3.36 \cdot 10^{-14}$ mol/mm$^2$, a signal change of $\Delta n_{eff} = 219 \cdot 10^{-6}$ for a 12.5 kDa cytochrome *c* yields $4.90 \cdot 10^{-14}$ mol/mm$^2$, resulting in an experimentally determined stoichiometry of 1:1.45.

| | IBS 201 | BIACORE 1000U |
|---|---|---|
| Refractive index range | $1.33 - 1.42$ | $1.33 - 1.36$ |
| Baseline drift | $< \pm 1.0 \cdot 10^{-6}$/h | $< \pm$ 18 R.U./h spec. |
| | (=17.6 R.U.) | ($=1.02 \cdot 10^{-6}$/h) |
| | | Exp.: 109 R.U./h |
| Noise | $< 1.0 \cdot 10^{-8}$ sd at 2.5 Hz | $<$ 0.6 R.U. sd at 1 Hz spec. |
| | (=0.176 R.U. sd) | ($=3.41 \cdot 10^{-8}$) |
| | | Exp.: 0.91 R.U. sd at 0.1 Hz |
| SNR from meas. data | $1.56 \cdot 10^4$ | $3.1 \cdot 10^3$ |

**Table 5.6:** Comparison of measurement data for cytochrome *c* binding: IBS 201 and BIACORE 1000U

## 5.8 Biotinylated $\alpha$-NPT IgG antigen: Comparison with BIACORE 2000 technology

This section describes the investigation of an antibody-antigen system commonly used for a protein production process at the Novartis Institute for Biomedical Research in Basel, Switzerland (NIBR). All measurements were performed on a BIACORE 2000 sensor system and the IBS 201 and conducted in cooperation with the NIBR, where the monitoring of recombinant proteins is an essential tool in the development of novel proteins for therapeutics. Common techniques for protein expression analysis and protein purification are SDS-PAGE or Western blot analysis. Yet these methods are time consuming and labor intensive and therefore not suited for a high throughput. One alternative allowing higher throughput are automated ELISAs. A list of these current technologies used for protein expression analysis can be found in (*Baker et al.*, 2002). A more detailed description of the methods is e.g. provided in (*Davies*, 2001).

A large variety of tags is to date available for labeling recombinant proteins (*Stevens*, 2000). In general, proteins carrying a large tag can be easily detected by ELISA, yet large tags can also interfere with the functionality of the protein. Therefore the focus at NIBR is the development of small tags and the detection of recombinant proteins expressing these tags. A fully automated competitive ELISA as general detection method for the quatitation of recombinant proteins has also been developed at NIBR. Yet a competitive ELISA has the intrinsic problem that any interference from the matrix can lead to a false positive signal, i.e. is misinterpreted as high protein concentration.

As an alternative to the competitive ELISA, optical biosensors allow the direct detection of the protein by its corresponding immobilized antibody. In the experiments described in this section, a recombinant standard protein of 21 kDa (E2-NPT expressed by *E. coli*), carrying a small tag developed at NIBR consisting of four amino acids, NPT (*N*ovartis *P*roprietary *T*ag), is detected by a biotinylated monoclonal mouse IgG directed against this tag ($\alpha$-NPT IgG). The $\alpha$-NPT IgG binds the antigen with the $F_{ab}$-fragments, i.e. two binding sites per antibody are available for antigen binding. In a first experiment, a concentration series of the protein in PBS/BSA as sample buffer is detected by the im-

mobilized antibody to determine the affinity constant of the system. Further experiments using cell lysate from *E. coli* show the suitability of both biosensor systems to detect the same protein in a more complex matrix. The detection of a ligand, e.g. a protein, directly from a cell lysate is of great importance in pharmaceutical screening studies, where the binding of new targets is investigated. Label-free detection methods are especially suited when screening for new targets due to possible side effects of labeling. Yet the assay has to be deliberately chosen to minimize unspecific binding effects from cell lysate components which might lead to a misinterpretation of the biosensor data. In the following the measurement data of the biosensor systems are compared and discussed.

All waveguide chips used for the IBS 201 were silanized according to the protocol in section 5.1.2 and functionalized via biotin linking to provide a streptavidin surface. For the BIACORE system, a sensor chip SA was obtained from BIACORE. This sensor chip is coated with a carboxymethylated dextran matrix pre-immobilized with streptavidin. Fig. 5.23 illustrates the surface chemistries of both sensor chips, which differ in one important aspect: while the silane chemistry on the IBS waveguide surface provides a two-dimensional streptavidin surface, the dextran matrix of the BIACORE sensor provides a three-dimensional structure where the streptavidin molecules are exposed in arbitrary orientation, resulting in a higher binding capacity for the biotinylated reagents.

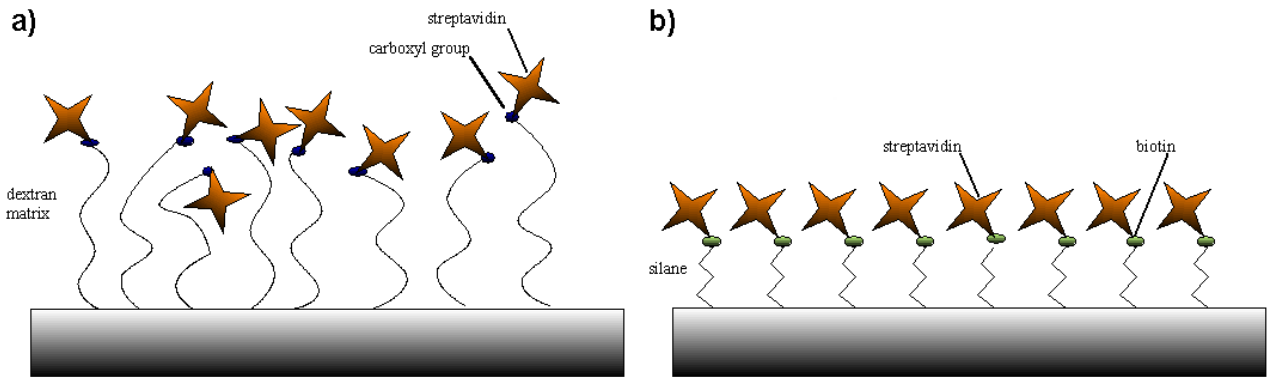


**Figure 5.23:** Comparison of the sensor chip surfaces. **a)** The dextran matrix on the BIACORE sensor chip SA provides a three-dimensional structure pre-immobilized with SAv. **b)** Silane chemistry on the IBS waveguide chip providing a two-dimensional SAv surface.

### 5.8.1 Measurements in PBS-BSA as sample matrix

A concentration series of E2-NPT ranging from 4.76 nM to 476 nM on biotinylated $\alpha$-NPT IgG was monitored on both biosensor systems. Identical sample dilutions were prepared to ensure optimal comparison of the sensorgrams. Degassed PBS with pH=7.4 at 25 ° C served as running buffer and reference unless otherwise noted.

Before the actual measurement on the interferometric biosensor, the silicone tubing was blocked with PBS/1%(w/v) BSA for 5 min to avoid adsorption of analyte molecules on the silicone surface while a blank waveguide chip was inserted. After blocking, the blank waveguide chip has been replaced by the SAv-functionalized chip and a PBS baseline monitored for ≈10 min, followed by PBS/1%(w/v) BSA for 4 min to check for unspecific binding. When changing back to PBS, it could be observed that basically no BSA has bound on the surface and thus we could assume that non-specific binding effects are minimized (see Fig 5.24a). After a stable PBS baseline has been reached, biotinylated $\alpha$-NPT IgG was injected at a concentration of 0.32 µM for 7 min, followed by PBS wash to remove unbound antibody. Fig. 5.24a shows the sensorgram of the antibody binding, yielding a signal increase of $\Delta n_{eff} = 48 \cdot 10^{-6}$.

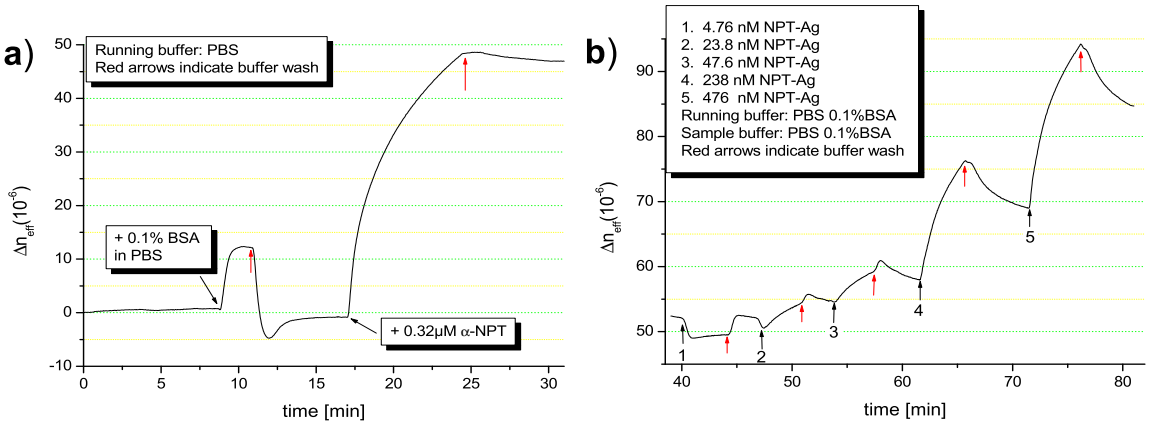


**Figure 5.24:** IBS sensorgram: **a)** BSA adsorption and binding of 0.32 µM biotinylated $\alpha$-NPT IgG yielding a signal increase of $\Delta n_{eff} = 48 \cdot 10^{-6}$ **b)** Concentration series of E2-NPT in PBS/0.1%(w/v) BSA as sample matrix ranging from 4.76 nM to 476 nM. Measurement parameters: R=12.5 kΩ, I=120 mA, $\tau$=1000 ms, TE mode.

Subsequently the running buffer has been changed to PBS/0.1%(w/v) BSA on the measurement channel to circumvent signal changes in $\Delta n_{eff}$ during protein binding, since

the sample buffer for the protein dilutions consists of PBS/0.1%(w/v) BSA. It should be noted here that only 0.1%(w/v) BSA was added to the PBS, since from experience higher BSA concentrations are likely to cause air bubbles during the measurement that might distort the signal, and 0.1%(w/v) BSA seemed sufficient to minimize unspecific binding effects. Fig. 5.24b illustrates the binding of E2-NPT to biotinylated $\alpha$-NPT IgG in concentrations of 4.76 nM, 23.8 nM, 47.6 nM, 238 nM and 476 nM, each followed by PBS/0.1%(w/v) BSA to remove unbound antigen. Both the injection time and the buffer wash was set to 240 sec. The concentration series was followed by a regeneration pulse with a phosphate buffer (10 mM $H_3PO_4$ adjusted to pH=2 with NaOH) for 30 sec to elute the bound antigen. To investigate the reproducibility of antigen binding, 238 nM E2-NPT in PBS/0.1%(w/v) BSA has been injected three times with subsequent PBS/0.1%(w/v) BSA wash and 30 sec regeneration as illustrated in Fig. 5.25a. Fig. 5.25b shows the evaluated binding and regeneration levels, indicating that after four regeneration steps the binding level approximates the regeneration level, i.e. it can be assumed that the surface is stable.

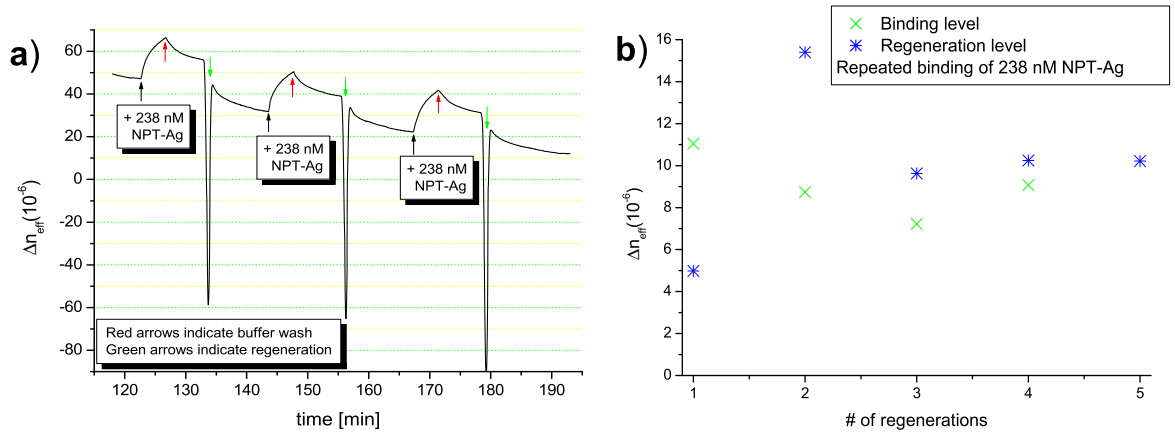


**Figure 5.25: a)** IBS sensorgram of a regeneration cycle: repeated binding of 238 nM E2-NPT and subsequent regeneration with phophate buffer (see text) **b)** Binding and regeneration levels. After four regenerations the binding level approximates the regeneration level and a stable surface is reached.

Fig. 5.26 shows the corresponding measurement on the BIACORE system, using antigen concentrations ranging from 4.76 nM to 238 nM. In this experiment, PBS served as running buffer and PBS/0.1%(w/v) BSA as sample buffer, thus an additional signal increase

during antigen injection can be observed due to a difference in the refractive index of the buffer solutions. The immobilization of 0.32 µM $\alpha$-NPT IgG was performed according to the aforementioned procedure on the IBS system, resulting in a signal increase of 1818 R.U. Each antigen concentration was again injected for 240 sec, followed by PBS for 240 sec. A regeneration with phosphate buffer eluted the bound antigen. For the evaluation of the effective signal increase the signal values obtained 15 sec after PBS injection were taken and plotted versus the respective concentration as depicted in Fig. 5.27a, compared with the end signal values obtained with the interferometric biosensor (Fig. 5.27b). Both data sets were fitted to a one-site binding model (Langmuir isotherm) to obtain the affinity constant of the $\alpha$-NPT IgG - E2-NPT affinity system. With the BIACORE sensor, an affinity constant of K=$1.35 \cdot 10^7$ $M^{-1}$ and a maximum antigen

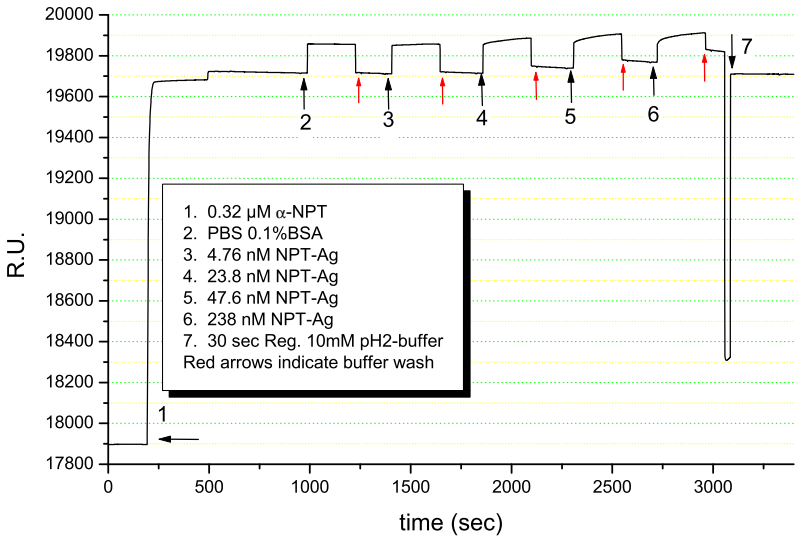


**Figure 5.26:** BIACORE sensorgram of $\alpha$-NPT IgG immobilization and the E2-NPT concentration series ranging from 4.76 nM to 238 nM. Measurement performed at a sampling rate of 1 Hz and a flow rate of ≈80 µl/min.

concentration equivalent to $149.77 \pm 9.66$ has been determined. The IBS data yield an affinity constant of K=$3.83 \cdot 10^6$ $M^{-1}$ and a maximum antigen concentration equating $\Delta n_{eff} = (22.81 \pm 1.52) \cdot 10^{-6}$. The values for the affinity constant thus differ by a factor ≈3.5 from another, which lies well within the experimental error. Applying the $3\sigma$-

criterion, the detection limit is 12 nM E2-NPT (IBS) or 45 nM E2-NPT (BIACORE). The flow rate of the measurement has been set to 83 µl/min for both biosensor systems to obtain a reasonable antibody load and antigen binding within the given time intervals despite the differently sized flow cells. With a flow cell volume of 3 µl per channel in the IBS compared to 60 nl per channel in the BIACORE, the flow is considerably faster in the BIACORE flow cell, which has crucial effects on the total antibody load and the kinetics of antigen binding. As it can be seen in Fig. 5.24 and Fig. 5.26, an antibody load of 1818 R.U. being equal to 1.82 ng/mm$^2$ exceeds the antibody load of $\Delta n_{eff} = 48 \cdot 10^{-6}$ corresponding to 0.14 ng/mm$^2$ by about a factor 13, using a refractive index of 1.38. [1]

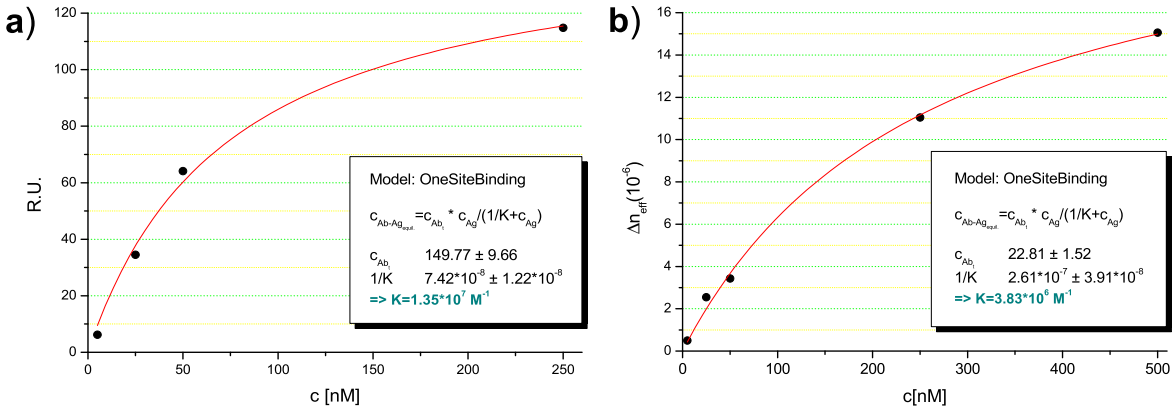


**Figure 5.27:** Langmuir fit of the $\alpha$-NPT IgG - E2-NPT binding data. Sample matrix: PBS-0.1%BSA. **a)** BIACORE data yield an affinity constant of K=$1.35 \cdot 10^7$ M$^{-1}$ and a maximum antigen concentration equivalent to $149.77 \pm 9.66$ R.U. **b)** IBS data yield an affinity constant of K=$3.83 \cdot 10^6$ M$^{-1}$ and a maximum antigen concentration equating $\Delta n_{eff} = (22.81 \pm 1.52) \cdot 10^{-6}$.

Furthermore the flow rate combined with the flow cell size of the IBS results in mass-transport limited conditions, therefore the association rate constant and dissociation rate constant could not be reliably determined. Nevertheless we considered the flow rate as reasonable to detect low concentrations of the antigen while keeping the total sample consumption low.

[1] In the following a refractive index of 1.38 for antibody layers and 1.45 for antigen layers is used. Surface coverages are calculated using 1pg/mm$^2$=1 R.U.

Signals given in R.U. are related with measurements on the BIACORE 2000 and signals given in $\Delta n_{eff}$ are related to the interferometric biosensor.

A calculation of the surface coverages for the $\alpha$-NPT IgG - E2-NPT affinity system yields $1.17 \cdot 10^{-14}$ mol/mm$^2$ $\alpha$-NPT IgG binding $7.13 \cdot 10^{-15}$ mol/mm$^2$ E2-NPT on the BIACORE resulting in a stoichiometry of 1.6:1, i.e. less antigen is bound than antibody binding sites are available. The IBS data yield surface coverages of $8.54 \cdot 10^{-16}$ mol/mm$^2$ $\alpha$-NPT IgG binding $3.02 \cdot 10^{-15}$ mol/mm$^2$ E2-NPT giving a stoichiometry of 1:3.5, although only two binding sites are available. This indicates that some antigen is unspecifically bound.

### 5.8.2 Measurements in cell lysate as sample matrix

We furthermore studied the $\alpha$-NPT IgG - E2-NPT affinity system in cleared *E. coli* cell lysate as sample matrix. The *E. coli* lysate was produced at the Biomolecular Production Unit of NIBR and prepared by incubating *E. coli* pellets for 30 min in PBS pH 7.4 at room temperature under addition of lysozyme and benzonase to facilitate cell lysis. The cell suspension was then frozen at -80 °C for 1 h and the lysate cleared after thawing by centrifugation at 5000 x g to remove cell debris.

According to the measurements in PBS/BSA a concentration series of E2-NPT ranging from 4.76 nM to 476 nM was detected by 0.32 µM immobilized biotinylated $\alpha$-NPT IgG on both biosensor systems, using identical sample dilutions for optimal comparison. Degassed PBS with pH=7.4 at 25 °C served as running buffer and reference.

Previous to the measurement on the IBS 201 the silicone tubing was blocked with 1.5 ml PBS/1%(w/v) BSA while a blank chip was inserted. After replacing the blank chip by the SAv-functionalized chip, a PBS baseline was monitored for ≈15 min. Fig. 5.28 shows the sensorgram of the measurement. Following the immobilization of 0.32 µM $\alpha$-NPT IgG, both the measurement channel (2 x) and the reference channel (1 x) were blocked with pure cell lysate to avoid unspecific binding of cell lysate components that might distort the analyte signal. The level of unspecific binding ($\Delta n_{eff} = 50 \cdot 10^{-6}$) was approximately equal on both channels, indicating a stable surface. The signal increase of $\Delta n_{eff} = 43 \cdot 10^{-6}$ resulting from antibody binding compares well to the previous measurement, indicating a good reproducibility of the surface chemistry and immobilization technique. The E2-

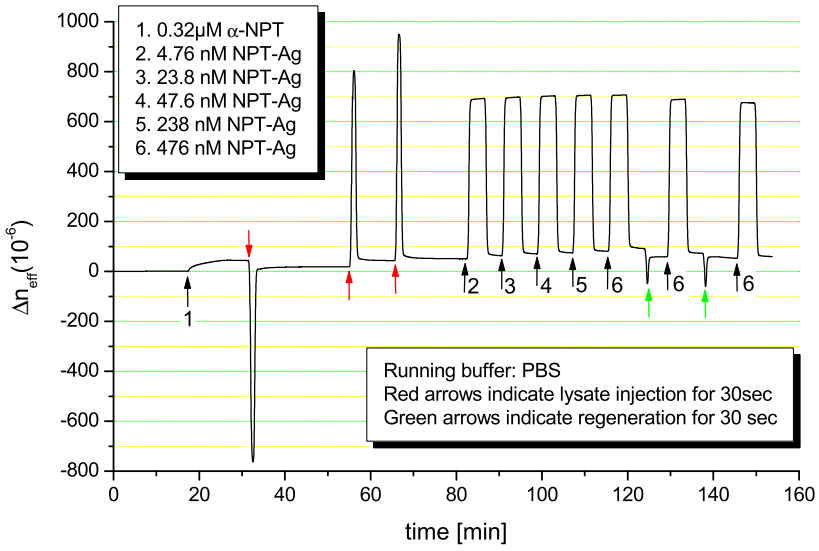


**Figure 5.28:** IBS sensorgram of an E2-NPT concentration series ranging from 4.76 nM to 476 nM on $\alpha$-NPT IgG in *E. coli* lysate as sample matrix. Measurement parameters: R=12.5 k$\Omega$, I=120 mA, $\tau$=1000 ms, flow rate 83 µl/min, TE mode.

NPT concentrations (4.76 nM, 23.8 nM, 47.6 nM, 238 nM and 476 nM) in cell lysate were applied according to the above mentioned measurement in 240 sec intervals with PBS as running buffer to remove unbound analyte. The very high signal changes during sample injection are due to the difference in refractive index of PBS compared to the cell lysate. Using cell lysate as running medium to eliminate the signal changes would not be feasible since in screening applications an unknown target molecule is directly detected from cell lysate. Therefore the signal reached 15 sec after PBS injection were taken for further evaluation as illustrated in Fig. 5.29b.

Fig. 5.30 shows the corresponding measurement of the E2-NPT concentration series from 4.76 nM to 476 nM on the BIACORE system and an enlargement of the sensorgram where the signal values for data evaluation are indicated (15 sec after PBS wash). The effective signal increases due to antigen binding were obtained from both sensorgrams and plotted versus their respective concentration in Fig. 5.31. Both data sets were fitted to the one-site binding model (Langmuir isotherm) to obtain the affinity constant of the $\alpha$-NPT IgG - E2-NPT affinity system. With the BIACORE sensor, an affinity constant

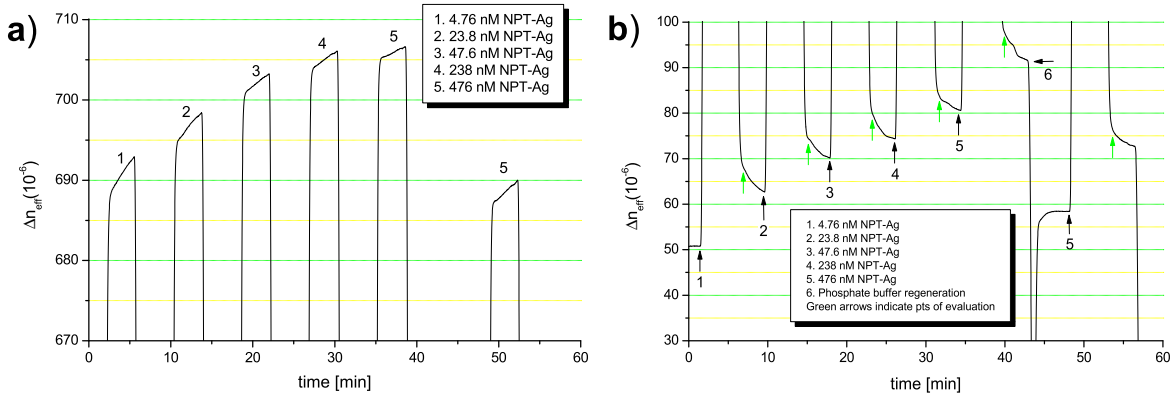


**Figure 5.29:** IBS sensorgram of the E2-NPT concentration series in *E. coli* lysate, enlarged **a)** Signal responses after sample injection **b)** End signals reached after PBS injection. Green arrows indicate points for evaluation.

of K=$1.07 \cdot 10^8$ $M^{-1}$ and a maximum antigen concentration equivalent to $157.87 \pm 16.10$ has been determined. The IBS data yield an affinity constant of K=$1.06 \cdot 10^8$ $M^{-1}$ and a maximum antigen concentration equating $\Delta n_{eff} = (41.87 \pm 5.12) \cdot 10^{-6}$. The affinity constant obtained with the IBS sensor compares very well to the affinity constant obtained with the BIACORE sensor, but both values differ from the affinity constants measured in PBS/0.1%(w/v) BSA as sample matrix. This might be explained by the more complex matrix environment of a cell lysate (*Hartmann*, 2005). This finding is also supported by the calculation of the surface coverages for the $\alpha$-NPT IgG - E2-NPT affinity system: the BIACORE data yield $1.34 \cdot 10^{-15}$ mol/mm$^2$ $\alpha$-NPT IgG binding $1.19 \cdot 10^{-15}$ mol/mm$^2$ E2-NPT on the BIACORE resulting in a stoichiometry of 1.1:1. The IBS data yield surface coverages of $9.5 \cdot 10^{-16}$mol/mm$^2$ $\alpha$-NPT IgG binding $5.6 \cdot 10^{-15}$ mol/mm$^2$ E2-NPT giving a stoichiometry of ≈1:6. Recalling that two binding sites on the antibody are available for antigen binding, the BIACORE data indicate that approximately one antigen molecule is bound per immobilized antibody, and the IBS data implies six antigen molecules per antibody, i.e. unspecific binding might have occured.

Apart from the blocking steps with cell lysate previous to antigen detection, a way to reduce the effects of unspecific binding is a simultaneous antigen injection over both channels possible with the IBS (one-channel configuration). Fig. 5.32 shows a measurement obtained with the IBS, where 0.32 µM $\alpha$-NPT IgG has been immobilized as

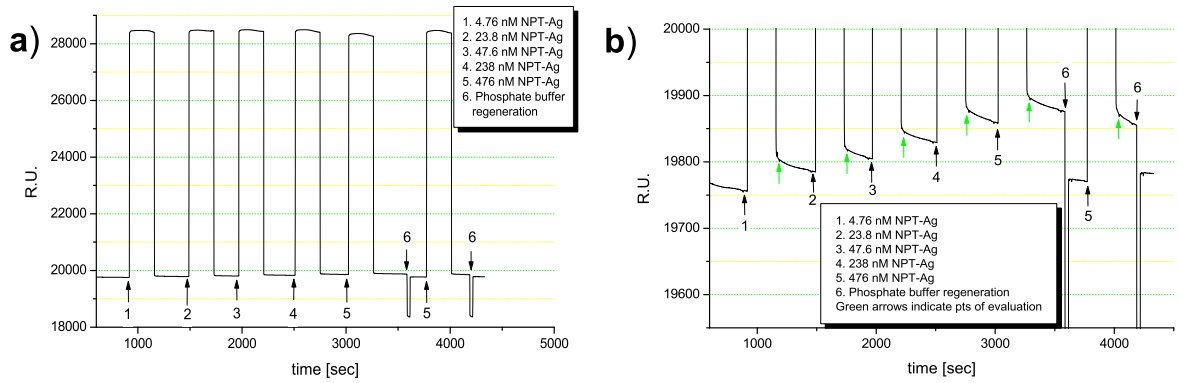


**Figure 5.30:** BIACORE sensorgram of an E2-NPT concentration series ranging from 4.76 nM to 476 nM on biotinylated $\alpha$-NPT IgG. Measurement performed at a sampling rate of 1 Hz and a flow rate of ≈80 µl/min.

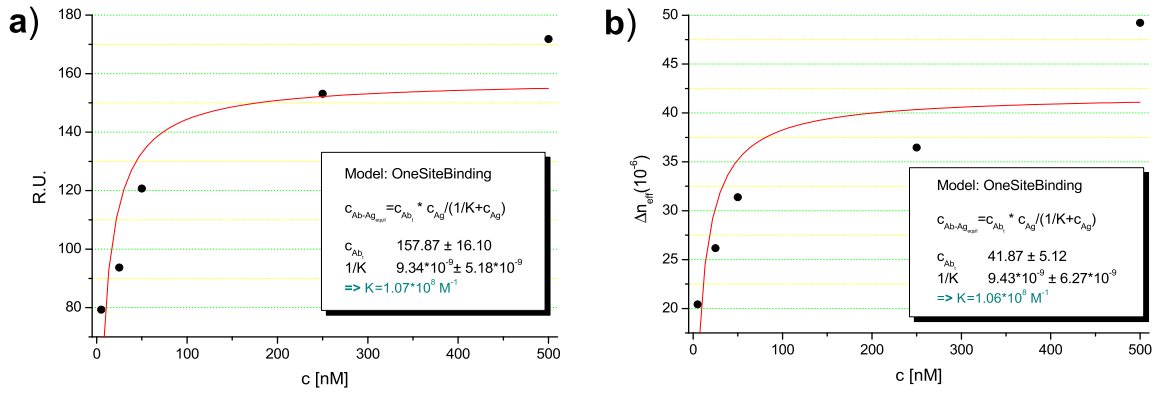


**Figure 5.31:** Langmuir fit of the $\alpha$-NPT IgG - E2-NPT binding data. Sample matrix: *E. coli* lysate. **a)** BIACORE data yield an affinity constant of K=$1.07 \cdot 10^8\ \mathrm{M}^{-1}$ and a maximum antigen concentration equivalent to $157.87 \pm 16.10$ R.U. **b)** IBS data yield an affinity constant of K=$1.06 \cdot 10^8\ \mathrm{M}^{-1}$ and a maximum antigen concentration equating $\Delta n_{\mathrm{eff}} = (41.87 \pm 5.12) \cdot 10^{-6}$.

described for the previous measurements. After successive blocking of both channels with pure cell lysate for 120 sec, an E2-NPT 1:2 dilution series ranging from 4.76 nM to 476 nM has been injected simultaneously over both channels at 240 sec intervals, each concentration followed by 240 sec PBS wash. The signal dips occuring at each sample and buffer injection are caused by a short time delay between the sample/buffer arrival in the channels. The end signal values for the Langmuir fit shown in Fig. 5.32b were taken 15 sec after PBS injection. Evaluation of the binding data yield an affinity constant of K=$5.6 \cdot 10^7\ \mathrm{M}^{-1}$ and a maximum antigen concentration equivalent to

$\Delta n_{eff} = (24.74 \pm 2.55) \cdot 10^{-6}$. These results are in good agreement with the results obtained from the measurement in PBS/0.1%(w/v) BSA as sample matrix.

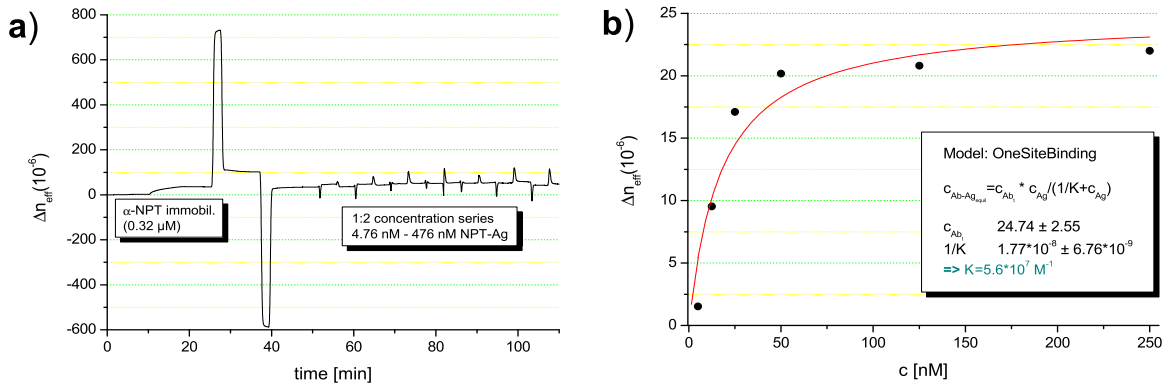


**Figure 5.32: a)** IBS sensorgram of an E2-NPT concentration series in *E. coli* lysate on immobilized $\alpha$-NPT IgG, one-channel configuration. Measurement parameters: R=12.5 k$\Omega$, I=120 mA, $\tau$=1000 ms, flow rate 83 µl/min, TE mode. **b)** Langmuir fit of the $\alpha$-NPT IgG - E2-NPT binding data yielding an affinity constant of K=$5.6 \cdot 10^7$ $M^{-1}$ and a maximum antigen concentration equating $\Delta n_{eff} = (24.74 \pm 2.55) \cdot 10^{-6}$.

## 5.9 Conclusion

In this chapter a detailed description of the materials and methods used for application and test measurements, a characterization of the surface chemistry on the $Ta_2O_5$ waveguide chips and finally application measurements on different affinity systems is provided. Differently functionalized surfaces are characterized by contact angle measurements and compared to literature values (*Elender et al.*, 1996; *Tsukruk et al.*, 1999; *Hoffmann*, 2002). Experiments with fluorescently labeled streptavidin allowed a detailed characterization of different surface modifications and a direct comparison to measurements with the interferometric biosensor with the aim to find a stable and robust surface functionalization for the immobilization of biotinylated reagents.

The immunoassay protein G - IgG has been tested on the flow-cell system as well as on the microplate system, yielding affinity rate constants that are in good agreement with values found in literature (*Saha et al.*, 2003). Furthermore the direct detection of IgG by immobilized protein A is shown and the affinity rate constants determined. Test measure-

ments with biotinylated cytochrome *c* on a streptavidin-functionalized surface compared directly to the same assay performed on the BIACORE 1000 showed the suitability of the developed surface chemistry for the $Ta_2O_5$ waveguide chips implemented in the interferometric biosensor. Furthermore the interferometric biosensor showed better SNR characteristics and a higher dynamic range with respect to refractive index resolution than the BIACORE 1000.

The measurements on the affinity system $\alpha$-NPT IgG - E2-NPT in cooperation with the NIBR providing the BIACORE 2000 system demonstrated an approximately equal performance of both biosensor systems regarding SNR and surface stability. Compared to BIACORE's dextran matrix, the silanized waveguide surface of the IBS showed a lower total surface capacity for antibody immobilization, but an equal limit of detection for the analyte antigen. The measurements in cell lysate showed that with the interferometric biosensor antigen concentrations in the low nM-range can be detected even out of a complex sample matrix without significant unspecific binding.

# Chapter 6

# Conclusions and Outlook

In this chapter the summary of the results achieved in this thesis will be presented and discussed. The interferometric biosensor system developed in this thesis is compared to other label-free biosensors, especially interferometric systems with respect to sensitivity, i.e. limit of detection. Finally an outlook including aspects of further improvements of the developed biosensor system and further possibilities for application measurements is given.

## 6.1 Summary of the results

In this thesis we presented the design and realization of a highly sensitive interferometric biosensor. A system configuration implementing a two-channel flow cell allows the monitoring of binding kinetics of immunoreactions, while with the biosensor system implementing an 8-well microplate the parallel detection of up to four different analytes is possible.

The work described in this thesis includes a background of the basic theory of planar waveguides and calculations with respect to waveguide sensitivity, the principle of the Young interferometer and system principles and relationships of the presented interferometric biosensor. A background considering the theory of binding kinetics of biomolecular interactions and the application measurement reagents is followed by a detailed description of the design, optimization and characterization of the system components, and the

realization of the interferometric biosensors. The developed technique is characterized and validated by refractometric test measurements and various application measurements. Table 6.1 gives an overview on the main properties of the developed biosensor systems.

| | IBS 201 | IBS 801 |
|---|---|---|
| Channels | 2 | 8 |
| Fluidics | Flow cell | Microplate |
| Signal noise | $\Delta n_{eff}=3 \cdot 10^{-9}$ | $\Delta n_{eff}=3 \cdot 10^{-9}$ |
| Resolution ($3\sigma$ at 1 Hz) | $\Delta n_{eff}=9 \cdot 10^{-9}$ | $\Delta n_{eff}=9 \cdot 10^{-9}$ |
| | $\Delta t_{ad}$=39 fm (TE) | $\Delta t_{ad}$=873 fm (TE) |
| | $\Delta t_{ad}$=20 fm (TM) | $\Delta t_{ad}$=455 fm (TM) |
| | $\Delta\Gamma$=25 fg/mm$^2$ (TE) | $\Delta\Gamma$=557 fg/mm$^2$ (TE) |
| | $\Delta\Gamma$=13 fg/mm$^2$ (TM) | $\Delta\Gamma$=289 fg/mm$^2$ (TM) |
| Interaction length | 5 mm | 5 mm |
| Drift | $< 1 \cdot 10^{-6}$/h in $\Delta n_{eff}$ | $< 5 \cdot 10^{-5}$/h in $\Delta n_{eff}$ |
| Repeatability | - | $< 2 \cdot 10^{-7}$ in $\Delta n_{eff}$ |
| Response time (fluid change) | 30 sec | - |

**Table 6.1:** Summary of the properties of the interferometric biosensors presented in this thesis.

From the analysis of system components for the interferometric biosensors a number of conclusions can be made, such as the choice of materials for the waveguide chips, the light source and the CCD detector. We found that the CCD sensor is the limiting system component concerning noise, whereas the phase noise is approximately equal for all three light sources tested and therefore the light source can be excluded as limiting factor.
Initial refractometric test measurements with glycerin have shown an effective refractive index resolution of $\approx 6.0 \cdot 10^{-8}$, corresponding to a refractive index resolution of $\approx 7.5 \cdot 10^{-7}$ for TE mode and $\approx 2.7 \cdot 10^{-7}$ for TM mode, respectively, at a sampling rate of 1 Hz implementing the Sony ILX 526A CCD sensor. This resolution is improved by a factor of 3 by implementing the Hamamatsu S9840 CCD sensor with full-line binning on the CCD chip.

The experimentally derived sensitivity constants of the interferometer system are in very good accordance with the theoretical values derived from waveguide theory. The flow-cell system shows a good long-term stability with a typical drift of $< 1 \cdot 10^{-6}$/h in $\Delta n_{eff}$.
We furthermore present the realized setup of the interferometric biosensor with an MTP-formatted 8-well frame as fluidic element. This system is also characterized by refractometric test measurements, including an evaluation of the experimental results compared to theory and the results obtained with the flow cell system. Initial refractometric test measurements with ethanol have shown an effective refractive index resolution of $\approx 1.0 \cdot 10^{-7}$, corresponding to a refractive index resolution of $\approx 1.2 \cdot 10^{-6}$ for TE mode and $\approx 4.5 \cdot 10^{-7}$ for TM mode, respectively, at a sampling rate of 1 Hz. It was also found that, apart from the CCD sensor being the limiting system component concerning noise, the resolution of the system is finally limited by the repeatability of the recorded data values. The experimentally derived sensitivity constants of the MTP interferometer system are also in good accordance with the theoretical values derived from waveguide theory. The system shows a long-term stability with a typical drift of $< 5 \cdot 10^{-5}$/h in $\Delta n_{eff}$ and a repeatability of $< 2 \cdot 10^{-7}$ in $\Delta n_{eff}$.
It has been shown experimentally that the interferometric biosensor with the two-channel flow cell as fluidic element can be used for application measurements when kinetic information about the affinity system is desired, while the microplate system allows the parallel detection of up to 96 analytes within one measurement. The flow-cell system has been successfully used for the detection of two standard affinity systems, biotin-streptavidin and protein G (protein A)-immunoglobulin G. Moreover, the detection of biotinylated cytochrome *c* and the detection of a tagged protein by its corresponding antibody relevant for protein purification analysis has been presented. A detailed analysis of the surface chemistry resulted in the optimization of the silanization and further modification for a stable and reproducible process needed for successful immobilization of biotinylated reagents. Estimations on the detection limit in terms of analyte concentration based on the results obtained by refractometric test measurements show that the developed interferometric biosensor can detect analyte concentrations in the low pM-range, even out of a complex sample matrix without significant unspecific binding.

We have furthermore demonstrated that in the microplate system the baseline drift in well pairs used for analyte detection can appreciably be compensated by correcting the baseline drift of these wells with the baseline drift in a negative control well pair which is kept under buffer conditions. This is important because the baseline drift also contributes to the final limit of detection and can be improved with this correction by a negative control.

## 6.2 Discussion

In this section we compare the performance of the interferometric biosensor with other label-free biosensor systems, especially interferometric systems with respect to sensitivity, i.e. limit of detection in terms of surface mass coverage.

| Biosensor principle | vendor/group | Detection limit | publication date |
|---|---|---|---|
| YI (this thesis) | Fraunhofer IPM | 13 fg/mm$^2$<br>20 fm<br>0.4 mrad | 2006 |
| Multichannel YI | University of Twente, NL | 20 fg/mm$^2$ | 2005 |
| Dual-waveguide YI | Farfield Sensors, UK | $\Delta\psi = 0.75$ mrad | 2003 |
| SPR | BIACORE, Sweden | 0.3 pg/mm$^2$ | 2004 |
| BIND | SRU Biosystems, UK | $< 1$ pg/mm$^2$ | 2004 |
| Hartmann MZI | Phot. Sensing Systems, USA | $< 2$ ng/ml | 1997 |
| RifS | Universität Tübingen, D | $\delta t$=21 pm | 2002 |
| SCM | GPI, Russia | $< 1$ pg/mm$^2$ | 2003 |
| WIOS | CSEM, CH | 0.3 pg/mm$^2$ | 2003 |

**Table 6.2:** Comparison of the interferometric biosensor presented in this thesis with other label-free sensors

Table 6.2 compares the interferometric biosensor described in this thesis with the other YI systems (*Ymeti et al.*, 2005; *Cross et al.*, 2003) and the commercially available SPR system from BIACORE (*Myszka*, 2004), the BIND system from SRU Biosystems (*Cun-*

*ningham et al.*, 2004) and the MZI developed by Photonic Sensing Systems (*Schneider et al.*, 1997). Examples of other non-commercial systems are the RifS system (*Kröger et al.*, 2002), the SCM (*Nikitin et al.*, 2003) and the WIOS system developed at the CSEM (*Cottier et al.*, 2003).

Compared to these other label-free techniques, the interferometric biosensor presented in this thesis demonstrates a higher sensitivity in terms of refractive index and surface mass coverage resolution. Furthermore our interferometric biosensor allows a configuration for parallel detection of currently up to 96 analytes, compared to a maximum of four channels implemented in other techniques.

Based on the application measurement results, it has been demonstrated that the interferometric biosensor can be used for various biological and biochemical applications in fields like diagnostics, assay development or medical screening. The technique is characterized by its very high sensitivity while allowing the parallel detection of up to 96 analytes. The intrinsic reference compensates for temperature fluctuations in the ambient as well as pH changes in the buffer. Effects caused by unspecific binding can also be reduced by simultaneously applying the same buffers or analyte solutions to the measurement and reference channel. The established surface chemistry on the $Ta_2O_5$ waveguide chips allows a stable and reproducible immobilization of commonly used biotinylated reagents.

Since the technology presented here does not rely on labeling of analytes, it saves several time- and cost-consuming preparation steps necessary for label-based techniques such as ELISA. It offers real-time monitoring of biomolecular binding events, allowing to evaluate reaction kinetics and concentration determinations.

## 6.3 Outlook

In this section we want to present some aspects on further improvements and possible application fields of the developed interferometric biosensor. The aforementioned application measurements already showed the suitability of the biosensor system in fields like immunoassay development, kinetic rate determination and secondary screening. Similarly the detection of other immunoreactants, combined with the development of the appro-

priate surface chemistry, would be possible in research areas like medical screening or diagnostics.

Currently waveguide chips fabricated on glass substrates are implemented into the interferometric biosensor. These waveguide chips showed a very good batch-to-batch reproducibility, as well as a homogeneous and reproducible waveguide layer. This high waveguide chip quality ensures high quality measurements, yet also means a considerable cost per measurement. Especially for HTS applications, the cost of consumables like sensor chips is an important issue. For this reason, sensor chips with polymers as substrate instead of glass might contribute to a decrease of the costs for the waveguide chips. First approaches of fabricating waveguide films on polymers have shown promising results (*Maisenhölder*, 2004), yet the reproducibility of the gratings and the waveguide homogeneity still need improvements to reach the same quality than the glass substrate-based sensor chips.

The developed biosensor system for microplate readout is currently designed to read a single data point (two wells) at a time. For a higher parallelization and faster readout the optical design of the system could be easily modified to read a complete row of an MTP (8 wells) at a time, or even extended to read a 384 well MTP. Yet for a 384 well MTP the interaction length of currently 5 mm would have to be decreased to ≈4.5 mm, thereby sacrificing ≈10% of the currently achieved sensitivity, but reading 4 times more data points. Here the main application focus would be primary screening, including new compounds.

The results presented in this thesis show the suitability of the interferometric biosensor as a higly sensitive sensing system for a wide variety of applications. These application fields could be even extended by further improvements of the sensor system, providing a label-free detection system as essential part in many different research areas.

# Appendices

# Appendix A: List of chemicals

| Name | Abbreviation | Purpose | Vendor |
|---|---|---|---|
| 3-Aminopropyl-triethoxysilane | APTS | Amino-terminated silane | Fluka (Sigma) |
| 3-Glycidoxypropyl-triethoxysilane | GOPS | Epoxy-terminated silane | ABCR,Karlsruhe,D |
| Albumin from bovine serum | BSA | general blocking reagent, running buffer additive | Fluka (Sigma) |
| Ammonium hydroxide | $NH_3$ | cleaning of waveguide chips | Fluka (Sigma) |
| Cell lysate from *E. coli* | | running buffer additive | provided by Novartis Basel, CH |
| Ethanol,absolute,denatured | | disinfectant | Riedel-de-Haën (Sigma) |
| Ethylene diamine | $C_2H_8N_2$ | conversion epoxy- to amino-terminus | Roth Karlsruhe,D |
| EZ-Link™ Sulfo-NHS-LC-Biotin | NHS-LC-Biotin | biochemical reagent | Perbio Science Bonn,D |
| Glycerol | | high refractive index test solution | Merck Darmstadt,D |
| Hellmanex | | alkaline concentrate for cleaning of glass | Hellma Muellheim,D |
| Hydrochloric acid | HCl | regeneration solution | Merck |

| | | | |
|---|---|---|---|
| Hydrogen peroxide | $H_2O_2$ | cleaning of waveguide chips | Riedel-de-Haën (Sigma) |
| Immunoglobulin G, human | IgG | blood serum antibody | Fluka (Sigma) |
| Isopropanol | | general cleaning | Riedel-de-Haën |
| Methanol | | solvent | Fluka (Sigma) |
| NPT antibody | α-NPT | antibody reagent | provided by Novartis Basel |
| E2-NPT (*N*ovartis*P*roprietary*T*ag) | E2-NPT | protein reagent | provided by Novartis Basel |
| Ortho-phosphoric acid, 85% | $H_3PO_4$ | regeneration solution | Fluka (Sigma) |
| Phosphate buffered saline 10x concentrate | PBS | Running buffer | Fluka (Sigma) |
| Protein A *(Staphylococcus aureus)* | Protein A | serum protein reagent | Fluka (Sigma) |
| Protein G *(Streptococcus)* | Protein G | serum protein reagent | Fluka (Sigma) |
| Saline sodium citrate buffer concentrate | SSC | wash buffer ingredient | Fluka (Sigma) |
| Sodium hydroxide | NaOH | cleaning of waveguide chips | Fluka (Sigma) |
| Sodium lauryl sulfate | SDS | wash buffer ingredient | Roth |
| Streptavidin *(Streptomyces avidinii)* | SAv | biochemical reagent | Fluka (Sigma) |
| Streptavidin AlexaFluor 647 | SAv-AF647 | biochemical reagent | Invitrogen Karlsruhe,D |
| Toluene,absolute | | solvent for silane | Fluka (Sigma) |
| Triethylamine | | catalyst for silane | Fluka (Sigma) |
| Tween® 20 | | wash buffer ingredient | Riedel-de-Haën (Sigma) |

# Appendix B: Protocol for silanization procedure

Chemicals needed: Toluene (absolute), triethylamine, 3-glycidoxy-propyl-triethoxysilane (GOPS)

- Chips have to be cleaned thoroughly before silanization!
- Put chips into the reaction vessels and plug them with stoppers.
- Start up manometer. Wait at least 2 minutes before the right atmospheric pressure is displayed. If the atmospheric pressure value given deviates more than 100mbar, the right value has to be reset manually.
- Start up vacuum pump.
- Put dewar filled with liquid nitrogen under cryo trap.
- Evacuate reaction vessels for approx. 10 minutes.
- Open main valve at the argon cylinder; first manometer shows pressure in the gas cylinder.
- Open small valve (on the right side) and check bubble counter for reaction!
- Flood reaction vessels with argon; caution! Silicone from the bubble counter might be dragged into the apparatus!
- Repeat evacuating and flooding of vessels at least once.
- Use remaining outlet for flooding of the toluene bottle with argon while taking 10ml of toluene for each reaction vessel and dispensing it respectively.
- Dispense 28.8 $\mu$l of triethylamine and 28.8 $\mu$l of silane into each vessel accordingly.
- Close small valves at the reaction vessels.
- Close main valve at the argon cylinder. Wait until both manometers show zero.
- Close small valve at the cylinder.

- Shut down vacuum pump.
- Remove dewar, dispose of liquid nitrogen.
- Aerate whole apparatus with remaining outlet.
- Shut down manometer.
- Wait at least 16 hours, then remove chips from reaction vessels into a glass perti dish and cure them at 120 °Cfor 4 hours.
- Rinse with deionized water.
- Dry under liquid nitrogen or air.
- Clean reaction vessels with isopropanol and let dry.

# Appendix C: Refractive index tables for ethanol and glycerol for calibration

| A % by wt | Refractive index | Polynom 2 | Polynom 4 |
|---|---|---|---|
| 40 | 1,3583 | 1,358972 | 1,358314 |
| 38 | 1,3575 | 1,357832 | 1,357539 |
| 36 | 1,3566 | 1,356671 | 1,356676 |
| 34 | 1,3557 | 1,355491 | 1,355725 |
| 32 | 1,3546 | 1,354291 | 1,354690 |
| 30 | 1,3535 | 1,353072 | 1,353573 |
| 28 | 1,3524 | 1,351832 | 1,352380 |
| 26 | 1,3511 | 1,350573 | 1,351116 |
| 24 | 1,3498 | 1,349294 | 1,349789 |
| 22 | 1,3484 | 1,347995 | 1,348406 |
| 20 | 1,3469 | 1,346676 | 1,346978 |
| 19 | 1,3462 | 1,346009 | 1,346250 |
| 18 | 1,3455 | 1,345338 | 1,345514 |
| 17 | 1,3447 | 1,344661 | 1,344773 |
| 16 | 1,3440 | 1,343979 | 1,344027 |
| 15 | 1,3432 | 1,343293 | 1,343279 |
| 14 | 1,3425 | 1,342601 | 1,342530 |
| 13 | 1,3417 | 1,341905 | 1,341782 |
| 12 | 1,3410 | 1,341203 | 1,341036 |
| 11 | 1,3403 | 1,340497 | 1,340296 |
| 10 | 1,3395 | 1,339786 | 1,339562 |
| 9,5 | 1,3392 | 1,339428 | 1,339199 |
| 9 | 1,3388 | 1,339069 | 1,338837 |
| 8,5 | 1,3384 | 1,338709 | 1,338479 |
| 8 | 1,3381 | 1,338348 | 1,338124 |
| 7,5 | 1,3377 | 1,337986 | 1,337772 |
| 7 | 1,3374 | 1,337622 | 1,337423 |
| 6,5 | 1,337 | 1,337257 | 1,337079 |
| 6 | 1,3367 | 1,336891 | 1,336739 |
| 5,5 | 1,3364 | 1,336523 | 1,336403 |
| 5 | 1,336 | 1,336155 | 1,336072 |
| 4,5 | 1,3357 | 1,335785 | 1,335746 |
| 4 | 1,3354 | 1,335414 | 1,335426 |
| 3,5 | 1,3351 | 1,335041 | 1,335112 |
| 3 | 1,3348 | 1,334668 | 1,334803 |
| 2,5 | 1,3345 | 1,334293 | 1,334501 |
| 2 | 1,3342 | 1,333917 | 1,334206 |
| 1,5 | 1,3339 | 1,333539 | 1,333918 |
| 1 | 1,3336 | 1,333161 | 1,333637 |
| 0,5 | 1,3333 | 1,332781 | 1,333365 |
| 0,4 | | 1,332705 | 1,333311 |
| 0,3 | | 1,332629 | 1,333258 |
| 0,2 | | 1,332553 | 1,333205 |
| 0,1 | | 1,332476 | 1,333152 |
| 0,05 | | 1,332438 | 1,333126 |
| 0 | 1,333 | 1,332400 | 1,333100 |

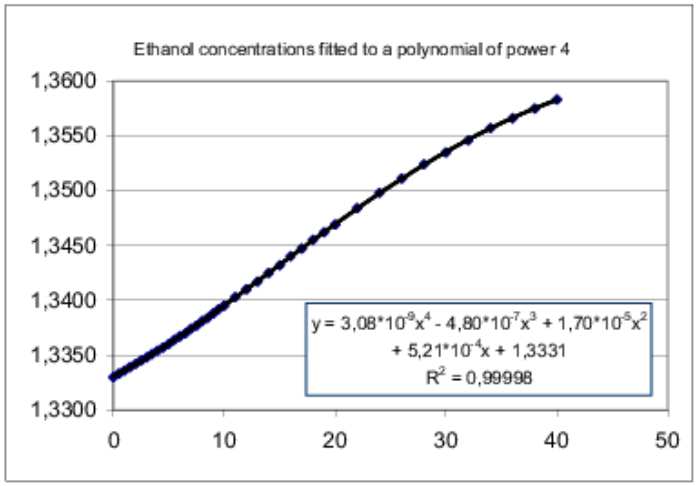


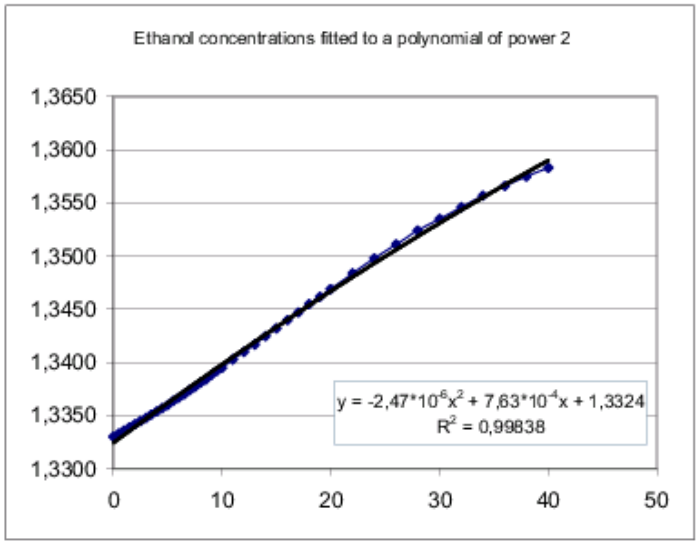


**Figure 6.1:** Refractive index values for ethanol solutions. Values from 0.5% to 40% by wt. are adapted from (*Weast*, 1976); values from 0% to 0.5% are estimated from polynomial fits

| A % by wt | Refractive index | Linear fit | Polynom 2 |
|---|---|---|---|
| 40 | 1,3845 | 1,3832 | 1,384352 |
| 36 | 1,3785 | 1,3781 | 1,378688 |
| 32 | 1,3730 | 1,3730 | 1,373145 |
| 28 | 1,3676 | 1,3679 | 1,367721 |
| 24 | 1,3624 | 1,3629 | 1,362416 |
| 20 | 1,3572 | 1,3578 | 1,357231 |
| 18 | 1,3547 | 1,3552 | 1,354683 |
| 16 | 1,3521 | 1,3527 | 1,352166 |
| 14 | 1,3496 | 1,3502 | 1,349678 |
| 12 | 1,3472 | 1,3476 | 1,347220 |
| 10 | 1,3448 | 1,3451 | 1,344792 |
| 9 | 1,3436 | 1,3438 | 1,343589 |
| 8 | 1,3424 | 1,3426 | 1,342394 |
| 7 | 1,3412 | 1,3413 | 1,341206 |
| 6 | 1,3400 | 1,3400 | 1,340025 |
| 5 | 1,3388 | 1,3387 | 1,338852 |
| 4 | 1,3376 | 1,3375 | 1,337687 |
| 3 | 1,3365 | 1,3362 | 1,336529 |
| 2 | 1,3353 | 1,3349 | 1,335379 |
| 1 | 1,3342 | 1,3337 | 1,334236 |
| 0,5 | 1,3336 | 1,3330 | 1,333667 |
| 0,4 | | 1,3329 | 1,333553 |
| 0,3 | | 1,3328 | 1,333440 |
| 0,2 | | 1,3327 | 1,333327 |
| 0,1 | | 1,3325 | 1,333213 |
| 0,05 | | 1,3325 | 1,333157 |
| 0 | 1,333 | 1,3324 | 1,333100 |

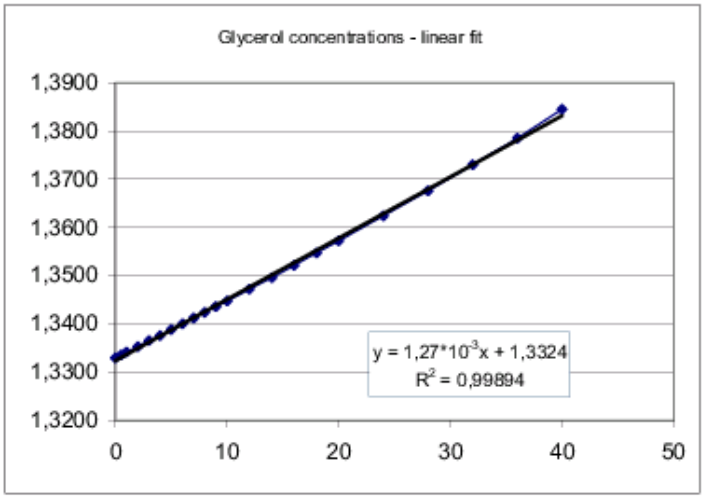


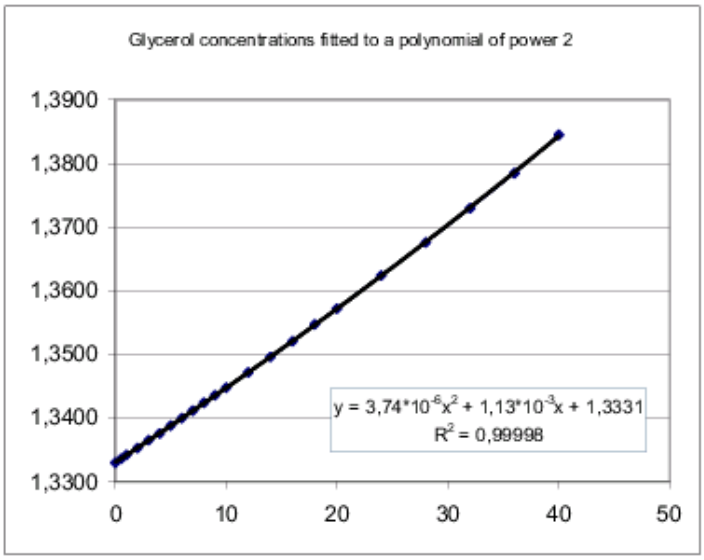


**Figure 6.2:** Refractive index values for glycerin solutions. Values from 0.5% to 40% by wt. are adapted from (*Weast*, 1976); values from 0% to 0.5% are estimated from polynomial fits

# Appendix D: LabView™ user interfaces and flowcharts

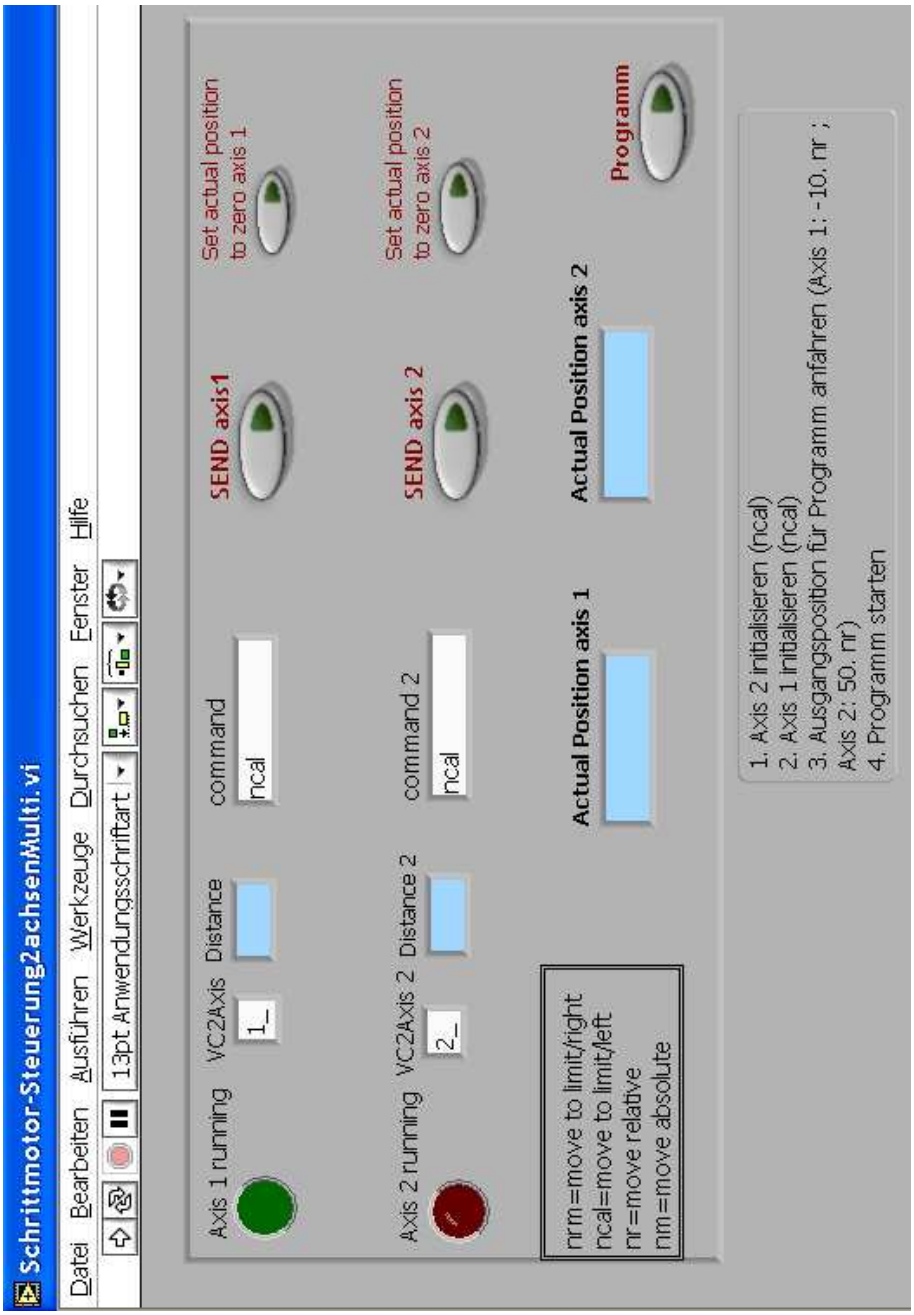


**Figure 6.3:** User interface for control of the two step motors. After input of the desired moving distance, the command is sent to the controller and executed. The actual position of the motors is returned by the controller and displayed. A routine for successive scan of several wells is started with the button "Programm".

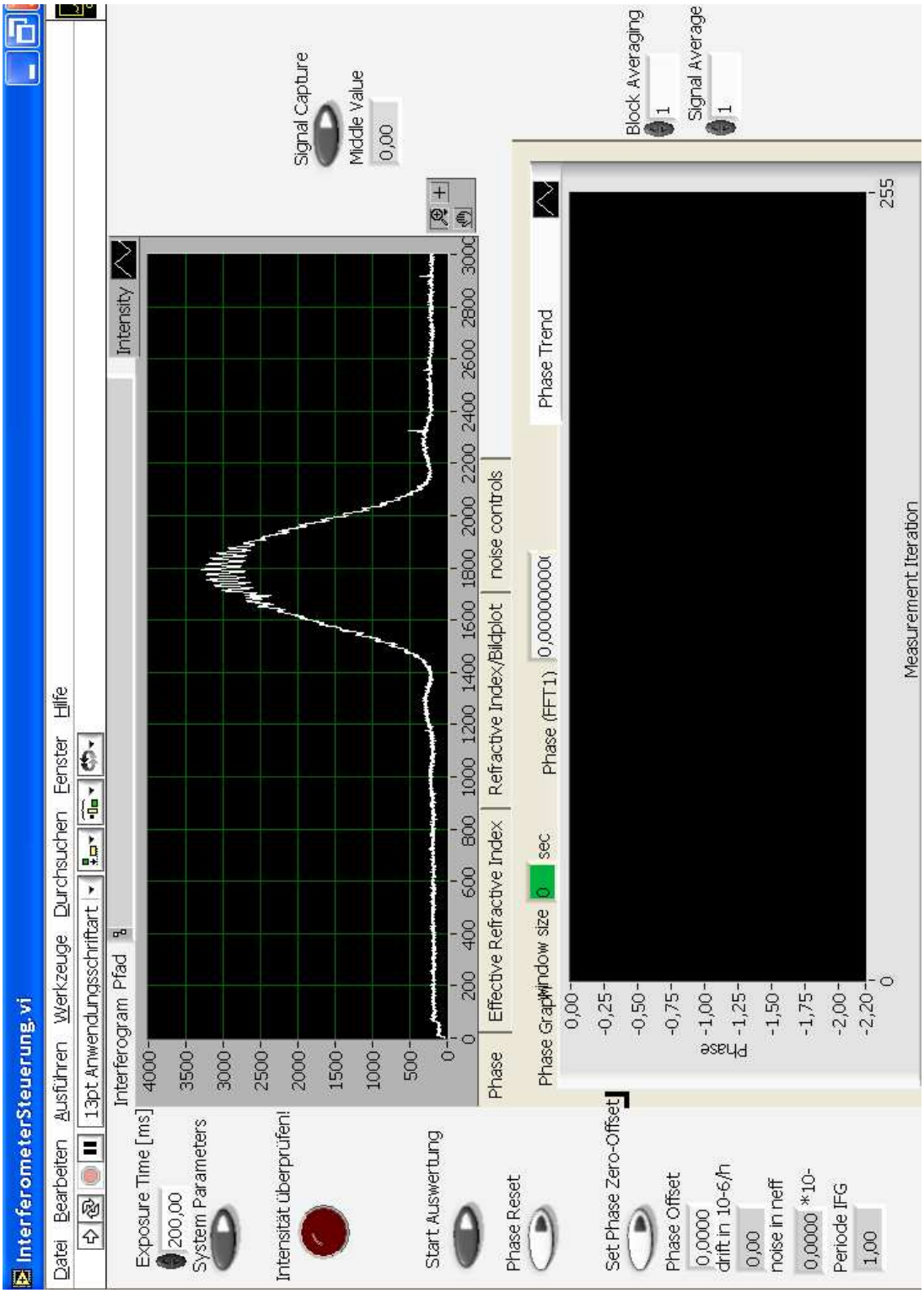


**Figure 6.4:** User interface for control of interferometer FFT algorithm. After input of the exposure time and a data file name, the CCD camera can be started and parameters like block average or signal average adjusted. With "Start Auswertung"the FFT algorithm is started and phase values, $n_{eff}$ values, noise controls and the interferogram period are displayed and stored in a data file for further evaluation.

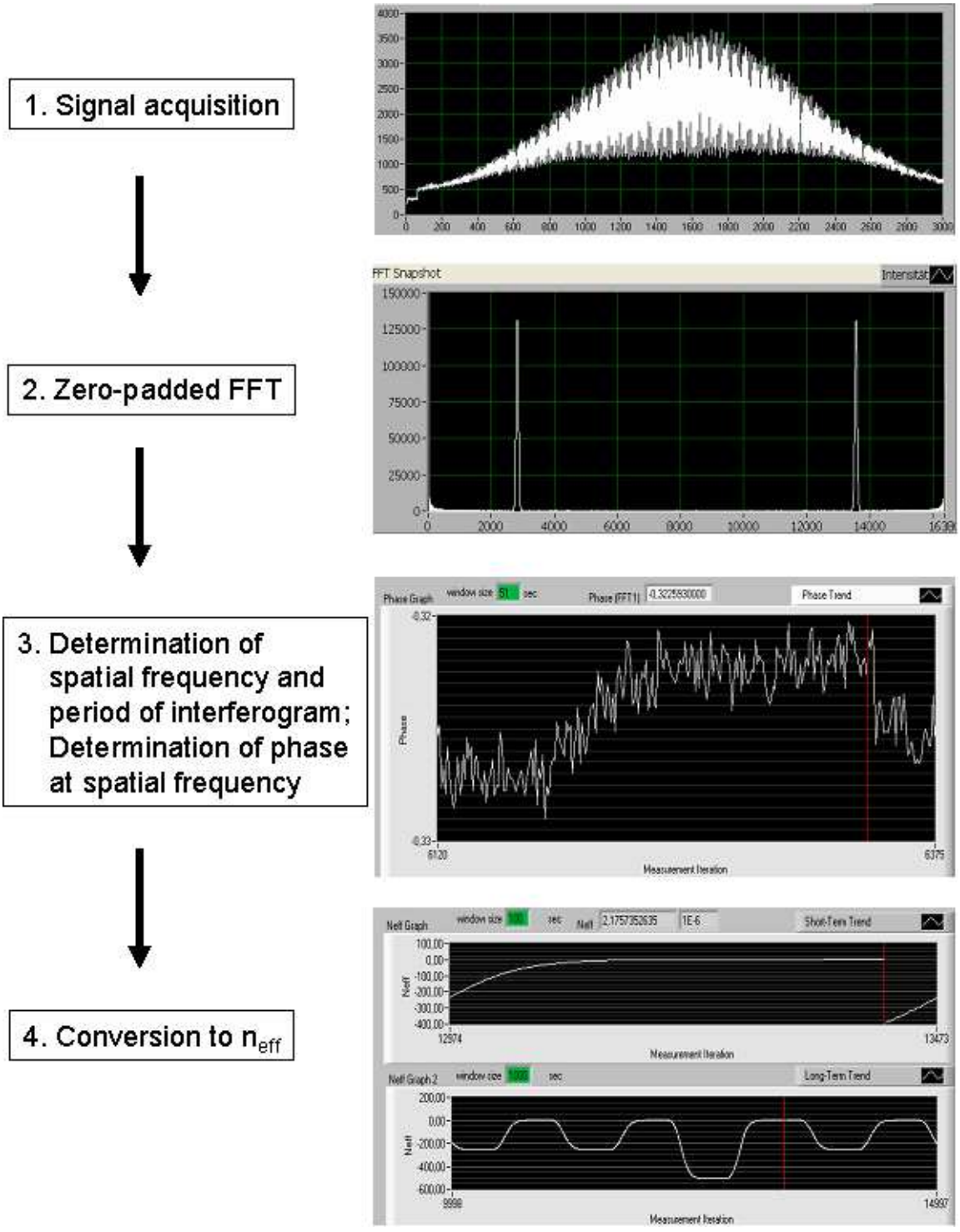


**Figure 6.5:** Flowchart FFT

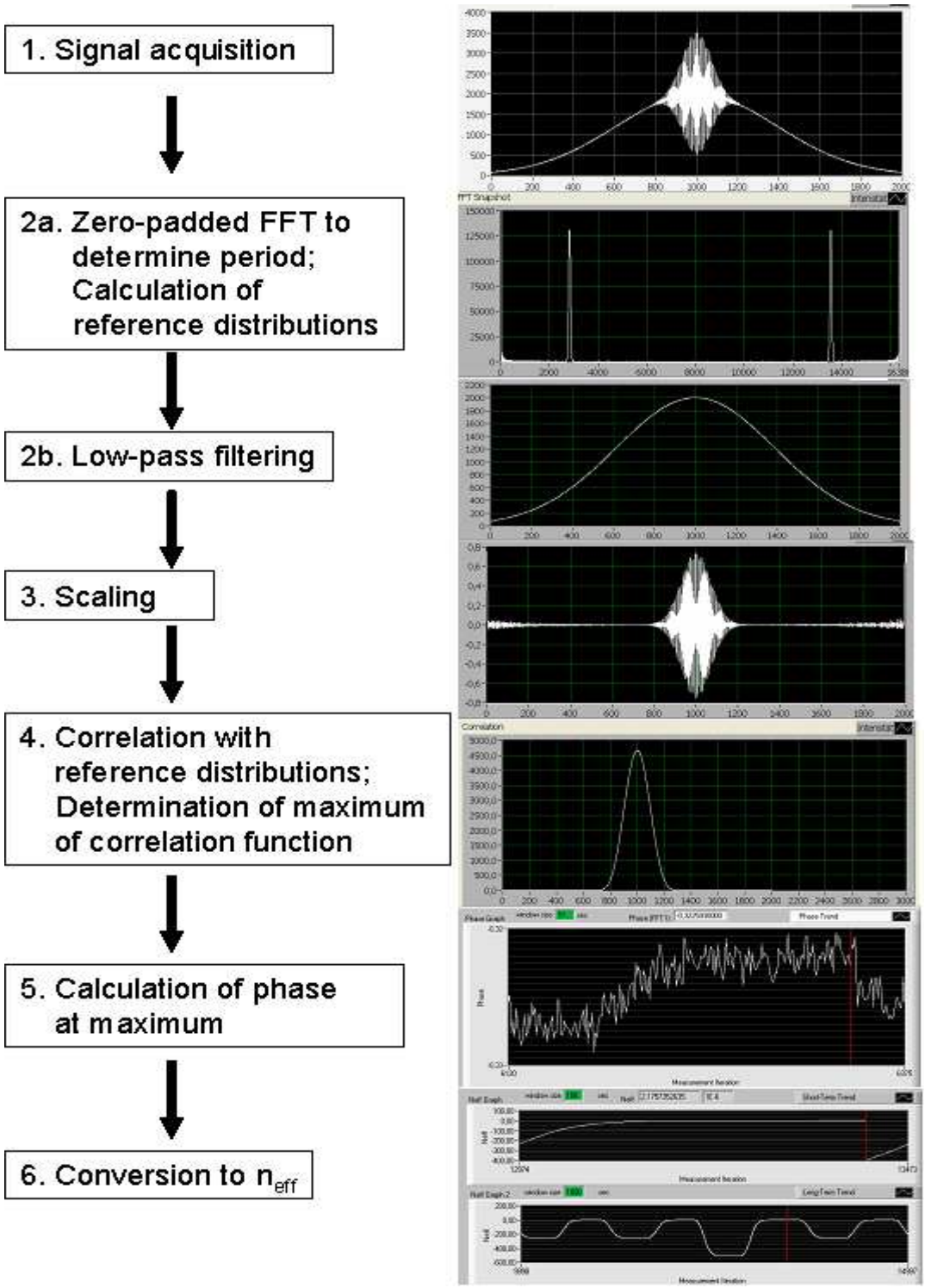


**Figure 6.6:** Flowchart CC

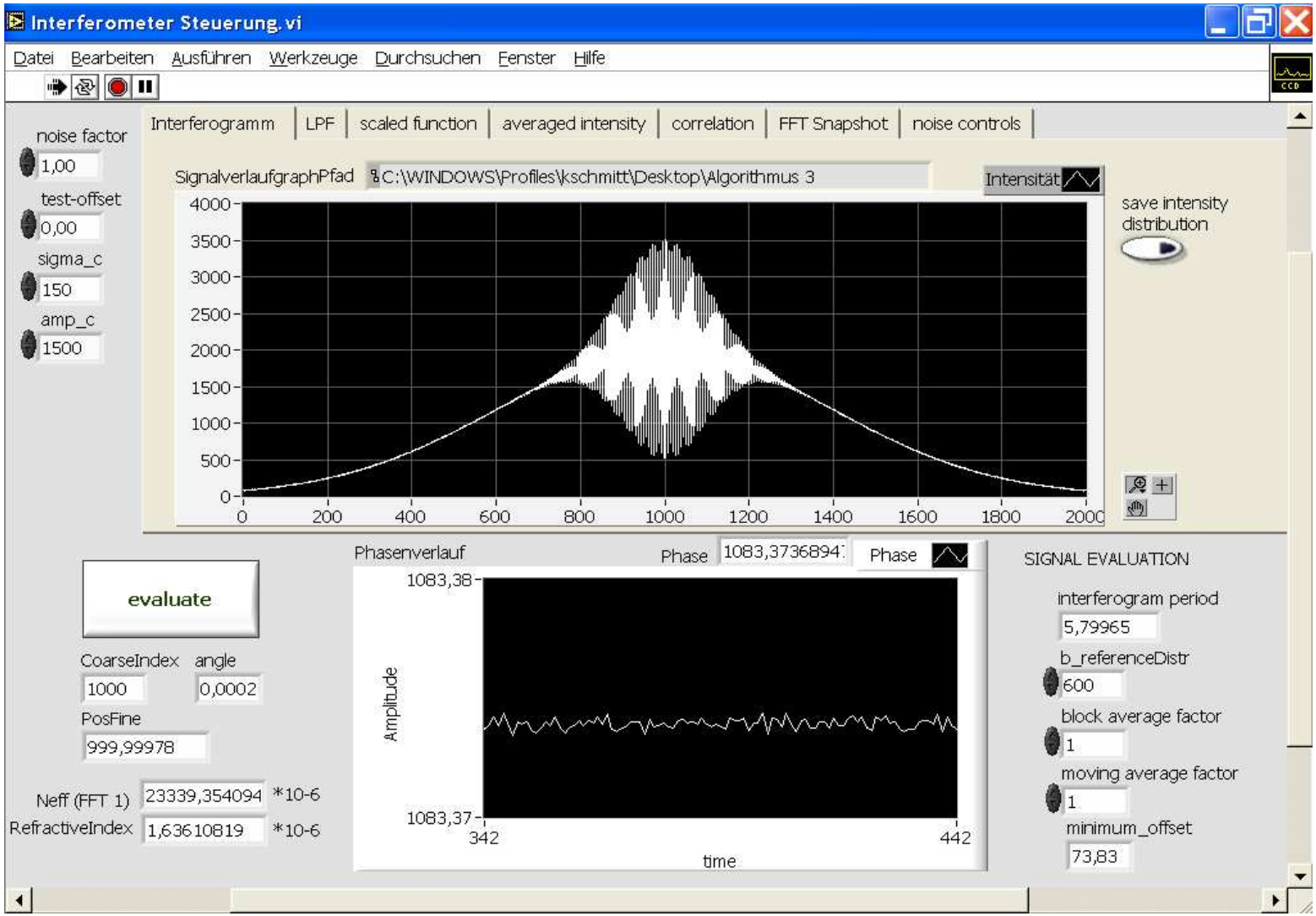


**Figure 6.7:** User interface simulation algorithm

```
/*Generation of test function*/
#include <stdio.h>
#include <stdlib.h>
#include <conio.h>
#include <math.h>
#include <time.h>
#include <sys/timeb.h>
#include <string.h>

#ifdef WIN32
#  define DLLEXPORT __declspec(dllexport)
#else
#  define DLLEXPORT
#endif

DLLEXPORT char Testfunktion_desc[] = "creates the testfunction for test purpose";

#define TWO_PI  6.28318530717959
static int counter=0;
static double indexshift=0;
static double randomarray [10000];



DLLEXPORT double Testfunktion (double *testfunktion, int arraysize,
                               double offset, double sigmac, double faktor, double ampc)
{
        // Declarations
        int i;
        // Envelope function
        double e;                   //function
        double ampe = 2000;   //amplitude of envelope function
        double xe0 = 1000;      //center pixel
        double sigmae = 550;     //fwhm in px
        //Coherence function
        double c;                  //function
        double xc0 = 1000;       //center pixel
        double p=5.80;                  //period

                for ( i=0; i < arraysize; i++ )
                {
                randomarray[i]=(rand()%10)*faktor;    //adds noise, faktor variable
                e = ampe * exp (-(i-xe0)*(i-xe0)/(sigmae*sigmae));   //envelope function
                c = ampc * exp (-(i-xc0-indexshift)*(i-xc0-indexshift)/(sigmac*sigmac));
//coher. function
                testfunktion[i] = e*(1+c/ampe * cos(TWO_PI*(i-xc-
0indexshift)/p))+offset+randomarray[i];
                }



        counter++;              // increase loop counter
        indexshift+=0.05;      //simulation of phase shift

        return 1;

}
```

**Figure 6.8:** DLL for generation of test function

# Bibliography


Adam, G., P. Läuger and G. Stark, Physikalische Chemie und Biophysik, Springer Verlag, **1995**

Baird, C. and D. Myszka, Current and emerging commercial optical biosensors, *Journal of Molecular Recognition*, Vol. 14 pp 261–268, **2001**

Baker, K., M. Rendall, A. Patel, P. Boyd, M. Hoare, R. Freedman and D. James, Rapid monitoring of recombinant protein products: a comparison of current technologies, *Trends in Biotechnology*, Vol. 20 pp 149–156, **2002**

Bilitewski, U., F. Bier and A. Brandenburg, Immunobiosensors based on grating couplers, in Rogers, K. R. and A. Mulchandani (Eds.), Affinity biosensors - techniques and protocols, Vol. 12, pp 121–134, Humana Press, **1998**

Bjorck, L. and G. Kronwall, Purification and some properties of streptococcal protein G, a novel IgG-binding reagent, *J. Immunol.*, Vol. 133 pp 969–974, **1984**

Blake, R., Cellular screening assays using fluorescence microscopy, *Current Opinion in Pharmacology*, Vol. 1 pp 533–539, **2001**

Born, M. and E. Wolf, Principles of Optics, 7th ed., Cambridge University Press, **1999**

Brandenburg, A., Differential refractometry by an integrated -optical Young interferometer, *Sensors and Actuators B*, Vol. 38-39 pp 266–271, **1997**

Brandenburg, A., R. Krauter, C. Künzel, M. Stefan and H. Schulte, Interferometric sensor for detection of surface-bound bioreactions, *Applied Optics*, Vol. 39 pp 6396–6405, **2000**

Busse, S., V. Scheumann, B. Menges and S. Mittler, Sensitivity studies for specific binding reactions using the biotin/SAv system by evanescent optical methods, *Biosensors & Bioelectronics*, **2002**

Cammann, K., Biosensoren, in: Instrumentelle Ananlytische Chemie, *Spektrum Akademischer Verlag, Weinheim*, pp 52–79, **2000**

Chen, K., C. Hsu and D.-C. Su, Interferometric optical sensor for measuring glucose concentration, *Applied Optics*, Vol. 42 pp 5774–5776, **2003**

Cooper, M., Optical biosensors in drug discovery, *Nature reviews*, Vol. 1 pp 515–528, **2002**

Cooper, M., Label-free screening of bio-molecular interactions, *Analytical and Bioanalytical Chemistry*, Vol. 377 pp 834–842, **2003**

Cottier, K., M. Wiki, G. Voirin, H. Gao and R. Kunz, Label-free highly sensitive detection of (small) molecules by wavelength interrogation of integrated optical chips, *Sensors and Actuators B*, Vol. 91 pp 241–251, **2003**

Cross, G., A. Reeves, S. Brand, J. Popplewell, L. Peel, M. Swann and N. Freeman, A new quantitative optical biosensor for protein characterization, *Biosensors & Bioelectronics*, Vol. 19 pp 383–390, **2003**

Cunningham, B., P. Li, S. Schulz, B. Lin, C. Baird, J. Gerstenmaier, C. Genick, F. Wang, E. Fine and L. Laing, Label-free assays on the BIND system, *Journal of Biomolecular Screening*, Vol. 9 pp 481–490, **2004**

Cunningham, B., B. Lin, J. Qiu, P. Li, J. Pepper and B. Hugh, A plastic colorimetric resonant optical biosensor for multiparallel detection of label-free biochemical interactions, *Sensors and Actuators B*, Vol. 85 pp 219–226, **2002**

Davies, C., Introduction to immunoassay principles, in Wild, D. (Ed.), The immunoassay handbook, Nature publishing group, **2001**

de Feijter, J. A., J. Benjamins and F. A. Veer, Ellipsometry as a tool to study the adsorption behaviour of synthetic and biolpolymers at the air-water interface, *Biopolymers*, Vol. 17 pp 1759–1772, **1978**

Elender, G., M. Kühner and E. Sackmann, Functionalisation of Si/SiO2 and glass surfaces with ultrathin dextran films and deposition of liquid bilayers, *Biosensors & Bioelectronics*, Vol. 11 pp 565–577, **1996**

Fox, P., R. Scholten, M. Walkiewicz and R. Drullinger, A reliable, compact, low-cost Michelson wavemeter for laser wavelength measurement, *American Journal of Physics*, Vol. 67 pp 624–630, **1999**

Goodman, J., Introduction to Fourier Optics, McGraw-Hill, **1988**

Hartmann, S., Personal communication, **2005**

Hebestreit, H., Proteomics: an holistic analysis of nature's proteins, *Current Opinion in Pharmacology*, Vol. 1 pp 513–520, **2001**

Hecht, E., Optik, Oldenbourg Verlag, **2001**

Hendrickson, W., A. Pähler, J. Smith, Y. Satow, E. Merritt and R. Phizackerley, Crystal structure of core streptavidin determined from multi-wavelength anomalous diffraction of synchrotron radiation, *Proc. Natl. Acad. Sci.*, Vol. 86 pp 2190–2194, **1989**

Hermanson, G. T., A. K. Mallia and P. K. Smith, Immobilized affinity ligand techniques, Academic Press N.Y., **1992**

Hertzberg, R. P. and A. J. Pope, High-throughput screening: new technology for the 21st century, *Current Opinion in Chemical Biology*, Vol. 4 pp 445–451, **2000**

Hoffmann, C., Selbstorganisierende Organosilansysteme zur Funktionalisierung oxidischer Siliziumoberflächen für die gerichtete Peptid- und Proteinimmobilisierung, **2002**

Karlsson, R. and S. Löfas, Kinetic analysis of the interaction between an analyte in solution and an immobilized protein, in Cass, T. and F. Ligler (Eds.), Immobilized

Biomolecules in Analysis-a practical approach, pp 149–165, Oxford University Press, **1998**

Kogelnik, H., Theory of Optical Waveguides, in Tamir, T. (Ed.), Guided-Wave Optoelectronics, pp 7–87, Springer Verlag, **1988**

Kretschmann, E. and H. Raether, Radiative decay of non radiative surface plasmons excited by light, *Zeitschrift fuer Naturforschung*, Vol. 23A pp 2135–2136, **1968**

Kröger, K., J. Bauer, B. Fleckenstein, J. Rademann, G. Jung and G. Gauglitz, Epitope-mapping of transglutaminase with parallel label-free optical detection, *Biosensors & Bioelectronics*, Vol. 17 pp 937–944, **2002**

Kühlke, D., Optik - Grundlagen und Anwendungen, Verlag Harri Deutsch, **2004**

Kujawinska, M. and J. Wojciak, High accuracy Fourier transform fringe pattern analysis, *Optics and Lasers in Engineering*, Vol. 14 pp 325–339, **1991**

Lane, H. D., Antibodies: a laboratory manual, Cold Spring Harbor Laboratory Press N.Y., **1998**

Lang, C. and N. Pucker, Mathematische Methoden in der Physik, Spektrum Akademischer Verlag Berlin, **1998**

Laureyn, W., F. Frederix, A. Campitelli, J. J. Pireaux and G. Maes, The silanization of tantalum pentoxide for biosensor realization, *Poster presentation, source: internet*, **2001**

Le Grange, J. D. and J. L. Markham, Effects of surface hydration on the deposition of silane monolayers on silica, *Langmuir*, Vol. 9 pp 1749–1753, **1993**

Leatherbarrow, R. J. and P. R. Edwards, Analysis of molecular recognition using optical biosensors, *Current Opinion in Chemical Biology*, Vol. 3 pp 544–547, **1999**

Lehninger, A., D. Nelson and M. Cox, Prinzipien der Biochemie, Spektrum Akademischer Verlag, **1994**

Lindner, H., H. Brauer and C. Lehmann, Taschenbuch der Elektrotechnik und Elektronik, Fachbuchverlag Leipzig, **1999**

Lottspeich, F. and H. Zorbas, Bioanalytik, Spektrum Akademischer Verlag, **1998**

Lukosz, W., Principles and sensitivities of integrated optical and surface plasmon sensors for direct affinity sensing and immunosensing, *Biosensors & Bioelectronics*, Vol. 6 pp 215–225, **1991**

Lukosz, W., D. Clerc, P. Nellen, C. Stamm and P. Weiss, Output grating couplers on planar optical waveguides as direct immunosensors, *Biosensors & Bioelectronics*, Vol. 6 pp 227–232, **1991**

MacKenzie, R., Development of an interferometric biosensor, **2003**

Maisenhölder, B., Personal communication, **2004**

Meyer, M., Signalverarbeitung, Vieweg Verlag, **2003**

Morgan, H. and D. Taylor, A surface plasmon resonance immunosensor based on the streptavidin-biotin complex, *Biosensors & Bioelectronics*, Vol. 7 pp 405–410, **1992**

Myszka, D., Improving biosensor analysis, *Journal of Molecular Recognition*, Vol. 12 pp 279–284, **1999**

Myszka, D., Analysis of small-molecule interactions using BiacoreS51 technology, *Analytical Biochemistry*, Vol. 329 pp 316–323, **2004**

Myszka, D., X. He, M. Dembo, T. Morton and B. Goldstein, Extending the range of rate constants available from BIACORE: interpreting mass transport-influenced binding data, *Biophysical Journal*, Vol. 75 pp 583–594, **1998**

Nakadate, S., Phase detection of equidistant fringes for highly sensitive optical sensing. I. Principle and error analyses, *Journal of the Optical Society of America A*, Vol. 5 pp 1258–1264, **1988**

Nieba, L., A. Krebber and A. Plckthun, Competition BIACORE for measuring true affinities: large differences from values determined from binding kinetics, *Analytical Biochemistry*, Vol. 234 pp 155–165, **1996**

Nikitin, P. I., M. V. Valeiko and B. G. Gorshkov, New direct optical biosensors for multi-analyte detection, *Sensors and Actuators B*, Vol. 90 pp 46–51, **2003**

Pierce, http://www.piercenet.com, **2005**

Polzius, R., E. Dießel, F. Bier and U. Bilitewski, Real-time observation of affinity reactions using grating couplers: determination of the detection limit and calculation of kinetic rate constants, *Analytical Biochemistry*, Vol. 248 pp 269–276, **1997**

Polzius, R., T. Schneider, F. Bier and U. Bilitewski, Optimization of biosensing using grating couplers: immobilization on tantalum oxide waveguides, *Biosensors & Bioelectronics*, Vol. 11 pp 503–514, **1996**

Prime, K. and G. Whitesides, Self-assembled organic monolayers: model systems for studying adsorption of proteins at surfaces, *Science*, Vol. 252 pp 1164–1167, **1991**

Prime, K. and G. Whitesides, Adsorption of proteins onto surfaces containing end-attached oligo(ethylene oxide): a model system using self-assembled monolayers, *J. Am. Chem. Soc.*, Vol. 115 pp 10714–10721, **1993**

Ramsden, J., Optical biosensors, *Journal of Molecular Recognition*, Vol. 10 pp 109–120, **1997**

Saha, K., F. Bender and E. Gizeli, Comparative study of IgG binding to proteins G and A: nonequilibrium kinetic and binding constant determination with the acoustic waveguide device, *Analytical Chemistry*, Vol. 75 pp 835–842, **2003**

Saleh, B. and M. Teich, Fundamentals of Photonics, Addison-Wesley, **1990**

Savage, M. D., Avidin-Biotin Chemistry: A handbook, Pierce Chemical Co, **1992**

Sayle, R., http://www.umass.edu/microbio/rasmol/, **1993**

Schneider, B., E. L. Dickinson, M. D. Vach, J. V. Hoijer and L. V. Howard, Highly sensitive optical chip immunoassays in human serum, *Biosensors & Bioelectronics*, Vol. 15 pp 13–20, **2000**

Schneider, B., J. Edwards and N. Hartman, Hartman interferometer: versatile integrated optic sensor for label-free, real-time quantification of nucleic acids, proteins, and pathogens, *Clinical Chemistry*, Vol. 43 pp 1757–1763, **1997**

Schrüfer, E., Signalverarbeitung: Numerische Verarbeitung digitaler Signale, 2nd ed., Hanser Verlag, **1992**

Schütz, A., Einsatz der reflektometrischen Interferenzspektroskopie (RIfS) zur markierungsfreien Affinitätsdetektion für das Hochdurchsatzscreening, Dissertation, Universität Tübingen, **2000**

Sober, H., Handbook of Biochemistry 2nd ed., Chemical Rubber Co., Cleveland, Ohio, **1970**

Stamm, C., R. Dangel and W. Lukosz, Biosensing with the integrated-optical difference interferometer: dual-wavelength operation, *Optics Communications*, Vol. 153 pp 347–359, **1998**

Stevens, R., Design of high-throughput methods of protein production for structural biology, *Structure*, Vol. 8 pp R177–R185, **2000**

Superlum, Superluminescent Diode Modules-General Operation Instructions, Superlum Moscow, **2003**

Surolia, A., D. Pain and M. I. Khan, Protein A: nature's universal anti-antibody - a review on properties and applications of protein A, *Trends Biochem. Sci.*, Vol. 7 pp 74–76, **1982**

Tiefenthaler, K. and W. Lukosz, Sensitivity of grating couplers as integrated-optical chemical sensors, *Journal of the Optical Society of America B*, Vol. 6 pp 209–220, **1989**

Tovar, G., Funktionalisierung und Strukturierung von oxidischen Oberflächen mit biologischen und synthetischen Polymeren, **1995**

Tsukruk, V., I. Luzinov and D. Julthongpiput, Sticky molecular surfaces: epoxysilane self-assembled monolayers, *Langmuir*, Vol. 15 pp 3029–3032, **1999**

van der Merwe, P., Surface plasmon resonance, *source: internet*, pp 1–50, **2005**

Weast, R., Handbook of Physics and Chemistry, CRC Press, **1976**

Weber, P., D. H. Ohlendorf, J. J. Wendoloski and F. R. Salemme, Structural origins of high-affinity biotin binding to streptavidin, *Science*, Vol. 247 pp 85–88, **1989**

Weisser, M., G. Tovar, S. Mittler, W. Knoll, F. Brosinger, H. Freimuth, M. Lacher and W. Ehrfeld, Specific bio-recognition reactions observed with an integrated Mach-Zehnder interferometer, *Biosensors & Bioelectronics*, Vol. 14 pp 405–411, **1999**

www.biacore.com, Surface plasmon resonance, **2003**

www.invitrogen.com, AlexaFluor647 information, **2005**

Ymeti, A., J. Kanger, J. Greve, G. A. J. Besselink, P. Lambeck, R. Wijn and R. Heideman, Integration of microfluidics with a four-channel integrated optical Young interferometer immunosensor, *Biosensors & Bioelectronics*, Vol. 20 pp 1417–1421, **2005**

Ymeti, A., J. Kanger, R. Wijn, P. Lambeck and J. Greve, Development of a multichannel integrated interferometer immunosensor, *Sensors and Actuators B*, Vol. 83 pp 1–7, **2002**

# Publications

- K. Schmitt, B. Schirmer, C. Hoffmann, A. Brandenburg, P. Meyrueis (2006)
  Interferometric biosensor based on planar optical waveguide sensor chips for label-free detection of surface bound bioreactions, *in preparation*

- C. Hoffmann, K. Schmitt, B. Schirmer, S. Hartmann (2006)
  Rapid protein expression analysis with an interferometric biosensor in laboratory environment, *in preparation*

- K. Schmitt, B. Schirmer, A. Brandenburg (2005)
  Label-free detection of biomolecules by waveguide interferometry
  *Proc. SPIE* Vol. 5855, p. 459-462

- K. Schmitt, B. Schirmer, C. Hoffmann, A. Brandenburg (2005)
  Interferometer for label-free detection of biomolecules in MTP format
  Poster presentation, *SBS 11th Annual Conference and Exhibition*, Sep 11-15, Geneva

- K. Schmitt, C. Hoffmann (2005)
  Interferometrisches Messsystem zur markierungsfreien Analyse von biomolekularen Bindungsreaktionen, in *Aktuelle Wochenschau der GDCh*, 44

- K. Schmitt, B. Schirmer, A. Brandenburg (2005)
  Development of a label-free interferometric read-out system in MTP format
  Presentation, *4. Deutsches Biosensor Symposium*, Mar 13-16, Regensburg

- K. Schmitt, B. Schirmer, A. Brandenburg (2004)
  Development of a highly sensitive interferometric biosensor
  *Proc. SPIE* Vol. 5461, p. 22-29

# Vita

| | |
|---|---|
| Name: | Katrin Schmitt |
| Date of birth: | 22.08.1979 |
| Place of birth: | Emmendingen |

Education:

| | |
|---|---|
| 2006: | PhD thesis supervisor: Prof. Patrick Meyrueis<br>Title: A new waveguide interferometer for the label-free detection of biomolecules |
| 2003-2006 | PhD at the Université Louis Pasteur Strasbourg<br>carried out at the Fraunhofer IPM in Freiburg |
| 2003: | Master of Arts<br>Master thesis supervisor: Prof. Mark Raizen<br>Title: Optical neuronal guiding on the hypothalamic GnRH cell line GT1 |
| 2002-2003 | Study of physics at the University of Texas at Austin |
| 2001: | Vordiplom |
| 1999-2002 | Study of physics at the Bayerische Julius-Maximilians-Universität Würzburg |
| 1999: | Abitur |
| 1992-1999 | Dietrich-Bonhoeffer-Gymnasium Wertheim a. Main |
| 1990-1992 | Gymnasium Kenzingen |

**Résumé**: Le travail présenté dans cette thèse décrit le développement d'un nouveau dispositif interférométrique pour la détection des interactions biomoléculaires sans adjuvant. Ce capteur par onde évanescente détecte des espèces adsorbées car la masse à la surface change, basé sur le principe optique d'un intérferomètre de Young. Nous introduisons la base théoriques concernant l'architecture du système intérferométrique et présentons l'assemblage réalisé et bien dans une configuration à débit à deux canaux d'écoulement et bien dans un système statique de micro plate. Le biocapteur réalisé est optimisé et caractérisé par des tests réfractométriques ainsi que validé à l'échelle expérimentale en l'appliquant à l'examen de différents réactions immunitaires. Les résultats de cette application prouvent l'aptitude de ce biocapteur à haute sensibilité pour applications sans adjuvant dans le spectre du diagnostic, du criblage et du développement de tests d'immunité.

**Title**: A new waveguide interferometer for the label-free detection of biomolecules

**Abstract**: The work presented in this thesis describes the development of a new waveguide interferometer for the label-free detection of biomolecular interactions. This evanescent field sensor detects changes in surface mass coverage on the waveguide sensor chip in a setup based on the optical principle of a Young interferometer. We introduce the theoretical basis for the design of the interferometer system and present the realized design in both a two-channel flow-cell configuration and a microplate reading format. The realized biosensor is optimized and characterized by refractometric test measurements and experimentally validated by application measurements on different immunoreactions. The application measurement results show the suitability of this highly sensitive biosensor for label-free applications in fields like diagnostics, screening and immunoassay development.

**Discipline**: Physique et Photonique

**Mots-Clés**: Capteur interférométrique, détection sans adjuvant, champ évanescent, $Ta_2O_5$ guide d'onde
**Keywords**: interferometric sensor, label-free detection, evanescent field, $Ta_2O_5$ waveguide

**INTITULE ET ADRESSE DE L'U.F.R. ET DU LABORATOIRE:**
Ecole Nationale Supérieure de Physique de Strasbourg
Laboratoire des Systèmes Photoniques
Parc d'Innovation, Pôle API, Boulevard Sébastien Brant, 67400 ILLKIRCH - France
Téléphone: +33 (0) 390 244616
Fax: +33 (0) 390 244619

Fraunhofer Institut für Physikalische Messtechnik IPM
Heidenhofstr. 8
79110 Freiburg - Allemagne
Téléphone: +49 (0) 761 88570
Fax: +49 (0) 761 8857224